

Computational modelling of lithium ion batteries for electric vehicle applications

Analysis, Design and Implementation

A thesis submitted for the degree of Doctor of Philosophy of Imperial College London by

Krishnakumar Gopalakrishnan

Department of Mechanical Engineering
Imperial College London

October 2018

Supervised by

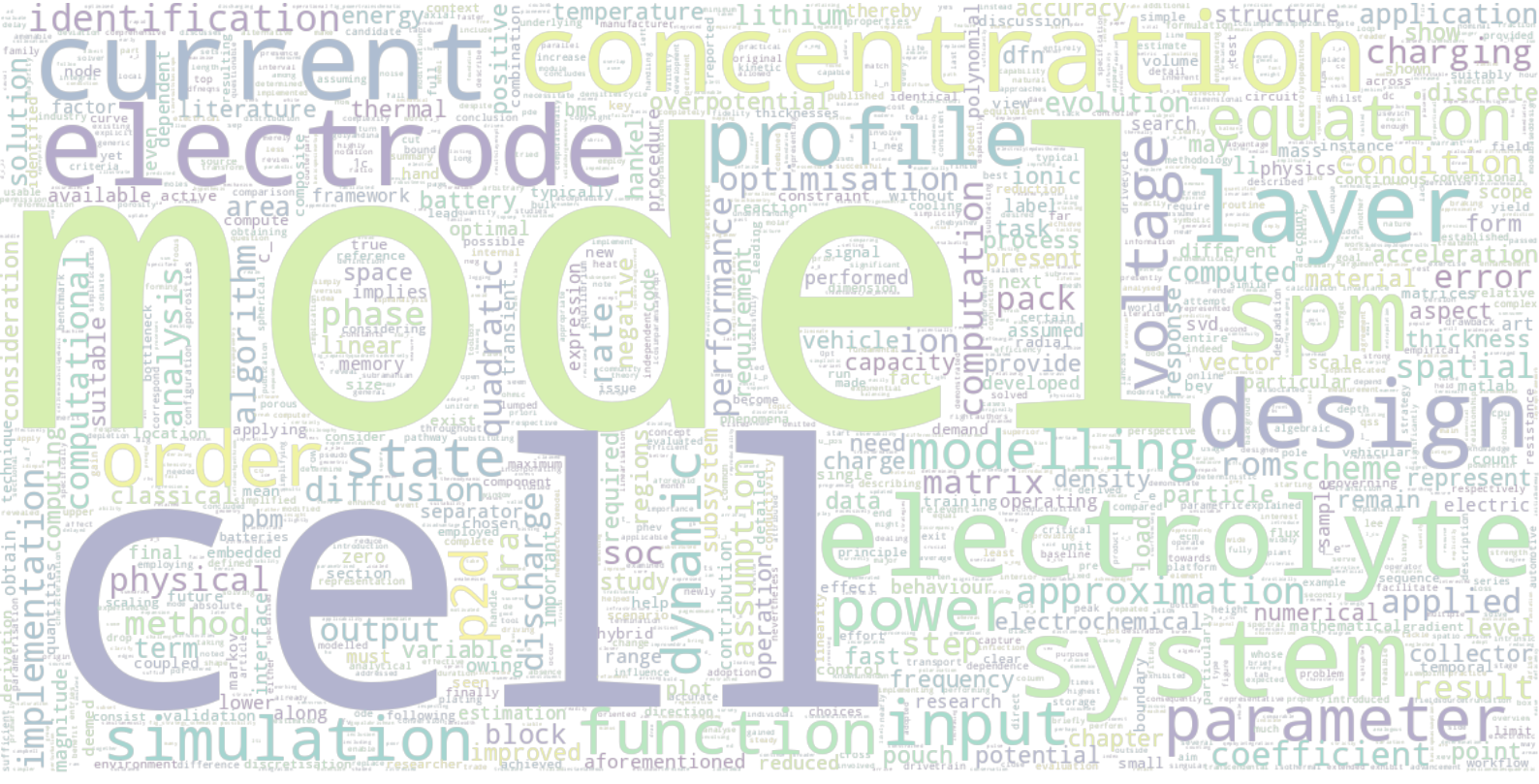
Dr Gregory J. Offer

Dr Monica Marinescu

Examined by

Dr Dhammika Widanalage

Dr Daniele Dini



The professional page of this thesis author is available at
www.linkedin.com/in/krishnakumargopalakrishnan/

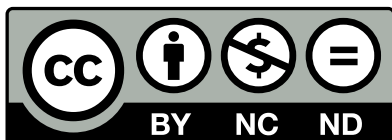


Declaration of Originality

I declare that the material presented in this thesis is the result of my own research except for specific portions wherein contributions from collaborators are acknowledged. Throughout this thesis, references are made to other published works and these have been appropriately cited. The material contained in this thesis has not been submitted, either in whole or in part, for a degree at Imperial College London or any other university.

Krishnakumar Gopalakrishnan
October 02, 2018
London, United Kingdom

Declaration of Copyright

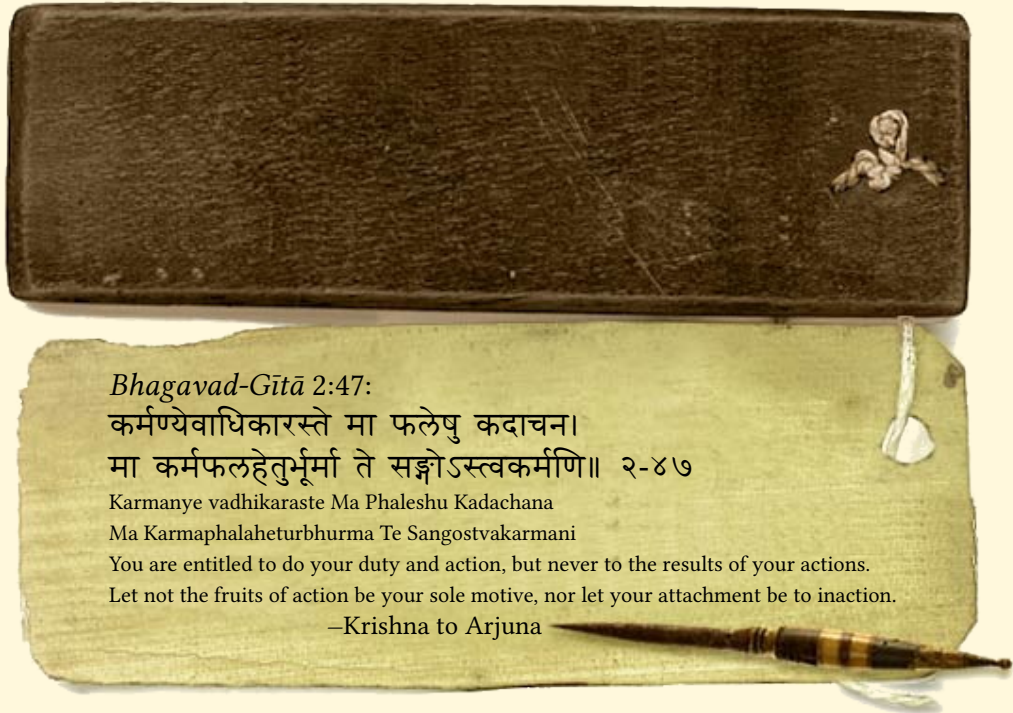


The copyright of this thesis rests with the author. Unless otherwise indicated, its contents are licensed under a [Creative Commons Attribution-NonCommercial-NoDerivatives 4.0 International \(CC BY-NC-ND 4.0\) Licence](#).

Under this licence, you may copy and redistribute the material in any medium or format on the condition that: you credit the author, do not use it for commercial purposes and do not distribute modified versions of the work. When reusing or sharing this work, ensure you make the licence terms clear to others by naming the licence and linking to the licence text. Please seek permission from the copyright holder for uses of this work that are not included in this licence or permitted under UK Copyright Law.

Dedication

To my
dear wife, Parvathy C.S.
and my parents, Gopalakrishnan P.K.
& Ananthalakshmi G. The sacrifices
that you all made for my success
is immeasurable and no amount
of words shall convey my sheer
gratitude. I am forever in
your debt for your
unconditional
love.



Bhagavad-Gītā 2:47:

कर्मण्येवाधिकारस्ते मा फलेषु कदाचन।

मा कर्मफलहेतुर्भूर्मा ते सङ्गोऽस्त्वकर्मणि॥ २-४७

Karmanye vadhikaraste Ma Phaleshu Kadachana

Ma Karmaphalaheturbhurma Te Sangostvakarmani

You are entitled to do your duty and action, but never to the results of your actions.

Let not the fruits of action be your sole motive, nor let your attachment be to inaction.

—Krishna to Arjuna

The image 'Thaliyola.jpg' (on which the Gita verse is overlaid by this thesis author) was sourced from Wikimedia Commons and is licensed CC-BY-SA 2.5

Acknowledgements

Obtaining a PhD has long been a dream of mine. This dream could not have come to fruition without the support of many of my well-wishers to whom I shall remain eternally grateful. Here, I would like to acknowledge their invaluable support in aiding this achievement.

I wish to incorporate *Sahadharminī* (companion soul) and *Bandhu-Mithradhikal* (relatives and friends) into the classical quartet of support pillars – *Matah* (mother), *Pitah* (father), *Guru* (teacher), *Deivam* (God) – commonly attributed as reasons for one's success in ancient Indian scriptures such as the Vedas, Shastras, Charitras, Itihasas and Purāṇas. Whilst making this personal amendment, I would like to de-emphasise any connotations of hierarchy amongst these support pillars, since they all play equally important roles in one's life.

During these four years, the level of support accorded by my wife Parvathy Chittur Subramanianprasad cannot be described in mere words. She voluntarily shouldered all matters of responsibility in the family so that I could focus solely on my research. At this prime of her youth, she has sacrificed so many material comforts and happily lived a relatively austere life by humbly accepting the financial constraints that are part and parcel of a student's life. In the same vein, I owe a lot to my parents Shri Gopalakrishnan P. K. and Smt. Ananthalakshmi G. It has been ten long years since I departed Indian shores in pursuit of higher studies. During all those years, despite ill-health and missing my presence at home, they have always urged me to carry on and complete my studies. Many a time, I have experienced a hopeless sense of incompleteness due to my inability to fulfil the basic duties of a son towards his parents, the least of which is spending quality time with them. However, my parents have always brushed aside their physical and financial difficulties to put my success above everything else.

It is needless to explain the crucial role of academic supervisors in the life of a doctoral candidate. I was extremely lucky to be bestowed with not just one, but two amazing supervisors here at Imperial College London – Dr Gregory J. Offer and Dr Monica Marinescu. I have immensely benefited from their supervision, both from technical and personal perspectives. Even during moments of sheer despair, my supervisors steadfastly held faith in my abilities. Their unflinching support contributed in no small measure for this success of mine. I also wish to acknowledge Dr Davide M. Raimondo who served as my unofficial supervisor and allocated months of his personal time for my research, often well outside regular working hours. I also wish to express my gratitude to Dr Gregory L. Plett who has always generously offered his technical expertise and guidance on all my research ideas. I am thankful to Dr Teng Zhang who mentored me in my initial days here and without his feedback, I could not have published my first journal article.

Although my interaction with them has sadly been on the wane in recent years, I am lucky to be a recipient of the blessings of my thatha (Shri Hariharan S) and paatti (Smt. Parvathi Hariharan), my affectionate grandparents, who have lived a life of humility, adhering to time-honoured traditions, whilst seeming to have an endless reserve of love

Acknowledgements

to bestow. During my childhood years, I have been fortunate to receive a tremendous amount of affection from my paternal grandmother, the late Smt. Annapoorni Ammal. On this momentous occasion, I hereby offer my *pranams* to her departed soul. I am immensely fortunate to have benedictions of the noble soul and towering figure, Acharyan Shri C R Krishna Iyer, affectionately known as 'thathanna', who has recently attained the lotus feet of Lord Guruvayoorappa. Although I have not yet attempted to imbibe the spiritual hints bequeathed by him, I hope to be a worthy beneficiary of its legacy with passage of time.

My father-in-law, Dr Subramaniaprasad C K or CKSP/Chithappa, as he is fondly known in our family circles, has been a father-like figure to me. From procuring transcripts at my alma-mater at the start of my PhD journey, all the way until providing regular feedbacks by proofreading this thesis, he has been a strong driving force behind my success.

Members of my extended family have long been staunch supporters of my educational aspirations. I vividly recollect the day I offered *namaskaarams* to Kaimal Chithappa before my first journey outside India prior to commencing Masters' studies at Virginia Tech. Shri Keshava Kaimal has been a strong motivator and was one of the earliest in my family to instigate a passion for engineering in me. His erudite teachings, such as the translation of "*Agnayeh, ithanna mamah (Oh Agni! This is not for me; this is for the society)*" still ring in my ears and I shall certainly strive to rise up to such lofty ideals.

I am immensely thankful to my sister, Smt. Radhika Balaji for constantly cheering me up. Not for a moment has her belief in me wavered, and I am relieved that I did not let her down. I would like to express my gratitude to Smt. Usha Prasad whose calmness and compassion were a solace during difficult personal times, and to Smt. Radha Ramaswamy, whose enthusiasm has been a buoyant motivator. I wish to thank Balaji Anna, Shri Ramaswamy Krishnan Chittur (Ramesh) and Dr Sandeep Sangameswaran, all of whom have been more than what even brothers could be and have always lent their support throughout.

Despite not having interacted much with her, the abilities of our beloved Manni Ammal from Chittur remind me that one should not be carried away by their achievements. In India, a female attending school in the pre-independence era, particularly in a rural Kerala village, is virtually unheard of. Not only did Manni top her high-school grades, she can reel off the Nobel-winning *Gitanjali* in fluent English, despite being hampered by the age-related afflictions of a nonagenarian. On the same note, I bow before the vast knowledge and humility of Shri Ramaswamy C. K. and Smt. Uma Sangameswaran which have endlessly inspired me.

I would like to express my sincere gratitude to my uncles and aunts (Shri Kannan, Smt. Subbalakshmi, Shri Jayakumar, Smt. Lalitha, Shri Nandakumar, Smt. Asha, Shri Kaimal, Smt. Ranjini, Shri Dwarakanath, and Smt. Brinda) and to all my cousins who used to note with pride that I was the first in the family to pursue higher studies outside India, and now the

Acknowledgements

first one to complete a doctoral degree. During difficult times in the PhD, I am glad to have had the cheerful support of Smt. Remya and Smt. Shyama, whose light-hearted approaches to many issues is certainly worth learning from. I am thankful to Lakshmi athai, Seetha athai and Shankar athimbere for their constant support and encouragement. I wish to express my gratitude to Shri. Sundar Krishnamurthy and Smt. Anu Sundar for all their help during the initial days to in the UK. The next generation in the immediate family – Arjith, Siddharth, Aditya and little Usha kutty – provided respite from the monotonicity of doctoral studies through their carefree joy and innocence.

On the technical front outside my specific research area, I would like to acknowledge the scores of individuals who have contributed to open-source projects for free. It is due to their efforts that much of the computational research work in the modern era is possible. I wish to express my admiration of Dr Donald E. Knuth and Dr Leslie Lamport for giving us the `TEX` typesetting system and the `LATEX` macro package respectively, that immensely helped in document authoring. I am also thankful to Bill Joy and Bram Moolenaar for developing the `vi` and `vim` text editors, whose sheer power eased my pain during coding and thesis writing sessions. I am thankful to the senior contributors (David Carlisle, Ulrike Fischer, Nicola Talbot, Jonathan Spratte to name just a few) of the TeX forum in the StackExchange family of portals, for their personalised support and patient answers to my rather dull questions. I also wish to tip my hat to Jorge Cham for his visceral portrayal of life in graduate school through PhD comics, that has never failed to put a smile on my face.

I would like to acknowledge members of my research group (Alexander Holland, Emma Vendola, Ian Campbell, Ian Hunt, Mei-Chin Pang, Oisin Shaw, Wasim Sarwar, Yan Zhao, Yu Merla to name a few) for their companionship during my studies here. Although few and far between, the conversations in the coffee room with my group members as well as those with other PhD students here at Imperial (James Tebbutt, Joel Henry, Manikandan Ganapathy, Marco Da Costa Alves, Xianyan Zhou and many others), had always lent the shared comfort of being fellow travellers on the same journey. I am deeply touched by the gesture of Mei-Chin, who prayed for me in the hours leading up to the thesis submission to give me strength and endurance. I am thankful to her for being a good friend with whom I could share technical as well as personal challenges. I would like to thank Abhilash, Ambuj, Anand, Arjun, Ashok, Bharath, Bibin, Divya, Elvira, Hari, Jagadees, Karthik, Krishnan, Lakshmi, Manu, Manoj, Nagu, PK, Praveen, Ram, Remya, Sakthi, Satya, Silby, Sita, Sreevisakh, Varsha, Vinay, Vivek, and Xavier for the camaraderie and time-tested friendship, the fond memories of which motivated me to carry on the battle, even in the bleakest of times.

Last, but not the least, I would like to thank God Almighty – the universal driving force well beyond any specific forms of personification – for enabling me to complete this doctorate degree. *Tathastu!* (so let it be).

Abstract

The realisation of Physics-Based Models (PBMs) of lithium ion cells in the Battery Management Systems (BMSs) of electric vehicles is studied through a three-pronged strategy – analysis, design and implementation. The survey of literature undertaken in the backdrop of this broad landscape reveals a dearth of model-based designs for automotive-grade pouch cells, which is therefore addressed in this work. Perusal of prior art in reduced-order battery modelling provides key guidance on topics meriting further investigation *viz.* the Discrete-Time Realisation Algorithm (DRA) scheme and the electrolyte-enhanced Single Particle Model (SPM) which are therefore carefully analysed here from the perspective of their embedded implementation. Owing to its familiarity and wide-spread popularity among relevant stakeholders, the Pseudo Two-Dimensional (P2D) implementation of the Doyle-Fuller-Newman (DFN) model is used as the PBM underpinning all research presented herein.

A computational framework to optimise the number of electrochemical layers within a pouch cell is developed. The chosen optimality criterion specifically addresses the two most pertinent issues that currently hinder the mass-market adoption of electric vehicles – range anxiety and fast charging. Driven by the need for a balanced capacity loading at both electrodes, a deterministic criterion for computation of electrode thicknesses is formulated. The search space of layer choices across all thermal scenarios is traversed with the least operation count through a novel application of the binary search algorithm. Numerical simulations of a lumped thermal model coupled with the P2D electrochemical model in conjunction with judiciously chosen exit conditions help to inform the number of layers needed to maximise the cell’s usable capacity whilst simultaneously satisfying the power requirements of fast charging. The P2D model is reformulated to accord it with the innate ability to accept power inputs. The model-led optimal layer design procedure thus developed is plating-aware, facilitating the extension of pack lifetimes whilst helping to bypass expensive empirical prototyping.

The computational bottleneck in the DRAs scheme for obtaining a state-space Reduced Order Model (ROM) is analysed and an improved alternative is proposed. It is revealed that the Singular Value Decomposition (SVD) of the large Block–Hankel matrix formed by the Markov parameters of the system is a key inefficient step. A streamlined approach that bypasses the redundant Block–Hankel matrix formation is presented as a drop-in replacement. Comparisons with existing scheme demonstrates a significant reduction in computation time

and memory usage brought about by the new method. The improved modelling accuracy of the new scheme in a resource-constrained computing environment is also demonstrated.

Owing to its simplicity, the SPM family of models is deemed to be the most promising ROM candidate that can usher in the use of PBMs in electric vehicles. An in-depth analysis of the SPM reveals an inherent mismatch between the accuracies of its voltage and State of Charge (SOC) predictions, thereby rendering it unsuitable as the plant model in state-estimation tasks. A comprehensive evaluation of the salient electrolyte-enhanced SPMs from literature reveals that most solutions are either mathematically intractable or overly simplistic. For the ionic concentration in the electrolyte, analysis of the quadratic approximation model, which straddles the boundary between computational complexity and mathematical tractability, reveals a poor temporal performance particularly at the current collector interfaces. However, it is capable of delivering acceptable levels of accuracy in computing the spatial profile of ionic concentration. Application of the Multi-Gene Genetic Programming (MGGP) technique exposes that the causal factor for this mediocre temporal performance is the equation deficiency of the underlying P2D model.

From an implementation perspective, the discrete-time formulation of SPMs is presented using the matrix exponential approach and its advantages over its continuous-time counterparts enumerated. Despite its inherent shortcomings, it is deemed that operating within the confines of the well-established foundations of the P2D dynamics represents a definitive step forward in bringing into fruition the goal of incorporating PBMs into vehicular BMSs. Therefore, the existing quadratic approximation model is retained for the electrolyte spatial concentration, whilst advocating the novel application of a system identification method for its temporal dynamics. After establishing linearity and time-invariance of the subsystems under consideration, discrete-time transfer functions of the number of moles per unit area of lithium ions in each electrode region is identified for the pertinent range of applied currents. The identified transfer functions are then employed in a composite SPM which demonstrates superior accuracy compared to the incumbent state of the art electrolyte-enhanced SPM, thereby demonstrating a substantial accomplishment from an implementation viewpoint. Although the advancements herein are reported for an isothermal implementation of the models, future enhancement through thermally coupled model derivations is advocated. Finally, the importance of parametrisation of the underlying PBM is acknowledged as a crucial unsolved aspect which needs the collective effort of the battery research community.

Project Outputs

Research Articles

- [1] **Ian D. Campbell**, **Krishnakumar Gopalakrishnan**, Monica Marinescu, Marcello Torchio, Gregory J. Offer and Davide M. Raimondo. “*Optimising lithium-ion cell design for plug-in hybrid and battery electric vehicles*”. *Journal of Energy Storage* 22 (Apr. 2019), pp. 228–238. ISSN: 2352-152X. DOI: [10.1016/j.est.2019.01.006](https://doi.org/10.1016/j.est.2019.01.006). *The highlighted authors are official joint first authors with equal contributions.*
- [2] Krishnakumar Gopalakrishnan, Teng Zhang and Gregory J. Offer. “*A Fast, Memory-Efficient Discrete-Time Realization Algorithm for Reduced-Order Li-Ion Battery Models*”. *Journal of Electrochemical Energy Conversion and Storage* 14.1 (Feb. 2017), p. 011001. ISSN: 2381-6872. DOI: [10.1115/1.4035526](https://doi.org/10.1115/1.4035526).
- [3] Andrea Pozzi, Gabriele Ciaramella, Krishnakumar Gopalakrishnan, Stefan Volkwein and Davide M. Raimondo. “*Optimal Design of Experiment for Parameter Estimation of a Single Particle Model for Lithiumion Batteries*”. *2018 IEEE Conference on Decision and Control (CDC)*. Dec. 2018, pp. 6482–6487. DOI: [10.1109/CDC.2018.8619340](https://doi.org/10.1109/CDC.2018.8619340).
- [4] Krishnakumar Gopalakrishnan and Gregory J. Offer. “*An Electrolyte Enhanced Composite Single Particle Model using System Identification Techniques*”. *IEEE Transactions on Sustainable Energy (manuscript in preparation)* (2018).

Conference Presentations


- [1] Ian D. Campbell, Krishnakumar Gopalakrishnan, Monica Marinescu, Marcello Torchio and Davide M. Raimondo. “*Optimising Lithium-ion Cell Design for Plug-in Hybrid and Battery Electric Vehicles*”. *UK Energy Storage Conference (UKES)*. Newcastle, UK, 2018. Presented by Ian D. Campbell.
- [2] Ian D. Campbell, Krishnakumar Gopalakrishnan, Monica Marinescu, Marcello Torchio, Gregory J. Offer and Davide M. Raimondo. “*Optimised Cell Layer Configurations via Modelling: Common Module Design for Electric Vehicle Platforms*”. *WMG/JLR-Catapult Energy Storage Conference 2017*. Coventry, UK, 2017. Presented by Ian D. Campbell.
- [3] Krishnakumar Gopalakrishnan, Teng Zhang and Gregory J. Offer. “*A Fast, Efficient Discrete-Time Realization Algorithm for Reduced-order Battery Models*”. *13th Symposium On Modeling & Experimental Validation Of Fuel Cells, Batteries & Electrolysers*. Lausanne: Swiss Federal Energy Office, 2016. URL: <https://modval13.epfl.ch/>.
- [4] Krishnakumar Gopalakrishnan, Teng Zhang and Gregory J. Offer. “*A Fast, Efficient Discrete-Time Realization Algorithm for Reduced-Order Battery Models*”. *Meeting Abstracts of the Electrochemical Society (ECS)*. Vol. MA2016-03. 2. June 2016, pp. 844–844. URL: <http://ma.ecsdl.org/content/MA2016-03/2/844.short>.

- [5] Wasim Sarwar, Gregory J. Offer, Krishnakumar Gopalakrishnan and Nick Green. “Combined Battery/Supercapacitor Hybridised Energy Storage Systems for Hybrid Electric Vehicles”. *Meeting Abstracts of the Electrochemical Society (ECS)*. Vol. MA2016-03. 2. Chicago, IL: The Electrochemical Society, June 2016, pp. 443–443. URL: <http://ma.ecsdl.org/content/MA2016-03/2/443.short>. Presented by Wasim Sarwar.

Posters

- [1] Krishnakumar Gopalakrishnan, Ian D. Campbell, Monica Marinescu, Marcello Torchio, Gregory J. Offer and Davide M. Raimondo. “Optimising lithium-ion cell design for plug-in hybrid and battery electric vehicles”. *15th Symposium on Modeling and Validation of Electrochemical Energy Devices, ModVal 2018*. Ed. by Erik J. Berg, Felix N. Büchi, Jens Eller and Lorenz Gubler. Aarau, Switzerland: Electrochemistry Laboratory, Paul Scherrer Institut PSI, Apr. 2018, p. 160. DOI: [10.3929/ETHZ-B-000240521](https://doi.org/10.3929/ETHZ-B-000240521). Created by Ian D. Campbell and presented by Monica Marinescu.
- [2] Ian D. Campbell, Krishnakumar Gopalakrishnan, Monica Marinescu, Marcello Torchio, Gregory J. Offer and Davide M. Raimondo. “Optimising Li-ion Cell Layers Rapid Cell Design For EV Fast Charging”. *Kraftwerk Batterie Advanced Battery Power Batterietagung 2018*. Münster, Germany: Haus Der Technik E.V., 2018. URL: <http://2018.battery-power.eu/en/>. Created and presented by Ian D. Campbell.
- [3] Ian D. Campbell, Krishnakumar Gopalakrishnan, Yatish Patel and Gregory J. Offer. *Reducing Li-ion Degradation with Applied Compression*. Solihull, UK, 2017. URL: <https://futurepowertrains.co.uk/2017/>. Created and presented by Ian D. Campbell.
- [4] Wasim Sarwar, Gregory J. Offer, Krishnakumar Gopalakrishnan and Nick Green. “Combined Battery/Supercapacitor Hybridised Energy Storage Systems for Hybrid Electric Vehicles”. *18th International Meeting on Lithium Batteries (IMLB)*. Chicago, IL: The Electrochemical Society (ECS), June 2016. URL: <https://ecs.confex.com/ecs/imlb2016/webprogram/Paper78263.html>. Created and presented by Wasim Sarwar.

Computer Software

- [1] Battery Optimal Layer Design (BOLD) toolbox (in MATLAB). Co-created by this thesis author along with Ian D. Campbell and Davide M. Raimondo. All three authors contributed equally to this toolbox. DOI: <https://doi.org/10.5281/zenodo.1016405>. MIT license.  https://github.com/ImperialCollegeESE/BOLD_Toolbox.
- [2] Finite volume codes (in Python) for numerical simulation of Pseudo Two-Dimensional (P2D) lithium ion battery model. Co-created in equal parts by this thesis author and Ian D. Campbell. Available upon request.

Contents

Title Page	1
Declaration of Originality and Copyright	3
Dedication	4
Acknowledgements	5
Abstract	8
Project Outputs	10
List of Figures	18
List of Tables	21
List of Algorithms	23
List of Program Code	23
List of Acronyms	24
List of Symbols	27
1 Introduction	34
1.1 Working Principle	35
1.2 Battery Modelling	37

1.2.1	Equivalent Circuit Models	38
1.2.2	Physics-Based Models	39
1.3	The Doyle-Fuller-Newman model	40
2	Review of Literature	44
2.1	Model Based Design for Batteries: Overview of Prior Art	44
2.1.1	Introduction	44
2.1.2	State of the art in cell-scale model-led design optimisations	47
2.2	Reduced Order Models: A New Classification Scheme	50
2.2.1	Frequency domain ROMs	53
2.2.2	Quasi-hybrid time/frequency domain ROMs	54
2.2.3	Hybrid ROMs based on equivalent circuits	58
2.2.4	Time-domain ROMs	60
2.2.5	Classification of ROMs – Interim summary	65
2.3	Review of Literature on the Single Particle Model Family	68
2.3.1	Overview of literature on conventional SPMs	68
2.3.2	State of the art in electrolyte enhanced SPMs	69
2.3.3	Conclusions	79
3	Model-based Design of Pouch Cells	81
3.1	Introduction	82
3.2	Energy/Power Trade-off in Pouch Cells by Layer Selection	82
3.2.1	Preliminary assumptions	83
3.2.2	Motivation	86
3.2.3	Quantitative demonstration of energy/power trade-off	88
3.3	Scope and Context within xEV Powertrain	91
3.3.1	System-level – vehicular platforms	91
3.3.2	Pack-level – strings, modules & cells	93
3.3.3	Cell-level – layers, cooling, electrochemical & thermal models	94
3.4	Enhancements/Modifications to Standard DFN Model	97

3.4.1	Augmentations to parameter set	97
3.4.2	Modification of standard DFN model to handle power inputs	103
3.4.3	Hybrid spectral-FV scheme	107
3.5	Computational Framework	110
3.5.1	Introduction and guidelines for flow diagram traversal	110
3.5.2	Acceleration pathway	111
3.5.3	Fast-charging pathway	115
3.5.4	Search algorithm	117
3.5.5	Upper and lower bounds on search space	119
3.5.6	Electrode thickness ratio for capacity balancing	120
3.5.7	Computation of electrode thicknesses per layer	121
3.5.8	Computation of layer-dependent cell mass	123
3.5.9	Computation of layer-dependent cell specific heat	124
3.6	Results and Discussion	124
3.6.1	Modelling Platform and Preconditioning	125
3.6.2	xEV configurations	127
3.6.3	Acceleration studies	129
3.6.4	Fast-charging studies	130
3.7	Conclusions	134
4	Computational Analysis and Numerical Reformulation of the DRA	136
4.1	Analysis of the Computational Bottlenecks of the DRA	138
4.1.1	Size of the Block-Hankel Matrix	140
4.1.2	Classical DRA – Memory (RAM) Requirements	141
4.1.3	Classical DRA – CPU Operation Count	142
4.1.4	Summary Effect of Computational Bottlenecks	143
4.2	Improved DRA for Battery Modelling	144
4.2.1	Candidate Schemes for Block-Hankel SVD	144
4.2.2	SVD Operation on a Virtual Block-Hankel Matrix	145

4.3	Golyandina-Usevich Algorithm	146
4.4	Customisations for Battery Modelling	147
4.5	Simulation Results and Discussion	148
5	Performance Evaluation of State of the Art in Single Particle Modelling	154
5.1	SPM Model Development	155
5.1.1	Geometry	155
5.1.2	Scope and Assumptions	156
5.1.3	Governing Equations	158
5.2	Numerical Implementation	169
5.2.1	Continuous-time Implementation	169
5.2.2	Conceptual Overview of Real-Time Processing	171
5.2.3	Sample Delay Considerations	174
5.2.4	Discrete-Time SPM Formulation	175
5.3	Desktop Simulation	178
5.3.1	Cell Parametrisation	180
5.3.2	Simulation Setup	185
5.3.3	Simulation Results	193
5.4	Quadratic Approximation of Ionic Spatial Concentration	201
5.4.1	Model derivation	201
5.4.2	Numerical implementation, simulation results and analysis	207
5.5	Conclusions	210
6	Implementing a New Electrolyte Model for Augmentation of the Basic SPM	211
6.1	Performance Analysis: Quadratic Approximation Model	212
6.1.1	Symbolic regression using Multi-Gene Genetic Programming	213
6.2	A New Electrolyte Model through System Identification	216
6.2.1	Scope and motivation	216
6.2.2	Selection of Methodology — Background and Rationale	218
6.3	Brief Introduction to System Identification	219

6.4	Overview of Black Box System Identification	220
6.4.1	Non-parametric methods	220
6.4.2	Parametric methods	221
6.4.3	Investigation of suitable system identification methodology	221
6.5	Introduction to Electrolyte Time-Evolution Subsystems	223
6.6	Design of Persistent Excitations	223
6.6.1	Training current profile	224
6.6.2	Validation current profile	225
6.7	Investigation of Linearity and Time Invariance	228
6.7.1	Time-invariance of the electrolyte time-evolution subsystems	228
6.7.2	Linearity analysis of the electrolyte time-evolution subsystems	230
6.8	Transfer Function Identification Procedure	234
6.8.1	The transfer operator and its model form	234
6.8.2	Estimation of transport delay	236
6.8.3	Choice of model structure	236
6.8.4	Starting guesses for coefficient orders	236
6.8.5	Refinement of coefficient orders using deterministic criteria	239
6.8.6	Final transfer function coefficients – Nonlinear optimisation	241
6.8.7	Numerical implementation of identified transfer functions	244
6.9	Performance Analysis of System Id Model: Ionic Concentration	246
6.9.1	Constant current inputs	246
6.9.2	Dynamic current inputs	251
6.10	Composite SPM Model with Electrolyte Dynamics	255
6.10.1	Computation of electrolyte overpotential	255
6.10.2	Terminal voltage computation of composite SPM	260
6.10.3	Validation of composite SPM: Terminal voltage accuracy	262
6.11	Conclusions	266

7	Conclusions	268
7.1	Physics-Based Models as a Design Tool	269
7.1.1	Conclusions from the model-based design study	269
7.1.2	Future work informed by the optimal layer design framework	270
7.2	Analysis of Salient Physics-based Reduced Order Models	271
7.2.1	Conclusions from analysis of the DRA-based state-space ROM	272
7.2.2	Future outlook for the DRA-based hybrid state-space ROM	272
7.2.3	Conclusions from analysis of the SPM family of models	273
7.2.4	Proposed analysis routes for the SPM modelling family	275
7.3	Implementation Aspects of Basic and Composite SPM	276
7.4	Closing Remarks	278
References		279
Appendix A Full Listing of Program Codes		297
A.1	MATLAB codes for continuous-time SPM	298
A.2	MATLAB codes for discrete-time SPM	301
Appendix B Permissions Summary		306
B.1	Summary of Copyright Permissions	307
B.2	Copyright Permissions for reuse of Figure 3.4	311
B.3	Copyright Permissions for reuse of Figure 3.8	313
B.4	Copyright Permissions for reuse of text, figures and tables of Chapter 4	315
B.5	Copyright Permissions for reuse of Figure 5.1	318
B.6	Copyright Permissions for reuse of Figure 5.3	322
B.7	Copyright Permissions for reuse of Figure 5.4	323
B.8	Copyright Permissions for reuse of Figure 5.13	324
Appendix C Colophon		329

List of Figures

1.1	Illustration of a lithium ion unit cell	36
2.1	Electrolyte conc. (time-snapshots) along cell thickness for 1C discharge	71
3.1	Qualitative comparison of the construction of one layer of a high-energy cell versus a high-power cell	87
3.2	Voltage curves for a 60 A galvanostatic discharge from 100 % SOC until cut-off voltage for a few layer choices in a pouch cell of fixed exterior height	89
3.3	Vehicle-to-cell hierarchical overview of an electrified powertrain architecture	92
3.4	Illustration of a cell-centred Finite Volume (FV) discretisation mesh	105
3.5	Schematic illustrating Chebyshev discretisation	109
3.6	Flow diagram of layer optimisation methodology	112
3.7	Stacking of layers within a pouch cell showing overhang of negative electrode	120
3.8	Two possible topologies for arranging the layers within a pouch cell	122
3.9	Optimal cell layer configurations for the BEV for a range of fast charging powers and thermal conditions	131
3.10	Optimal cell layer configurations for the PHEV for a range of fast charging powers and thermal conditions	131
3.11	Nominal capacity and charge passed versus layer count for constant current and constant power charging	133
4.1	ROM workflow using the classical DRA scheme	140

LIST OF FIGURES

4.2	Markov parameters of solid surface concentration at positive current collector	141
4.3	ROM workflow using the improved DRA scheme	148
4.4	Singular values computed by conventional and improved SVD methods	149
4.5	Memory usage of classical and improved DRA	150
4.6	Computation times for classical and improved DRA schemes	150
4.7	Comparison of singular values computed by conventional and improved SVD methods under a practical RAM limit of 10 GB	151
4.8	Solid surface concentrations at positive electrode/separator interface	152
5.1	Schematic illustration depicting geometrical origins of the SPM	156
5.2	Overview of real-time software implementation of a typical BMS	173
5.3	Timing diagram of a real-time software loop of a BMS	174
5.4	Timeline of BMS activities over multiple CPU cycles of a real-time controller	175
5.5	Surface plot of electrolyte conductivity	187
5.6	Electrolyte conductivity versus concentration at various cell temperatures . .	188
5.7	Voltage response of SPM and P2D models for capacity validation	192
5.8	Voltage responses of P2D and SPM to constant current discharge	194
5.9	SOC computed by P2D and SPM models for constant current discharge	195
5.10	Voltage and SOC computed by P2D and SPM for 1C constant current charge .	197
5.11	The UDDS drivecycle profile	198
5.12	Simulation results of P2D and SPM models to UDDS current profile	200
5.13	Co-ordinate systems for quadratic approximation of electrolyte concentration	202
5.14	Spatial distribution of electrolyte concentration for 1C discharge	208
5.15	Ionic concentrations at current collector interfaces over time for 1C discharge	209
6.1	Input current profile used as the training set for system identification	225

6.2	Input current profile used as the validation set for system identification	226
6.3	Demonstration of time-invariance of $Q_{e,n}(t)$ and $Q_{e,p}(t)$ subsystems	230
6.4	Illustration of linearity test for the $\tilde{Q}_{e,n}$ and $\tilde{Q}_{e,p}$ subsystems	233
6.5	Bode plots of the electrolyte time-evolution sub-systems	238
6.6	$\tilde{Q}_{e,n}(t)$ outputs from P2D and identified transfer function for training profile .	244
6.7	$\tilde{Q}_{e,p}(t)$ outputs from P2D and identified transfer function for training profile .	245
6.8	Spatial distribution of ionic concentration in electrolyte for a 1C discharge computed by the P2D, quadratic approximation & system identification models	247
6.9	Time evolution of ionic concentrations at current collectors computed by P2D, quadratic approximation & system identification models for 1C discharge	249
6.10	Transient phase of ionic concentration evolution at the two current collectors computed by P2D, quadratic & system identification models for 1C discharge	250
6.11	Time evolution of ionic concentrations at current collectors for P2D, quadratic approximation & system identification models with a UDDS input profile . . .	253
6.12	Zoomed view of ionic concentration at both current collectors computed by the P2D, quadratic & system identification models for the UDDS profile . . .	254
6.13	Contribution to electrolyte overpotential from the gradient-induced polarisa- tion term and the bulk solution resistance term for a 1C discharge	258
6.14	Electrolyte overpotential computed by the P2D and system identification models for a 1C discharge	259
6.15	Electrolyte overpotential computed by the P2D and system identification models for a UDDS load profile	260
6.16	Comparison of terminal voltages of composite SPM, basic SPM and the P2D model for a 1C discharge	263
6.17	Time evolution of ionic concentration computed by the P2D and system identification models at both current collectors for a 2C discharge	265
6.18	Terminal voltage output of – <i>a</i>) the P2D model, <i>b</i>) the basic SPM, and <i>c</i>) the composite SPM for a UDDS input profile	267

List of Tables

1.1	Governing equations and boundary conditions of the DFN model	41
2.1	Interim summary of salient literature on various ROMs categories	65
2.2	Summary of salient literature on electrolyte enhanced SPMs	77
3.1	Theoretical capacity & usable energy of a Li-ion cell for a few layer choices under a 60 A galvanostatic discharge	90
3.2	System-level simulation conditions & thermal parameters of an LCO cell . . .	126
3.3	Acceleration test parameters (common across xEV platforms)	127
3.4	Acceleration test parameters (specific to each xEV)	128
3.5	xEV acceleration test results	129
4.1	Parameters for Reduced Order Model (ROM) Computation	149
4.2	Salient Results – Classical vs. Improved DRA	153
5.1	Solid phase diffusion approximation methods	161
5.2	Simulation parameters of an LCO cell	181
5.3	Simulation data for capacity characterisation of P2D and SPM models	191
5.4	Error-metrics summary of basic SPM for constant current discharge	196

LIST OF TABLES

5.5	Error-metrics summary of basic SPM for UDDS current profile	199
5.6	Electrolyte equations & boundary conditions of DFN model in separator . . .	203
6.1	Transient & QSS expressions for electrolyte concentration obtained by MGGP	215
6.2	A sample of system identification results for $\tilde{Q}_{e,n}$	242
6.3	Error statistics for 1C galvanostatic discharge comparing the quadratic & system identification models	251
6.4	Error statistics for UDDS current for quadratic & system-id models	253
6.5	Error statistics for the basic, quadratic approximation and composite SPMs for 1C galvanostatic discharge	262
6.6	Error statistics for the basic, quadratic approximation and composite SPMs for a UDDS load profile	266
B.1	Summary of permissions for reuse of third-party copyrighted material	307

List of Algorithms

5.1	Continuous-time SPM	172
5.2	Discrete-time SPM	179
5.3	Quadratic approximation model for spatio-temporal electrolyte concentration	207

List of Program Code

A.1	MATLAB code for simulation of continuous time SPM	298
A.2	MATLAB code for simulation of discrete time SPM	301

List of Acronyms

ADC	Analog to Digital Converter
AER	All-Electric Range
AIC	Akaike's Information Criterion
ARMAX	Auto Regressive with Moving Average and Exogenous Inputs
ARX	Auto Regressive with Exogenous Inputs
BEV	Battery Electric Vehicle
BMS	Battery Management System
BOLD	Battery Optimal Layer Design
CAS	Computer Algebra System
CCCV	Constant Current Constant Voltage
CP	Constant Power
CPU	Central Processing Unit
DAC	Digital to Analog Converter
DAE	Differential Algebraic Equation
DFN	Doyle-Fuller-Newman
DFT	Discrete Fourier Transform
DMC	Dimethyl Carbonate
DRA	Discrete-Time Realisation Algorithm
EC	Ethylene Carbonate
ECM	Equivalent Circuit Model
EIS	Electrochemical Impedance Spectroscopy
EMC	Ethyl Methyl Carbonate
ERA	Eigensystem Realisation Algorithm
ETFE	Empirical Transfer Function Estimate
EUDC	Extra-Urban Driving Cycle

FDM	Finite Difference Method
FFT	Fast Fourier Transform
FRF	Frequency Response Function
FV	Finite Volume
GITT	Galvanostatic Intermittent Titration Technique
GPM	Galerkin Projection Method
HWFET	Highway Fuel Economy Test
ICE	Internal Combustion Engine
IMA	Integral Method Approximation
ISR	Interrupt Service Routine
IV	Instrumental Variable
IVP	Initial Value Problem
LCO	Lithium Cobalt Oxide
LFP	Lithium Iron Phosphate
LHS	Left-Hand Side
LTI	Linear Time-Invariant
MAE	Mean Absolute Error
MDL	Rissanen's Minimum Description Length
MGGP	Multi-Gene Genetic Programming
MIMO	Multi Input Multi Output
MPM	Markov Parameter Matrix
NEDC	New European Driving Cycle
OCP	Open Circuit Potential
OCV	Open Circuit Voltage
ODE	Ordinary Differential Equation
OE	Output Error
OLS	Ordinary Least Squares
P2D	Pseudo Two-Dimensional
PBM	Physics-Based Model

PDAE	Partial Differential Algebraic System
PDE	Partial Differential Equation
PHEV	Plug-in Hybrid Electric Vehicle
PMSM	Permanent Magnet Synchronous Motor
PP2D	Polynomial Profile P2D
PRBS	Pseudorandom Binary Signal
PWL	Piecewise Linear
QSS	Quasi-Steady State
RAM	Random Access Memory
RBS	Random Binary Signal
RGS	Random Gaussian Signal
RHS	Right-Hand Side
RLS	Recursive Least Squares
RMS	Root Mean Square
ROM	Reduced Order Model
SEI	Solid-Electrolyte Interphase
SIMO	Single Input Multiple Output
SISO	Single Input Single Output
SNR	Signal to Noise Ratio
SOAP	State of Available Power
SOC	State of Charge
SoV	Separation of Variables
SPDT	Single Pole Double Throw
SPM	Single Particle Model
SSA	Singular Spectrum Analysis
SVD	Singular Value Decomposition
UDDS	Urban Dynamometer Driving Schedule
VOP	Variation of Parameters
xEV	Battery Electric/Plug-in Hybrid Electric Vehicle
ZOH	Zero Order Hold

List of Symbols

List of Latin Symbols

$a_{\text{man.}}$	Acceleration rate specified by the vehicle manufacturer [m s^{-2}]
$a_{\text{std.}}$	Acceleration rate specified by a governing vehicular standard [m s^{-2}]
a_s	Specific interfacial surface area of the electrode [$\text{m}^2 \text{m}^{-3}$]
\vec{a}	Time-varying coefficient vector for the quadratic spatial approximation model of ionic concentration in electrolyte
A, A_{cell}	Overall electrochemically active cross-sectional surface area of all cell layers [m^2]
A_{refcell}	Overall electrochemically active surface area of the reference cell [m^2]
A_{elec}	Active cross-sectional surface area per layer <i>i.e.</i> , for a unit cell [m^2]
$A \in \mathbb{R}^{n \times n}$	System matrix corresponding to ‘ n ’ states following standard state-space notation
A_{tabs}	Area of the cell tabs [m^2]
A_v	Frontal area of the (hybrid) electric vehicle [m^2]
brugg	Bruggeman coefficient (empirical) to account for the tortuosity of a medium
$B \in \mathbb{R}^{n \times m}$	Input matrix corresponding to ‘ n ’ states and ‘ m ’ inputs following standard state-space notation
c_λ	Specific heat capacity of each component $\lambda \in \{\text{neg, sep, pos, Al, Cu, pouch, LiPF}_6\}$ in a pouch cell [$\text{J kg}^{-1} \text{K}^{-1}$]
c_{avg}	Lumped (average) specific heat capacity of a pouch cell [$\text{J kg}^{-1} \text{K}^{-1}$]
c_e	Concentration of Li^+ ions in the electrolyte [mol m^{-3}]
$c_{e,0}$	Initial concentration of Li^+ ions in the electrolyte [mol m^{-3}]
c_s	Concentration of Li^0 in the solid phase <i>i.e.</i> , electrode [mol m^{-3}]

List of Symbols

\bar{c}_s	Bulk concentration of Li^0 in the electrode [mol m^{-3}]
$c_{s,\text{max}}$	Saturation concentration of the electrode [mol m^{-3}]
$c_{s,\text{surf}}, c_{s,e}$	Concentration of Li^0 at the electrode surface [mol m^{-3}]
c_s^*	Surface concentration of Li^0 <i>i.e.</i> , same as $c_{s,\text{surf}}, c_{s,e}$, but specifically for the negative electrode in the layer optimisation framework for fast charging [mol m^{-3}]
$C \in \mathbb{R}^{p \times n}$	Output matrix corresponding to ‘ p ’ outputs and ‘ n ’ states following standard state-space notation
C_d	Coefficient of drag for the vehicle body
C_r	Coefficient of rolling resistance for the vehicle body
D	Intrinsic ionic diffusivity of the electrolyte [$\text{m}^2 \text{s}^{-1}$]
D_{eff}	Effective ionic diffusivity of the electrolyte [$\text{m}^2 \text{s}^{-1}$]
D_s	Intrinsic diffusivity of the electrode material [$\text{m}^2 \text{s}^{-1}$]
$D_{s,\text{eff}}$	Effective diffusivity of the solid phase [$\text{m}^2 \text{s}^{-1}$]
$D \in \mathbb{R}^{p \times m}$	Output matrix corresponding to ‘ p ’ outputs and ‘ m ’ inputs following standard state-space notation
$e[k]$	White noise sequence assumed in system identification
E_{a,D_s}	Activation energy for solid phase diffusivity [J mol^{-1}]
E_{a,k_r}	Activation energy for solid phase reaction rate coefficient [J mol^{-1}]
F	Faraday constant [C mol^{-1}]
F_1	Continuous time emulation frequency for formulating the DRA [Hz]
g	Acceleration due to gravity [m s^{-2}]
G_q	Generic transfer operator used in system identification to denote system dynamics
h	Convective heat transfer coefficient [$\text{W m}^{-2} \text{K}^{-1}$]
H	Generic notation for a Block-Hankel matrix
H_{pouch}	Pouch height [m]
H_q	Generic transfer operator in system identification for disturbance dynamics
i	Current density experienced by each electrochemical layer (unit cell) [A m^{-2}]

List of Symbols

I	Load current applied at the terminals of the cell (at time-step k) [A]
j	Molar flux density at particle surface [$\text{mol m}^{-2} \text{s}^{-1}$]
k_r	Intrinsic reaction rate coefficient at the electrode surface [$\text{m}^{2.5} \text{mol}^{0.5} \text{s}^{-1}$]
$k_{r,\text{eff}}$	Effective reaction rate coefficient at the electrode surface [$\text{m}^{2.5} \text{mol}^{0.5} \text{s}^{-1}$]
l_λ	Thickness of a specific region λ of a unit cell, $\lambda \in \{\text{neg, sep, pos, Al, Cu}\}$ [m]
l_{ce}	Sum of thicknesses of the negative and positive electrodes in each layer [m]
l_{ratio}	Ratio of thickness of negative electrode to that of positive electrode
l_{tot}	Combined thickness of negative electrode, separator and positive electrode [m]
$L(\cdot)$	Scalar loss function used in non-linear optimisation step of system identification
L_{pouch}	Exterior length of pouch used to accommodate a typical automotive-grade electrochemical cell [m]
L_{stack}	Combined thickness of all unit cells within a pouch [m]
m_λ	Mass of each constituent component $\lambda \in \{\text{neg, sep, pos, Al, Cu, pouch, LiPF}_6\}$ for all electrochemical layers within a pouch cell [kg]
m_{cell}	Cell mass, computed as $\sum m_\lambda$ [kg]
M_{cells}	Total mass of all cells in a battery pack [kg]
M_c	Mass of the chassis of a (hybrid) electric vehicle [kg]
M_o	Mass of pack overhead (without cells) [kg]
M_p	Payload mass for vehicular acceleration test [kg]
M_v	Total mass of the vehicle [kg]
n	Number of layers <i>i.e.</i> , electrochemical unit-cells within the cell's pouch
n_a	Number of feedback coefficients used in system identification
n_b	Number of feedforward coefficients used in system identification
n_{cells}	Overall number of cells in the battery pack
$n_{c,\lambda}$	Number of coefficients for a suitable spatial approximation polynomial model of Li^+ ions in electrolyte for each of the cell regions $\lambda \in \{\text{neg, sep, pos}\}$
n_{feas}	An intermediate layer choice during iterative search that achieves success in satisfying acceleration/fast charging power requirements
$n^{(i)}$	Layer choice presently being trialled in an iterative search for the optimal value

n_k	Number of transport delay samples used in system identification
n_{\max}	Upper bound for the search space for the optimal layer search algorithm
n_{\min}	Lower bound for the search space for the optimal layer search algorithm
$n_{\text{opt}}^{\text{acc}}$	Optimal number of layers that satisfies power demanded during acceleration without violating termination criteria
$n_{\text{opt}}^{\text{fastchg}}$	Optimal number of layers that satisfies fast charging requirements without violating termination criteria
n_{refcell}	Number of layers (unit cells) within the chosen reference cell
N	Number of samples collected for each Markov parameter
N_a	Number of FV discretisation nodes in the through-thickness (axial) direction
N_r	Number of Chebyshev collocation nodes in the radial direction
p	Generic notation for power density experienced by each layer (unit cell) [W m^{-2}]
p^{acc}	Power density experienced by each electrochemical layer (unit cell) during acceleration phase [W m^{-2}]
p^{fastchg}	Power density experienced by each electrochemical layer (unit cell) during fast charging [W m^{-2}]
$p_{\text{cell}}^{\text{acc}}$	Power demanded at the terminals of each cell during the acceleration phase of a (hybrid) electric vehicle [W]
$p_{\text{cell}}^{\text{fastchg}}$	Power applied at the cell terminals while fast charging a (hybrid) electric vehicle [W]
$p_{\text{batt}}^{\text{acc}}$	Power demanded at the terminals of the battery pack during acceleration phase of a (hybrid) electric vehicle [W]
$p_{\text{batt}}^{\text{fastchg}}$	Power applied at the terminals while fast charging the battery pack of a (hybrid) electric vehicle [W]
P_k	Power applied to a discrete-time equivalent circuit cell model (at time-step k) [W]
P_{drag}	Power required to overcome air resistance to a vehicle's motion [W]
P_{grade}	Power required to negotiate a road gradient [W]
P_{mass}	Power required to accelerate a vehicle's mass from standstill [W]
P_{roll}	Power required to overcome rolling resistance to a vehicle's motion [W]
P_w	Power experienced at the wheels of a (hybrid) electric vehicle [W]

List of Symbols

\bar{q}_λ	Volume averaged concentration flux <i>i.e.</i> , the average change of concentration with respect to the radial position r , $\lambda \in \{\text{neg, pos}\}$ [$\text{mol m}^{-2} \text{s}^{-1}$]
$Q_{e,\lambda}$	Moles of Li^+ ions in the electrolyte for each of the cell regions $\lambda \in \{\text{neg, sep, pos}\}$ per unit cross-sectional area [mol m^{-2}]
$\tilde{Q}_{e,\lambda}$	Debiased (by removal of initial value) moles of Li^+ ions in the electrolyte for each of the cell regions $\lambda \in \{\text{neg, pos}\}$ per unit cross-sectional area [mol m^{-2}]
Q_n	Theoretical capacity of a pouch cell with n layers [Ah]
Q_{neg}	Theoretical capacity of the negative electrode of a pouch cell with n layers [Ah]
Q_{pol}	Thermal power dissipated due to internal heat of polarisation [W]
Q_{pos}	Theoretical capacity of the positive electrode of a pouch cell with n layers [Ah]
r	Radial dimension <i>i.e.</i> , the continuous co-ordinate along the particle radius where solid phase concentration is to be computed [m]
Δr	Spacing between discretisation nodes in the radial direction within each particle [m]
\tilde{r}	Radial dimension in the Chebyshev domain $\tilde{r} \in [-1, 1]$ [m]
R	Universal gas constant [$\text{J mol}^{-1} \text{K}^{-1}$]
R_0, R_{eq}	Effective series resistance of an equivalent circuit cell model (at time-step k) [Ω]
\mathbb{R}	Real co-ordinate space
R_p	Representative particle radius of the solid phase as used in the model [m]
t	Time [s]
$t_{\text{f,man.}}$	Manufacturer-specified acceleration time (from standstill to $v_{\text{f,man.}}$) [s]
$t_{\text{f,std.}}$	Acceleration time (from standstill to $v_{\text{f,std.}}$) as specified by a governing standard [s]
t_{max}	Time limit for fast charging (as per level 3 fast charging specifications) [s]
t_+^0	Transference number of Li^+ ions in the electrolyte with respect to the solvent
T, T_{cell}	Lumped cell temperature (at time-step k) [K]
T_{sink}	Coolant temperature used in tab-cooling of the cell [K]
T_{init}	Cell temperature at the beginning of acceleration/fast charging [K]
T_{max}	Maximum allowed cell temperature [K]
T_{pouch}	Thickness of the pouch material [m]

T_s	Discrete-Time model sample rate [s]
$\mathbf{u} \in \mathbb{R}^{m \times 1}$	Input vector with ‘ m ’ inputs following standard state-space notation
\mathcal{U}	Open circuit potential of the electrode [V]
v_b, v_{base}	Base speed of a (hybrid) electric vehicle <i>i.e.</i> , the speed at which the drivetrain motor switches from the torque-limited region to power-limited region [m s^{-1}]
$v_{f,man.}$	Manufacturer-specified final speed to be achieved at the end of acceleration phase [m s^{-1}]
$v_{f,std.}$	Final speed to be achieved at the end of acceleration phase as specified by a governing standard [m s^{-1}]
V, V_{cell}	Terminal voltage of the cell (at time-step k). Also denoted by v_k [V]
V_{max}	Upper cut-off voltage of the cell [V]
V_{min}	Lower cut-off voltage of the cell [V]
W_{pouch}	Exterior width of pouch used to accommodate a typical automotive-grade electrochemical cell [m]
x	Axial dimension <i>i.e.</i> , the continuous co-ordinate along the through-thickness direction of the cell [m]
Δx	Spacing between nodes in the axial (through-thickness) direction [m]
$\mathbf{x} \in \mathbb{R}^{n \times 1}$	State vector with ‘ n ’ states following standard state-space notation
$\dot{\mathbf{x}} \in \mathbb{R}^{n \times 1}$	Time derivative of the state vector \mathbf{x} <i>i.e.</i> , $\frac{d\mathbf{x}}{dt}$ in a state-space formulation
$\mathbf{y} \in \mathbb{R}^{p \times 1}$	Output vector with ‘ p ’ outputs following standard state-space notation
z	State of Charge of the cell
z^*	Target State of Charge for fast charging
z_{max}	Upper cut-off for the State of Charge of the cell
z_{min}	Lower cut-off for the State of Charge of the cell
\mathbb{Z}	Set of integers
Z	Road gradient for acceleration tests of a (hybrid) electric vehicle is performed

List of Greek Symbols

α	Charge transfer coefficient at the surface of an electrode
ε	Electrode porosity <i>i.e.</i> , volume fraction of electrolyte phase within the electrode

ε_{fi}	Filler/binder volume fraction
ε_{s}	Solid phase volume fraction
η	Electrode overpotential [V]
η_{dt}	Overall lumped efficiency of the drivetrain components (excluding battery pack) of a (hybrid) electric vehicle
κ	Intrinsic ionic conductivity of the electrolyte [S m^{-1}]
κ_{eff}	Effective ionic conductivity of the electrolyte [S m^{-1}]
ω_{c}	Corner frequency in a frequency response function [rad s^{-1}]
Ω	Control volume in a standard finite-volume discretisation scheme
ϕ_{e}	Electric potential in the electrolyte phase [V]
ϕ_{s}	Electric potential of the electrode [V]
ρ_{λ}	Density of each constituent component $\lambda \in \{\text{neg, sep, pos, Al, Cu, pouch, LiPF}_6\}$ of the cell [kg m^{-3}]
ρ_{air}	Air density at acceleration test conditions [kg m^{-3}]
σ	Intrinsic electronic conductivity of the electrode [S m^{-1}]
σ_{eff}	Effective electronic conductivity of the electrode [S m^{-1}]
Σ	Matrix of singular values
θ	Surface stoichiometry of an electrode
$\theta_{0\%}$	Surface stoichiometry of the given electrode that corresponds to 0 % State of Charge of the cell
$\theta_{100\%}$	Surface stoichiometry of the given electrode that corresponds to 100 % State of Charge of the cell

Other Generic Nomenclature

neg	Denotes the negative electrode region. Alternatively, a subscripted 'n' is also used.
sep	Denotes the separator region. Alternatively, a subscripted 's' is also used.
pos	Denotes the positive electrode region. Alternatively, a subscripted 'p' is also used.
neg/sep	Denotes the negative electrode/separator interface
sep/pos	Denotes the positive electrode/separator interface
neg/Cucc	Denotes the negative electrode/Copper current collector interface
pos/Alcc	Denotes the positive electrode/Aluminium current collector interface

1

Introduction

1.1	Working Principle	35
1.2	Battery Modelling	37
1.2.1	Equivalent Circuit Models	38
1.2.2	Physics-Based Models	39
1.3	The Doyle-Fuller-Newman model	40

TIGHTENING emissions regulations in various industrial sectors have led to a renewed interest in sustainable energy sources in recent years. In particular, the burgeoning demand for clean energy has prompted the automotive and consumer electronics industries to explore advanced methods of energy storage [1]. Li-ion batteries are seen as key enablers in this quest due to the attractiveness of their high energy and power densities compared to other competing non-conventional energy storage technologies [2]. However, with this surge in energy storage demands comes stricter requirements for their longevity, performance, and adhesion to safety requirements, particularly for adoption in mainstream transport electrification [3]. In contrast to other incumbent technologies, lithium-ion batteries have

several advantages such as high energy density, long life-cycles, low internal resistance, low self-discharge, long cycle life, fast charge and discharge cycles [4, 5]. This makes them the preferred choice for storage and on-demand retrieval of energy in modern consumer electronics and Battery Electric/Plug-in Hybrid Electric Vehicles (xEVs).

1.1 Working Principle

This section provides a brief overview of the essential chemistry principles that helps to describe the working principle of a lithium ion battery and represents the author's digested summary of the introductory concepts presented in Plett [5].

Figure 1.1 depicts the construction of one electrochemical layer of a lithium ion unit cell. The positive electrode consists of porous particles of Lithium-Transition Metal Oxide (MO) compounds. The negative electrode typically employs some variant of microporous graphite. The porous nature of the electrodes provide pathways for lithium ion conduction through the electrolyte. Due to the special construction of the electrode structure, there exist interstitial sites which act as intercalation spots for lithium shuttling between the two electrodes. The electrolyte, which floods the cell, helps in the conduction of Li^+ ions. The separator membrane allows the passage of these ions between the two electrodes, but prevents internal short-circuit by inhibiting electronic conduction through it. The current collectors facilitate passage of electrons generated during the charge transfer at particle surface to the external circuit.

At the fully charged condition, the majority of lithium in the system is stored within the negative electrode microstructure. During discharge, Li^0 atoms diffuse out of deep interstitial sites towards the surface of the particles in the negative electrode. At the surface (electrode-electrolyte interface), a charge-transfer process takes place according to Butler-Volmer kinetics (see eq. (1.7)), leading to the formation of Li^+ ions and electrons. The electrons are passed to the external circuit through the Cu current collectors onto which the conductive matrix composed of the negative electrode material and binders is coated. The Li^+ ions travel through the electrolyte phase, crossing the separator membrane to the positive electrode where they encounter an electron influx from the external circuit. A charge transfer reaction takes place at the surface of the positive electrode particles, leading to the formation of neutral Li^0 atoms that diffuse into the positive electrode microstructure.

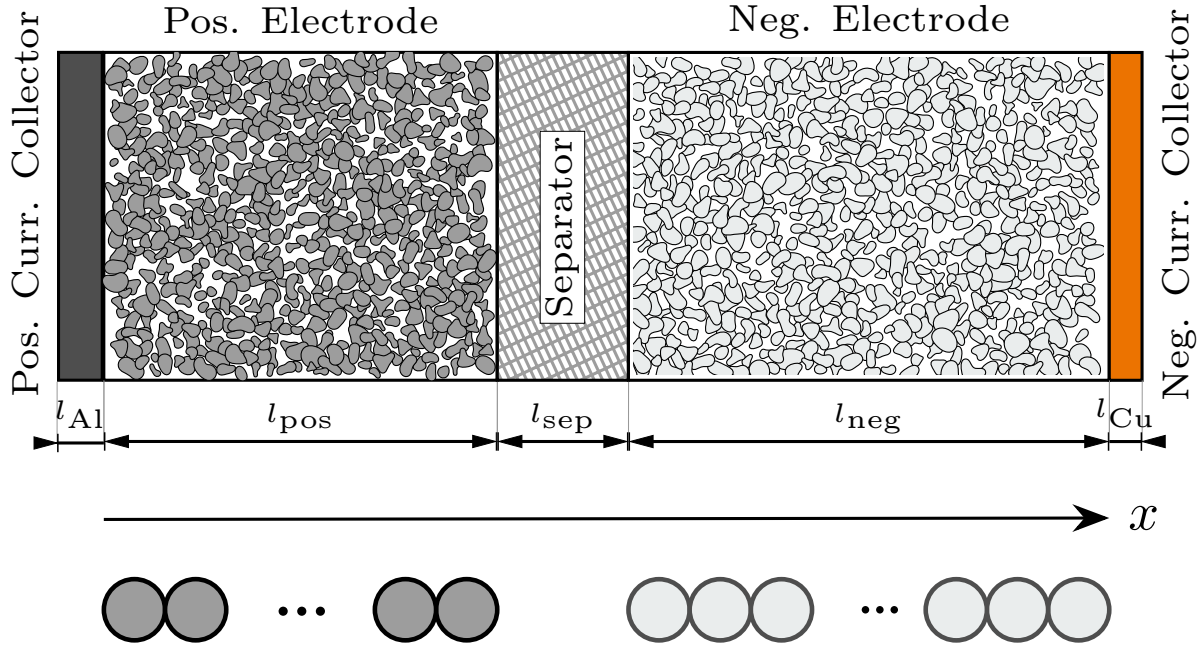
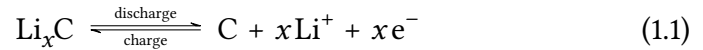


Figure 1.1 Schematic depicting the basic construction of a lithium ion unit cell.

During the charging process, the reverse phenomena occur. Lithium is de-intercalated from the positive electrode and a similar charge-transfer happens at the surface, leading to the formation of Li^+ ions which reach the negative electrode by passing through the separator. At the surface of the negative electrode particles, these ions absorb electrons from the external circuit, leading to the formation of neutral Li^0 that diffuses into interior vacant spaces in the layered graphite electrode. Equations (1.1) and (1.2) summarise the reactions during the charging and discharging process at the surfaces of both electrode materials.



where M represents a transition metal compound such as $\text{Ni}_{1/3}\text{Co}_{1/3}\text{Mn}_{1/3}$ (NMC), $\text{Ni}_{0.8}\text{Co}_{0.15}\text{Al}_{0.05}$ (NCA) amongst other choices [4]. Assuming no loss of cycleable lithium due to parasitic side reactions or through other mechanisms, the process is fully reversible.

The electrochemical potential at each electrode is dependent upon the extent of its lithiation. An empirical relationship of each electrode's potential as a function of its stoichiometry can be obtained, and is dependent upon the specific design and material

properties of each active material under consideration. Finally, the Open Circuit Voltage (OCV) of the cell is obtained by subtracting the negative electrode potential from its positive electrode counterpart.

1.2 Battery Modelling

Through accurate model representations of the electrochemical-thermal behaviour of the cell, advanced monitoring and control strategies can be deployed to tackle the current research topics in Li-ion batteries such as increasing cycle-life, improving operational safety and performance [5]. Over the past two decades, efforts have been made to construct models to describe the physical, electrical, thermal, electrochemical and system-level performance of Li-ion cells, leading to modelling strategies with various levels of sophistication. For the interested reader, the article by Grazioli *et al.* [6] provides a broad introduction to the topic of computational modelling of lithium ion batteries. Large in-roads into the depth of the modelling art can be made by perusing comprehensive books on this topic such as those by Plett [5], Hariharan [7], and Rahn and Wang [8].

The need to address the operational challenges of lithium ion batteries in an embedded environment such as on-board an electric vehicle has led to an increased impetus on the development of advanced Battery Management Systems (BMSs) [9]. In vehicular applications, the only measurable quantities of a lithium ion cell are its terminal voltage, current and temperature. This implies that several internal states of the cell such as its State of Charge (SOC), whose real-time computation is vital to the optimal performance of the cell, need to be estimated from these available measurements. Therefore, the performance of a BMS for tasks such as online state estimation is dependent upon the fidelity of the underlying cell model. Sophisticated models of the cell enable these quantities to be estimated more accurately and facilitate the implementation of advanced control algorithms. Therefore, it is imperative that the cell model used is suitable for being embedded in a real-time BMS.

Most battery models have the primary goal of accurately predicting the cell's terminal voltage at each time-step. This is so that the output from the predictor routine can be compared to the measured voltage and the difference between them may be used in a suitable corrector routine to improve future predictions. The combined information from the model and measurement is then blended in a suitable way to estimate the cell's SOC.

More advanced models strive to provide insight into various other physico-chemical quantities that could affect the cell's health. The field of Li-ion battery modelling can be classified into two broad categories – i) empirical/ad hoc Equivalent Circuit Models (ECMs), and ii) detailed Physics-Based Models (PBMs) that are based upon first principles. A comprehensive summary of various models that belong to each of the two categories is discussed in Seaman *et al.* [10]. A characteristic aspect that contrasts them is the fact that they are typically at loggerheads with each other in terms of their computational complexity.

1.2.1 Equivalent Circuit Models

ECMs employ circuit elements such as voltage sources, resistors and capacitors to model the behaviour of batteries at their electrical terminals. The cell's thermal subsystem may also be modelled by an analogous electrical circuit. The parameters of the circuit are typically functions of the cell's current, SOC and temperature. These can be incorporated as a lookup table by curve-fitting the model to experimental data. Using such equivalent circuit models, two simple methods are available to compute the cell's SOC – *a*) by using manufacturer-supplied lookup table or graph of OCV versus SOC, and *b*) by numerically integrating the charge passed in and out of the cell over time (commonly referred to as coulomb counting). Both methods are computationally amenable for small-scale embedded applications such as consumer electronics; however, neither one is robust enough to handle the stringent demands in performance imposed by modern vehicular applications.

Advanced state estimation algorithms such as nonlinear Kalman filters may still be able to use ECMs as the plant model and obtain reasonable estimates of the cell's SOC [11, 12]. However, the usefulness of ECMs is limited by the fact that their parameters are derived essentially by a curve-fitting process using a standard set of training data. Since these models are not based on any physical phenomena, their ability to predict the cell's general behaviour is extremely poor especially when subject to current profiles well outside their training realm. Another important disadvantage of equivalent circuit models is that they do not allow insights into the various internal states of the cell.

ECMs of lithium ion batteries have been extensively studied and are widely applied. However, the aforementioned difficulties render their reliability and accuracy questionable, especially under highly demanding load profiles experienced by the battery packs in xEVs.

The boundaries of their performance have been well-quantified (see [5, 13]). Although various estimation and control algorithms continue to be developed around them, the ECMs themselves are no longer the subject of extensive research. Hence, this thesis does not discuss them further.

1.2.2 Physics-Based Models

Physics-Based Models (PBMs) consist of governing equations that construct a realisation of the behaviour of the cell based upon electrochemical principles such as equilibrium thermodynamics, material diffusion and reaction kinetics. The fundamental advantage to this modelling approach is that it is possible to compute the evolution of internal states of the cell such as the concentration of lithium in the two electrodes during its operation with arbitrary current profiles. Precise knowledge of such internal states *e.g.* the concentration of lithium at the electrode surfaces, can help to design control strategies to prevent degradation due to lithium plating. The difficulty with the physics-based modelling approach lies with obtaining the values of all the physical, geometric, electrochemical, thermal and kinetic parameters of the cell. Usually, these parameters are closely guarded trade secrets by cell manufacturers.

In some cases, it may be possible to obtain a subset of these physical parameters by dissecting cells in an inert environment followed by further characterisation using specialised lab equipment. For instance, Ecker *et al.* [14] demonstrate the reverse-engineering of a 7.5 Ah pouch cell by Kokam Ltd. in order to obtain its physical parameters. Nevertheless, this is a tedious process and is feasible only with access to such sophisticated lab equipment. Furthermore, the results from these experiments are susceptible to characterisation errors as well as to cell-to-cell variations due to production spread. Therefore, some form of system identification method needs to be employed for estimating the majority of the physical parameters required for a PBM. Furthermore, it is a common practice to rely on published data for the values of certain cell parameters that do not depend on physical construction, especially for those that remain universally true for a particular Li-ion chemistry.

The challenges involved in model parametrisation is a research exercise of its own merit and is not addressed in this thesis. Once the model parameters are available, PBMs can be used in aiding a deeper understanding of the working of the cell and in answering research questions that could otherwise not be answered with simple ECMs. One area of focus of this

this thesis is to broach a less-probed area — exploring the possibility of using a PBM for the *design* of pouch cells used in automotive applications which shall be presented in chapter 3.

A major disadvantage of PBMs from an implementation point of view is that solving for the model's field variables is time-consuming. In particular, the more sophisticated PBMs require the use of multi-physics Partial Differential Equation (PDE) solvers and hence are not typically suitable for embedded applications. Nevertheless, for high performance applications such as in automotive BMSs wherein state-of-health monitoring is crucial, there is an overwhelming demand for obtaining insight into internal cell variables. For instance, the real-time computation of surface concentration of Li^0 in the solid particles enable the BMS to regulate power flow into and out of the cell to proactively avoid plating and degradation of the cell.

In view of this consideration, model order reduction techniques are seen as key enablers that facilitate in porting the first-principles based predictive powers of PBMs into a real-time microcontroller. This thesis shall therefore have a strong focus on both the analysis and implementation aspects of Reduced Order Models (ROMs).

1.3 The Doyle-Fuller-Newman model

Doyle, Fuller and Newman [15, 16] developed an isothermal physics-based porous electrode model of the cell capable of describing its internal variables such as *a*) potential on the solid particles ϕ_s , *b*) potential in the electrolyte solution ϕ_e , *c*) concentration of Li^0 in the solid particles c_s , *d*) ionic concentration in the electrolyte solution c_e , and *e*) molar flux density of lithium at the solid-electrolyte boundary j . The most popular computational implementation of the Doyle-Fuller-Newman (DFN) equations is the Pseudo Two-Dimensional (P2D) model [5]. In the P2D implementation, all field variables of the DFN model are computed at each spatial location along the axial thickness of the cell. However, the solid concentration in spherical electrode particles is solved in a radial co-ordinate system that is perpendicular to the axial direction of the cell's thickness. The axial and radial dimensions are coupled at each particle's surface through the molar flux density describing the rate of pore-wall flux that crosses from solid into electrolyte or vice-versa. The equations and boundary conditions for the P2D implementation of the DFN model is shown in table 1.1.

1.3 The Doyle-Fuller-Newman model

Table 1.1 Governing equations and boundary conditions of the Doyle-Fuller-Newman (DFN) model cast in its Pseudo Two-Dimensional (P2D) description. Apart from those equations whose sources are explicitly indicated with inline references, all equations of the DFN model presented herein are obtained from the lecture notes by Plett [17], suitably cast in their P2D formulation. To maintain compatibility with computer codes from the simulation tool LIONSIMBA [18], the electrolyte potential at the positive electrode/current collector interface is set to zero (second boundary condition in eq. (1.5)) *i.e.*, chosen as the ground reference. The notation of symbols has been suitably adapted from the cited sources and is detailed in [List of Symbols](#) (see page 27).

Region	Governing equations	Boundary conditions
All regions, $\mu \in \{\text{neg, sep, pos}\}$ Electrodes only, $\lambda \in \{\text{neg, pos}\}$	$\frac{\partial c_{s_\lambda}}{\partial t} = \frac{D_{s_\lambda}}{r^2} \frac{\partial}{\partial r} \left(r^2 \frac{\partial c_{s_\lambda}}{\partial r} \right)$	$\left. \frac{\partial c_{s_\lambda}}{\partial r} \right _{r=0} = 0, \quad \left. \frac{\partial c_{s_\lambda}}{\partial r} \right _{r=R_{p_\lambda}} = \frac{-j_\lambda}{D_{s_\lambda}} \quad (1.3)$
	$\varepsilon_\mu \frac{\partial c_e}{\partial t} = \frac{\partial}{\partial x} \left(D_{\text{eff}_\mu} \frac{\partial c_e}{\partial x} \right) + (1 - t_+^0) a_{s_\lambda} j_\lambda$	$\left. \frac{\partial c_e}{\partial x} \right _{x=0} = 0, \quad \left. \frac{\partial c_e}{\partial x} \right _{x=l_{\text{tot}}} = 0 \quad (1.4)$
	$-a_{s_\lambda} F j_\lambda = \frac{\partial}{\partial x} \left(\kappa_{\text{eff}_\mu} \frac{\partial \phi_e}{\partial x} \right) + \frac{\partial}{\partial x} \left(\kappa_{\text{eff}_\mu} \frac{2RT(t)}{F} (t_+^0 - 1) \frac{\partial \ln c_e}{\partial x} \right)$	$\left. \frac{\partial \phi_e}{\partial x} \right _{x=0} = 0, \quad \phi_e \Big _{x=l_{\text{tot}}} = 0 \quad (1.5)$
	$a_{s_\lambda} F j_\lambda = \frac{\partial}{\partial x} \left(\sigma_{\text{eff}_\lambda} \frac{\partial \phi_{s_\lambda}}{\partial x} \right)$	$\left. \frac{\partial \phi_{s_\lambda}}{\partial x} \right _{x=x_{\text{neg/sep}}/x=x_{\text{sep/pos}}} = 0, \quad \left. \frac{\partial \phi_{s_\lambda}}{\partial x} \right _{x=0/x=x_{\text{tot}}} = \frac{-I}{\sigma_{\text{eff}_\lambda} A} \quad (1.6)$
	$j_\lambda = 2k_{r,\text{eff}_\lambda} \sqrt{c_e (c_{s,\text{max}_\lambda} - c_{s,\text{surf}_\lambda}) c_{s,\text{surf}_\lambda}} \sinh \left(\frac{0.5F}{RT(t)} \eta_\lambda \right)$	— — — — — (1.7)

- $c_e := c_e(x, t), \phi_e := \phi_e(x, t) \quad \{x \in [0, l_{\text{tot}}], (x = 0) \hat{=} \text{neg/Cucc}, (x = l_{\text{tot}}) \hat{=} \text{pos/Alcc}\}$

$\lambda \in \{\text{neg, pos}\}$

- $c_{s_\lambda} := c_{s_\lambda}(r, t), c_{s,\text{surf}_\lambda} := c_{s_\lambda}(r = R_{p_\lambda}, t) \quad \{r \in [0, R_{p_\lambda}], (r = 0) \hat{=} \text{center}, (r = R_{p_\lambda}) \hat{=} \text{surface}\}$

- $\phi_{s_\lambda} := \phi_{s_\lambda}(x_\lambda, t), j_\lambda := j_\lambda(x_\lambda, t) \quad \{x_\lambda \subset x, x_{\text{neg}} \in [0, l_{\text{pos}}], x_{\text{pos}} \in [l_{\text{pos+neg}}, l_{\text{tot}}]\}$

- $\eta_\lambda := \eta_\lambda(x, t) = \phi_{s_\lambda}(x, t) - \phi_e(x, t) - \mathcal{U}_\lambda(c_{s,\text{surf}_\lambda})$

- $\sigma_{\text{eff}_\lambda} = \sigma_\lambda \varepsilon_{s_\lambda}, D_{s,\text{eff}_\lambda} = D_{s_\lambda} e^{\frac{-E_a D_{s_\lambda}}{R} \left(\frac{1}{T(t)} - \frac{1}{T_{\text{sink}}} \right)}, k_{r,\text{eff}_\lambda} = k_{r_\lambda} e^{\frac{-E_a k_{r_\lambda}}{R} \left(\frac{1}{T(t)} - \frac{1}{T_{\text{sink}}} \right)} \dots \dots \dots (\text{Torchio et al. [18]})$

$\mu \in \{\text{neg, sep, pos}\}$

- $D_{\text{eff}_\mu} = D \varepsilon_\mu^{\text{brugg}_\mu}$

- $D := D(c_e, T) = 10^{-4} \times 10^{-4.43 - \frac{54}{T(t) - 229 - 5 \times 10^{-3} c_e(x, t)} - 0.22 \times 10^{-3} c_e(x, t)} \dots \dots \dots (\text{Torchio et al. [18]})$

- $\kappa_{\text{eff}_\mu} = \kappa \varepsilon_\mu^{\text{brugg}_\mu}$

- $\kappa := \kappa(c_e, T) = 10^{-4} \times c_e(x, t) \left(-10.5 + 0.668 \times 10^{-3} c_e(x, t) + 0.494 \times 10^{-6} c_e^2(x, t) + (0.074 - 1.78 \times 10^{-5} c_e(x, t) - 8.86 \times 10^{-10} c_e^2(x, t)) T(t) + (-6.96 \times 10^{-5} + 2.8 \times 10^{-8} c_e(x, t)) T^2(t) \right) \dots \dots \dots (\text{Torchio et al. [18]})$

In this thesis, this P2D implementation of the DFN model is considered as the reference (and only) PBM. Although thermal dependence of parameters such as electrolyte conductivity and diffusivity is shown in table 1.1, a sophisticated description of detailed thermal dynamics *i.e.*, a description of spatio-temporal evolution of cell's temperature using a set of ordinary/partial differential equations is not considered in this work. Secondly, the SOC-dependence of parameters is not incorporated, but the studies conducted here may be suitably extended to include this dependence in the future.

For those aspects of this thesis dealing with the analysis and implementation of various ROMs and the improvements imparted herein to them, only an *isothermal* implementation (at 298.15 K) of the P2D equations is considered. The performance of the various ROMs are compared against this reference benchmark. In consideration of the relative sparsity of such detailed analysis of ROMs in existing literature (see chapter 2), the author of this thesis considers that such an analysis, albeit isothermal, is the need of the hour and is imperative to gain a deeper understanding of the performance boundaries of various popular ROMs.

Since temperature plays a crucial role in the operation of cells and battery packs in xEVs, an isothermal model is unsuitable for design purposes. A model-based design that does not consider thermal effects is likely to stray far from the operating regimen and fail spectacularly. On the other hand, including a sophisticated thermally coupled model is unlikely to yield significant gains. Firstly, running fully coupled electrochemical-thermal model based simulations over the entire design space is computationally expensive. Secondly, the design results of the model have to be verified using a reasonable number of experimental prototypes. Taking into account these considerations it is deemed that, for the design aspect of this thesis, a lumped thermal model suffices. This simplified thermal model is bidirectionally coupled to the P2D equations (see table 1.1) of the electrochemical model and is used as the PBM underpinning the model-based design discussed in chapter 3.

The rest of the thesis is organised as follows. Chapter 2 presents an overview of pertinent modelling art. The literature on model-based design shall be evaluated here and the present shortcomings identified. The survey of literature also considers the advancements in the field of reduced order modelling from their analysis and implementation perspectives. A computational framework for optimising the number of layers within an automotive pouch cell is presented in chapter 3. In chapter 4, the computational bottlenecks in a specific ROM

method *viz.* the Discrete-Time Realisation Algorithm (DRA) is analysed in detail and an improved alternative is proposed. In Chapter 5, the simplest time-domain PBM, the Single Particle Model (SPM) is introduced and its performance is analysed. Salient advancements made to the basic SPM in the literature are presented and their shortcomings analysed. A discrete-time formulation focusing on the numerical implementation aspects is also presented. In chapter 6, the causal factor for the lacklustre performance of a state of the art electrolyte-enhanced SPM is unearthed. Additionally, chapter 6 proposes a new electrolyte model which represents a novel application of the system identification technique. The superior performance of this electrolyte-enhanced composite SPM is demonstrated. Finally, chapter 7 highlights the salient conclusions that can be drawn from the findings presented in this thesis and paves the way for future research by identifying key unsolved tasks in physics-based battery modelling for such automotive applications.

2

Review of Literature

2.1	Model Based Design for Batteries: Overview of Prior Art	44
2.2	Reduced Order Models: A New Classification Scheme	50
2.3	Review of Literature on the Single Particle Model Family	68

THIS chapter discusses the state of the art in the field of lithium ion battery modelling pertinent to the research sub-topics discussed in this thesis. The modelling art is therefore presented in three parts, each providing a critical review of

- a) the body of literature discussing model-based design of lithium ion cells.
- b) prior works dealing with the analysis and implementation aspects of reduced order modelling of lithium ion cells, whose revelations lead to a focus on
- c) publications discussing the Single Particle Model (SPM) and its variants.

2.1 Model Based Design for Batteries: Overview of Prior Art

2.1.1 Introduction

In sharp contrast to the cornucopia of published literature dealing with reduced order modelling of cells (see section 2.2), there is currently a relative paucity of prior art that discusses model-based cell design. Albeit the relevant pool of knowledge is presently sparse, this section nevertheless aims to critically evaluate it.

2.1 Model Based Design for Batteries: Overview of Prior Art

At the outset, it is important to clarify this thesis author's general views on model-based design. It is also important to state why this topic was chosen as an aspect of this thesis. In the recent decades, industries pertaining to different walks of life, cutting across any one discipline, have begun to establish a model-led product/process development culture. For instance, a broad overview of industrial research policy by Thomke [19] towards the turn of the last millennium provides quantifiable evidence that a simulation based design approach in the automotive industry has had a positive impact in the crash-worthiness of resulting vehicular designs. At a high level, the salient benefits of any model-based design include – *a*) reducing the number of design iterations thereby speeding up the time to a production-ready prototype, and *b*) facilitating improved understanding of the variables influencing design that is gained by formalising empirical/ad hoc knowledge through modelling. Furthermore, it is a well-known fact that computer time is cheaper than human time. Therefore, with a simulation-oriented design approach, it is often cheaper to explore Monte Carlo-like design scenarios using a computer model than iterating over a series of rudimentary prototypes in the lab. Finally, once the results predicted by the model have stabilised enough to satisfy the design specifications, prototypes closely matching the final design objectives can be realised, thereby reducing the overall lead time to the market.

The aforementioned views of the thesis author is echoed by Becker *et al.* [20] who present a persuasive view that, since it shall be mandatory to have a deeper understanding of the simulation tools in order to successfully employ a model-led design, this can trigger sweeping changes percolating into the very core of the problem-solving culture in an organisation. Although relatively at its infancy when it comes to cell design, model-based designs have been applied at the battery pack-level in the past, and is therefore not a newcomer to the battery industry in general. In the middle of the last decade, a clarion call for industry to adopt simulation tools in battery engineering was issued by Spotnitz [21]. In the said article, the author questioned the anachronistic industry trend of relying heavily on 'making and testing' rather than aiming to understand the fundamental governing equations and principles of a battery and using this know-how for design. Spotnitz further argues that using Physics-Based Models (PBMs) of batteries could provide reliable understanding of their behaviour and that, as the understanding of the community steadily grows, it could bring about a significant speed-up of battery development.

2.1 Model Based Design for Batteries: Overview of Prior Art

The nature and scope of ‘model-based design’ as intended by this thesis author needs to be clarified. Since this thesis focuses exclusively on physics-based modelling, the term ‘model’ as used here pertains to Physics-Based Models (PBMs) and not to Equivalent Circuit Models (ECMs) or any other type of battery models including other empirical/ad hoc models such as surrogate models. Therefore, the survey of literature here does not include any prior efforts on model-based design that lie outside of this scope.

Among the published set of literature, there is evidence that computational modelling has been successfully used to facilitate the development of novel energy storage materials. The review article by Islam and Fisher [22] provides an overview of the use of computer simulation to gain a deeper insight into the working of new types of cathode materials. Meng and Arroyo-de Domp [23] also surveyed the topic of using computational tools for the design and optimisation of energy storage materials. The computer models referred to in these review articles are not volume-averaged models operating at the cell-level, but detailed ab-initio models constructed using techniques such as Density Functional Theory (DFT). While it is heartening to see such comprehensive studies of computational techniques being applied to energy storage, there are two distinct reasons why the body of research reviewed in the aforementioned articles do not align with the goals of this thesis. Firstly, in the works reviewed in the aforementioned articles, computer simulation is used primarily to enhance researchers’ current understanding of these materials that can help to develop the next generation of energy storage components. The computational methods presented therein are *not* directly employed as design tools. Secondly, these articles use computational modelling to study structural properties at the meso and nano scales. While these are of utmost importance to researchers involved in synthesising prototypes of next generation of energy storage materials, they are less relevant for production-ready cell-designs at scale. Since this thesis has a strong focus on providing readily applicable solutions to industry for incumbent lithium ion chemistries, it was decided not to pursue the methods discussed in the aforementioned works for the design studies discussed herein.

A holistic computational screening was performed by Sendek *et al.* [24] to study the suitability of 12831 candidate materials for their suitability as solid state electrolytes in electrochemical cells. These authors cite the same rationale of this thesis author *i.e.*, rapid prototyping, as the motivation behind their model-based design simulations. The study helped to prune the initial candidate pool down to just 21 viable family structures. This effort serves

2.1 Model Based Design for Batteries: Overview of Prior Art

as a concrete example in this literature survey wherein computer simulation is directly used as a design tool for components of a lithium ion cell. The scope of the aforesaid work falls into the realm of material synthesis and applied physics – topics outside the educational background and expertise of this thesis author. Nevertheless, the success of this effort strongly motivates the case for performing a computational study of similar scale, wherein instead of screening out thousands of candidate materials, the framework presented in chapter 3 computationally screens out thousands of layer configurations within a pouch cell.

Curiously, the use of volume-averaged models for design simulations of PBMs at the cell-scale has not yet gained sufficient traction. This is despite the prevalence of the popular Pseudo Two-Dimensional (P2D) implementation of the Doyle-Fuller-Newman (DFN) model in areas such as degradation analysis and state-estimation. Ramadesigan *et al.* [25] postulate that this slow uptake could be attributed to the computational challenges presented by the complex reaction, diffusion and kinetics of lithium ion cells occurring over different length and time scales. A few design efforts using electrochemical models at the cell scale have nevertheless been reported in literature, which are examined next in section 2.1.2.

2.1.2 State of the art in cell-scale model-led design optimisations

The pioneering work by Newman [26] was the first of its kind to develop a scheme to optimise cell design based on an electrochemical model. The two parameters optimised were electrode thicknesses and porosities. The aforesaid study makes the assumption that electrode kinetics are fast relative to diffusion, and furthermore ignores local concentration gradients. A reaction-zone model, which considers that reactions occur in a narrowly confined area, was used as the underlying model. The separator thickness was assumed to be fixed and the specific energy of the cell was maximised. However, the aforesaid work does not impose any constraints on the extent of specific power that can be drawn from the cell. Nevertheless, this seminal effort provided the key guidance to other researchers that electrode thicknesses and porosities can be considered as the critical design variables to be optimised for in a cell design. Building upon the foundation laid by the aforementioned study, a few other model-led design efforts have been published. However, in order to provide a focused review, only a subset of the prior art that is deemed pertinent for the model-based design of *pouch* cells for *automotive* applications is considered here.

2.1 Model Based Design for Batteries: Overview of Prior Art

Arora *et al.* [27] used an electrochemical model to inform design decisions on cell parameters such as particle size, electrode thickness and mass ratio. Furthermore, the model thus obtained was used to optimise the cell design against the risk of lithium plating. Cells are susceptible to plating during fast charging and hence, this is a key aspect to consider in their design for electric vehicles. This thesis author considers this contribution to be a vanguard in model-based design for cells that is potentially applicable for vehicular applications. Nevertheless, the aspect of stacking layers inside pouch cells and how this influences the optimisation of the aforementioned design variables has not been studied.

Xue *et al.* [28] presented a simulation based design study wherein a cell design was optimised using a gradient-based algorithm. Specifically, the said work dealt with a numerical framework for providing automated design outputs for maximising the cell's energy density whilst meeting specific power density requirements. This criterion appears to be highly relevant in the context of cell design for electric vehicles and hence, was adopted as the basis for the layer optimisation framework presented in chapter 3. In the aforementioned work, various power levels were also tried. However, these power requirements were computed indirectly rather than a direct reformulation of the P2D model to accept power density inputs.

The design study by Xue *et al.* [29] represents a rare example of a model-led design attempt performed in the backdrop of electrified transportation. In the said work, an electrochemical cell model *viz.* the P2D model was successfully adapted to perform the design optimisation of a Plug-in Hybrid Electric Vehicle (PHEV). Although the underlying model operates at the cell-scale, this study considers a pack-level optimisation through a series-parallel combination of cells. Furthermore, an advanced numerical algorithm in the form of a hybrid solver was used. This solver adopted a unique scheme of employing a gradient-free optimiser in conjunction with a gradient-based optimiser. Albeit a standout example in the context of vehicular application, the aforesaid work falls slightly outside the scope of this thesis wherein the design study is strictly confined to be at the cell level.

The article by Xue *et al.* [29] does take into account pack-level constraints such as safety limits as well as energy and power levels. Furthermore, these authors even accounted for important details such as the presence of layers within each cell in their design optimisation process. The system-level constraints considered in Xue *et al.* [29] were instrumental in informing the choice of constraints in the design study presented in chapter 3. However, in

2.1 Model Based Design for Batteries: Overview of Prior Art

the aforementioned article, the translation from pack-level into cell-level quantities does not account for secondary effects *i.e.*, the influence of layers on pack mass (a quantity that is optimised in the said publication) is not studied. Simulations conducted as part of the work reported in chapter 3 reveals that such effects are non-negligible.

A critical issue in the approach by Xue *et al.* [29] is that the number of design variables were excessively large which necessitated the use of complex numerical algorithms. The said work assumes that cell design shall be an integral part of pack optimisation. However, in real-world designs, cells are sourced from a specialised manufacturer. Furthermore, these cells are designed independently to merely adhere to certain specifications [30]. Pack configuration decisions such as the choice of number of series-parallel modules in the vehicular pack are undertaken at a system level in conjunction with the rest of the drivetrain specifications by vehicle manufacturers. This natural separation paradigm helps to decouple the cell design from the pack design thereby drastically reducing the number of degrees of freedom and simplifying the optimisation task. This is a key assumption in the design optimisation study presented in chapter 3.

A comprehensive multi-objective optimisation for optimal design of batteries was recently proposed by Changhong Liu and Lin Liu [31]. This optimisation involved a multiphysics model of the cell wherein a number of design variables such as electrode thicknesses, porosities and particle sizes were considered. The optimisation objectives were to maximise the specific power and specific energy during discharge as well as to minimise capacity loss. The model was solved by using a genetic algorithm. While this contribution is certainly the first of its kind to use a formal mathematical optimisation framework for cell design, in the opinion of this thesis author, the complexity of the problem is excessively high – both mathematically and computationally. For instance, with three design variables considered, it requires a careful interpretation of the resulting pareto front to distinguish their relative importance. While *prima facie* this is not an issue, the question of resolving the pareto front for cells with different parameter sets needs to be addressed. The optimisation algorithm used is an exotic genetic algorithm to be run on a parallel cluster. From a near-term industrial application viewpoint, this scheme is less attractive since real-world constraints such as supply-chain dictated raw-material sourcing typically restrict the number of degrees of freedom available for optimisation. Nevertheless, this scheme is valuable from a long-term research perspective and merits attention from researchers interested in model-based design.

From the body of the relevant literature surveyed here, it is clear that the issue of optimally stacking up layers within a pouch cell has not been dealt with in a systematic manner. Pouch cells are the most common type of cells in automotive applications. Therefore, optimising their design shall yield a beneficial improvement to the overall driving range and fast charging capability of electric vehicles while simultaneously helping to increase the lifetime of their battery packs. With these goals in mind, chapter 3 presents a mathematical framework for a model-based optimal design of pouch cells.

2.2 Reduced Order Models: A New Classification Scheme

Battery modellers face the classic conundrum of conjuring PBMs that remain amenable for control applications. The prior attempts made by the research community to tackle this challenge is examined here. The term ‘control-oriented model’ can be considered synonymous with the term Reduced Order Model (ROM). This is due to the fact that the complexity of PBMs inherently necessitates the use of some order reduction strategy for their adoption in control and real-time applications. In this thesis as well as in the relevant literature discussed here, these two terms have been used interchangeably.

Research into ROMs is motivated by the pressing need for a real-time model with accuracy properties of full-order PBMs but possessing the computational simplicity of ECMs (see sections 1.2.1–1.2.2 for an overview). A number of approaches to reduce the computational complexity of PBMs have been explored in literature. Jokar *et al.* [32] provide a comprehensive review of the various categories of reduced order PBMs for lithium ion batteries. However, the aforesaid work does not aim to classify models based on time-vs-frequency domains. Fan *et al.* [33] conducted a review of reduced order modelling methods, but only provide a generic overview of deriving and implementing models in these dual domains without an expository analysis of the implications of these modelling choices. Unlike Jokar *et al.* [32], the review by Fan *et al.* did not aim to provide a classification of various reduced order models, but instead emphasises on a broad survey of relevant methodologies and tools towards *obtaining* them. Hence, neither of these works provide an insight into the rubrics and implications of the choice of either of these domains to underpin the ROMs. Although in principle, the transformation between them is often a straightforward mathematical exercise, availability of models for final implementation in the time domain aids immediate uptake by industry for

2.2 Reduced Order Models: A New Classification Scheme

adoption in online Battery Management Systems (BMSs). The treatment of ROMs from this aspect is so germane to the central hypothesis of this thesis (a simple time domain model is the key to large scale deployment of PBMs), that the author of this thesis feels compelled to undertake a simpler classification exercise of the existing modelling art, within the context of their suitability for online implementation.

In this discussion, various modelling methodologies and their resultant models are viewed as a single continuum. Consequently this thesis discusses them from such a unified perspective without microscopic separation of the final models from their progenitor mathematical methods. Furthermore, there is also a need to highlight the salient works among the more recent advances and extensions to the then prevailing models to obtain an updated view of the modelling art that have gained traction since the publication of Jokar *et al.* [32] and Fan *et al.* [33]. Hence, the specialised review of reduced order modelling literature covered in this section intends to supplement, not supplant, the breadth of research covered between the aforesaid works. In particular, care has been taken to minimise repetition of background art already analysed in these aforementioned review articles, thereby striving to report the subset of prior research that is pertinent to illustrate the new classification scheme introduced here. The author does not aim to adhere to a chronological presentation of such background works. Instead, salient ROM families are introduced in the context of discussion of their significance within a particular mathematical modelling technique.

In the views of this thesis author, physics-based control-oriented models can be classified as belonging to one of the following categories

- Frequency domain ROMs
- Quasi-hybrid time/frequency domain ROMs
- Hybrid ROMs based on equivalent circuits
- Time-domain ROMs

A common characteristic of all control-oriented models is that their ultimate goal is to lower the computational burden of the pertinent physical quantities during operation of the cell. However upon a closer study, a few contrasting aspects that set them apart become

2.2 Reduced Order Models: A New Classification Scheme

apparent. Understanding the behavioural differences that stem from their lineage is the motive behind distinguishing between those models that are derived directly in the time domain versus those that are derived first in the frequency domain, but later converted to time domain.

The classical *modus operandi* in frequency domain modelling is to transform the underlying physical equations into the Laplace space (the complex S plane) followed by a Padé approximation to reduce the number of coefficients in the resulting transfer functions. This category of models is briefly evaluated in section 2.2.1. At the other end of the spectrum are the time-domain ROMs which typically adopt the strategy of either *a*) simplifying the computational mesh used, *b*) capturing only the salient dynamics of the cell which leads to a smaller parameter set, and/or *c*) a combination of the two. The state of the art in these models is studied in section 2.2.4. An overlapping continuum of mathematical techniques is encountered in the literature discussing the wide assortment of ROMs spanning the intervening space between these extrema. The classification presented here reflects their broad approach to model reduction. For instance, equivalent circuits have only a few parameters and are an attractive option from an implementation perspective. In recent years, there has been an up trend in published efforts employing mathematical methods to generate physics-based equivalent circuits, the salient among which are discussed in section 2.2.3. Finally, there exist Quasi-hybrid ROMs which do not necessarily seek to formulate equivalent circuits, but rather strive to arrive at time domain reduced order state-space realisations by proceeding through a series of mathematical transformations starting from the frequency domain. In these models, order reduction is typically achieved through a reduction in the number of *states* and not directly through a reduction in the number of parameters. These methods typically employ both time-domain and frequency-domain aspects of control theory, such as Markov parameters and the Ho-Kalman algorithm. An evaluation of the salient quasi-hybrid ROMs from literature is presented in section 2.2.2.

In principle, any modelling method that yields a time domain mathematical description of physical phenomena that is lower in computational complexity by some arbitrary magnitude than the original DFN model can be considered as a candidate for further investigation. In the absence of a canonical or quantitative definition of what constitutes a ROM, the number of candidate family of models to consider is overwhelmingly large. In practice, the constraint imposed by the scope of this work *i.e.*, suitability for real-time implementation, limits the

choice of candidate modelling families. For instance, models relying primarily on classical finite difference [34], Galerkin's approximation [35] or Galerkin's projection [36, 37] methods for transformation and order reduction of one or more field variables of the DFN model are excluded from further study. This is done in view of the impracticability of implementing such models in a resource-constrained environment such as an embedded BMS controller.

2.2.1 Frequency domain ROMs

Owing to the low entry-barrier for adoption in a real-time controller that typically logs data samples at specific time intervals, this thesis prioritises those models that are cast in a mathematical form directly suitable for final implementation in the time domain. This choice implies the exclusion of those models that are derived and implemented entirely in the frequency domain. For the sake of readers interested in frequency domain methods, the discussion here briefly introduces salient literature employing the Padé approximation method that serves as a backbone of a wide variety of frequency domain models. "A Padé approximant is the 'best' approximation of a function by a rational function of given order – under this technique, the approximant's power series agrees with the power series of the function it is approximating" [38].

The transfer function oriented Padé approximation method for low order physics-based battery modelling pioneered by Forman *et al.* [39] has gained widespread adoption in the areas of cell design [40], charge-trajectory optimisation [41], controller design [42] and state estimation [40, 43]. Although Prasad and Rahn [44] present an online identification of a subset of ageing parameters using a Padé model and the Recursive Least Squares (RLS) algorithm, specific implementation details such as the transformation of the Padé reduced impedance to discrete-time difference equations were not provided. Padé models are typically limited to offline applications owing to the aggressive trade-offs required in its approximation order so as to maintain high accuracies. Those models truncated to very low Padé order exhibit poor fidelity and perform no better than classical ECMs, although recent research attempts have focused to mitigate this drawback [45, 46].

2.2.2 Quasi-hybrid time/frequency domain ROMs

Smith *et al.* [47] pioneered a semi-hybrid approach to reduced order modelling and obtained closed form expressions for all electrochemical field variables in the frequency domain except for those describing electrolyte concentration and potential (which were solved separately using the classical finite difference discretisation method). To the author's knowledge, this is the earliest published instance wherein all the dynamics of the full order model were completely retained in the frequency domain. This was facilitated through the use of transcendental transfer functions that helped to avoid the accuracy degradation brought about by truncation techniques such as Padé approximation. In the first stage of the model derivation detailed in the said article, a composite impedance model for the frequency range of interest from 0–10 Hz was obtained. This was then converted to a 12th order state space model using the technique of residue grouping and truncation, thereby demonstrating the first instance of the so-called hybrid modelling workflow. The ROM derived in Smith *et al.* [47] was capable of predicting the cell's terminal voltage within 1 % of the full-order DFN model.

The modelling effort by Smith *et al.* [47] also has the unique distinction of being the first of its kind to render a PBM suitable for implementation in the classical Linear Time-Invariant (LTI) state-space formulation

$$\begin{aligned}\dot{\mathbf{x}} &= \mathbf{A}\mathbf{x} + \mathbf{B}\mathbf{u} \\ \mathbf{y} &= \mathbf{C}\mathbf{x} + \mathbf{D}\mathbf{u},\end{aligned}\tag{2.1}$$

where $\mathbf{x} \in \mathbb{R}^{n \times 1}$, $\mathbf{A} \in \mathbb{R}^{n \times n}$, $\mathbf{B} \in \mathbb{R}^{n \times m}$, $\mathbf{y} \in \mathbb{R}^{p \times 1}$, $\mathbf{C} \in \mathbb{R}^{p \times n}$, $\mathbf{D} \in \mathbb{R}^{p \times m}$ and $\mathbf{u} \in \mathbb{R}^{m \times 1}$

that is amenable for controller design and for further system-level simulation studies *e.g.* as a component in the energy storage subsystem of a (hybrid) electric vehicle drivetrain.

The requirement of a relatively large number of state variables (12 in this case) for describing the system's dynamics dilutes the effectiveness of state estimation algorithms. In the classical isothermal implementation of this ROM, with the cell's terminal voltage being the only measured quantity, the observability of the model degrades significantly. Although Smith *et al.* performed an observability analysis of the model in a noise-free context, the presence of process noise (via unmodelled electrochemical phenomena and parameter

2.2 Reduced Order Models: A New Classification Scheme

uncertainties) coupled with corruption of measurement values through sensor noise in a harsh electrical environment such as in a vehicle's drivetrain, makes this model unattractive for state estimation tasks in such embedded applications.

Several attempts have been undertaken to improve and extend the ideas pioneered in Smith *et al.* For instance, Lee *et al.* [48] addressed a critical missing aspect *viz.* the derivation of transcendental transfer functions for both the electrolyte concentration and its potential. These transfer functions were obtained by using a Sturm-Liouville approach by retaining the first five modes of an eigenfunction expansion procedure which is detailed in [48, 49]. To the author's best knowledge, this is the first published work wherein all electrochemical field variables of the DFN model were considered for inclusion in a deterministic model order reduction procedure whilst keeping the derivation entirely in the frequency domain.

Obtaining closed form expressions for the electrochemical variables achieved in Smith *et al.* (for all quantities other than electrolyte transfer functions) and Lee *et al.* (all quantities including electrolyte transfer functions) also has an important computational implication. With these capstone derivations serving to complete the model description in the frequency domain, all electrochemical variables of the DFN model could now be solved independently at any desired spatial location, in particular at certain crucial locations such as the interface of each electrode with the respective current collector or separator. This ground breaking idea sharply contrasted with the then prevalent state of the art in reduced order modelling. For the simplification of the original Partial Differential Algebraic System (PDAE) of equations in table 1.1, most order reduction approaches (excluding the SPM that shall be discussed later) invariably required the solution of all electrochemical quantities at multiple node locations along the thickness of the cell, thereby adding to the computational burden. This was a significant deterrent to the adoption of such ROMs, particularly if the intended purpose of the model is to simply predict the cell's terminal voltage or serve as the plant model in State of Charge (SOC) estimation applications.

In the same publications [48, 49], Lee *et al.* also devised the Discrete-Time Realisation Algorithm (DRA), a novel scheme to systematically transform all transcendental transfer functions to the time domain so as to obtain an LTI state-space model given by eq. (2.1). The DRA method retains the physical character of the original DFN equations until the very last

2.2 Reduced Order Models: A New Classification Scheme

step wherein the matrices governing the system's dynamics are generated. This yields a one-dimensional discrete-time ROM of the cell that is entirely based upon fundamental physical principles. The ROM thus obtained could then be used to compute the time-evolution of all the internal electrochemical quantities of the DFN model. As an illustrative application of the method, Lee *et al.* [48] performed a simulation study of *a)* the reaction flux density, *b)* surface concentration of Li, *c)* ionic concentration of Li^+ in the electrolyte, *d)* potential in electrolyte, and *e)* potential in solid in the anode and cathode at the respective domain boundaries and demonstrated their high accuracies relative to a benchmark DFN model. In Lee *et al.* [48, 49], the cell voltage was computed through linear combinations of these time-domain variables with suitable non-linear corrections. Yet another advantage of this model order reduction process is that the method does not involve any form of non-linear optimisation that is typical of other order reduction schemes that attempt a top-down approach of simplifying the PBM equations. In particular, the DRA scheme provides a deterministic method for selection of the order of the simplified model, which is a pioneering contribution in the field of reduced order modelling of Li-ion cells.

The author of this thesis considers the formulation of the DRA to be a breakthrough contribution that has helped in bringing physics-informed time domain models a step closer to online implementation without having to resort to forming a lumped impedance and then truncating it suitably. This seminal work is a first of its kind that is amenable to implementing real-time controls for an entire cell without relying upon such empirical and ad hoc modelling constructs. In a subsequent paper by the same lead author [50], this approach was then extended to a wider range of operating conditions spanning various choices of initial SOCs, temperature and C-rates. Although the final state space model thus obtained is simple to implement, the classical DRA scheme suffers from significant computational bottlenecks in forming the required block-Hankel matrices during the model-derivation phase.

In both the original as well as the improved DRA, the eigenfunction modal expansion of electrolyte concentration transfer function is computationally intensive. A slightly less detrimental disadvantage with the series of transcendental transfer functions associated with the electrolyte concentration was that their derivation entailed mathematically cumbersome symbolic manipulations that dictated the need of a capable Computer Algebra System (CAS). Although from a standalone viewpoint this requirement does not seem to be critical, the Ho-Kalman algorithm that forms a core component of the DRA scheme is

2.2 Reduced Order Models: A New Classification Scheme

steeped in numerical linear algebra routines. Furthermore, for facilitating state estimator and controller designs, it is convenient to implement the resultant state-space model in a classical numerical computation environment such as MATLAB. Taking these into consideration, Rodriguez *et al.* [51] introduced a simplified computation of the electrolyte concentration transfer function by applying the Variation of Parameters (VOP) scheme. With this final improvement, the hybrid ROM implementation originally envisaged by Lee *et al.* can be considered feature-complete with low computational requirements during both model derivation and implementation phases.

A key drawback of the transcendental transfer function approach is the requirement for linearisation at a specific SOC. This implies that the entries in the matrices of the state space model depends on the linearisation point. In all published works employing this approach, these transfer functions were obtained by linearising the P2D equations of the DFN model (see table 1.1), typically at an operating point of 50 % SOC. The linearisation requirement renders the model usable only in a narrow range of SOCs. Furthermore, this adversely affects the usability of the model for state estimation tasks, wherein the SOC is in fact an unknown quantity and is to be estimated.

In order to extend the model's range of validity, Lee *et al.* [50] had used a simple model-blending approach by interpolating between several linear models pre-computed at different SOC and temperature combinations. To guarantee robustness during change-over, a naive approach is to incorporate a large number of break-points in the look-up table. Since the model is intended for online operation, this would entail significant requirements of both operating memory and non-volatile storage. An alternative approach is to implement a fairly coarse break-point table with a sophisticated changeover mechanism. However, this demands careful tuning of the blending parameters and gain values, an in-depth treatment of which has not been provided in Lee *et al.* [50]. Furthermore, employing these interpolated matrices—whose entries are obtained from pre-computed matrices at various SOCs and temperature—for state-estimation creates a subtle cyclic loop. The stability of this internal feedback loop thus introduced has not been analysed in literature. This renders the idea of state-estimation using such run-time interpolated models questionable.

The author of this thesis hypothesises that any perceivable drawbacks such as non-smooth changes in SOC estimates arising from using blended matrices could be potentially

2.2 Reduced Order Models: A New Classification Scheme

mitigated by using smoothing filters and other ad hoc mathematical apparatus. However, there exists no published work that discusses these engineering aspects or on how to actually implement them in BMSs. Coupled with the absence of a theoretical analysis of loop stability, these models are deemed as not being suitable for immediate adoption by industry, at least until these aforementioned gaps have been addressed satisfactorily. The non-linear state variable model presented by Guo *et al.* [52] aims to address this issue through a ROM in the frequency domain by eliminating the linearisation phase from the workflow. However, the online solution of its field variables entails a complex prediction-refinement procedure, loosely defined as implicit and explicit solution methods, for each subsystem of the DFN model. The formulation of the final model is not clearly illustrated and in the views of this author, is not easily comprehensible. In the absence of actual source code, a numerical example or pseudo-code of the model reduction workflow could have immensely helped with the reproducibility of the results claimed in the aforesaid publication.

In summary, the concept of quasi-hybrid ROMs is certainly promising, although more work is required to address the present gaps, most prominently the need to linearise their equations at certain operating points.

2.2.3 Hybrid ROMs based on equivalent circuits

Physics-inspired ECMs [53–57] are a class of hybrid models that have rapidly gained prominence since the publication of Jokar *et al.* [32] and Fan *et al.* [33]. In this case, the derivation of the relevant model equations is performed in the frequency domain. This frequency domain representation is then converted to a form suitable for implementation as an equivalent circuit. Prasad and Rahn [54] extended their Padé order reduced model, first presented in [44], by converting their impedance model into standard equivalent circuits. A key point to be highlighted is that these family of models do not necessarily strive to retain the classical Randles structure [58] for their equivalent circuit representation. Instead, the values of the electrical circuit components such as series resistance and equivalent capacitance are obtained through various mechanisms such as Electrochemical Impedance Spectroscopy (EIS) measurements under load. The biggest advantage of such models is that they serve as drop-in replacements to traditional ECMs whilst still retaining their origins in physical principles rather than on empirical curve-fitting.

2.2 Reduced Order Models: A New Classification Scheme

A common characteristic of all hybrid models is the lack of a physical meaning to their model parameters. This severely limits the insights offered by such models into electrochemical phenomena internal to the cell. The biggest attraction of using PBMs is the possibility of predicting quantities such as the State of Available Power (SOAP) or phenomena such as cell degradation through accurate computation of the solid phase surface concentration and potentials. Furthermore, a model capable of implying a direct and causal relationship between a group of physical parameters and internal overpotentials at various spatial locations within the cell serves as a powerful tool for in-situ lifetime estimation of batteries. Although the circuit components of physics-informed ECMs and the state-space models discussed here trace their origins to the original parameters of the DFN model, the link between the final model coefficients and their progenitor physical parameter sets is tenuous at best.

With the goal of translating physical parameters of a cell into circuit components, Zhang *et al.* [55] presented a lumped ECM based on Padé approximation and model truncation. However, the sensitivity of the final model values owing to perturbations in the original physical parameters was not evaluated. Consequently, there is a lack of clarity in the relative importance of physical parameters and their influence on circuit component values.

Merla *et al.* [57] introduced an ECM that can be parametrised by attempting a systematic decoupling of the kinetics and diffusion at both electrodes and the electrolyte. Although these interacting phenomena can be complex to resolve over all length and time-scales, acceptable trade-offs in accuracy was demonstrated to be achievable from a system-level simulation perspective. A drawback of this approach is that key physical parameters such as solid and electrolyte diffusion coefficients are attributed to the two electrodes through ad hoc, non-verifiable assumptions. Furthermore, in the aforesaid article, notable discrepancies exist in the values of parameters such as electrolyte conductivity (obtained through calculations from EIS measurements) to that typically reported in literature.

It must be acknowledged that presently there exists no modelling candidate that provides all the desirable characteristics sought after in a ROM to unconditionally adopt it for final implementation in the time domain. However, it is strongly desirable that the majority of the final model values retain their physical meaning, yielding system engineers and cell designers alike with a direct and causal relationship between groups of parameters and their

influence on the cell's operational performance. Since one of the goals of this thesis is to provide a readily usable ROM that is immediately deployable in an online implementation, the author concludes that at present, the benefits offered by physics-inspired hybrid ECMs do not decisively outweigh their drawbacks.

2.2.4 Time-domain ROMs

General strategies in time-domain reduced order battery modelling

The working rubric of all time domain ROMs typically consists of attempts to reformulate the original P2D model equations towards the goal of simplifying them to as much extent as possible. In contrast to the hybrid models, all tasks involved in both model derivation and final implementation are carried out entirely within the time domain. While a subset of prior research has focused only on simplifying certain aspects of the cell's dynamics *e.g.* diffusion in the two electrodes, other published works have aimed at providing a simplified description of the time domain evolution of *all* physical quantities of the cell. An evaluation of the salient literature based upon both these approaches is performed here.

In this discussion, the modelling approaches that entail computations with medium or large dense matrices [59–61] or those involving concepts such as fractional order derivatives [62–66] shall not be discussed. In the views of this author, it appears that the academic community has implicitly considered them to be so abstruse that there has not yet been a comparative study pitting these families of models against the prevalent art. Comparing with the typical published work in this field, it is not clear on how such models distinguish themselves uniquely within the broader landscape of reduced order battery modelling.

A few mathematical techniques for Partial Differential Equation (PDE) simplification in the time domain, such as Hilbert space representation and singular perturbation, were applied for cell modelling in Manzie *et al.* [67]. However, their presentation lacks expository visual information such as plots of time domain evolution of the internal and terminal variables for dynamic load profiles. Furthermore, the authors have not provided a tabulated set of physical parameters of the cell being simulated which therefore impedes reproducibility of the results. Consequently, these methods have not seen a healthy uptake either in academia or in industry. The author of this thesis considers the aforesaid presentation to be of a cursory nature and therefore shall not discuss it here.

2.2 Reduced Order Models: A New Classification Scheme

In the DFN model, the evolution of lithium in the solid phase is described by the classical diffusion equation given by Fick's first law [68]. In order to solve for this concentration profile in full-order models, it is required to discretise every spherical particle (represented by the placement of a node in the axial *i.e.*, through-thickness direction) along its radial direction (pseudo dimension). This additional discretisation along the pseudo dimension dramatically increases the overall number of discretisation nodes and adversely affects computational efficiency. The impact of such high node densities on the computational requirements of the original P2D model coupled with the fact that diffusion in the solid phase is typically the rate-limiting aspect of batteries have led researchers to adopt various mitigation strategies to tackle this issue. In contrast to the pure frequency domain and the semi-hybrid/hybrid approaches discussed thus far, these attempts typically strive to arrive at a simpler computational mesh, whilst aiming to retain high fidelity. It should be noted that high node densities are mainly required near the surface of the spherical particles for the pseudo dimension. Similarly, it is desirable to have a clustering of nodes near the separator and current collector interfaces along the axial dimension. Thus, a sizeable number of order reduction strategies in the time domain seek to adopt non-uniform node spacing towards lowering the aforesaid computational issues. The remainder of this section discusses several popular families of time domain models and provides a summary evaluation of their relative merits and weaknesses.

Overview of prior art in the formulation of time-domain ROMs

Computationally efficient pseudo-spectral schemes for numerical solution of PDEs can be employed by placing discretisation nodes at orthogonal collocation points obtained by solving for the zeros of certain class of polynomial basis functions [69–73]. The accuracy of such schemes extend beyond the algebraic orders of that achievable with classical Finite Difference, Finite Element or Finite Volume Schemes. Northrop *et al.* [74] pioneered their application in battery modelling by employing Jacobi polynomials as the underlying basis functions. A Lagrangian-like integral method to describe diffusion in the electrolyte and solid phase was proposed by Rahn and Wang [8], which however works well only at low C-rates. Suthar *et al.* [75] replaced the Jacobi polynomials originally proposed by Northrop *et al.* [74] with Chebyshev polynomials to help extend the applicability of the resulting ROM to higher C-rates. Bizeray *et al.* [76] provide a detailed treatment on the usage of Chebyshev discretisation

2.2 Reduced Order Models: A New Classification Scheme

for the full P2D model on a global scale *i.e.*, along both the axial and radial directions for all equations of the DFN model.

In pseudo-spectral methods, the reduced number of nodes as well as their clustered placement at desirable spatial locations facilitated by these discretisation schemes lower the computational burdens of simulating a physics-based cell model. In such schemes, the P2D equations, their boundary conditions and corresponding field variables are mathematically transformed to the Chebyshev space within which they are solved. The solved quantities are then converted back to the physical space through a corresponding inverse transformation. Although this bi-directional transformation is purely algebraic in nature, the requirement of running a spatially resolved model coupled with the overheads of such variable transformations render these class of models unsuitable for online implementation. The contribution of Lee *et al.* [48, 49] *i.e.*, the ability to solve for any electrochemical variable at arbitrary spatial locations by completely eliminating the need for spatial discretisation assumes particular significance in this context.

In all non-uniform discretisation schemes discussed here, the implications of using a non-adaptive support mesh obtained by the placement of nodes whose locations are optimised a priori must be considered carefully. For instance, in the prolonged operation of the cell with a net unidirectional charge flow *e.g.* in an electric vehicle application, the reaction front drifts from separator back towards the current collectors. This is due to the exhaustion of lithium at the surface of particles near the separator interfaces. In this scenario, the solutions produced by these models could be worse than simpler models with uniform mesh-density. Although adaptive meshing strategies can be employed for desktop simulation with minimal effort, it remains to be seen if this can be deployed successfully in a resource-constrained environment such as an embedded BMS controller, and hence is a candidate for future research.

The computational bottlenecks arising due to discretisation in the radial direction have motivated researchers to explore mesh-free approaches to solve for the solid phase concentration profile. Subramanian *et al.* [77] pioneered the concept of employing polynomial approximations of the Fickian diffusion equation to solve for lithium concentrations in the porous electrodes. In this approach, the solid-phase surface concentrations were expressed as correction terms applied to their average concentrations (which was described using a second degree polynomial). In a follow-on study [78], the same authors presented a solution

2.2 Reduced Order Models: A New Classification Scheme

using higher order polynomials and performed a dimensionless analysis of their proposed reformulation. The details of the 4th order polynomial approximation is presented in the context of this thesis author's comprehensive analysis of the SPM modelling art and is discussed in section 5.1.3. In the 2nd and 4th order solutions, the polynomial equation for surface concentration was accompanied by a corresponding Ordinary Differential Equation (ODE) for describing the temporal evolution of average concentration, thereby leading to a system of Differential Algebraic Equations (DAEs). Furthermore, Subramanian *et al.* [79] convincingly demonstrated the application of polynomial approximation for the solid phase diffusion equation in the numerical simulation of a complete DFN cell model.

Using polynomial approximation for the solid phase concentration results in a drastic reduction in the number of DAEs needed to solve the full model since now discretisation needs to be performed only along the axial direction. The polynomial approximation solution applied to solve for the surface concentration in the solid phase can hence be viewed as a dimension reduction approach, as it removes the need to numerically solve the concentration dependence in the radial direction. The textbook by Carslaw and Jaeger [80] provides detailed derivations for obtaining the standard analytical solution to Fick's law of diffusion in the context of heat conduction in solids. Liu [81] derived this analytical solution for the lithium intercalation process in the solid phase, taking into account the idiosyncrasies of porous electrodes. However, this expression involves an infinite sum expansion of eigen modes. Guo and White [82] formulated an expression for a truncated approximation of this solution to arbitrary number of terms. Furthermore, they demonstrated the validity of this approximation by comparing the analytical solution truncated to the first 5 terms to that obtained from a classical finite element solution. However, this truncated analytical solution involves exponential and trigonometric terms and is non-trivial to implement on BMS chips, particularly in those that lack support for floating point computations. Moreover, there has been no extensive study comparing the analytical solution to the polynomial approach. Consequently, this approach has not yet gained widespread popularity in the inherent elimination of the radial dimension that is so deeply ingrained as a core aspect of the cell-level order reduction approaches discussed here.

The computational speed-up facilitated by using polynomial approximations for the solid phase diffusion has motivated other researchers to extend this approach to all other

2.2 Reduced Order Models: A New Classification Scheme

electrochemical variables of the DFN model. Deng *et al.* [83] presented a polynomial-centric evaluation of the full P2D model, whose notable contribution is in providing such an approximation for the molar flux density along the thickness of the cell. To the best knowledge of this thesis author, this is the first published work that provides a spatially dependent simplified computation of the interfacial flux density. This represents a balanced choice between the need to use the strongly non-linear Butler-Volmer kinetics eq. (1.7) or having to resort to a lumped representation of average kinetic behaviour. Hence, this approach is particularly suited to reduced order modelling of cells with medium electrode thicknesses wherein the lumped representation of flux density is not generally applicable.

One serious drawback in Deng *et al.* [83] is the use of a Finite Difference approximation for computing the spatial gradients of the Open Circuit Potential (OCP) at three electrode locations. This adversely affects computational performance and is not suitable for online implementation. Unless a proven solution for such computational challenges is made available, it is worthwhile to continue to explore other avenues to identify the most apropos first candidate for adoption in real-time BMS environments.

Frag *et al.* [84] proposed a Piecewise Linear (PWL) approximation of all governing equations of the electrochemical model. Given that straight-line fits to complex phenomena are inherently too simplistic, these authors acknowledged that a naive implementation of their approach shall therefore result in a crude approximation of the cell's dynamics. Hence, an optimal knot-placement scheme was proposed and solved through a genetic algorithm to compute the break-points of the PWL fit. Since this computationally intensive step occurs offline, it does not adversely affect the real-time performance of the model. The final ROM is implemented using standard state-space matrices. However, this model exhibits the primary drawback seen in the hybrid modelling approaches *i.e.*, a complete lack of physical interpretation of its parameters. As with any other ROM involving SOC-based linearisation points, the stability of the model to uncertainties in physical parameters is questionable. A detailed sensitivity analysis of the knot placement scheme's output to such parametric variation is to be performed in order to establish confidence in the model's robustness, before such PWL approaches can gain widespread acceptance in online applications.

2.2.5 Classification of ROMs – Interim summary

Although the presentation of prior art on time-domain ROMs is not yet complete, it is helpful to have a brief interlude to summarise the body of literature reviewed thus far. This exercise shall help to inform the rationale behind the next directions to be undertaken. Table 2.1 provides a high level overview of the key contributions and limitations of the salient literature on various categories of ROMs discussed in sections 2.2.1–2.2.4.

Table 2.1 Overview of key contributions and limitations of the salient literature on various categories of ROMs discussed in sections 2.2.1–2.2.4.

Category	Source	Key Contributions	Limitations/ Other Remarks
Frequency-domain ROMs	Forman <i>et al.</i> [39]	Pioneered Padé approximation technique for battery modelling	Limited to offline applications due to aggressive trade-offs in approximation order
	Prasad and Rahn [44]	Online identification of a few ageing parameters using RLS	Lack of implementation details hampers reproducibility
	Yuan <i>et al.</i> [45, 46]	Proposed a high-fidelity low order transfer function type ROM	Being too recent, unproven to rely as the foundation
Quasi-hybrid ROMs	Smith <i>et al.</i> [47]	Obtained transcendental transfer functions of all field variables except electrolyte concentration and potential, followed by conversion to time domain state-space model	Needs a large number of states for capturing system dynamics, which impacts observability

Continued on next page

2.2 Reduced Order Models: A New Classification Scheme

Table 2.1 – continued from previous page

Category	Source	Key Contributions	Limitations
	Lee <i>et al.</i> [48]	Sturm-Liouville approach to obtain transcendental transfer functions of the electrolyte, followed by a novel DRA scheme for state space implementation	Computational bottlenecks owing to large sized matrices; needs linearisation at specific SOCs which raise questions on state estimation
	Rodriguez <i>et al.</i> [51]	Simplified computation of electrolyte transfer functions through a VOP scheme	VOP scheme has not seen traction in published literature; Requires linearisation at multiple points
	Guo <i>et al.</i> [52]	Eliminates linearisation from the workflow through a non-linear state variable model	Final model formulation is not clearly illustrated; Lack of examples or pseudo-code hinder comprehension
Hybrid ROMs based on equivalent circuits	Prasad and Rahn [54]	Pioneered this concept by converting an impedance model into an equivalent circuit	Does not provide a direct relationship between physical parameters and values of circuit components
	Zhang <i>et al.</i> [55]	Lumped ECM based on Padé approximation and model truncation	Lacks clarity in the relative importance of physical parameters and their influence on circuit component values
	Merla <i>et al.</i> [57]	Systematic decoupling of kinetics & diffusion, followed by their mapping to circuit components	Discrepancies in a few parameter values compared to those reported in literature

Continued on next page

2.2 Reduced Order Models: A New Classification Scheme

Table 2.1 – continued from previous page

Category	Source	Key Contributions	Limitations
Time-domain ROMs (excluding SPMs)	Manzie <i>et al.</i> [67]	Direct simplification of PDEs by Hilbert space representation and singular perturbation	No expository visual information and absence of cell parameter set
	Northrop <i>et al.</i> [74]	Pioneered the use of pseudo-spectral schemes in cell modelling using Jacobi polynomials	Applicable only at low C-rates
	Suthar <i>et al.</i> [75]	Used Chebyshev polynomials as basis functions for numerical robustness and hence, to facilitate higher C-rates	Provides only a cursory mention of the scheme; lacks mathematical details to aid battery modellers
	Bizeray <i>et al.</i> [76]	Detailed treatment on the usage of Chebyshev discretisation for both the axial & radial dimensions of a lithium ion cell	Computational burden of discretisation in the axial direction is not justified for embedded BMS applications
	Subramanian <i>et al.</i> [79]	Pioneered the use of polynomial approximation for solving diffusion in the solid phase	All other field variables were solved using a traditional finite difference method; not amenable to embedded implementation
	Deng <i>et al.</i> [83]	Extended the use of polynomials for the molar flux density of the DFN model	Finite Difference approximation for the spatial gradients of OCP is an adverse side-effect not seen in other polynomial ROMs

2.3 Review of Literature on the Single Particle Model Family

It is evident that all physics-based ROMs presented thus far entail extensive parametrisation efforts to render them suitable for a practical application. The difficulties associated with such parametrisation, coupled with inherent uncertainties in the obtained parameter values act as a strong deterrent to stakeholders outside academia to adopt PBMs for online implementation in a BMS. This motivates the need for even further simplified PBMs. One such modelling candidate is the Single Particle Model (SPM), the prior research on which is presented next in section 2.3.

2.3 Review of Literature on the Single Particle Model Family

2.3.1 Overview of literature on conventional SPMs

Haran *et al.* [85] proposed a highly simplified representation of porous electrodes for the metal hydride cell chemistry. In the aforesaid article, each porous electrode was represented as a single spherical particle. This concept was adopted for lithium ion batteries by Ning and Popov [86] and has since become quite popular. Models employing this lumped representation of electrodes are referred to as Single Particle Models (SPMs). These models have three advantages. Firstly, SPMs involve only a subset of parameters of the original DFN model. Furthermore, they are computationally cheap, especially when coupled with the polynomial approximation for solving the solid diffusion equation for each electrode. Finally, all model parameters in the SPM retain their physical character, aiding in a direct and intuitive understanding of physical parameters on the cell's operation.

During the initial years following its inception, the formulation of the basic SPM was discussed extensively within application-specific contexts such as SOC evaluation [87, 88], parameter estimation [89], and life cycle/ageing predictions [90, 91]. There have also been detailed stand-alone publications discussing various facets of the basic SPM, such as its inherent assumptions and governing equations [92, 93]. The basic SPM suffers from poor voltage accuracy which is discussed in the simulation results presented in section 5.3.3. Since the turn of the decade, researchers have attempted to tackle this issue and a holistic discussion of such efforts is presented next in section 2.3.2.

2.3.2 State of the art in electrolyte enhanced SPMs

The lack of electrolyte dynamics in the conventional SPM results in poor voltage accuracy even at moderate C-rates. This is illustrated in the author's simulation results presented in section 5.3.3. This poor performance in voltage prediction renders the model unsuitable for observer design in SOC estimation applications. This is because the output voltage from the model maps to a radically different SOC operating point. A number of candidate solutions have been proposed in literature that strive to mitigate this drawback, the salient among which are evaluated here.

The earliest works which attempt to include electrolyte dynamics in the conventional SPM were published only within the present decade. Schmidt *et al.* [94] proposed an infinite-sum eigenfunction modal expansion paradigm to solve for the electrolyte concentration. It was claimed that by accounting for contribution from only the first two terms, sufficient accuracies may be achieved. Furthermore, a simple ODE was proposed for the rate of evolution of the first temporal mode. The solved electrolyte concentration is then substituted into an approximate analytical solution for the DFN model's charge conservation PDE (see eq. (1.5)) to obtain the electrolyte potential. However, the presentation lacks depth in the explanation which hinders reproducibility. For instance, the origin and explanation of the approximation terms in the electrolyte potential solution is omitted. Derivations are performed from a rigorous mathematical perspective without providing contextual reference to cell parameters or electrochemical quantities. Introducing numerical examples would have been a redeeming factor to help keeping the mathematical aspects tractable. This method has not seen further uptake for SPM modelling.

Guo *et al.* [95] presented an empirical approach to account for the solution-phase dynamics. Using standard curve-fitting techniques, a non-linear resistance as a function of current and temperature was introduced. Thus, the equation for cell terminal voltage presented in eq. (5.29) is modified as

$$V_{\text{cell}} = \eta_{\text{pos}} - \eta_{\text{neg}} + U_{\text{pos}} - U_{\text{neg}} - IR_{\text{eq}} \quad (2.2)$$

2.3 Review of Literature on the Single Particle Model Family

where R_{eq} is the equivalent resistance newly introduced. In the opinion of this thesis author, this approach is too simplistic and does not generalise well. Even if giving up physics-based model origins can be tolerated for one or two subsystems within the model, the equivalent resistance is not just a minor correction term since it needs to account for a large polarisation voltage of the order of tens of millivolts. Secondly, the current-dependence introduced to account for the complex mass and charge transport within the electrolyte places a disproportionately large weight on the accuracy of the curve-fitting process. Non-linear fits as proposed in Guo *et al.* are inherently problematic as the optimisation routine may simply converge to a local minimum. The specific form and nature *e.g.* the convexity of the proposed hypothesis function is not discussed. It is also not guaranteed that the same fitting function is applicable to a different cell with another set of parameters. Finally, the correction term being resistive in nature is zeroth order *i.e.*, cannot account for the frequency dependent behaviour of the electrolyte's dynamics. This approach is more suited for small-scale static corrections that do not depend on the current *e.g.* to account for a few tens of microvolts due to a constant contact resistance of the current collectors.

Di Domenico *et al.* [96] were the first to present a step-by-step derivation of the approximate analytical solution to the electrolyte overpotential. The potential drop in the electrolyte is given by

$$\phi_{\text{e,pos}} - \phi_{\text{e,neg}} = -\frac{I}{2A} \left(\frac{l_{\text{neg}}}{\kappa_{\text{eff,neg}}} + 2 \frac{l_{\text{sep}}}{\kappa_{\text{eff,sep}}} + \frac{l_{\text{pos}}}{\kappa_{\text{eff,pos}}} \right) \quad (2.3)$$

and can be substituted into the subtraction operation involving eq. (5.26) and eq. (5.27) in computing the overall overpotential of eq. (5.28) and hence the terminal voltage. The effective conductivity of the electrolyte in a given region $j \in \{\text{pos, sep, neg}\}$ within the cell, is defined as $\kappa_{\text{eff},j}(c_e) = \kappa(c_e) \varepsilon_j^{\text{brugg}}$. As discussed in section 5.3.2, the intrinsic, and hence the effective electrolyte conductivity is a function of the concentration of Li^+ ions in the electrolyte. Di Domenico and co-workers did not, however discuss the spatio-temporal calculation of electrolyte concentration. It is likely that a constant electrolyte concentration at its initial equilibrium value was used. As seen in fig. 2.1, significant spatial gradients in the electrolyte are established even at low to moderate C-rates during the cell's operation. Sustained application of a unidirectional current even leads to starvation of ions in the electrolyte, particularly near the current collectors. This phenomenon is visualised in fig. 2.1 wherein

2.3 Review of Literature on the Single Particle Model Family

the electrolyte at the positive current collector is virtually depleted of ions at the end of discharge. This ion-starvation process occurs earlier at higher C-rates and spreads throughout the thickness of the electrode. Thus, the assumption of constant ionic concentration in the electrolyte is not true. Neglecting mass transport due to diffusion implies that the terms in eq. (2.3) constitute only a part of the expression for computing the electrolyte overpotential. Furthermore, Di Domenico and colleagues do not present any results of applying dynamic current profiles. Since the critical aspect of mass transport contribution to electrolyte overpotential is omitted, this model cannot be viewed as a *sufficient* enhancement to the basic SPM.

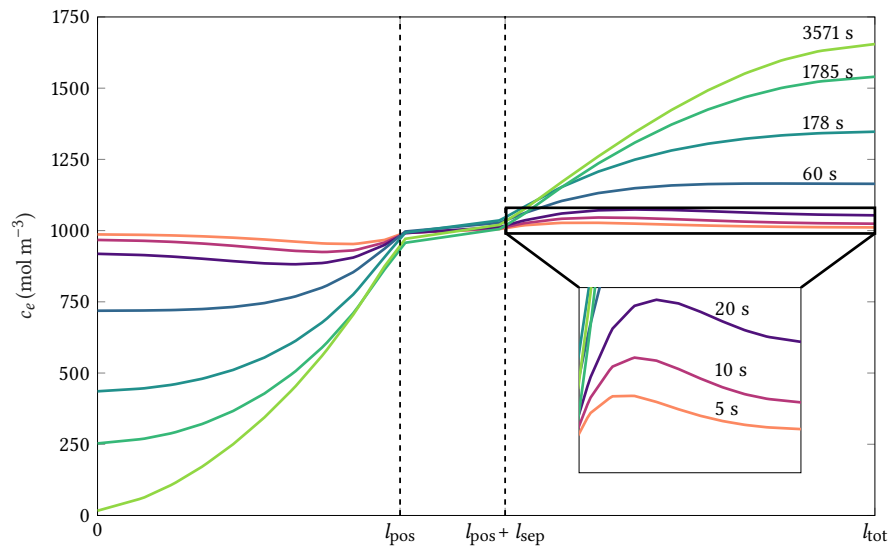


Figure 2.1 Li^+ ion concentration in electrolyte along cell thickness at various time-snapshots during a 1C discharge simulation of the P2D model. A Quasi-Steady State (QSS) spatial profile with inflection point at each separator interface begins to form at ≈ 60 s after discharge begins. However, the ionic concentration in electrolyte exhibits a significantly different transient behaviour (zoomed inset) possessing another inflection point that disrupts the monotonic trend. Depletion of ionic concentration at positive current collector towards end of discharge is also seen (bottom left).

Although not presented in the context of incorporating into the SPM, Guduru *et al.* [97] derived an analytical solution of the spatio-temporal evolution of electrolyte concentration using the Separation of Variables (SoV) method. The SoV method was first applied to modelling of lithium ion cells by Subramanian *et al.* [98] to solve for solid phase concentration profiles in spherical electrode particles. Although the ionic concentration in the electrolyte computed by the analytical expression in Guduru *et al.* [97] seems like a feasible choice for inclusion into the SPM, it is only applicable for galvanostatic boundary conditions

2.3 Review of Literature on the Single Particle Model Family

i.e., when the applied current is held constant over time. By natural extension, researchers could hypothesise that this restriction may be removed by considering the input current as piecewise constant over small sample intervals. Such a hypothesis could be reinforced by the fact that standard drivecycles are specified as discrete samples and the discrete-time SPM processes these input samples assuming Zero Order Hold (ZOH) behaviour. However, the analytical solution presented by Guduru and co-workers assumes a Quasi-Steady State (QSS) concentration profile. These authors consider a near-instantaneous establishment of this QSS and suggest a parameter-independent analysis through use of dimensionless concentrations and time-constants instead of absolute time.

In the studies conducted by this thesis author, significantly different transient behaviour is exhibited by the electrolyte concentration profile. In particular, the time taken to establish the QSS profile is not negligible. This difference in behaviour could be attributed to the different parameter set used. Figure 2.1 shows the spatial profile of ionic concentration at various snapshots of time during a 1C constant current discharge. Starting at 100 % SOC, the discharge lasts 3571 s. It is seen that it takes nearly 60 s to establish the approximately parabolic shape assumed by the electrolyte concentration. After the initial transient has elapsed, the underlying structure of the mathematical equations can be assumed to be static. This is evidenced by the fact that at 1785 s *i.e.*, after half of the discharge is completed, the shape of the curve is nearly identical to the one towards end of discharge. These QSS curves have their sole inflection points at their separator interfaces and remains monotonic within their respective electrode regions. The difference in height for various times can be accounted by the coefficients solved using the analytical modal solution proposed in Guduru *et al.*

The axes in the inset of fig. 2.1 shows a zoomed-in view of the electrolyte concentration during the transient phase, wherein the QSS has not yet been established. In particular, there exist additional inflection points, one within the interior of each electrode, which render the transient concentration profile mathematically incompatible with the monotonicity exhibited by the QSS profile. Thus, in highly dynamic operating conditions with frequent reversals in the direction of current, the QSS assumption for the galvanostatic analytical solution becomes harder to uphold without introducing significant errors. Finally, the analytical solution profile in Guduru *et al.* is not amenable to embedded implementation, since it consists of a set of non-trivial trigonometric computations at each time-step.

2.3 Review of Literature on the Single Particle Model Family

Prada *et al.* [99] were the first to provide a simplified expression for potential drop in the electrolyte by including the terms representing ionic concentration gradient within the cell thickness. Thus, eq. (2.3) gets modified as

$$\phi_{e,\text{pos}} - \phi_{e,\text{neg}} = (1 - t_+^0) \frac{2RT}{F} \ln \frac{c_{e,\text{pos/cc}}}{c_{e,\text{neg/cc}}} - \frac{I}{2A} \left(\frac{l_{\text{neg}}}{\kappa_{\text{eff,neg}}} + 2 \frac{l_{\text{sep}}}{\kappa_{\text{eff,sep}}} + \frac{l_{\text{pos}}}{\kappa_{\text{eff,pos}}} \right) \quad (2.4)$$

Although the complete expression for electrolyte overpotential was provided, it was presented in a cursory manner *i.e.*, without detailing the spatio-temporal computation of ionic concentration values at the current collector interfaces. Nevertheless, it is important to note this contribution as eq. (2.4) is widely relied upon by subsequent literature and shall be used in section 6.10.1.

The pioneering work by Rahimian *et al.* [100] provided approximate expressions for *both* charge transport and mass transport properties of the electrolyte specifically with the focus on improving the basic SPM. These authors discuss the usage of a polynomial approximation for electrolyte concentration and potentials. In particular, a cubic polynomial was chosen for approximating the electrolyte concentration within the porous electrodes. This necessitates the need to solve for eight coefficients for uniquely describing the electrolyte concentration profile within the electrode regions. However, in the standard DFN model, the number of electrolyte-specific PDEs and their corresponding boundary conditions describing charge and mass transport is insufficient to uniquely solve for all unknown coefficients of this polynomial approximation. A detailed explanation of this equation deficiency shall be discussed in section 6.1.1.

To overcome the issue of equation deficiency, Rahimian *et al.* adopted a scheme wherein one additional spatial location in the interior of each electrode was also needed. The coefficients of the polynomial approximation were then obtained by iteratively solving a large coupled system of algebraic equations, embedding within them the additional equations evaluated at the interior points. A complicating issue that arises is regarding the optimal positioning of these additional interior points. An online numerical optimisation was performed to obtain the optimal placement of this interior node. In the opinion of this thesis author, these optimisation results could be sensitive to the thickness of the electrodes among other parameters. A discussion of the stability of the proposed routine and its robustness

2.3 Review of Literature on the Single Particle Model Family

to parameter variations shall help in lending confidence in the proposed method. Although sufficient accuracy of the improved SPM was demonstrated for currents up to 5C, a notable omission is the discussion of the model's performance to dynamic input profiles. In conclusion, the author of this thesis opines that, although this method serves as a proof of concept towards implementing polynomial approximations for electrolyte dynamics, until the aforementioned gaps are addressed with clarity, it is not convincing for uptake by relevant stakeholders.

Kemper and Kum [101] presented an approach wherein the spatial gradients of the electrolyte concentration are neglected. The time-evolution of *average* ionic concentration in each of the three cell regions *viz.* positive electrode, separator and negative electrode are described by a set of three ODEs. As established by the discussion thus far, the concentration gradients along the axial thickness of the cell is significant, even at moderate C-rates. Lending strength to doubts on the model's wider applicability is the fact that results from constant current inputs (which induce large concentration gradients in electrolyte) have not been reported in this work. Thus, this approach is deemed as not satisfactory enough to warrant further engagement.

Luo *et al.* [102] derived a parabolic approximation of the electrolyte concentration distribution along the thickness of the cell. The derivation is obtained for the case of steady-state wherein the rate of change of concentration is zero. However, the author of this thesis is sceptical about this since in the set of independent simulations conducted, there was no situation other than prior to application of current that this exact steady-state condition is satisfied. In the QSS profile concept discussion based on fig. 2.1, it is clear that only the *spatial* profile reaches a shape that can be potentially described by a mathematically invariant family of curves. The electrolyte concentration is still *time-varying* and therefore violates the static time-evolution assumption. Although Luo *et al.* [102] do not explicitly acknowledge this, they do provide an extension for general operating conditions by introducing two exponential scaling functions $f_n(t)$ and $f_p(t)$ while retaining the assumption of parabolic spatial behaviour. The computation of certain time-constants in these scaling functions are not elucidated nor are the procedural steps for determination of the aforementioned scaling functions provided.

In a subsequent paper by the same authors *i.e.*, Luo *et al.* [103], the electrolyte concentration model together with a similarly-derived electrolyte potential model was incorporated into the conventional SPM to arrive at what the authors term as extended SPM. In the

2.3 Review of Literature on the Single Particle Model Family

aforementioned work, the electrolyte potential is set to account for contribution from two terms — *a*) ohmic drop due to bulk solution resistance, and *b*) polarisation potential due to concentration gradients. Although it seeks to correctly account for the two causes of overpotential in the electrolyte, there is no detailed explanation on the computation of quantities such as time-constants involved in the polarisation potential term.

A modified version of the electrolyte model proposed in Luo *et al.* [102] was used in Zou *et al.* [104] for observer design in an SOC estimation application. The modification essentially consists of truncating the complex expression in Luo *et al.* [102], which originally consisted of six coefficients p_1 through p_6 to just two, and elimination of the aforementioned time-constants. However, to the disappointment of the author of this thesis, the claim that truncation to $n = 2$ terms is sufficient to describe the dynamics proved to be optimistic for the parameter set considered. In the thesis author's efforts to reproduce the aforesaid work, an arbitrary scaling factor was needed to correct for the electrolyte potential drop and match the P2D simulations. The requirement for such scaling factors whose physical origins are not clearly identifiable lends to scepticism on the model's robustness. Furthermore, it was found that this value needed to be hand-tuned for each parameter-set. Until these gaps are addressed, it is worth seeking other viable alternatives to model the cell's electrolyte dynamics.

After completing the simulations with the aforementioned scaling factors and continuing in the quest for other alternatives, the author of this thesis made an observation that other researchers have had to resort to similar techniques for describing the electrolyte overpotential. For instance, Han *et al.* [105] use a similar scaling factor $p < 0$ for the entire expression of eq. (2.4) representing the electrolyte overpotential using the polynomial approximation approach proposed by Rahimian *et al.* [100]. However, these unexplained scaling factors lower the confidence regarding the model's general applicability.

Tanim *et al.* [106] accounted for electrolyte dynamics by deriving reduced order transfer functions for ionic concentration distribution and electrolyte overpotential using the Integral Method Approximation (IMA) technique. However, the coefficients of these transfer functions are excessively long and comprised of chained algebraic operations expressed in a high-entropy sum-of-products form in the appendix of the aforesaid article. For instance, ten coefficients are needed to describe the concentration profile while six coefficients are required for the electrolyte potential. The median length of each atomic sub-expression of these

2.3 Review of Literature on the Single Particle Model Family

coefficients is sufficiently high to obfuscate their physical significance. A low-entropy form for the coefficients of these transfer functions similar to that pioneered by Middlebrook [107] and exemplified in the design-oriented analysis of electric circuits [108, 109] could have been helpful to aid the readers' understanding. The author of this thesis recognises that mathematical complexity should not be the sole basis to evaluate the merits of such proposed improvements. Although the presentation of these long coefficients have been judiciously moved to the appendix, their derivations — essential to prove the model's validity — is curiously omitted. The unwieldiness of the mathematical expressions presented therein increases the probabilities of introducing human errors during implementation.

It is worth noting that Marcicki *et al.* [40] had independently proposed a similar approach *viz.* deriving a transcendental transfer function from electrolyte concentration to applied current, albeit for a cell of Lithium Iron Phosphate (LFP) chemistry. This transfer function consisted of a series of hyperbolic trigonometric functions which were later truncated by Padé approximation (see section 2.2.1 for a brief introduction to frequency domain ROMs). However, upon the trial of this approach for the Lithium Cobalt Oxide (LCO) parameter set (see table 5.2) by this thesis' author, in order to obtain sufficient accuracy, the truncation order had to be raised to at least seven, similar in complexity to that of Tanim *et al.* [110]. In both Marcicki *et al.* [40] and Tanim *et al.* [110], the electrolyte-specific enhancements to the SPM are in the frequency domain, placing further burden, particularly on industry stakeholders to accurately interpret and transform the coefficients to a time-domain implementation for deployment in an embedded BMS. Owing to this, as already stated in section 2.2.1, these models fall outside the scope of this thesis.

Fan *et al.* [36] proposed an Extended SPM that includes electrolyte dynamics using the Galerkin Projection Method (GPM) which achieves an acceptable accuracy in terminal voltage performance. Although these authors claim that the GPM is computationally *cheaper* than other model order reduction techniques such as proper orthogonal decomposition and balanced truncation, this claim has not been substantiated. The sole comparison of Central Processing Unit (CPU) times presented in the said work only contrasts the GPM against the classical Finite Difference Method (FDM). Although an impressive computational speed is achieved, it is unclear whether the model equations, particularly those involving solutions of non-linear integral expressions resulting from applying the Galerkin's method can be

2.3 Review of Literature on the Single Particle Model Family

solved in real-time for embedded implementation. It appears that the GPM is more suitable for desktop simulations. In congruence with this thesis author's scepticism, Fan *et al.* [36] have not claimed the suitability of their work for online/embedded application in a BMS. Therefore, in accordance with the stance taken in section 2.2, models employing such methods are deemed to be not in alignment with the goals of this thesis.

Moura *et al.* [111] proposed an improved SPM by simply augmenting the conventional SPM with a simplified form of electrolyte-specific equations of the original DFN model. The resulting model therefore has PDEs in it and therefore not easily amenable for embedded implementation. Lotfi *et al.* [112] presented an algebraic approximation for the spatial distribution of electrolyte concentration by modifying standard parabolic expressions with leading exponential coefficients. There are two main issues with this approach. It is not explained why that particular mathematical formulation was chosen. For instance, its superiority over other feasible family of curves is not discussed. Secondly, the aforesaid coefficients are to be determined through solution of equations obtained by applying continuity and flux boundary conditions from the DFN model for electrolyte concentrations at the electrode-separator interfaces. Since exponential-type expressions are assumed in the aforesaid mathematical formulations, the resulting set of equations are non-linear, the solving of which in the context of a resource-constrained environment is problematic. Table 2.2 provides a digested summary of the salient electrolyte enhanced SPMs from literature.

Table 2.2 Summary of salient literature on electrolyte enhanced SPMs

Source	Key Contributions	Limitations/ Other Remarks
Schmidt <i>et al.</i> [94]	Electrolyte concentration solved by an eigenfunction expansion for spatial profile and an ODE solution for temporal dynamics	Excessive theoretical emphasis without regular contextual references to cell modelling, which hinders reproducibility
Guo <i>et al.</i> [95]	Non-linear resistance as a function of current and temperature to capture electrolyte overpotential	Empirical approach which is difficult to generalise across parameter sets since large corrections of the order of a few mV become essential; Non-linear optimisation may converge to a local minimum

Continued on next page

2.3 Review of Literature on the Single Particle Model Family

Table 2.2 – continued from previous page

Source	Key Contributions	Limitations/ Other Remarks
Di Domenico <i>et al.</i> [96]	First to present an approximate analytical solution for electrolyte overpotential	Lacks discussion on spatio-temporal calculation of ionic concentration; presumably used constant initial value which is problematic with sustained unidirectional currents
Guduru <i>et al.</i> [96]	Pioneered an analytical solution for the spatio-temporal evolution of electrolyte concentration using the Separation of Variables (SoV) method	The derived analytical solution is applicable only for galvanostatic discharge; assumption of near instantaneous establishment of QSS hinders extensions using PWL approximations while trigonometric computations at each time-step impacts embedded applicability
Prada <i>et al.</i> [99]	First to incorporate polarisation due to ionic diffusion in the expression for electrolyte overpotential	The solution of spatio-temporal ionic concentration is not detailed. However, post-computation of this term, the equation in Prada <i>et al.</i> [99] is widely used for the electrolyte overpotential contribution to cell terminal voltage
Rahimian <i>et al.</i> [100]	Cubic polynomials for spatial approximation of electrolyte concentration and demonstrated satisfactory accuracy for currents up to 5C	Limited by the issue of equation deficiency in the P2D model; proposed workaround involves computations at additional interior points which is determined by an expensive placement optimisation algorithm
Luo <i>et al.</i> [102, 103]	Derived a modified parabolic approximation (with exponential scaling functions) for electrolyte spatial concentration profile	Computation of time constants of the exponential scaling functions is not explained; improvements over a standard quadratic approximation model is not elucidated
Tanim <i>et al.</i> [106]	Derived transfer functions for ionic concentration distribution and electrolyte overpotential using Integral Method Approximation	Coefficients of transfer functions are excessively long and mathematically intractable; Is based upon many high entropy expressions whose analytical derivations are omitted

2.3.3 Conclusions

A survey of the recent literature dealing with the SPM family of models reveals a diminishing rate of advancement in quantifiable improvements to the underlying plant model itself. This nearly-static trend can be attributed to the general consensus within the research community that these models may be too simplistic and not of suitable accuracy to warrant further studies. Other than a small minority of papers that either propose core modelling improvements to tackle their inaccuracies, or add new enhancements such as mechanical-stress physics [113, 114], latest work in this family of models predominantly pertains to their application in areas like state estimation [104, 111, 115–117], optimal charging [118, 119], cycling performance [120], conversion to equivalent circuits [121], parametrisation [122–125], pack-balancing studies [126] and observer design for joint state-parameter estimation [127]. The SPM approach has also been extended to the case of composite electrodes, leading to a state estimator design after basic observability analysis [128]. Owing to their simplicity, this thesis author believes that SPMs hold the highest potential to bring physics-based models to embedded BMSs. With this goal in view, this thesis seeks to resurrect interest in SPMs by addressing the recent paucity in fundamental modelling improvements.

Based upon the thesis author's experiences in trying to replicate the results from the literature presented in section 2.3.2, any questionable elements in such prior efforts can be attributed to inaccuracies in estimating the spatio-temporal evolution of electrolyte concentration. Upon obtaining a good estimate of the electrolyte concentration profile, eq. (2.4) is deemed to be satisfactory for the electrolyte overpotential computation. Thus, it can be concluded that the focus of research efforts must be on accurate determination of the electrolyte concentration profile.

Analysing the literature presented in section 2.3.2, it can be seen that the proposed enhancements to computing the ionic concentration in electrolyte falls into one of the following two categories

- model description through physical principles followed by mathematical simplification
- fitting of pre-assumed simplified mathematical structures to some physical phenomena

2.3 Review of Literature on the Single Particle Model Family

In the author's view, it appears that using the former approach yields technically correct, yet mathematically convoluted expressions for overpotentials that are fraught with implementation difficulties. Although the latter approach looks promising in terms of ease of implementation, their sub-optimal performance and lack of wider-applicability leaves much to be desired. Among the latter class of models, owing to its simplicity, the quadratic (parabolic) approximation method for electrolyte concentration is an attractive option. It is therefore important to perform an in-depth analysis of this sub-class of models and understand their source of potential weaknesses. Such an analysis has yet not been performed in literature and is therefore presented in section 5.4.

This concludes the author's review of literature of the various reduced order modelling strategies. Based on the wealth of information gleaned from this study, it was possible to make an informed choice to pursue the SPM approach for further research. In particular, it came to light that there has been no systematic analysis of the state of the art SPM-based approach with a view to quantify their performance boundaries. This author's contributions to the time domain implementation-oriented reduced order modelling field include

- performing a thorough analysis of the basic SPM and the quadratic approximation concentration model for inclusion of electrolyte dynamics into it
- identifying the issues plaguing each of the aforementioned models
- conducting a wide range of hypotheses-driven trials in an attempt to enhance the basic SPM (some of which did not yield the desired improvements)
- Obtaining an electrolyte-enhanced composite SPM through system identification, and
- arriving at a feasible approach capable of moulding the SPM framework into a readily implementable solution for electric vehicle applications

This research was performed through an iterative cycle of analysis, design and simulation-based verification and shall be elucidated in a discourse spanning two chapters *viz.* chapter 5 and chapter 6.

3

Model-based Design Of Pouch Cells*

3.1	Introduction	82
3.2	Energy/Power Trade-off in Pouch Cells by Layer Selection	82
3.3	Scope and Context within xEV Powertrain	91
3.4	Enhancements/Modifications to Standard DFN Model	97
3.5	Computational Framework	110
3.6	Results and Discussion	124
3.7	Conclusions	134

***Attribution of content** The groundwork for converting the existing computer code (LIONSIMBA v1.0x) into a suitable form for layer optimisation was initiated by this thesis author, Krishnakumar Gopalakrishnan. However, with the exception of the spectral scheme, for which Krishnakumar Gopalakrishnan was responsible, and the zero-dimensional thermal model for which Ian D. Campbell (PhD student, Imperial College London) was responsible, the advancements inherent to the enhanced computer software (LIONSIMBA v2.0) were made in equal parts by Krishnakumar Gopalakrishnan and Ian D. Campbell. These advancements would not have been possible without the contributions and support of Dr Davide M. Raimondo (Associate Professor, University of Pavia) who served as an unofficial supervisor for the work reported in this chapter. The concept of layer reconfiguration for energy and power trade-off, the layer optimisation framework, and the source code by which it is implemented were co-developed in equal parts by Krishnakumar Gopalakrishnan and Ian D. Campbell. Krishnakumar Gopalakrishnan was the major contributor to the development of the binary search while Ian D. Campbell was the major contributor in the analysis of results. Parvathy Chittur Subramanianprasad (MSc student, Queen Mary University of London) was instrumental in developing the analytical expression for the maximum possible number of layers n_{\max} .

3.1 Introduction

THE issue of ‘range anxiety’ is a pervasive mental blockade for potential buyers of electric vehicles which in-turn hampers their widespread adoption. From a consumer viewpoint, yet another practical issue is the fact that upon encountering a ‘low battery’ scenario on a long distance journey, the charging times required for sufficiently replenishing the battery to enable completion of the journey are prohibitively large, to the point of being non-competitive against conventional fossil fuel powered vehicles.

Unfortunately, the aforementioned scenarios are not unimaginable with the present state of the art in lithium ion batteries. Hence, improving the All-Electric Range (AER) and providing fast charging capabilities are two near-term goals of manufacturers of electric vehicles. Increasing the AER necessitates a battery pack with higher energy content in it while lowering the charging time demands a pack with higher power capability. The contrasting nature of these goals can be traced all the way down to the cell level and is presented in section 3.2. By trading off the number of layers in a pouch cell against the content of active electrode material accommodated within it, bespoke cell designs addressing either the energy demand or the power demand can be obtained. In the absence of accessible documentation (as either industry white papers or academic literature) on the layer selection methodologies employed in automotive pouch cell designs, this author postulates that manufacturers iterate through an extensive empirical testing process of prototypes with a range of layer choices. In the view of this thesis author, this procedure is not only time-consuming, but is also likely to result in sub-optimal designs. This chapter envisages a model-based engineering solution to more optimal cell designs by determining the appropriate number of layers needed to maximise its *usable* energy while simultaneously satisfying certain power capability constraints. The rest of the chapter provides a detailed treatment of topics such as the proposed layer optimisation framework, its assumptions involved, and various modifications to standard numerical code required to facilitate this design procedure.

3.2 Energy/Power Trade-off in Pouch Cells by Layer Selection

Varying the number of electrochemical layers stacked within a pouch cell has contrasting effects on its energy storage and power handling capabilities. In this section, a high-level

intuitive explanation of this phenomenon is first offered, before delving into a detailed presentation of this effect and its implications for a specific example cell in section 3.2.3. Interwoven into the narrative is a set of simplifying assumptions which establishes the broader context within which a computational framework for determining the optimum number of layers for a specific target design shall be formalised (to be discussed in section 3.5).

3.2.1 Preliminary assumptions

To obtain a balanced loading of both electrodes and to avoid asymmetrical exhaustion of lithium from one of the electrodes during operation, it is desirable to carefully calculate the volume of electrochemical active materials to be accommodated within the cell. This concept is well-known and is commonly discussed in standard textbooks in the field such as those by Rahn and Wang [8] wherein example calculations are presented for non-porous electrodes. The study by Ramadesigan *et al.* [25] also supports the statement that capacity matching of anode and cathode materials is a standard practice in cell design.

In the case of lithium ion cells with porous electrodes, the concept of electrode-balancing involves an additional variable *viz.* the porosity of the active materials. The roles of porosity and its corollaries *i.e.*, the material volume fraction and filler/binder fraction are discussed in section 5.3.1. In this work, a major assumption about material porosities (and hence active-material/filler volume fraction) is that they are held constant. The rationale behind using this simplified assumption is as follows.

This author visualises the integration of cell-level design optimisation (through an optimal layer selection procedure) into the overall drivetrain design by the *cell manufacturer* before a custom design is delivered to vehicle/system integrators. Cell manufacturers, especially small-scale manufacturers do not necessarily synthesise each electrochemical component, but instead may opt to source certain raw-materials from an upstream supply-chain. From a manufacturing viewpoint, the porosity of the electrode materials is governed by the extent of calendaring of the electrode reel. Using pre-calendered electrode materials or sourcing large volumes of electrode reels with a fixed extent of calendaring can help to keep costs low. Since researchers in the field are typically not privy to the specifics of the industrial procurement process, in the absence of further information, the assumption of constant porosities provides a good starting point for this model-oriented design study.

3.2 Energy/Power Trade-off in Pouch Cells by Layer Selection

From a technical viewpoint, there exists another redeeming argument to support the constant porosity assumption. Keeping material porosities constant enables to eliminate one degree of freedom from the design optimisation study, thereby narrowing the dimensionality of the search space. To the best of the author's knowledge, there has not yet been any published work tackling layer optimisation of pouch cells. Building an initial infrastructure in terms of a computational framework that is based upon this constant porosity approximation shall at least provide a solid foundation to build upon for such real-life use-cases. The author foresees this study as a vanguard research into cell engineering and therefore places a high value in obtaining ballpark estimates of an optimal layer count, albeit with constant porosities. Ramadesigan *et al.* [25] present an opinion that the choice of porosities of electrode materials is currently being done on a trial and error basis. Nevertheless, for real-world use, the influence of varying the material porosities on the cell's performance is to be quantified. Hence, prior to adopting this model-based methodology for production yields at scale, a fully-integrated design optimisation process with variable porosities has to be developed. Therefore, in this work, the study is restricted to constant porosity values, whilst acknowledging variable porosity designs as an important aspect for future studies.

At the system level, the efficiency of the drivetrain is considered to be constant. The drivetrain of an electric vehicle consists of a whole host of electrical and mechanical components such as power electronics, electric motors, gearing, differential shaft and other transmission systems. The efficiencies of each of these individual components has a cascading effect on the overall drivetrain efficiency. The efficiency of each component is strongly dependent upon the operating point. For instance, the efficiency of an electric motor is a function of its torque-speed curve. In practice, it is rarely easy to decouple these efficiencies at least during the initial design stage. The datasheet/technical specification of each component in the platform is required to make a comprehensive multiphysics-based design optimisation study. This is well beyond the scope of this work and requires access to various design blueprints. Therefore, a constant lumped efficiency value for the drivetrain is adopted for this work. However, the proposed optimisation methodology is a modular one which implies that it can be suitably adapted *e.g.* to include a efficiency value dependent upon power delivered at the wheels. However, the biggest redeeming aspect (observed after the completion of the study) is that using a constant efficiency value did not influence the final

3.2 Energy/Power Trade-off in Pouch Cells by Layer Selection

layer choice for the cell design. As seen in section 3.5.2, the drivetrain efficiency plays a role only during acceleration studies. As per the results presented in section 3.6, the layers required for satisfying even the basic fast-charging requirements far exceed the layers required for handling the acceleration power demands. Therefore, this assumption is justified for keeping the computations tractable.

From a pack perspective, the primary assumption in the formulation of the proposed optimisation methodology is that the pack configuration (series/parallel arrangement of modules, number of cells per module and other system-level specifications) are held constant throughout. The validity of this assumption is easily justified since a cell-level design may be performed independently of the larger drivetrain design. In fact, the author postulates that present design process for electrified transportation is a modular one *i.e.*, empirical cell designs are developed based on certain specifications laid out by vehicle manufacturers and is not integrated into the drivetrain design. This modularity in the design approach enables to keep such system-level parameters constant.

A further assumption in this study is that the overall height of the pouch is held constant at 10 mm. The rationale behind choosing this specific pouch height is discussed in section 3.4.1. In the absence of this constraint, any arbitrary pouch size can be chosen, leading to an infinite-dimensional optimisation problem wherein no unique optimality criterion exists. This assumption is in-fact enforced by a current trend in the automotive industry *viz.* adoption of common-module designs wherein the physical dimensions of the pack are chosen a priori and modularising the pack helps in tailoring them suitably to cater to different market segments. Extending this philosophy down to the cell level, it is easy to visualise the benefits of having cells of identical exterior dimensions. For instance, having a common inventory helps a vehicle manufacturer to keep costs in check for subsequent designs *e.g.* for derivative model families of their product portfolio. This means that, for any layer choice to be tried, the constituent components of the cell is to be arranged and contained within the same pouch (of fixed exterior dimensions). This naturally leads to the assumption that the thickness of the pouch material used shall remain constant throughout, which in-turn implies that the overall height of the electrochemical stack within the pouch is constant. The detailed calculations of the stack height is presented in section 3.4.1.

3.2 Energy/Power Trade-off in Pouch Cells by Layer Selection

The current collectors and the separator in each electrochemical layer are assumed to have uniform thickness irrespective of the number of layers used. Barring minor manufacturing variability and tolerances, these values are merely factual data requiring no further justification. For instance, a constant separator thickness was used in the design optimisation study by Newman [26]. The final assumption from an electrochemical point of view, introduced specifically for the first time in literature by this thesis author, is that the relative thicknesses of each electrode is held constant to a fixed ratio. This warrants further explanation, but is ill-suited for this introductory discussion. The details of this aspect are discussed in section 3.5.6. Certain assumptions are to be made about the temperature distribution within the layers owing to the choice of cooling arrangement. These aspects merit more than a cursory listing in this introductory section and hence is discussed in section 3.3.3.

3.2.2 Motivation

This section provides a qualitative description of the effect of varying the number of layers within a pouch cell and presents the motivation to embark upon this layer optimisation effort.

Based upon the discussion in section 3.2.1, it is clear that by changing the choice of layer counts accommodated within a pouch of fixed height, the thicknesses of the two electrodes within each unit cell has to be suitably recomputed. Such use of different electrode thicknesses imply that the electrochemical-thermal behaviour of a cell constructed with one particular layer count shall be different from those employing any other layer count. With very few layers, thicker electrodes can be used. This implies that a higher utilisation of the available pouch volume can be used towards energy storage leading to higher theoretical capacity for these cells. Based on the discussion thus far, using low layer counts to construct cells may seem appealing for range extension of xEVs. However, prior to this, certain application-specific aspects of designing cells for automotive packs must be duly considered.

Thick electrodes resulting from using low layer counts present an increased impedance for the diffusion of lithium ions through their microporous structure, which implies that when operating under even moderate external loads, the cell may hit voltage cutoffs before all the stored energy can be extracted. Thus, with ultra low layer designs, the power handling capability of the cell suffers. The requirement of evenly distributing the external load power over the available active surface area without inducing large overpotentials necessitates

3.2 Energy/Power Trade-off in Pouch Cells by Layer Selection

a certain minimum number of layers. With higher layer counts, the increased active surface area translates to a reduced power density, which in-turn leads to a lower rate of heat generation. Furthermore, with increased layer counts, the fraction of pouch volume occupied by current collectors is proportionately higher. This leads to more conduction pathways to help channel heat generated away from the cell's interior which helps in faster cooling. With high layer counts, this aspect of lower heat generation coupled with its faster removal leads to an overall reduction in cell's temperature, which helps to extend the pack's lifetime owing to a reduced degradation rate.

In summary, for very low number of layers, there exists more active material, leading to a high energy capacity. However, the reaction surface area is diminished proportionately leading to lower power capability. Furthermore, owing to the presence of very thick electrodes, the current density within the solid conductive matrix shall not be homogeneous [129], nullifying some fundamental modelling assumptions of the standard Doyle-Fuller-Newman (DFN) model. On the other hand, very high number of layers imply vanishingly thin electrodes and correspondingly less active material accommodated within the cell, thereby resulting in a lower energy capacity. Figure 3.1 shows a qualitative comparison of the construction of one layer of an energy cell versus power cell which illustrates all the aspects discussed thus far.

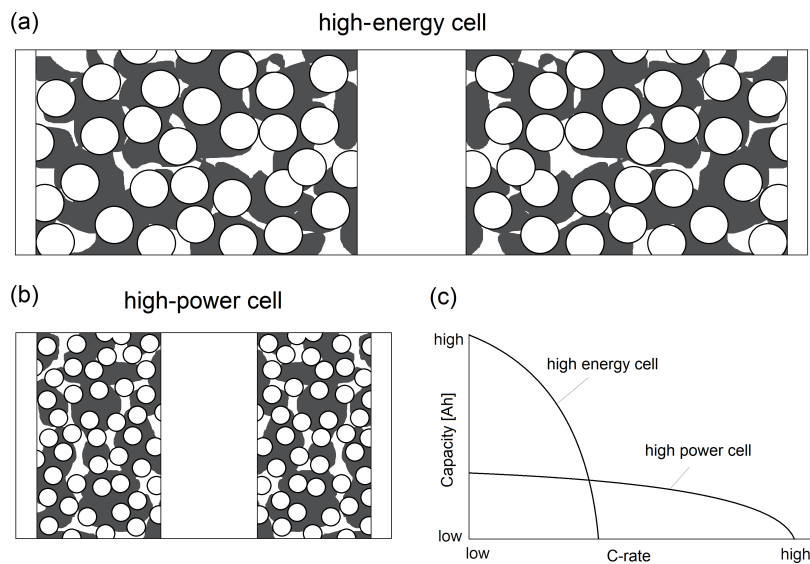


Figure 3.1 Schematic depicting a qualitative comparison of the construction of one layer of a high-energy cell versus a high-power cell. The illustration at top depicts one layer of a high-energy cell wherein thick electrodes are used. The bottom-left illustration depicts a single layer of a high-power cell wherein very thin electrode regions are used. Both cell diagrams are drawn to the same scale. The bottom right plot qualitatively indicates the relationship between C-rate and the nominal cell capacity. Illustration reproduced from von Srbik [130].

Therefore, there exists a research question on what constitutes the best layer choice that straddles this trade-off with the least penalty to the power capability of the cell whilst simultaneously having the maximum possible capacity. This saddle point determination needs to be performed for a curated set of power input/output conditions to the cell. This niche problem has not yet been tackled by researchers and therefore motivates the need to perform a careful design study which is documented in this chapter.

3.2.3 Quantitative demonstration of energy/power trade-off

The discussion in section 3.2.2 has motivated the need for an in-depth exploration of the energy to power trade-off expressed as a function of the number of layers. Before embarking on constructing a framework to optimise the layer choice by formalising various constraints that govern this optimality, this section aims to quantitatively demonstrate this relationship by applying a fixed galvanostatic discharge to an example cell. Additionally, the crucial idea of *usable* energy versus *total* stored energy is also introduced.

A Lithium Cobalt Oxide (LCO) cell whose physical properties and simulation parameters is drawn from the combined set of data from tables 3.2 and 5.2 is used as the example cell. The only set of values that overlap between these two tables are – *a*) the cut-off voltages, and *b*) the number of nodes used for numerical discretisation of the governing Partial Differential Algebraic System (PDAE) equations. For these conflicting quantities, the values in table 3.2 prevail for all simulation studies in this chapter. Furthermore, the individual electrode thicknesses from table 5.2 are not directly used, but instead calculated for every layer choice by keeping the ratio of their relative thicknesses constant. This aspect shall be explained in section 3.5.6.

Figure 3.2 illustrates the influence of the number of layers on the energy and power capability of the example cell. Starting at 100 % State of Charge (SOC), a constant current discharge of 60 A^\dagger is applied to a DFN model of the cell until reaching the lower cut-off voltage. For each discharge run, the model is reconfigured with a different layer choice. Five distinct layer choices have been carefully chosen so as to provide a clear illustration of the energy/power trade-off phenomenon.

[†]The rationale behind choosing this specific magnitude of applied current is explained in the section dealing with [selection of a suitable reference capacity cell](#) (also see section 3.4.1).

3.2 Energy/Power Trade-off in Pouch Cells by Layer Selection

As seen in fig. 3.2, during the initial phase of discharge, the terminal voltage of the cell is the highest for the two highest layer choices *i.e.*, $n = 90$ and $n = 70$. Consistent with the explanation in section 3.2.2, these two layer choices have thin electrodes and hence comparatively low resistances leading to only a small internal overpotential drop. However, as expected, their total energy is lower than the cell with $n = 50$ layers as evidenced by their relative run-times until lower cut-off voltage. This is to be expected as the thin electrodes of these high layer count cells cannot store a large volume of active material. Based on the explanation from section 3.2.2, it is expected that this trend will continue *i.e.*, the lower the layer count, the higher the run-time until cut-off. If this were the case, *prima facie* it seems that the layer optimisation task is trivial.

Inspecting the discharge curves of lower layer choices brings into light the concept of *usable* energy. Contrary to expectations, the discharge curves corresponding to very low layer counts in fig. 3.2 terminate even earlier than $n = 50$. This is owing to the fact that although

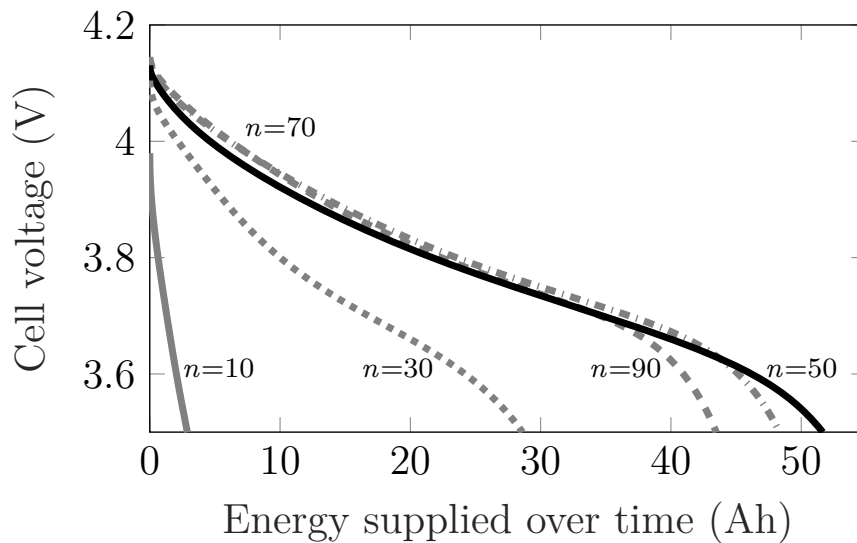


Figure 3.2[‡] Terminal voltage curves of a Li-ion cell (with parameters given in table 3.2) under a 60 A galvanostatic discharge beginning from 100 % SOC until lower cut-off voltage for a few layer choices n , in a pouch cell of fixed exterior height. The maximum usable energy is achieved for an intermediate choice of n that corresponds to neither the highest nominal capacity layer configuration ($n = 10$) nor the highest electrode surface area configuration ($n = 90$).

[‡]This figure has been extensively adapted (by this thesis author, Krishnakumar Gopalakrishnan) from the original figure created by Ian D. Campbell showing run times of cells with various layer counts instead of their energy supplied. The copyright on the original figure prior to this adaptation is held by Ian D. Campbell, with intellectual contributions from and the right to use asserted by Krishnakumar Gopalakrishnan.

3.2 Energy/Power Trade-off in Pouch Cells by Layer Selection

the total stored energy in cells with low layer counts is much higher, only a fraction of it is usable. This aspect introduces non-trivial dynamics (as discussed below) to an otherwise linear optimisation task.

For instance, when $n = 10$, the terminal voltage of the cell collapses almost instantaneously, reaching cut-off voltage whilst its SOC remains as high as 96%. At very low layer counts, the thickness of each electrode is high. This presents a high resistance to the flow of charges thereby leading to high overpotential drops within the cell. The usable energy under this 60 A galvanostatic discharge for various layer choices is compared in table 3.1. It can be seen that for very low layer counts, the usable energy that can be extracted is minuscule, albeit their theoretical capacity Q_n are in-fact the highest[§]. The usable energy in Wh reported in table 3.1 is obtained by multiplying the integral of the area under each discharge curve by the applied current (60 A) with the appropriate scaling of the time-base (*i.e.*, conversion from minutes to hours).

Table 3.1 Theoretical capacity and usable energy of a Li-ion cell (with parameters given in table 3.2) for a few layer choices under a 60 A galvanostatic discharge.

n	C-rate	Theoretical Capacity (Ah)	Usable Energy (Wh)	Remaining SOC (%)	Resistance at cutoff (m Ω)
90	1.24	48.25	166.46	9.84	0.97
70	1.11	53.99	184.80	10.26	1.35
50	1.00	59.73	195.47	13.51	3.44
30	0.92	65.47	101.20	58.95	10.24
10	0.84	71.21	10.15	96.22	11.18

Table 3.1 also brings into view the fact that the C-rate of the cell becomes a variable quantity even for a galvanostatic discharge, due to the dependence of its nominal capacity on the number of layers n . This represents a departure from the norm in the modelling community wherein the performance of cells are quantified as a function of the applied C-rate *e.g.* in chapters 5 and 6 of this thesis. However, the preliminary investigation thus far has quickly revealed that this normalised quantity does not hold much importance in any study where the number of layers within a pouch cell is varied.

Taking into account these factors, a reasonable choice of the number of layers in this specific 60 A galvanostatic application for this example cell could be $n = 50$. This represents

[§]The computation of theoretical capacity as a function of number of layers is discussed in section 3.6.4.

3.3 Scope and Context within xEV Powertrain

a practical compromise between the surface area available for reaction and the total volume of active material accommodated. Out of the finite layer configurations considered, this layer choice offers the highest usable energy for the given discharge rate.

In this sample study, only a handful of layer choices were considered, which represents only a small possibility of the overall design space to be considered. Furthermore, thermal considerations were not explored so far. For robust cell design, manufacturers shall need a widely applicable model-led design tool that can tackle the various scenarios that can occur in real-life operating conditions. A deterministic set of optimality criteria for the layer selection is also to be formulated. The choice $n = 50$, therefore does not represent the general optimal layer choice even for this example cell. However, this sample study serves as an illustrative demonstration of the trade-offs in energy versus power handling capability of a cell for a specific set of conditions. Furthermore, it introduces the complicating aspect of *usable* capacity into what would have otherwise been a trivial exercise, thereby setting the tone for the development of a general layer optimisation framework for pouch cells.

3.3 Scope and Context within xEV Powertrain

It is important to provide the contextual setting for this layer optimisation work since it is nestled deep within the broader horizon of electric drivetrain optimisation. Figure 3.3 provides a graphical overview depicting the hierarchical architecture of a typical xEV powertrain, from the system level down to a single electrochemical layer. The rest of this section describes the scope of this layer optimisation work and its integration into this overall architecture. A further set of assumptions that were deemed inopportune to be discussed in section 3.2.1, is introduced at apropos junctures throughout this narrative. The overall architecture of an xEV powertrain can be studied through a systematic, hierarchical evaluation at – *a*) the system-level, *b*) the pack-level, and *c*) the cell-level.

3.3.1 System-level – vehicular platforms

The top row of fig. 3.3 represents the typical layout of a *series*-hybrid powertrain [30]. Partly to supply the mechanical power and/or partly to charge the battery during propulsion, a downsized Internal Combustion Engine (ICE) is employed. The ICE is coupled to the pack's DC bus through a generator and three-phase rectifier. While tackling the power handling

3.3 Scope and Context within xEV Powertrain

requirements, irrespective of whether a BEV or PHEV powertrain is being considered, the cells in the pack are to be designed for the worst-case operating scenario *i.e.*, without any power support from the ICE. This implies that all discharge simulations of the PHEV are to be conducted with the powertrain operating in all-electric mode resulting in a net charge-depletion. The only distinction is that the *magnitude* of power to be handled by the pack in this worst case scenario is vastly different between the BEV and PHEV cases. This allows for some simplification as explained below and helps to narrow down the scope of the problem to be tackled.

Omitting the components to the left of the battery pack (represented as text boxes with light grey border) shall render a powertrain corresponding to that of a BEV. The proposed layer optimisation methodology is developed and presented in the context of this BEV

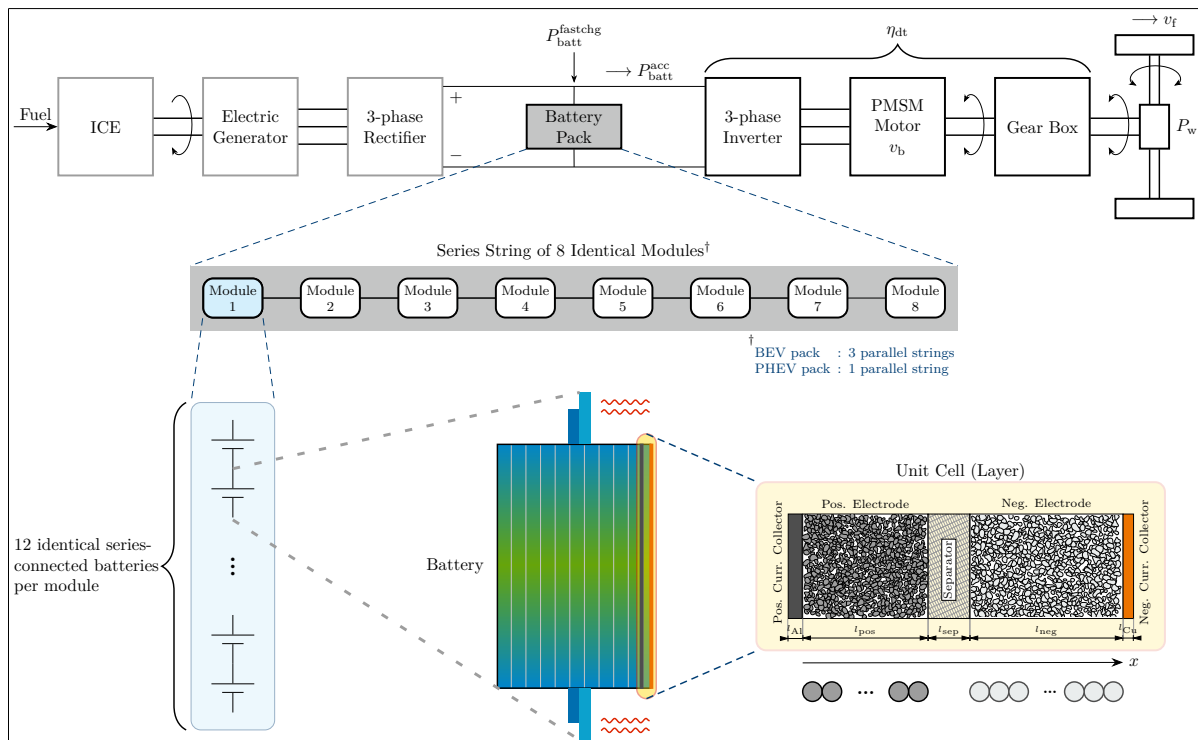


Figure 3.3[¶] Schematic depicting the vehicle-to-cell hierarchical overview of a typical electrified powertrain architecture. This represents the system-level context within which the proposed layer optimisation framework has been developed. Two xEV powertrains – *a*) a Battery Electric Vehicle (BEV), and *b*) a series Plug-in Hybrid Electric Vehicle (PHEV) are chosen as examples to demonstrate how the methodology facilitates common module designs for such battery packs.

[¶]This figure was created by Krishnakumar Gopalakrishnan who asserts copyright, with intellectual contributions from and the right to use asserted by Ian D. Campbell.

powertrain. However, being a modular framework, the optimisation methodology may be readily extended to a PHEV powertrain.

As shown in fig. 3.3, the BEV powertrain typically comprises of – *a*) a battery pack, *b*) a three phase inverter, *c*) a Permanent Magnet Synchronous Motor (PMSM), *d*) a gearbox for torque multiplication, and *e*) the rest of the powertrain (differential shaft and driven wheels). Considering the worst-case scenarios, the power to be handled by the battery pack arises due to – i) fast charging from the mains $P_{\text{batt}}^{\text{fastchg}}$ (charge), or ii) acceleration from standstill $P_{\text{batt}}^{\text{acc}}$ (discharge). The acceleration power is computed from the power required at the wheels P_w . The details of this calculation is presented in section 3.5.2. The sign convention used in this chapter is that the charging power is positive (and consequently, the discharging power is negative).

3.3.2 Pack-level – strings, modules & cells

Delving into the battery pack under consideration, this thesis considers a standard modular layout wherein the PHEV pack has one string while the BEV pack has three parallel strings, in congruence with a contemporary pack design [131]. Within each string, both vehicular platforms employ 8 series-connected modules. Taking cognisance of the benefits of common module design, identical pack modules are assumed across both xEV platforms which is then extrapolated to impose a stronger condition of identical geometry for the constituent cells (see section 3.2.1). The exterior dimensions of the pouch cells under consideration are listed in table 3.2.

Each module consists of 12 identical series-connected cells denoted by battery circuit symbols (cyan-filled blocks in fig. 3.3). The PHEV pack is smaller and consists of only 1/3rd of the cells in the BEV pack. Assuming that the BEV pack consists of a 96S-3P cell assembly, this implies that the PHEV pack shall conform to a 96S-1P layout. The DC bus voltage is unaltered since both packs have same amount of series cells. The power flow is assumed to be uniformly distributed across all the cells within the pack(s). At first, the power required at the terminals of the pack is computed. From this, a first-order design ball-parking of the layers of the cell is made through a single cell simulation. This process enables reduced simulation run-time with the conditions of one cell assumed to be representative of all cells in the pack.

While the aforementioned assumption of identical cell conditions across the pack seems infeasible at first glance, three careful considerations have been made to justify this assumption. Firstly, power (and not current) is used as the stimulus to the cell. This implies that, despite the *parallel* connection of cells (in groups of three cells within each module), each cell experiences the same power, $p_{\text{cell}} = \frac{P_{\text{batt}}}{n_{\text{cells}}}$. Even across parallel-connected strings, the power handled by each cell shall be the same. This necessitates the modification of the standard DFN model in order to accommodate power inputs which is discussed in section 3.4.2. Such a modification assumes particular significance in the context of making the model amenable to a charging scheme wherein the control algorithm in a modern grid charger's power electronics enable it to continuously operate close to its power-delivery limits with suitable voltage feedback from the battery pack. Secondly, although the current in all cells of a *series* string remain the same (by virtue of Kirchoff's current law), their terminal voltage levels could drift away from each other and becomes unbalanced over time [3]. This naturally raises questions on the assumption of identical conditions for all cells. However, this voltage unbalance is mitigated with the help of modern Battery Management Systems (BMSs) that employ balancing techniques such as passive bleeder resistors or sophisticated active dc/dc converters. Yet another adverse effect that poses a threat to the assumption of identical conditions is the uneven distribution of cell temperatures. In automotive packs employing natural convection, cells that are physically located innermost in the string tend to get hotter than the outermost cells. Through good thermal management design e.g. forced cooling through circulation of the coolant through conduits grooved into the pack, thermal balance may be achieved. Therefore, it can be argued that, when operating in a well-designed and controlled environment, cell-to-cell deviations are minimised. This justifies the global representation of all cells in the pack through a single-cell simulation, although modifications to the simulation model are deemed necessary to facilitate power inputs and is discussed in section 3.4.2.

3.3.3 Cell-level – layers, cooling, electrochemical & thermal models

The illustration at the centre of the bottom row in fig. 3.3 shows a schematic representation of a cell arranged within each module. In practice, the physical layout of cells within a module is slightly more complex. For instance, a typical arrangement consists of groups of 3 parallel cells. However, the illustration in fig. 3.3 suffices to explain the necessary details required for the specific task at hand.

3.3 Scope and Context within xEV Powertrain

Each cell in the pack consists of a number of identical layers n . The words ‘layer’ and ‘unit-cell’ are used interchangeably in this thesis to denote a single basic electrochemical unit consisting of – i) a positive current-collector, ii) a positive electrode region, iii) a separator material, iv) a negative electrode region, and v) a negative current-collector (see fig. 1.1). Particular attention is called out in regard to the distribution of temperature within the cell. In the schematic of fig. 3.3 the shading scheme is such that greener tints represent the hotter regions of the cell while bluer tints represent colder regions. The temperature distribution within the cell as indicated by this shading scheme is consistent with that reported in literature [132–134]. Furthermore, heat exchange with the surroundings is also graphically illustrated through cooling plates mounted at the tabs of the cell. This highlights the specific type of cooling assumed *viz.* *tab-cooling* as opposed to conventional *surface-cooling* historically employed for automotive applications. The assumption of tab-cooling is an essential requirement for upholding the validity of the proposed layer optimisation scheme, and therefore warrants further justification.

An experimental study by Hunt *et al.* [135] compared tab cooling of cells against conventional surface cooling. It was found that $\approx 8\%$ increase in the usable capacity of pristine cells was achieved with tab cooling relative to that achieved with surface cooling. Secondly, with surface cooling, the loss rate of usable capacity over thousand cycles was nearly thrice of that with tab cooling. This implies that using tab cooling can potentially help to extend the lifetime of the pack by three times. Thirdly, at higher discharge rates, surface cooling resulting in a loss of usable capacity of 9.2% compared to just 1.2% for tab cooling. The simulations discussed as part of the optimisation framework reported in section 3.5 are intended to obtain robust cell designs capable of handling worst-case power inputs. In these scenarios, tab cooling is more appropriate. Therefore, this author has no qualms about recommending this specific cooling mechanism to be used in conjunction with the results reported (see section 3.6) by applying the proposed layer optimisation scheme.

Apart from its aforementioned beneficial effects on cell longevity and performance, with the integral assumption of tab cooling, there exists an important side effect that affects the very core of the numerics of the layer optimisation methodology. Carefully examining the shading scheme used for the schematic in the centre-bottom of fig. 3.3, it is clear that at any vertical co-ordinate in space within the cell, the shading across the entire cell width

3.3 Scope and Context within xEV Powertrain

remains uniform throughout. Furthermore, it has been reported in literature that the thermal gradients established within a unit cell are relatively small and may be safely ignored [136]. These imply that each layer along a one-dimensional cross-section of the cell is at the same temperature. Based on the inferences from Hunt *et al.* [135], with tab cooling, only small thermal gradients are induced in the planar direction. In this unique scenario, the thermal effects within the cell are not large enough to warrant a detailed numerical discretisation. On the other hand, ignoring the temperature distribution of the cell shall not lead to robust cell designs, especially given that design simulations typically involve high magnitudes of power.

In situations akin to aforementioned circumstances, a lumped thermal model of the cell has been recommended by Pals and Newman [129]. This represents a good trade-off between accuracy and simplicity and hence, is deemed to be appropriate for this design application. A suitable value for the convective heat transfer coefficient h (see table 3.2), comparable to the typical magnitudes in forced air convection, is used to represent the heat transfer from the cell to the environment. The heat exchange area is the combined surface area of the two cooling tabs that are situated at either end of the cell. The temperature of the coolant (a thermal ‘sink’ in thermodynamic terminology) is denoted by T_{sink} . In this work, this ambient temperature is held constant during the course of a simulation run, but is allowed to change to different constant values between set of simulations as per relevant vehicle testing standards. The details of this aspect is discussed in section 3.5. The material properties of the constituent components of each layer coupled with the total number of layers are used to determine the lumped mass and specific heat capacity of the pouch cell. These computations are discussed in sections 3.5.8 and 3.5.9 respectively. The assumption of tab cooling thus leads to this qualitative description of the lumped thermal model to be used for the design simulations. Further quantification by way of relevant model equations and the computation of the constituent parameters of the thermal model is embedded as an integral aspect of the layer optimisation framework and shall be presented in section 3.5.9.

As a final observation, all layers within the cell are electrically in parallel which implies that their terminal voltages are identical. The current (or power) at the cell terminals is shared equally among each layer. The aforementioned considerations have important ramifications on the cell modelling and helps to drastically simplify it. Specifically, these considerations imply that the electrochemical performance of any one layer is identical to every other

3.4 Enhancements/Modifications to Standard DFN Model

layer. Therefore, in conjunction with a lumped thermal model, a standard Pseudo Two-Dimensional (P2D) discretisation of the DFN model suffices to capture the electrochemical behaviour of the entire cell. The bottom-right illustration of fig. 3.3 presents a one-dimensional discretisation of the cell layer across its thickness. The spheres along the axial direction represent computational nodes wherein the solid-phase diffusion equation is to be solved (see section 1.3 for a brief overview). It is this standard DFN model, suitably amended to accept power inputs, that will be the backbone of the electrochemical aspects of the design simulation. The electrochemical model shall be strongly coupled in a bidirectional sense to the lumped thermal model *i.e.*, the temperature of the cell shall influence various cell parameters (see table 3.2) while the overpotentials and currents in the cell shall play a role in the rate of heat generation and cell temperature simultaneously.

Thus, through a systematic set of simplifying assumptions that are justifiable in a real-world design, the system-level requirements at the pack-level can be suitably scaled down to power-density inputs at the layer level. Having established the contextual setting and scope of this work within the broader landscape of drivetrain optimisation, it is now possible to proceed to the set of numerical enhancements required to be incorporated into the DFN model to handle the specific requirements of this layer optimisation task.

3.4 Enhancements/Modifications to Standard DFN Model

3.4.1 Augmentations to parameter set

Cell capacity and electrochemically active surface area

The Pseudo Two-Dimensional (P2D) implementation of the standard Doyle-Fuller-Newman (DFN) model lacks certain parameters that are vital to the layer optimisation process. The cell's nominal capacity is a fundamental quantity that gets altered as the number of layers is varied. However, it may be surprising to discover that this parameter is absent in the research literature discussing the P2D model. The rationale behind this glaring omission becomes clear upon closer examination of the model equations presented in table 1.1. These equations do not operate on a cell level, but instead are formulated on a normalised basis. To clarify, only one layer of the cell is being modelled wherein the stimulus driving the model is the applied current *density per unit area* rather than the total external current. The model to be used in

3.4 Enhancements/Modifications to Standard DFN Model

the layer optimisation task therefore faces a unique predicament – the need to adhere to the present modelling paradigm for compatibility with the status quo whilst being flexible enough to incorporate the cell’s capacity as a function of number of layers.

To tackle the aforementioned quandary, it is key to realise that the core parameter that varies with the number of layers in a pouch cell is the electrochemically active cross-sectional surface area A_{cell} . Curiously, published literature on physics-based cell modelling do not place rigorous emphasis on this key parameter. More often, much to this author’s chagrin, this parameter is simply listed in a standard table of parameters and is typically sourced from a historic parameter-set without further explanation.

For a pouch cell, the overall electrochemically active surface area can be defined as

$$A_{\text{cell}} = n \times A_{\text{elec}} \quad (3.1)$$

where n is the number of layers and A_{elec} is the active surface area per layer.

Surface area per layer

A literature search reveals that akin to the cell’s capacity, there is no information of cross-sectional geometry in articles dealing with the P2D implementation of the DFN model. To determine the surface area per layer, relying on certain assumptions and the recent literature, a novel methodology is proposed involving a sequence of steps. The process involves the selection of a real-world cell, and determining its surface area per layer. To the best knowledge of the author, this reverse parametrisation process (explained next), mapping from a real-world cell to a new P2D parameter, is a unique idea.

1) Selection of a suitable reference capacity cell

This is a crucial first-step towards obtaining a complete parameter set – particularly to determine the surface area per layer.

The focus of this chapter is to provide a ready-to-use solution to industry that improves upon the present empirical designs through optimal layer configuration of pouch cells. There is a clear motivation to further increase cell capacities so as to maximise the All-Electric Range (AER), as laid out in the beginning of this chapter (see section 3.1).

3.4 Enhancements/Modifications to Standard DFN Model

With this guiding principle, as a starting point towards choosing a reference capacity cell, a survey was performed to identify the production BEV with the highest driving range. As of 2018, the Chevrolet Bolt BEV bears this distinction with a range of 383 km as rated by the United States Environmental Protection Agency (EPA). The specifications of its battery pack is listed in Liu *et al.* [131]. The battery pack of this BEV consists of 288 cells arranged in a 96S-3P configuration, in agreement with the configuration discussed in the drivetrain hierarchy of section 3.3.2.

The Chevrolet Bolt BEV pack has an energy capacity of 60.0 kWh with a nominal pack voltage of 350 V [131]. However, for this specific task, the Ah capacity is required. This can be obtained as

$$\text{Ah capacity of reference cell} = \frac{\text{Pack Energy (Wh)}}{\text{Nominal pack voltage (V)} \times \text{No. of cells in parallel}} \quad (3.2)$$

$$= \frac{60000}{350 \times 3} \quad (3.3)$$

$$= 57.14 \text{ Ah} \quad (3.4)$$

• DC bus voltage and revised cell capacity

Even without a dc/dc boost converter, robust design of the powertrain during brown-outs should allow for continued operation even with a slightly diminished DC bus voltage $\approx 4\text{--}5\%$ lower than nominal [30]. Considering a maximum permissible dip of 4% in the bus voltage *i.e.*, 336 V, the cell's capacity may be refined as

$$\text{Ah capacity of reference cell} = \frac{\text{Pack Energy (Wh)}}{\text{Lowest pack voltage (V)} \times \text{No. of cells in parallel}} \quad (3.5)$$

$$= \frac{60000}{336 \times 3} \quad (3.6)$$

$$= 59.52 \text{ Ah} \quad (3.7)$$

The reference cell's Ah capacity is therefore rounded to **60 Ah**[‡]. The 1C-rate of this reference cell is therefore 60 A.

[‡]In the interest of maintaining consistency, this computed capacity is retained for the cell used in chapters 5 and 6 of this thesis. This also explains the use of 60 A for the simulations used for demonstrating energy/power trade-off of section 3.2.3 since this current level corresponds to the 1C-rate of this reference cell.

- **Lower cutoff voltage for cells**

In this layer optimisation work, following the assumptions of section 3.2.1, the overall pack configuration remains unchanged *i.e.*, independent of number of layers within the pouch. This implies that the undervoltage threshold for DC bus voltage throughout this work shall remain fixed at 336 V. Therefore, with 96 series connected cells in a string, the lower cut-off voltage for an individual cell is 3.5 V. This value is reported in table 3.2 and is used as a termination condition for all simulations as explained in section 3.5.

2) **Computation of electrochemically overall active surface area for reference cell**

For the cell properties in tables 3.2 and 5.2, the majority of parameters are sourced from Subramanian *et al.* [137] and Northrop *et al.* [74]. In Northrop *et al.* [74], the *current density* that corresponds to a 1C-rate discharge of a cell with this parameter set is reported to be $\approx 30 \text{ A m}^{-2}$. With the help of carefully designed numerical simulations (very slow discharge with a trickle current from fully charged state until charge depletion), this value is refined to 29.23 A m^{-2} , so as to match the residual stoichiometries in both electrodes to that quoted in Northrop *et al.* [74].

The task of determining the electrochemically active overall surface area of the reference cell is now straightforward, and is obtained as

$$\text{Overall surface area of reference cell, } A_{\text{refcell}} = \frac{\text{1C-rate for the reference cell (A)}}{\text{1C-rate density (A m}^{-2}\text{)}} \quad (3.8)$$

$$= \frac{60}{29.23} \quad (3.9)$$

$$= 2.053 \text{ m}^2 \quad (3.10)$$

This value is listed in table 5.2 for use in chapters 5–6, but is *not* used directly in this layer optimisation work. This is because, as the number of layers change, the overall surface area changes as per eq. (3.1). However, determining this value is an important initial step in the determination of the surface area per layer.

3) **Setting the pouch height for the reference cell**

Although the official press release [138] from the manufacturer of the Bolt BEV does contain data on the cross-sectional geometry of the cell, it does not report the cell's height. Hence, this information needs to be assumed by extrapolation from an alternate source wherein the conditions are similar and so that value may be applied for the reference cell.

3.4 Enhancements/Modifications to Standard DFN Model

The review article by Gröger *et al.* [139] discusses the state of the art in energy densities of electrode materials used in various lithium ion chemistries. At the time of its publication, the areal capacity of cells were $\approx 2.0 \text{ mAh cm}^{-2}$. Gröger and colleagues recommended an areal capacity target of 4.0 mAh cm^{-2} for future automotive applications. The said publication also considers the aspect of stacking layers into pouches of certain geometries. In particular, table IV of Gröger *et al.* [139] considers a pouch of 10 mm height, for which the aforementioned areal capacities were calculated.

In the case of the reference cell under consideration, the areal capacity is

$$\text{Areal capacity of reference cell} = \frac{60\,000 \text{ mAh}}{20\,527 \text{ cm}^2} = 2.92 \text{ mAh cm}^{-2} \quad (3.11)$$

which is close to the desired value in automotive applications as per the recommendations in Gröger *et al.* Considering that the reference cell is based on the high energy density Chevrolet Bolt BEV cell, a pouch height of 10 mm is justifiable for this task and is reported in table 3.2. This numerical value is comparable to that of commercially available cells for automotive applications. For instance, a 56.3 Ah cell with a pouch height of 7.91 mm is manufactured by the Automotive Energy Supply Corporation [140] while a 63 Ah pouch cell with a pouch height of 11.0 mm is available from Kokam Inc. [141]. Therefore, it is reasonable to use a value of 10.0 mm for this 60 Ah reference cell. As per the assumptions discussed in section 3.2.1, this value is held constant throughout the layer optimisation process.

4) Computation of stack thickness of reference cell

The pouch material itself has a finite thickness (a value of 160 μm is used here; see table note g for this entry in table 3.2) and hence after accounting for this, the stack thickness available for placement of unit cells is smaller than the pouch thickness.

$$\text{Stack thickness, } L_{\text{stack}} = \text{Pouch height} - 2 \times \text{pouch thickness} \quad (3.12)$$

$$= H_{\text{pouch}} - 2T_{\text{pouch}} \quad (3.13)$$

$$= 10.0 - 2 \times (160 \times 10^{-3}) \quad (3.14)$$

$$L_{\text{stack}} = 9.68 \text{ mm} \quad (3.15)$$

The computed value of stack thickness is held constant for all layer choices trialled in the entire layer optimisation process.

5) Determination of number of layers within reference cell

The next step is to determine the number of layers within the reference pouch cell n_{refcell} . The thickness of a complete electrochemical sandwich multiplied by the number of layers yields the total stack height

$$n_{\text{refcell}} (l_{\text{Al}} + l_{\text{pos}} + l_{\text{sep}} + l_{\text{neg}} + l_{\text{Cu}}) = L_{\text{stack}} \quad (3.16)$$

The product of number of layers and the thickness of an electrochemical sandwich cannot exceed the overall stack height. This implies that the equality in eq. (3.16) is to be changed to an inequality, with the upper bound of the expression on the Left-Hand Side (LHS) of eq. (3.16) set to the stack height.

$$n_{\text{refcell}} (l_{\text{Al}} + l_{\text{pos}} + l_{\text{sep}} + l_{\text{neg}} + l_{\text{Cu}}) \leq L_{\text{stack}} \quad (3.17)$$

$$n_{\text{refcell}} \leq \frac{L_{\text{stack}}}{l_{\text{Al}} + l_{\text{pos}} + l_{\text{sep}} + l_{\text{neg}} + l_{\text{Cu}}} \quad (3.18)$$

Since fractional layers do not have any physical meaning, the number of layers that can be accommodated within any pouch must be an integer quantity. Therefore, n_{refcell} is computed as the 'floor' of the quantity in the Right-Hand Side (RHS) of eq. (3.18)

$$n_{\text{refcell}} = \left\lfloor \frac{L_{\text{stack}}}{l_{\text{Al}} + l_{\text{pos}} + l_{\text{sep}} + l_{\text{neg}} + l_{\text{Cu}}} \right\rfloor \quad (3.19)$$

$$= \left\lfloor \frac{9.68}{(15 + 72 + 25 + 88 + 10) \times 10^{-3}} \right\rfloor \quad (3.20)$$

$$n_{\text{refcell}} = 46 \quad (3.21)$$

The reference cell is thus determined to consist of 46 layers.

6) Computation of surface area per layer

Substituting the values of n_{refcell} and A_{refcell} into eq. (3.1), the electrochemically active surface area per layer is obtained as

$$A_{\text{elec}} = \frac{A_{\text{refcell}}}{n_{\text{refcell}}} \quad (3.22)$$

3.4 Enhancements/Modifications to Standard DFN Model

$$A_{\text{elec}} = \frac{2.053 \times 10^6 \text{ m}^2}{46} \quad (3.23)$$

$$= 44\,630.43 \text{ mm}^2 \quad (3.24)$$

$$= 44.63 \times 10^{-3} \text{ m}^2 \quad (3.25)$$

The surface area per layer thus computed is listed in table 3.2 and is held constant across all layer choices tried during the layer optimisation process. This assumption is immediately justifiable from a physical viewpoint, since the process of assembling layers is performed along the axial thickness direction (aligned with pouch height) and is independent of the planar (cross-sectional) direction.

3.4.2 Modification of standard DFN model to handle power inputs

As discussed in section 3.3.2, assuming identical cell conditions during operation necessitates that the external stimulus to each cell is an applied power value. The cell's terminal voltage and current can be viewed as its natural response to this power input. To simulate this condition and achieve a model-based optimal layer design, the standard DFN model, which conventionally handles current stimuli, has to be suitably modified to accept power inputs.

Plett [13] suggests a methodology for applying power inputs to equivalent circuit models for simulation at a fixed sample rate. This involves converting the input power P_k to a current I_k using an equivalent series resistance R_0 . The value of R_0 is updated at each time index k as per eq. (3.26).

$$I_k = \frac{v_k - \sqrt{v_k^2 - 4R_0P_k}}{2R_0} \quad (3.26)$$

where v_k is the cell's terminal voltage at time index k , evolved from the applied current up to and including the $(k - 1)^{\text{th}}$ time step.

There are two disadvantages in using Plett's simplified approach for the proposed layer optimisation study. Firstly, this necessitates the quantification of a lumped electrical resistance for a Physics-Based Model (PBM). Such an idea is at loggerheads with the fundamental philosophy of PBMs which strive to represent a detailed picture of underlying phenomena, as opposed to the system-level terminal behavioural characterisation facilitated by Equivalent

3.4 Enhancements/Modifications to Standard DFN Model

Circuit Models (ECMs). Translating power to current in this manner also necessitates a two-pass conversion between the physical and electrical domains – a process likely to significantly degrade modelling fidelity. Since the results from application of the model shall inform the number of layers to be used in a real-world cell design, such loss of fidelity is unacceptable. Secondly, the constraint of using fixed interval updates implies that a high-speed adaptive time-stepping solver cannot be used for handling this power input condition. This shall slow down the simulation speed considerably since the search space of layer combinations to be considered is fairly large. Furthermore, the simulations have to be repeated over multiple combinations of initial and ambient temperatures which shall significantly slow down the model-based design simulations and offset its advantages over a conventional prototype-based design.

Dees *et al.* [142] identified the requirement of having a P2D model that can run on applied power. However, in the aforementioned work, the relevant equations for reformulation of solid-phase boundary conditions are not presented. An independent derivation of reformulating the P2D model to facilitate an innate power input capability is therefore provided. Since the equations are derived for a single layer, the power *density* p , obtained by dividing the applied power by the overall active cross-sectional area A_{cell} , is used as the driving input.

$$p = \frac{P_{\text{cell}}}{A_{\text{cell}}} = \frac{P_{\text{cell}}}{nA_{\text{elec}}} \quad (3.27)$$

In the P2D model, charge conservation in solid phase is given by eq. (1.6), which is revisited below. Eqs. (3.28)–(3.29) represent the corresponding boundary conditions. In these equations, the current density i represents the applied input, σ_{eff} the effective electronic conductivity and a_s the specific interfacial surface area of an electrode respectively, j the molar flux density of lithium at the electrode surface and ϕ_s the solid phase potential.

$$\frac{\partial}{\partial x} \left(\sigma_{\text{eff}} \frac{\partial \phi_s(x, t)}{\partial x} \right) = a_s F j(x, t) \quad (\text{eq. (1.6) revisited})$$

$$\sigma_{\text{eff}} \frac{\partial \phi_s(x, t)}{\partial x} \Big|_{x_{\text{pos/Alcc}}}^{x_{\text{neg/Cucc}}} = -i \quad (3.28)$$

$$\sigma_{\text{eff}} \frac{\partial \phi_s(x, t)}{\partial x} \Big|_{x_{\text{pos/sep}}}^{x_{\text{neg/sep}}} = 0 \quad (3.29)$$

3.4 Enhancements/Modifications to Standard DFN Model

Equation (3.30) replaces the boundary condition in eq. (3.28) to use the applied power density p to drive the model.

$$\sigma_{\text{eff}_{\text{neg}}} \left(\phi_s(x, t) \frac{\partial \phi_s(x, t)}{\partial x} \right) \Big|_{x=x_{\text{neg}/\text{CuCC}}} - \sigma_{\text{eff}_{\text{pos}}} \left(\phi_s(x, t) \frac{\partial \phi_s(x, t)}{\partial x} \right) \Big|_{x=x_{\text{pos}/\text{Alcc}}} = p \quad (3.30)$$

Eqs. (3.31)–(3.32) represent constraints pertaining to physical laws and are to be satisfied.

$$vi - p = 0 \quad (3.31)$$

$$v > 0 \quad (3.32)$$

Equation (3.31) conveys the condition that the product of the terminal voltage and computed current density shall equal the externally applied power density, whereas eq. (3.32) implies that the cell's terminal voltage shall always remain positive during operation. Eqs. (3.30)–(3.32) are then discretised for numerical implementation as follows.

Figure 3.4 describes a schematic overview of a one-dimensional cell-centred Finite Volume (FV) discretisation scheme. Here, evenly spaced nodes are considered to form the support mesh along the through-thickness dimension of a layer. Vertical lines denote the edges of control volumes whereas the filled circles depict computational nodes where the axial-direction variables from table 1.1 are solved.

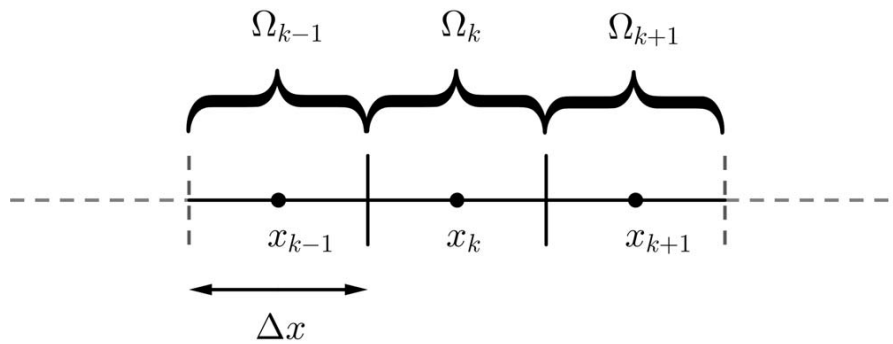


Figure 3.4 Simplified illustration of a standard cell-centred FV discretisation scheme. Illustration reproduced from Torchio *et al.* [18].

Equation (3.33) represents the weak form of eq. (1.6) applied on the FV mesh for each control volume, wherein subscripts k and $k \pm \frac{1}{2}$ denote the k^{th} FV node and its associated left

and right edges respectively.

$$\sigma_{\text{eff}} \frac{\partial \phi_s(x, t)}{\partial x} \bigg|_{x_{k-\frac{1}{2}}}^{x_{k+\frac{1}{2}}} = a_s F j_k(t) \Delta x \quad (3.33)$$

At this juncture, a simplifying approximation for the solid-phase potentials can be considered. In the standard FV scheme, the solution values at the faces (edges of control volumes) is obtained by interpolating from the two nearest FV node values. At either extrema of this one-dimensional computational domain, a linear extrapolation of the values from the first and last nodes can be performed. This increases the accuracy of computations, thereby providing good estimates of solid potentials at the two current collector interfaces. However, with the increased fidelity comes the penalty of a mathematically complex set of boundary conditions. When using high node densities in the negative and positive electrode regions (see table 3.2), for the two outermost control volumes, the values of $\frac{\Delta x}{2}$ become small. With a reasonably small mesh interval, the potentials at the cell centres can be considered to be nearly equal to that at their corresponding current collector interfaces. This assumption helps to keep the resulting mathematical expressions tractable.

Applying eq. (3.33) to the first control volume (0^{th} node) in the positive electrode and to the last control volume (n^{th} node) in the negative electrode,

$$\frac{-\sigma_{\text{eff, pos}} \phi_{s_0}}{\Delta x_{\text{pos}}} + \frac{\sigma_{\text{eff, pos}} \phi_{s_1}}{\Delta x_{\text{pos}}} + i = a_{s_{\text{pos}}} F j_0 \Delta x_{\text{pos}} \quad (3.34)$$

$$\frac{-\sigma_{\text{eff, neg}} \phi_{s_n}}{\Delta x_{\text{neg}}} + \frac{\sigma_{\text{eff, neg}} \phi_{s_{n-1}}}{\Delta x_{\text{neg}}} - i = a_{s_{\text{neg}}} F j_n \Delta x_{\text{neg}} \quad (3.35)$$

Multiplying eq. (3.34) by ϕ_{s_0} and eq. (3.35) by ϕ_{s_n} and subtracting,

$$\begin{aligned} \frac{-\sigma_{\text{eff, pos}} \phi_{s_0}^2}{\Delta x_{\text{pos}}} - \frac{\sigma_{\text{eff, neg}} \phi_{s_n}^2}{\Delta x_{\text{neg}}} + \frac{\sigma_{\text{eff, pos}} \phi_{s_0} \phi_{s_1}}{\Delta x_{\text{pos}}} + \frac{\sigma_{\text{eff, neg}} \phi_{s_n} \phi_{s_{n-1}}}{\Delta x_{\text{neg}}} \\ + p - a_{s_{\text{pos}}} F j_0 x_{\text{pos}} \phi_{s_0} - a_{s_{\text{neg}}} F j_n x_{\text{neg}} \phi_{s_n} = 0 \end{aligned} \quad (3.36)$$

3.4 Enhancements/Modifications to Standard DFN Model

Two solutions exist for the quadratic equation in eq. (3.36). However, the solid phase potential, being a physical quantity of the cell, has a unique solution. Therefore, in order to achieve numerical convergence, an additional positivity constraint, the FV-discretised equivalent of eq. (3.32), is imposed.

$$\phi_{s_0} - \phi_{s_n} > 0 \quad (3.37)$$

Finally, since the input to the model is the applied power density p , in addition to the cell's terminal voltage, the current density within each layer i at each time-step needs to be solved. This is facilitated by employing the discretised form of eq. (3.31). Furthermore, since this equation is mathematically simple, the aforementioned assumption of using node values at current collector interfaces is no longer required. Applying a linear extrapolation scheme at the outermost control volumes, the algebraic residual equation is obtained as

$$0 = i - \frac{p}{1.5\phi_{s_0} - 0.5\phi_{s_1} + 0.5\phi_{s_{n-1}} - 1.5\phi_{s_{n-1}}} \quad (3.38)$$

The computer code used (LIONSIMBA v2.0, to be discussed in section 3.6.1) employs the Differential Algebraic Equation (DAE) solver IDA [143] to handle such algebraic constraints.

Eqs. (3.36)–(3.38) therefore represents the discretised form of the reformulated boundary condition and associated algebraic constraints for the solid phase potential Partial Differential Equation (PDE) that can be applied to either electrode to facilitate the use of an input power density to the P2D model.

3.4.3 Hybrid spectral-FV scheme

Fast and accurate estimation of the solid phase lithium concentration, particularly its value at the surface of electrode particles is an inherent requirement of the layer optimisation procedure presented in section 3.5. The high power densities to be handled, particularly at low layer counts necessitate this requirement. It has been acknowledged that solid-phase concentration calculations employing polynomial approximations lack fidelity at high charge/discharge rates [92]. Hence, a conventional full-order solution based on Fick's law of diffusion is required for this layer optimisation task.

3.4 Enhancements/Modifications to Standard DFN Model

With full-order solid phase diffusion dynamics, applying the FV scheme (that has been employed in LIONSIMBA v1.0x (see section 3.6.1 for a discussion of this modelling platform) to discretise all through-thickness PDEs of the P2D model) results in a very large system of equations. This is due to the requirement of using a high radial node density per spherical particle for improved accuracy. Consequently, the computational cost is high and simulation run-time becomes prohibitive when exploring the search space of all possible layer configurations. Moreover, with a cell-centered FV discretisation, it is non-trivial to directly apply the ionic flux boundary condition at the particle surface, since this involves extrapolation from at least two other nodes within the particle. While such extrapolations are acceptable in the axial dimension — particularly with high node densities providing small values of $\frac{\Delta x}{2}$ — they are undesirable in the radial dimension. This is because the cell's Open Circuit Potential (OCP) and terminal voltage strongly depends on the concentration at the particle surface. Spectral methods offer a combination of high accuracy and speed while permitting the use of a lower number of radial discretisation nodes. To implement a spectral scheme on a non-periodic domain, a Chebyshev discretisation [70] may be applied. Bizeray *et al.* [76] discretised all of the P2D model equations using this approach. However, this entails a bi-directional mapping of all field variables between the physical and Chebyshev domains, incurring computational overhead.

For the proposed layer optimisation simulations, a hybrid formulation of the P2D model is proposed wherein a standard FV scheme in the axial dimension and a spectral scheme in the radial domain are used. Exploiting this natural separation of the axial and radial domains enables to — i) retain the ability to easily couple the molar flux density at the particle surface through reformulation of the boundary conditions of the solid diffusion PDE, and ii) solve for solid-phase lithium concentration in the Chebyshev domain and locally transform to physical domain, without requiring system-wide Chebyshev reformulations. Although the proposed implementation does not *globally* employ a spectral scheme, the combined beneficial effects of radial-domain spectral scheme and automatic differentiation of system equations using CasADi [144] facilitate rapid simulations, enabling the completion of the layer optimisation in a short duration. Eqs. (3.39)–(3.42) detail the steps leading up to the reformulated solid phase diffusion and its associated boundary conditions in the Chebyshev domain.

3.4 Enhancements/Modifications to Standard DFN Model

Figure 3.5 depicts the schematic of a standard Chebyshev discretisation. For solving the solid-phase diffusion equation, N_r Chebyshev collocation nodes defined on a 1D mesh in the radial direction is employed. The nodal co-ordinates are the roots of the Chebyshev polynomials of the first kind and are given by eq. (3.39) (see Trefethen [70]).

$$\tilde{r} = \cos\left(\frac{i\pi}{N_r}\right), \quad i = 0, 1, \dots, N_r \quad \tilde{r} \in [-1, 1] \quad (3.39)$$

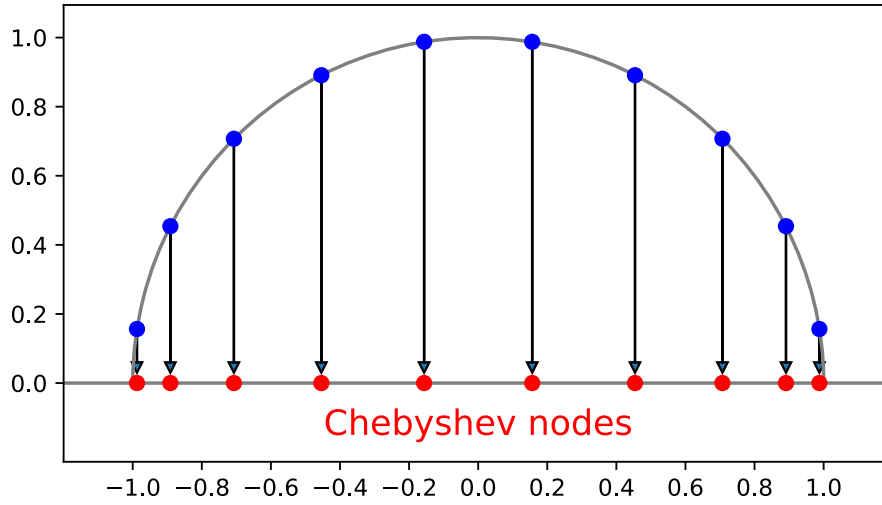


Figure 3.5 Schematic of the discretisation process depicting the generation of Chebyshev collocation nodes. A unit semicircle in the upper quadrants of a standard Cartesian plane is uniformly divided, whose projections on the horizontal co-ordinate axis through the origin yields the location of the Chebyshev nodes. Illustration reproduced from Johnson [145].

Assuming constant diffusivity, expanding the derivative in the standard form of the Fickian spherical diffusion equation (see eq. (1.3)) for each particle, we obtain eq. (3.40), presented along with its Neumann boundary conditions, eqs. (3.40a) and (3.40b). j is the molar flux density ($\text{mol m}^{-2} \text{s}^{-1}$) and R_p is the particle radius (m).

$$\frac{\partial c_s}{\partial t} = D_s^{\text{eff}} \left(\frac{2}{r} \frac{\partial c_s}{\partial r} + \frac{\partial^2 c_s}{\partial r^2} \right) \quad r \in [0, R_p] \quad (3.40)$$

$$\left. \frac{\partial c_s}{\partial r} \right|_{r=0} = 0 \quad (3.40a)$$

$$D_s^{\text{eff}} \left. \frac{\partial c_s}{\partial r} \right|_{r=R_p} = -j \quad (3.40b)$$

Mapping $r \in [0, R_p] \mapsto \tilde{r} \in [-1, 1]$,

$$r = \frac{R_p}{2} (\tilde{r} + 1) \quad (3.41)$$

Applying eq. (3.41) to eqs. (3.40)–(3.40b) whilst retaining c_s in the physical space yields eqs. (3.42)–(3.42b).

$$\frac{\partial c_s}{\partial t} = 4 \frac{D_s^{\text{eff}}}{R_p^2} \left(\frac{2}{\tilde{r} + 1} \frac{\partial c_s}{\partial \tilde{r}} + \frac{\partial^2 c_s}{\partial \tilde{r}^2} \right) \quad (3.42)$$

$$\left. \frac{\partial c_s}{\partial \tilde{r}} \right|_{\tilde{r}=-1} = 0 \quad (3.42a)$$

$$2 \frac{D_s^{\text{eff}}}{R_p} \left. \frac{\partial c_s}{\partial \tilde{r}} \right|_{\tilde{r}=1} = -j \quad (3.42b)$$

During the iterative solution process, the spatial gradients of solid phase lithium concentration in eq. (3.42) in this case are not computed through an explicit differentiation procedure as usual, but instead evaluated by pre-multiplying the concentration values at the collocation nodes by a Chebyshev differentiation matrix. This particular aspect is responsible for the inherent reduction of simulation run-time achieved by introducing a spectral method. In the updated version of LIONSIMBA v2.0 (created specifically for this layer optimisation work; see section 3.6.1 for a brief overview of the modelling platform), differentiation matrices of suitable dimensions as well as the Chebyshev collocation nodes are generated using the MATLAB function `cheb.m` distributed along with the book by Trefethen [70].

3.5 Computational Framework

3.5.1 Introduction and guidelines for flow diagram traversal

The methodology adopted by the proposed layer optimisation framework can be explained by using the flow diagram in fig. 3.6. The power handled by the cell during normal operation (evaluated by considering various drivecycles) is much lower than that experienced during acceleration (discharge) and fast-charging (charge) scenarios. Section 3.6 provides a brief summary of the peak and median powers across all standard drivecycles. Therefore, from a design perspective, it is sufficient to consider the power requirements for these two extreme

cases. Hence, the schematic in fig. 3.6 can be studied by broadly dividing the flow diagram into two parts – i) an acceleration pathway (primarily consisting of blocks shaded in grey), and ii) a fast-charging pathway (predominantly composed of blocks shaded in cyan).

As indicated by the legend in fig. 3.6, blocks with a light grey border represent input data/-parameters for computations. Blocks with a standard black border represent computations common to both acceleration and fast charging pathways. The design output is given by the double-bordered block at the bottom centre of fig. 3.6. Other types of blocks and arrows are appropriately listed in the legend key. To aid the understanding of the layer optimisation framework, the reader is encouraged to correlate the narrative in this section with the blocks and arrows in the schematic. The acceleration and fast charging pathways are not amenable for standalone comprehension and are to be parsed in conjunction with the flow of control through the infrastructure blocks as if the entire flow diagram is a single cohesive unit. These ‘control’ blocks, common to both pathways in fig. 3.6, govern how these two pathways are to be traversed with the presently trialled layer choice and quantify the suitable reformulations needed whenever a new layer choice is to be used. The computational aspects covered by these blocks are described in sections 3.5.4–3.5.9.

3.5.2 Acceleration pathway

The computations for acceleration-based layer optimisation begins at the anchor block labelled ‘Start Acc. Calcs.’.

Determination of acceleration rate, final speed and acceleration time

The first step is to determine the rate of acceleration to be used for computing the power requirements for accelerating an xEV from standstill. For various other regulatory reasons, vehicular standards for electrified transport are codified by various standardisation bodies (e.g. the SAE J1772 standard [146]). The standards published by these regulatory agencies typically specify a minimum required acceleration rate for the vehicle under consideration to be certified as an electric vehicle. Additionally, vehicle manufacturers often provide their own specifications, which typically exceed these minimum standards. However, for certain classes of electric vehicles such as golf carts, the manufacturer-specified standards might fall below that of a roadworthy electric vehicle. This thesis advocates a conservative design by choosing the higher of the two values.

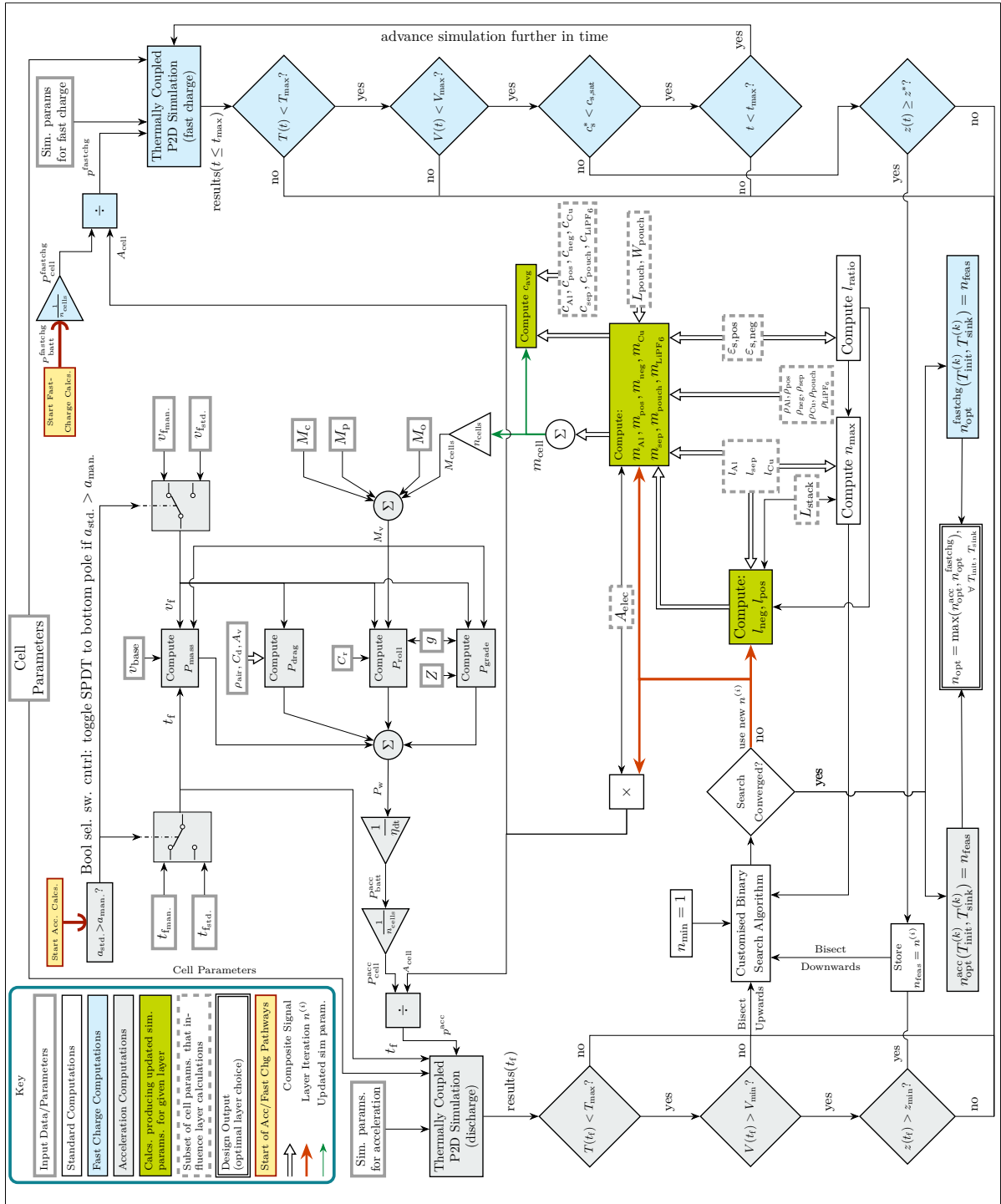


Figure 3.6** Flow diagram depicting an overview of the proposed layer optimisation methodology for Li-ion pouch cells.

**This figure was created by Krishnakumar Gopalakrishnan who asserts copyright, with intellectual contributions from and the right to use asserted by Ian D. Campbell.

The acceleration rate is calculated by dividing a pre-determined final speed v_f by the time t_f taken to attain that speed from standstill. The manufacturer-specified acceleration rate $a_{\text{man.}}$ is compared against the minimum acceleration rate specified by the governing vehicular standards $a_{\text{std.}}$. The two Single Pole Double Throw (SPDT) switches assign the final speed v_f and acceleration time t_f using the corresponding values from the appropriate source depending on which of the two acceleration rates is higher.

Computation of acceleration power at the wheels

The next step is to calculate the acceleration power required at the driving wheels P_w . Using the governing equations from basic vehicle dynamics (See Maksimovic [30]), the power at the wheels of an xEV is given by eq. (3.43).

$$P_w = P_{\text{mass}} + P_{\text{drag}} + P_{\text{roll}} + P_{\text{grade}} \quad (3.43)$$

$$P_{\text{mass}} = \frac{1}{2} \frac{M_v(n)}{t_f} (v_b^2 + v_f^2) \quad (3.43a)$$

$$P_{\text{drag}} = \frac{1}{2} (\rho_{\text{air}} C_d A_v v_f^3) \quad (3.43b)$$

$$P_{\text{roll}} = C_r M_v(n) g v_f \quad (3.43c)$$

$$P_{\text{grade}} = M_v(n) Z g v_f \quad (3.43d)$$

The individual components contributing to the summation for wheel-power computation presented in eq. (3.43) is briefly explained. P_{mass} represents the power required to accelerate the vehicle's mass. P_{drag} and P_{roll} denote the powers required to overcome air resistance and rolling resistance respectively. Finally, P_{grade} represents the power required to negotiate a road gradient. Except for $M_v(n)$ which is described next, all terms in the RHS of eqs. (3.43a)–(3.43d) are constants. The nomenclature for each of these terms is explained in tables 3.3 and 3.4 along with their numerical values used in simulation.

Computation of layer-dependent vehicle mass

Changing the layer count used within a cell changes its mass. This in-turn affects the mass of the pack, which further influences the overall vehicle mass. Hence, for precise computation of P_{mass} in eq. (3.43a), the vehicle's mass is computed as a function of number of layers within each cell.

In the schematic of fig. 3.6, this layer-dependent calculation of mass of all cells in the pack M_{cells} is shown by the product of the signal labelled m_{cell} and the triangular gain block representing the overall number of cells in the pack n_{cells} .

$$M_{\text{cells}} = n \times m_{\text{cell}} \quad (3.44)$$

The mass of the vehicle is given by the sum of chassis mass M_c , vehicle payload M_p , pack overhead M_o and the layer-dependent mass of all cells in the pack M_{cells} as computed in eq. (3.44). The computation of mass of a single cell m_{cell} is detailed in section 3.5.8.

Computation of acceleration power density per layer

Since the P2D equations of the DFN model are based upon a normalised unit area and is applicable only to each electrochemical layer, the goal is to compute the power density experienced by each layer. This is arrived at by a sequence of simple scaling steps.

Firstly, the power demanded at the pack terminals $P_{\text{batt}}^{\text{acc}}$ is computed by dividing the power at the wheels by the efficiency of the drivetrain. As explained in section 3.2.1, the drivetrain consists of a number of components, the efficiencies of which depend on the operating point (such as the speed and torque of the electric motor, current drawn by the power electronics etc.). Following the assumptions detailed in section 3.2.1, a single lumped efficiency η_{dt} can be used for the powertrain. The power demand on the pack is then divided by the number of cells in the pack n_{cells} to obtain the power demand at the input of the cell's terminals $p_{\text{cell}}^{\text{acc}}$. For each layer choice n , the overall electrochemically active surface area is computed using by using eq. (3.1), wherein the surface area per layer A_{elec} listed in table 3.2 is held constant throughout. Finally, the acceleration power density per layer p^{acc} is computed by dividing $p_{\text{cell}}^{\text{acc}}$ by the overall surface area A_{cell} .

Thermally-coupled P2D simulation and exit conditions

For the presently trialled layer choice n , a thermally-coupled P2D simulation is performed for a duration of t_f seconds with the applied power density $p_{\text{cell}}^{\text{acc}}$ corresponding to the present layer choice as input to the model. When the simulation terminates, the cell's condition is compared against the following three criteria:

1. the maximum possible values of cell temperature T_{\max} ,
2. the minimum allowed terminal voltage V_{\min} , and
3. the lowest allowed cell SOC z_{\min} .

This helps to determine whether the cell constructed from the present layer choice is able to successfully satisfy the acceleration power demands. These comparison operations are represented by decision blocks placed in the leftmost region of the schematic in fig. 3.6.

If any one of the three aforementioned exit checks fail, the present layer configuration is deemed to be not feasible and the entire workflow is repeated by trialling a new layer choice. A sophisticated search algorithm, to be described in section 3.5.4, is employed to minimise the number of iterations needed until a successful layer choice $n_{\text{opt}}^{\text{acc}}$ is obtained. The above process is repeated for different combinations of initial and ambient temperatures ($T_{\text{init}}, T_{\text{sink}}$). The largest successful layer value from all temperature combinations is deemed as the canonical optimal design choice when considering acceleration demands. This concludes the narrative describing the acceleration-specific pathway.

3.5.3 Fast-charging pathway

The workflow describing the optimal layer calculation for the fast charging scenario begins with the anchor block labelled ‘Start Fast-Charge Calcs.’ in fig. 3.6. The charging algorithm used in this framework is based upon the model-based strategy proposed by Choe *et al.* [147], wherein the surface concentration is never allowed to exceed its saturation value. Adopting this charging scheme leads to a robust cell design that is resilient to lithium plating. A major departure from the scheme in Choe *et al.* [147] is the fact that the constant current phase used therein is replaced by a constant power phase. This is so that the assumption of identical conditions across all cells in the pack holds true (see section 3.2.1 for details). Furthermore, the pulsing phase used to top-up the cell’s SOC in Choe *et al.* [147] is omitted. This is because, the level 3 fast charging specifications typically require charging to a target SOC that is typically well below 100 % (see table 3.2).

At first, the charging power applied at the pack’s terminals $P_{\text{batt}}^{\text{fastchg}}$ is scaled down by the overall number of cells in the pack. This results in the charging power experienced by each

cell in the pack $P_{\text{cell}}^{\text{fastchg}}$. Following the strategy used in section 3.5.2, the power at the cell's terminals is scaled down by the electrochemically active overall surface area A_{cell} . This yields the power density p^{fastchg} experienced by each layer in the cell and is now amenable to be applied to the normalised P2D equations of the DFN model (that has been suitably modified to handle power inputs).

Thermally-coupled fast-charging simulations and exit conditions

After computing the power density per layer, the thermally-coupled P2D model is then invoked. While the simulation runs, the cell's state is continually evaluated against various termination criteria.

1. the maximum possible values of cell temperature T_{max} ,
2. the maximum allowed terminal voltage V_{max} , and
3. the surface concentration c_s^* not to exceed the saturation concentration $c_{s,\text{sat}}$

If any of these three criteria are violated, the simulation immediately stops and the trialled layer choice is deemed to not satisfy the fast charging power requirements. The search algorithm then updates the layer choice suitably and the entire workflow is repeated.

If the simulation for any layer choice passes the aforementioned termination criteria, the SOC achieved by the cell is compared against the fast-charging target z^* . If $z(t) > z^*$, then the present layer choice represents the minimum (and therefore optimum) value for this specific fast charging application. The successful layer choice is labelled $n_{\text{opt}}^{\text{fastchg}}$. If the surface concentration has not yet reached the saturation limit, then the charge time is compared against the upper bound for fast charging specifications t_{max} . If this preset duration has not been reached, then the simulation is allowed to advance further in time, with the aforementioned termination criteria being continuously tested at each subsequent time-step.

The above process is repeated for different combinations of initial and ambient temperatures ($T_{\text{init}}, T_{\text{sink}}$). The largest successful layer value from all temperature combinations is deemed as the canonical optimal design choice when considering the fast charging power demands. This concludes the narrative describing the fast charging pathway.

Finally, the maximum of the layer choices across all temperature combinations from the acceleration and fast charging scenarios is deemed as the globally optimal number of layers to be used for this model-led cell design. The maximum value is chosen because, if any smaller layer count is used to construct the cell, that design shall fail to satisfy its power requirements without violating at least one termination criterion. Hence, the worst case runs across all desired thermal scenario under which the cell is intended to operate shall inform the final design choice.

3.5.4 Search algorithm

A customised binary search algorithm is designed for the layer optimisation framework. Binary search is a computationally efficient search algorithm requiring a worst-case operational count of $\mathcal{O}(\log k)$ where k is the overall number of layer candidates to be searched [148]. However, this algorithm is applicable only when the array to be searched is already sorted in either ascending or descending order. By recognising the relationship between the magnitude of power density applied versus the factors that deem a layer suitable or unsuitable for the application, a customised set of ‘exit conditions’ that meet the aforementioned sorted-array requirement can be enforced. This specific mapping is a unique idea and is claimed as a contribution by this thesis author to the art.

This search strategy is equally applicable (with small modifications to exit conditions as explained next) for both acceleration and fast charging pathways.

Binary search for acceleration pathway

If all the termination criteria are successfully met, the exit condition is set to a value of 1. If any of these conditions fail, then the exit condition is assigned a value of 0. Thus, the search vector in this bespoke strategy consists of only two Boolean possibilities. For ultra-low layer counts, the applied power densities are extremely high. Therefore, one of the exit conditions is likely to fail. For very high layer counts, the power densities are very low, implying that acceleration runs shall always be successful. When considering layer counts from the lowest to the highest, there exists a critical transition point *viz.* the first layer count for which the exit vector toggles from 0 to 1. Through a systematic bisection of the layer search space, the search algorithm speedily converges to the optimal layer value.

Binary search for fast-charging pathway

If all the fast-charging termination criteria are successfully met, the exit condition is set to a value of 1. For violating any of the following three failure conditions (see section 3.5.3) *viz.* exceeding *a*) upper cutoff temperature, or *b*) upper cutoff voltage, or *c*) the maximum allowed charging despite encountering surface saturation, the exit condition is assigned the value of 0. The search array is bisected by using this failed layer choice as the new lower bound. If no termination criterion is violated, then the presently trialled layer choice is deemed a success and the exit condition is set to 1. The search space is narrowed down by using the current layer choice as the new upper bound.

However, there exists possible scenarios of needing to assign a third exit condition for the fast charging case. If the aforementioned termination criteria are not violated, but the charging process fails to meet the target SOC specification for very high values (close to n_{\max}) of the presently trialled layer choice, this implies operation in a capacity-limited region (see fig. 3.11 and section 3.6 for a brief explanation of this case). The exit condition corresponding to this failure mode is assigned a value of 2. Thus, the search vector in this bespoke strategy consists of three distinct numbered exit conditions. Despite being a failure, from the perspective of narrowing down the search space, this third exit condition is treated in the same way as the second exit condition *i.e.*, the trialled layer choice is deemed to be too high, which implies a downward bisection for the next search iteration.

Akin to the acceleration pathway, the optimal layer choice for fast charging is deemed to be at the critical transition point wherein the exit condition toggles from 0 to 1 and hence, minimal customisation is needed in the computer code to handle these two cases. The handling of exit condition 2 is shown in the lower rightmost portion of fig. 3.6. Despite being a failure, from the search algorithms point of view this is treated as a success, with the only difference being the assignment of the exit condition value purely for logging and debugging purposes.

Alternative search algorithm – linear search

A simpler alternative to using the binary search algorithm is the standard linear search algorithm. This is a simple search strategy which involves sequentially iterating from n_{\min} to n_{\max} until arriving at the lowest value $n_{\text{opt}}^{\text{acc}}$ that satisfies all the termination criteria.

However, a naive use of the linear search algorithm is computationally expensive with a worst case operation count of $\mathcal{O}(n)$. Therefore, this thesis author recommends the use of the bespoke binary search algorithm. The choice of minimum and maximum values for the layer search space is discussed in section 3.5.5.

3.5.5 Upper and lower bounds on search space

It is helpful to determine the highest possible number of layers that can be physically accommodated in a stack of height L_{stack} . For instance, this value may be used as the upper bound to the binary search algorithm (which compulsorily requires such an upper bound) described in section 3.5.4. This can be obtained by defining a simple integer optimisation task as shown in eq. (3.45). The objective function here is to maximise the value of the layer count n subject to the physical constraint that the thicknesses of both electrodes always remains positive.

$$\begin{aligned}
 & \mathbf{max}_{n \in \mathbb{N}} \quad n \\
 & \text{s.t.} \quad l_{\text{pos}} = \left(\frac{L_{\text{stack}} - L_{\text{Al}}(n) - L_{\text{Cu}}(n) - nl_{\text{sep}}}{n(1 + l_{\text{ratio}})} \right) > 0 \\
 & \quad \quad l_{\text{neg}} = \left(\frac{l_{\text{ratio}}(L_{\text{stack}} - L_{\text{Al}}(n) - L_{\text{Cu}}(n) - nl_{\text{sep}})}{n(1 + l_{\text{ratio}})} \right) > 0
 \end{aligned} \tag{3.45}$$

Equation (3.46) represents the analytical closed-form solution to the integer optimisation problem of eq. (3.45).

$$n_{\text{max}} = \max \left(\left\lfloor \frac{2(L_{\text{stack}} - l_{\text{Cu}})}{l_{\text{Al}} + l_{\text{Cu}} + 2l_{\text{sep}}} \right\rfloor, \left\lfloor \frac{2L_{\text{stack}} - l_{\text{Al}} - l_{\text{Cu}}}{l_{\text{Al}} + l_{\text{Cu}} + 2l_{\text{sep}}} \right\rfloor \right) \tag{3.46}$$

The first argument to the max function in eq. (3.46) represents the maximum number of physically feasible odd layers while the second argument represents the maximum such value when considering odd layers. Therefore, the greater of these two values is chosen as the maximum permissible layer choice n_{max} and is used as an input to the search algorithm.

In the absence of published information on how the minimum layers within a pouch cell is currently set, there is presently no unique way to determine n_{min} . Therefore, for this layer optimisation study, the value of n_{min} used by the search algorithm is currently set to one —

the minimum physically feasible number of layers. Design engineers from industry may opt to tweak this to a higher value based on insights gained from present empirical designs.

3.5.6 Electrode thickness ratio for capacity balancing

A key idea of the layer optimisation scheme is that, for computing the physical lengths of electrodes as a function of number of layers, the ratios of their thicknesses l_{ratio} , is held constant. This coefficient is germane to the concept of capacity balancing of electrodes with a view to equalise their loading. The idea of matching the capacity of anode and cathode materials is widely accepted as a standard principle in cell design [25]. The computation of this l_{ratio} parameter is discussed here.

Equating the active material volume of both electrodes,

$$A_{\text{elec,pos}} l_{\text{pos}} \epsilon_{\text{s,pos}} = A_{\text{elec,neg}} l_{\text{neg}} \epsilon_{\text{s,neg}} \quad (3.47)$$

While stacking the layers within a pouch cell, for the negative electrode layers, there exists an extra overhang of (< 2 mm) with respect to the positive electrode layers. Figure 3.7 shows a CT scan depicting the two-dimensional longitudinal-sections with a close-up view of this overhang region. This is a design feature to prevent plating of lithium at the edges.

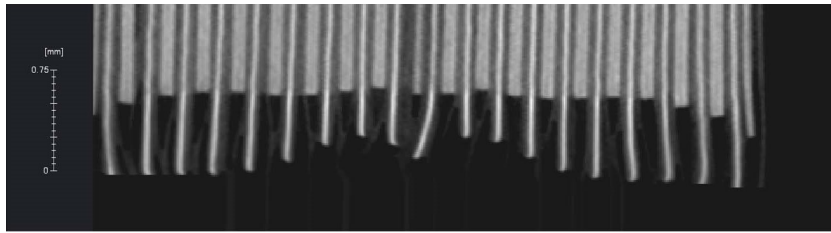


Figure 3.7 CT scan showing the two-dimensional longitudinal-sections from the edge of the pouch cell with a close-up view of the graphite overhang region. For the negative electrode layers, there is an extra overhang of (< 2 mm) with respect to the positive electrode layers. This design feature helps to avoid plating of lithium at the edges. Image reproduced from Bond *et al.* [149].

Neglecting overhangs of the negative electrode (typically < 2 mm), both electrodes have the same cross-sectional area A_{elec} . Therefore, eq. (3.47) reduces to

$$\cancel{A_{\text{elec}}} l_{\text{pos}} \epsilon_{\text{s,pos}} = \cancel{A_{\text{elec}}} l_{\text{neg}} \epsilon_{\text{s,neg}} \quad (3.48)$$

$$l_{\text{pos}} \epsilon_{\text{s,pos}} = l_{\text{neg}} \epsilon_{\text{s,neg}} \quad (3.49)$$

Owing to the reasons outlined in section 3.2.1, the volume fractions of the electrode materials are assumed to be constant, which implies that their ratio is also a constant. The electrode thickness ratio l_{ratio} is therefore obtained as

$$l_{\text{ratio}} = \frac{l_{\text{neg}}}{l_{\text{pos}}} \quad (\text{by definition}) \quad (3.50)$$

$$= \frac{\varepsilon_{\text{s,pos}}}{\varepsilon_{\text{s,neg}}} \quad (\text{rearranging eq. (3.49)}) \quad (3.51)$$

$$= \frac{1 - \varepsilon_{\text{pos}} - \varepsilon_{\text{fi,pos}}}{1 - \varepsilon_{\text{neg}} - \varepsilon_{\text{fi,neg}}} \quad (\text{by definition, see eq. (5.60)}) \quad (3.52)$$

$$= \frac{1 - 0.385 - 0.025}{1 - 0.485 - 0.033} \quad (\text{substituting values from table 5.2}) \quad (3.53)$$

$$l_{\text{ratio}} = 1.22 \quad (3.54)$$

3.5.7 Computation of electrode thicknesses per layer

In this section, a deterministic way to compute the thickness of electrode materials is present. In the views of this thesis author, this represents a departure from the norm wherein electrode thicknesses are designed on a trial and error basis [25]. Following the assumptions listed in section 3.2.1, the exterior dimensions of the pouch are held constant. Furthermore, as explained in section 3.4.1, the thickness of the electrochemical stack within the pouch cell L_{stack} , is also considered to be constant. Therefore, when the number of layers forming the stack is varied, this implies that the only quantities that may be allowed to change are the thicknesses of the two electrodes within each layer *i.e.*, higher the layer count, lower the electrode thicknesses and vice-versa. In this section, this relationship between the number of layers n and the electrode thicknesses l_j ($j \in \text{neg, pos}$) is quantified with the help of the key l_{ratio} parameter obtained in section 3.5.6.

Figure 2 of Northrop *et al.* [74] (suitably adapted and reproduced in fig. 3.8) considers two possible configurations of stacking up layers within a pouch cell. In the first topology shown in fig. 3.8a, the outermost current collectors are of copper. In the alternative configuration shown in fig. 3.8b, a copper current collector occupies one end of the stack while an aluminium current collector occupies its other end. The formulae derived here is equally applicable to both these cases. Although the use of aluminium current collectors at both extrema of the stack is not studied, the approach presented here may be easily extended to this case.

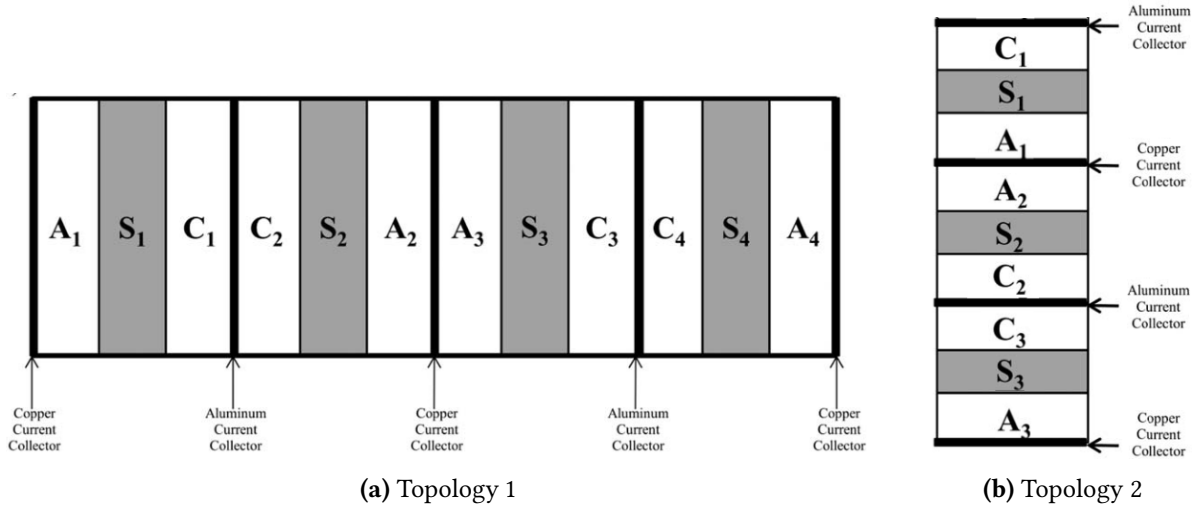


Figure 3.8 Two possible topologies for arranging the layers within a pouch cell. The first possibility entails using an even number of layers as shown in the example illustration with four layers in the left sub-figure. Here, both extrema of the stack are occupied by copper current collectors. The second possible arrangement consists of using an odd number of layers and is depicted in the sample illustration with three layers in the right sub-figure. This represents a heterogeneous topology wherein the outermost current collectors of the stack consist of copper at one end and aluminium at its other end. Illustration adapted from Northrop *et al.* [74].

The stack height may be obtained by the sum of thicknesses of the constituent regions.

$$L_{\text{stack}} = \sum_j L_j(n) + L_{\text{Al}}(n) + L_{\text{Cu}}(n) \quad \forall n \in \mathbb{N}, j \in \{\text{pos, sep, neg}\} \quad (3.55)$$

where

$$L_j(n) = nl_j \quad (3.55a)$$

$$L_{\text{Al}}(n) = \begin{cases} \left(\frac{n}{2}\right) l_{\text{Al}}, & \text{if } n \text{ is even} \\ \left(\frac{n+1}{2}\right) l_{\text{Al}}, & \text{if } n \text{ is odd} \end{cases} \quad (3.55b)$$

$$L_{\text{Cu}}(n) = \begin{cases} \left(\frac{n+2}{2}\right) l_{\text{Cu}}, & \text{if } n \text{ is even} \\ \left(\frac{n+1}{2}\right) l_{\text{Cu}}, & \text{if } n \text{ is odd} \end{cases} \quad (3.55c)$$

The combined thickness of the two electrode regions in each layer l_{ce} can be then obtained by rearranging eq. (3.55)

$$l_{\text{ce}} = \frac{L_{\text{stack}} - [0.5(n+1)]l_{\text{Cu}} - [0.5n]l_{\text{Al}}}{n} - l_{\text{sep}} \quad (3.56)$$

The individual electrode thicknesses can then be obtained from eq. (3.56) by suitably substituting in l_{ratio} and performing simple algebraic manipulations.

$$l_{\text{pos}} = \frac{l_{\text{ce}}}{l_{\text{ratio}} + 1} \quad (3.57)$$

$$l_{\text{neg}} = l_{\text{ce}} - l_{\text{pos}} \quad (3.58)$$

The two electrode thicknesses thus obtained using Eqs. (3.57)–(3.58) are used as computational domain lengths in the P2D simulations. Therefore, these thicknesses have to be recomputed each time the trialled number of layers n is updated by the search algorithm.

3.5.8 Computation of layer-dependent cell mass

The mass of the cell varies as a function of number of layers. This is because, the thicknesses of the two electrodes within each layer changes each time a different layer choice is used. Following the discussion in section 3.5.6, for computing masses of the constituent components of a cell, the anode overhang is neglected. Therefore, the common cross-sectional area A_{elec} is used for all calculations. For a given layer choice n , the cell mass is computed as per eq. (3.59).

$$m_{\text{cell}} = \sum_j m_j + m_{\text{Al}} + m_{\text{Cu}} + m_{\text{LiPF}_6} + m_{\text{pouch}}, \quad j \in \{\text{pos, sep, neg}\} \quad (3.59)$$

$$m_j = A_{\text{elec}} L_j \varepsilon_j \rho_j \quad (3.59a)$$

$$m_{\text{Al}} = A_{\text{elec}} L_{\text{Al}} \rho_{\text{Al}} \quad (3.59b)$$

$$m_{\text{Cu}} = A_{\text{elec}} L_{\text{Cu}} \rho_{\text{Cu}} \quad (3.59c)$$

$$m_{\text{LiPF}_6} = A_{\text{elec}} \left(\sum_j L_j (1 - \varepsilon_{\text{fi}_j} - \varepsilon_j) \right) \rho_{\text{LiPF}_6} \quad (3.59d)$$

$$m_{\text{pouch}} = 2H_{\text{pouch}} L_{\text{pouch}} W_{\text{pouch}} \rho_{\text{pouch}} \quad (3.59e)$$

Owing to lack of information on their thickness, the mass of the cell's tabs has been omitted in eq. (3.59). However, upon availability of the relevant data, this may be easily incorporated through an equation analogous to eq. (3.59e).

3.5.9 Computation of layer-dependent cell specific heat

A lumped thermal model of the cell given by eq. (3.60) is used to model the thermal dynamics of the cell. This thermal model is coupled with the electrochemical model equations of the P2D model for the simulations used to determine the optimal layer configurations. The cell's temperature $T_{\text{cell}}(t)$ is also obtained from this lumped thermal model.

$$m_{\text{cell}}c_{\text{avg}} \frac{dT_{\text{cell}}}{dt} = -hA_{\text{tabs}} (T_{\text{cell}}(t) - T_{\text{sink}}) + Q_{\text{pol}} \quad (3.60)$$

$$Q_{\text{pol}} = A_{\text{cell}} \cdot |i| \cdot |U - V| \quad (3.60a)$$

$$U = U_{\text{pos}}(\theta_{\text{pos}}) \Big|_{x=x_{\text{pos/Alcc}}} - U_{\text{neg}}(\theta_{\text{neg}}) \Big|_{x=x_{\text{neg/Cucc}}} \quad (3.60b)$$

$$V = \phi_{\text{s}} \Big|_{x=x_{\text{pos/Alcc}}} - \phi_{\text{s}} \Big|_{x=x_{\text{neg/Cucc}}} \quad (3.60c)$$

The average specific heat of the cell c_{avg} used in eq. (3.60) is a function of the number of layers and is given by eq. (3.61).

$$c_{\text{avg}} = \frac{1}{m_{\text{cell}}} \left[\sum_j c_j m_j + c_{\text{Al}} m_{\text{Al}} + c_{\text{Cu}} m_{\text{Cu}} + c_{\text{LiPF}_6} m_{\text{LiPF}_6} + c_{\text{pouch}} m_{\text{pouch}} \right], \quad j \in \{\text{pos, sep, neg}\} \quad (3.61)$$

The first three terms in eq. (3.61) are evaluated as a function of the number of layers n by substituting the appropriate layer-dependent mass values computed in eqs. (3.59a)–(3.59c). The latter two terms *i.e.*, the specific heats of the electrolyte material and the pouch are held constant since their corresponding mass values do not vary with the number of layers used.

This concludes the overall narrative describing the layer optimisation framework. The results obtained by applying this methodology to a specific numerical example is presented in section 3.6.

3.6 Results and Discussion

At the outset, it is worth mentioning that the focus of this chapter is on the layer optimisation *methodology* itself. The results as such do not stand alone outside of the modelling universe with all its inherent assumptions discussed thus far. Presently, the value added by this work


is its ready adaptability to industry through its modular design. A numerical implementation in the form of a toolbox ^{††} is also provided which is immediately available for download and use by relevant stakeholders. This author recommends that until the tool matures, cell manufacturers substitute their own parameters and adjust other numerical coefficients suitably so that the toolbox supplements, rather than supplants present empirical layer designs. Hence, the results presented in this section must be interpreted in the backdrop of the context within which the methodology was developed implying that the reader must consciously strive to interpret all numerical values in *relative* terms of magnitude. To aid this thought process, this author chooses to deliberately limit the discussion around the *absolute* magnitude of numbers presented here.

3.6.1 Modelling Platform and Preconditioning

The complete parameter set used for simulation is presented in table 3.2. All cells are assumed to be in their equilibrium state prior to beginning of simulations. The thermally-coupled, P2D electrochemical model used for simulating each layer choice is implemented in MATLAB [159] using a heavily-modified version of the LIONSIMBA toolbox [18]. The work reported in this chapter helped to advance the toolbox from v1.0x to v2.0. The updated computer codes to which this author heavily contributed, is available from the project's official repository^{‡‡}.

The rationale behind choosing this specific software to implement layer optimisation is as follows. The LIONSIMBA v1.0x toolbox has already been validated against the results of the DUALFOIL [160] codes (which can be considered as the present benchmark standard). The toolbox is implemented in the MATLAB programming language. Since this chapter has a strong industry focus, the omnipresence of MATLAB in industry, its mature code-base and familiarity was a strong motivator in the adoption of this toolbox. The simulation speeds using LIONSIMBA have been shown to be comparable to the FORTRAN implementation of DUALFOIL, primarily owing to the sophisticated computation of the analytical Jacobian of the system through automatic differentiation [18]. In addition to fundamental enhancements to the modelling platform presented in section 3.4, numerous bug fixes and other minor

^{††}As an accompaniment to this chapter, an open-source software toolbox, (co-created with Ian D. Campbell and Davide M. Raimondo) for optimal layer selection in pouch cells *viz.* Battery Optimal Layer Design (BOLD) is made available for download from GitHub.

 https://github.com/ImperialCollegeESE/BOLD_Toolbox

^{‡‡}LIONSIMBA v2:  <https://github.com/lionsimbatoolbox/LIONSIMBA>

3.6 Results and Discussion

Table 3.2 Cell parameters and system conditions for a simulating an LCO cell with the DFN electrochemical model and a lumped thermal model. These parameters, when augmented with the values of the kinetic, geometric and transport properties of the cell (from table 5.2) represents the complete information required for all simulations in this layer optimisation framework.

System Conditions							
Parameter				Parameter			
Lower cutoff cell voltage, V_{\min} (V)	^a 3.50	Target cell SOC for fast charge, z^* (%)	^c 80.00				
Upper cutoff cell voltage, V_{\max} (V)	^b 4.22	Cell upper temperature limit, T_{\max} (°C)	^d 55.00				
Geometric Parameters							
Parameter							
Surface area of pos. & neg. electrode overlap within a layer, A_{elec} (m ²)							^b 44.63×10^{-3}
Exterior pouch length, L_{pouch} (m)							^e 332.74×10^{-3}
Exterior pouch width, W_{pouch} (m)							^e 99.06×10^{-3}
Exterior pouch height, H_{pouch} (m)							^f 10.00×10^{-3}
Pouch material thickness, T_{pouch} (m)							^g 160.00×10^{-6}
Stack thickness, L_{stack} (m)							^r 9.68×10^{-3}
Thermal Parameters							
Parameter	Al. CC	Pos	Sep	Neg	Cu. CC	LiPF ₆	Pouch
Sp. heat capacity, c_j (J kg ⁻¹ K ⁻¹)	^h 903	^h 1269.2	^h 1978.2	^h 1437.4	^h 385	^h 2055.1	ⁱ 1464.8
Density, ρ_j (kg m ⁻³)	^j 2700	^k 2291.6	^b 1100.0	^j 2660.0	^l 8960	^j 1290.0	^m 1150.0
Activ. energy, diff. E_{act,s_j} (J mol ⁻¹)	—	^p 5000	—	^p 5000	—	—	—
Activ. energy, rxn. E_{act,k_j} (J mol ⁻¹)	—	^p 5000	—	^p 5000	—	—	—
Other Geometric/Cell-Level Parameters							
Parameter							
Thickness of pos. current collector, l_{Al} (m)							^f 15×10^{-6}
Thickness of neg. current collector, l_{Cu} (m)							^p 10×10^{-6}
Total tab area, A_{tabs} (m ²)							^b 5.94×10^{-3}
Lumped heat transfer coefficient, h (W m ⁻² K ⁻¹)							^b 150
Initial electrolyte concentration, $c_{e,0}$ (mol m ⁻³)							^q 1000
Saturation Concentration for fast-charging, $c_{s,\text{sat}}$ (mol m ⁻³)							^s 30555
Spatial Discretisation							
Parameter	Pos		Sep		Neg		
Nodes, through-thickness (axial), N_{a_j}	40		40		40		
Nodes, within spherical particle (radial), N_{r_j}	15		—		15		

^a Calculated in section ‘Lower cutoff voltage for cells’ (also see section 3.4.1) ^b Assumed ^c Ref. [146]

^d Ref. [150] ^e Converted from imperial units reported in Ref. [138] ^f Table IV of Ref. [139]

^g Sum of values in table 1 of Ref. [151] ^h Ref. [152] ⁱ From constituent values (see [151]) using Ref. [153]

^j Ref. [154] ^k Ref. [155] ^l Ref. [156, 157] ^m Ref. [158] ^p Ref. [74] ^q Ref. [137]

^r See section ‘Computation of stack thickness of reference cell’ ^s Ref. [137]

enhancements to the original LIONSIMBA code-base have been provided by this thesis author. Interested readers may peruse these from the README.md file from the project's [repository](#).

3.6.2 xEV configurations

Table 3.3 Acceleration test parameters (common across xEV platforms)

Parameter	
Coefficient of drag for xEV body, C_d	^a 0.31
Frontal area of xEV, A_v (m^2)	^b 2.40
Acc. time dictated by standards, $t_{f, std}$ (s)	^c 6.00
Acc. time specified by manufacturer, $t_{f, man}$ (s)	^d 6.50
Speed, end of acc. (standards), $v_{f, std}$ ($m s^{-1}$)	^e 8.94
Speed, end of acc. (manufacturer), $v_{f, man}$ ($m s^{-1}$)	^f 26.82
Base speed of xEV, v_b ($m s^{-1}$)	^e 13.41
Air density at acc. test conditions, ρ_{air} ($kg m^{-3}$)	^f 1.20
Drivetrain efficiency, η_{dt}	^g 0.75
Payload, M_p (kg)	^c 150.60
Rolling resistance coefficient of road surface, C_r	^f 0.01
Road gradient, Z	^g 0.00

^a Ref. [161] ^b Calculated from typical BEV dimensions in [162]
^c Ref. [163] ^d Ref. [164] ^e Ref. [131] ^f Ref. [165] ^g Assumed

Tables 3.3 and 3.4 show the xEV parameters used in simulations. To obtain an estimate of the worst case design condition for which layer optimisation needs to be performed, the 60 Ah reference cell with 46 layers is used as the benchmark. The power demands on a battery pack comprised of the reference cell during normal operation are found to be significantly lower than that experienced during the two extreme cases of discharging and charging *viz.* *acceleration* and *fast charging* respectively. This conclusion was arrived at after analysing the power demands of four different drivecycles – *a*) Urban Dynamometer Driving Schedule (UDDS), *b*) New European Driving Cycle (NEDC), *c*) Extra-Urban Driving Cycle (EUDC), and *d*) Highway Fuel Economy Test (HWFET). 50.83 kW is the highest peak discharge power while 14.20 kW is the highest median discharge power encountered across all the drivecycles considered. Even with the assumption that 100 % of braking energy can be recovered, the highest peak and median charging powers are only 43.13 kW and 26.03 kW respectively across all these drivecycles.

The discharging and charging powers experienced by the pack with the same reference cell during acceleration and fast charge are significantly higher than those experienced with any standard drivecycle. Considering the acceleration parameters in table 3.3 for the BEV pack, 181.45 kW is the power requirement for acceleration of a fixed vehicle mass on a flat road surface. Four distinct fast-charging power levels *viz.* 50 kW, 80 kW, 110 kW and 130 kW are considered in this study. This is in adherence to the minimum and maximum values of level 3 rating as suggested by Yilmaz and Krein [166]. Furthermore, near-term fast charging goals laid out in literature [167, 168] and the peak power capability of charging infrastructure further justify these choices. The above power comparison study helps to inform the two worst case conditions for layer optimisation.

Table 3.4 Acceleration test parameters (specific to each xEV)

Parameter	BEV	PHEV
Mass of xEV chassis, M_c (kg)	^a 1340.0	^b 1438.0
Mass of pack overhead (w/o cells), M_o (kg)	^a 196.4	^c 65.5
Upper cutoff SOC of cell, z_{\max} (%)	^d 95.0	^d 90.0
Lower cutoff SOC of cell, z_{\min} (%)	^d 5.0	^e 30.0

^a Calculated based on [169] ^b Calculated based on [169, 170]

^c Calculated (see sections 3.5.2 & 3.5.8) ^d Assumed ^e Ref. [165]

For the acceleration tests, the initial cell SOC has been set to 40 %. This is in conformity with the test criterion (50 ± 10) % of the SAE J1666 standard [146]. By choosing the worst case starting SOC *i.e.*, 40 %, a conservative design can be achieved. The chassis mass of the vehicle as well as the mass of two passengers at 75.3 kg each [146] is considered for both xEV platforms. The pack mass is computed as a function of number of layers as described in section 3.5. Vehicle manufacturers General Motors Inc. provide the mass value of the GM Ecotec series of engines [170] that can be used for the PHEV case which consists of a range-extending ICE. The mass of the Bolt BEV pack reported in [169] minus the computed mass of the overall cells used in the pack gives the overhead mass of the BEV pack. The PHEV pack's overhead mass is determined by suitably scaling the mass by the proportion of reduction in the number of cells used.

For the BEV platform, a fast-charging scheme operated on a Constant Power (CP) mode with an initial SOC of 20 % is employed. In the case of the PHEV, an initial SOC of 30 %

(10 % higher than that for BEV) is used. This facilitates a smaller SOC window by taking into account the higher number of charge-discharge cycles which are typical with PHEV designs [30]. Both xEV platforms are fast charged to a target SOC of 80 % in CP mode. This SOC value corresponds to the end-of-charge target in level 3 charging standards [171].

3.6.3 Acceleration studies

For both vehicle platforms under study, the acceleration at a worst-case rate of 4.13 m s^{-2} is assumed for simulation. This corresponds to the manufacturer's acceleration specifications for the BEV listed in table 3.3. The acceleration rate corresponding to the SAE J1772 standards is lower than this rate. Therefore, to obtain a robust cell design, the higher of the two acceleration rates needs to be considered.

Table 3.5 gives the simulation results based on the binary search strategy for various combinations of $(T_{\text{init}}, T_{\text{sink}})$ for both the BEV and PHEV platforms. The overall simulation time for this acceleration study was 24 min.

Table 3.5 xEV acceleration test results

$(T_{\text{init}}, T_{\text{sink}})$ (degC)	$n_{\text{opt}}^{\text{acc}}$ BEV	$n_{\text{opt}}^{\text{acc}}$ PHEV
(38,5)	21	55
(38,49)	21	57
(25,25)	23	63
(15,5)	27	69

The following discussion is applicable for both vehicular platforms. The specific combinations of temperatures for traversing the thermal design space are chosen following the SAE J1772 guidelines. High power densities result from using very low numbers of layers. For instance, with $n = 1$, the power density is -14.92 kW m^{-2} . This leads to large overpotentials causing the cell's terminal voltage to drop lower than V_{min} , thereby unable to satisfy acceleration power requirements. As n increases, the overall electrochemically active surface area available to absorb the externally power increases. This, in-turn leads to lower power densities and proportionally lower overpotentials.

At higher initial temperatures, owing to the reduction in overpotentials, a larger voltage overhead is available to accommodate the internal polarisation drop. This, in-turn, implies

that smaller layer counts suffice to satisfy acceleration power demands for higher values of T_{init} . For all temperature combinations, the largest deviation from T_{init} experienced by the BEV cell is a 0.48 °C increase. This is because the acceleration event, wherein the highest magnitude of discharge powers get applied, are of a short duration. Consequently, it can be concluded that a single isolated acceleration event does not heat the BEV battery pack, and therefore the cell temperature remains close to that of the initial value. The PHEV cell experiences higher power levels and although its temperature increases much higher than the corresponding BEV cell, the maximum temperature during acceleration remains well below the upper cutoff limit for all thermal scenarios considered. Finally, even for the worst case simulation run, the cell's SOC is depleted only by a maximum of 0.32 % for the BEV cell and by a slightly higher value for the PHEV cell.

The foregoing discussion reveals that the lower cut-off voltage strongly influences the optimal layer value for acceleration tests. Based upon the simulation results of table 3.5, for satisfying acceleration power requirements, $n = 27$ and $n = 69$ represent the optimal layer choices for the BEV and PHEV platforms respectively for the assumed xEV configurations.

3.6.4 Fast-charging studies

Figures 3.9 and 3.10 shows the results produced by the layer optimisation framework for the BEV and PHEV platforms respectively when considering fast charging requirements. Each heat map in these figures show the optimal number of layers $n_{\text{opt}}^{\text{fastchg}}$ for various combinations of initial and ambient temperatures for four different charging powers. In each case, the values of $n_{\text{opt}}^{\text{fastchg}}$ correspond to the temperature combination $(T_{\text{init}}, T_{\text{sink}}) = (15, 5)^\circ\text{C}$ as shown in fig. 3.9. This represents the least number of layers required to fast charge the pack under CP conditions until the target SOC is reached. The charging scheme additionally considers the constraint that the cell temperature must stay within $T_{\text{max}} = 55^\circ\text{C}$. Furthermore, its voltage must remain less than or equal to $V_{\text{max}} = 4.22\text{ V}$. Finally, the charging algorithm is plating-aware *i.e.*, the charging stops as soon as the concentration at the particle surface reaches the maximum possible concentration limit of $30\,555\text{ mol m}^{-3}$, thereby preventing lithium plating at the surface of negative electrode particles.

Thus, using the model-based design strategy presented in this chapter, an effective cell design is achieved which helps to maximise energy density and BEV range, without forgoing

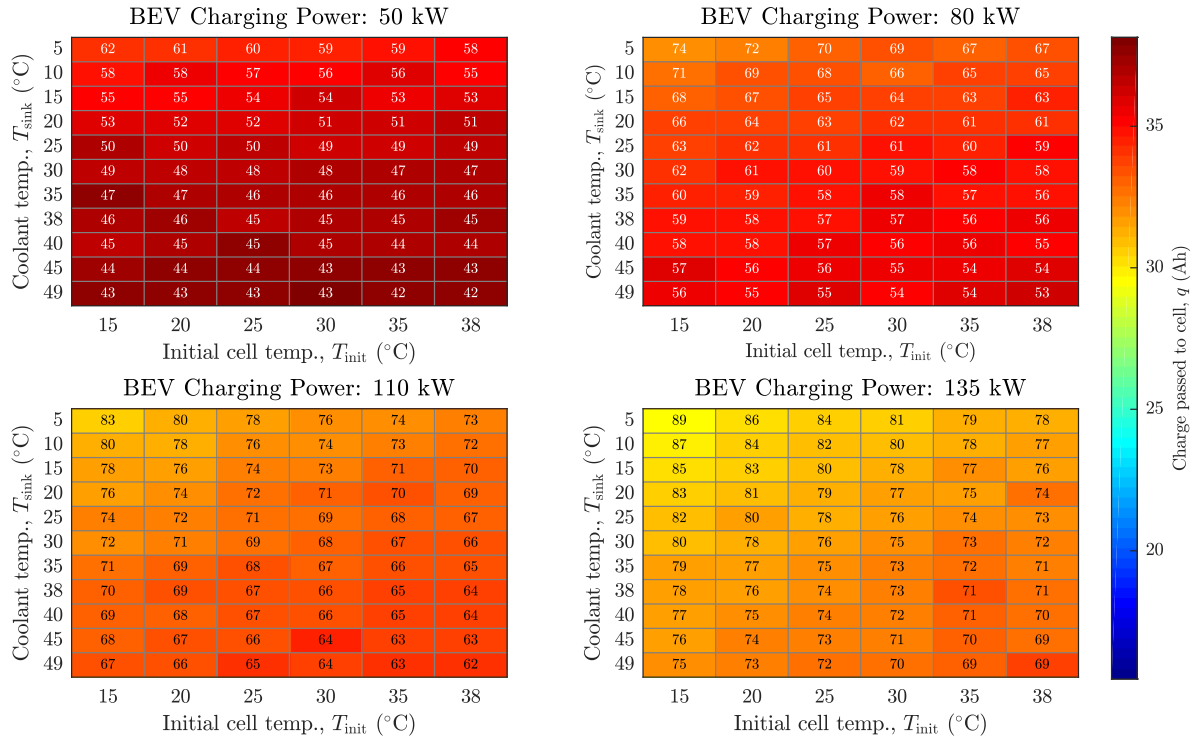


Figure 3.9^{§§} Optimal cell layer configurations for the BEV

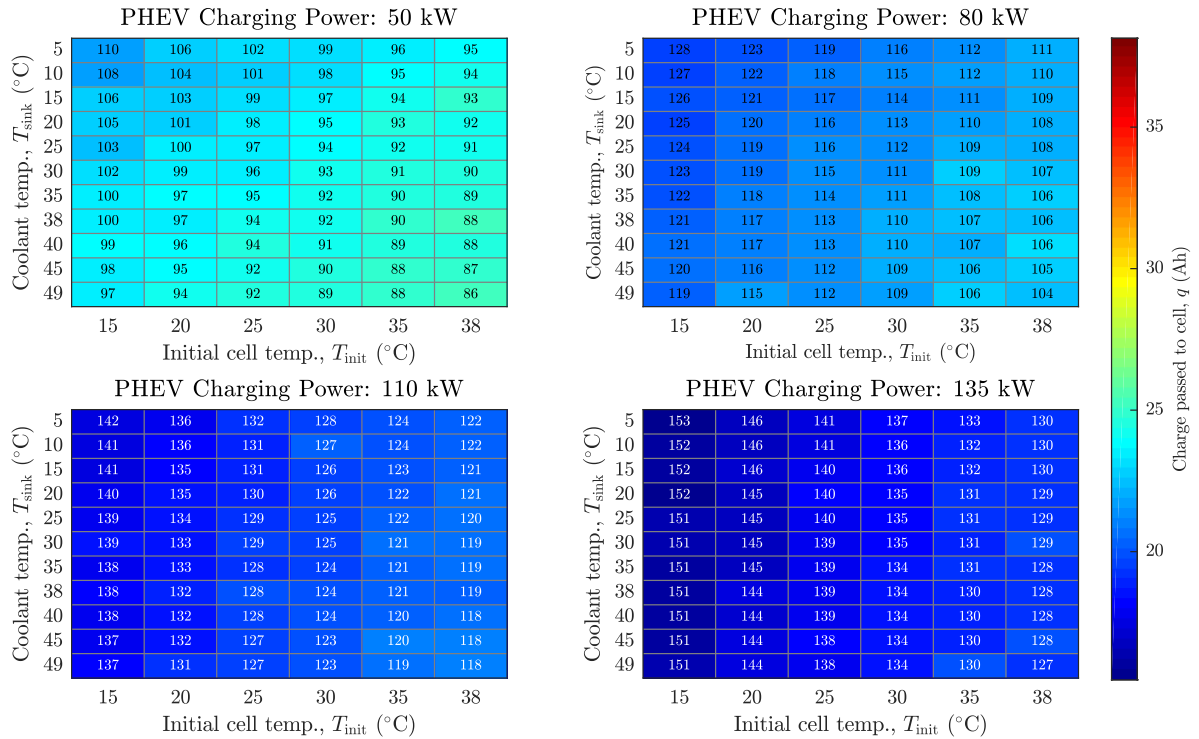


Figure 3.10^{‡‡} Optimal cell layer configurations for the PHEV

^{‡‡}These figures were created by Ian D. Campbell who asserts copyright, with intellectual contributions from and the right to use asserted by Krishnakumar Gopalakrishnan.

fast charging power targets. From figures 3.9 and 3.10, it is seen that $n_{\text{opt}}^{\text{fastchg}}$ increases with increase in the charging power. This is because, as the charging power increases, the minimum number of layers required to maintain the cell voltage below the maximum permissible value also increases. This requires higher interfacial surface area to accommodate the increased power demand. Furthermore, rapid surface saturation occurs due to steep concentration profiles in the negative electrode particles when the charging power is high which causes plating. With higher layers, the resulting electrodes are thinner, thereby allowing faster diffusion of lithium in the solid particles and avoiding steep concentration gradients in them. This suggests that the number of layers must be large enough to prevent plating.

The computation of the cell's nominal capacity as a function of the number of layers merits explanation. The overall capacity of each of the two individual electrodes is obtained as follows (suitably adapted from Plett [172] to account for the concept of layers)

$$Q_{\text{neg}} = nA_{\text{elec}}Fl_{\text{neg}}\varepsilon_{\text{s,neg}}c_{\text{s,max}_{\text{neg}}}\left|\theta_{100\%_{\text{neg}}} - \theta_{0\%_{\text{neg}}}\right| \quad (3.62)$$

$$Q_{\text{pos}} = nA_{\text{elec}}Fl_{\text{pos}}\varepsilon_{\text{s,pos}}c_{\text{s,max}_{\text{pos}}}\left|\theta_{100\%_{\text{pos}}} - \theta_{0\%_{\text{pos}}}\right| \quad (3.63)$$

The cell's nominal capacity is the lower of the electrode capacities *i.e.*, $Q_n = \min(Q_{\text{neg}}, Q_{\text{pos}})$. Considering non-constant parts (barring n) of eqs. (3.62)–(3.63) and applying eq. (3.49), it is clear that the quantities to be compared are the two product terms $c_{\text{s,max}_{\text{neg}}}\left|\theta_{100\%_{\text{neg}}} - \theta_{0\%_{\text{neg}}}\right|$ and $c_{\text{s,max}_{\text{pos}}}\left|\theta_{100\%_{\text{pos}}} - \theta_{0\%_{\text{pos}}}\right|$. Substituting the numerical values from table 5.2, it is seen that the negative electrode is the limiting electrode for cell *i.e.*, $Q_n = Q_{\text{neg}}$.

Figure 3.11 shows the nominal capacity of cells and charge passed versus the number of layers during fast charging. In these plots, the nominal capacity Q_n of the cell versus the layer count n is represented by the linear downward-sloping line.

For any layer choice, Q_n therefore represents the upper bound on the charge that can be passed during charging. For both constant current and constant power charging, the loci of actual charge passed q lie much below this theoretical nominal capacity. For very low layer counts, as the number of layers decreases, the power density drops rapidly which implies that the rate of heating is low. This allows for more charge to be passed. However, at ultra-low layer counts, the overpotential due to the cell's internal resistance is quite high. Therefore, hitting the upper bound on the terminal voltage is the reason for the failure of these layer

choices. This is indicated by the narrow V_{\max} -limited region in fig. 3.11. For an intermediate range of layer choices, the rate of power-density drop with layer count begins to flatten, thereby leading to a plating-limited region. For these layer choices, the surface concentration starts to exceed the saturation value before any thermal or voltage limits are reached. Finally, further increasing the layer count beyond an intermediate optimal value leads to a linear drop in the cell's charge accepting capability. During fast charging with the chosen power levels, although these layer choices do not reach the thermal, voltage or concentration limits, they are unable to attain the target SOC of 80 %. This is simply due to the lower nominal capacity of the these cells. There is no benefit in choosing layers in this region. Figure 3.11 provides clues on the degree of optimisation that can be achieved by careful design choices. For instance, by using electrode materials capable of operating at higher plating voltage or with higher saturation concentration, the optimisation point can be appropriately adjusted.

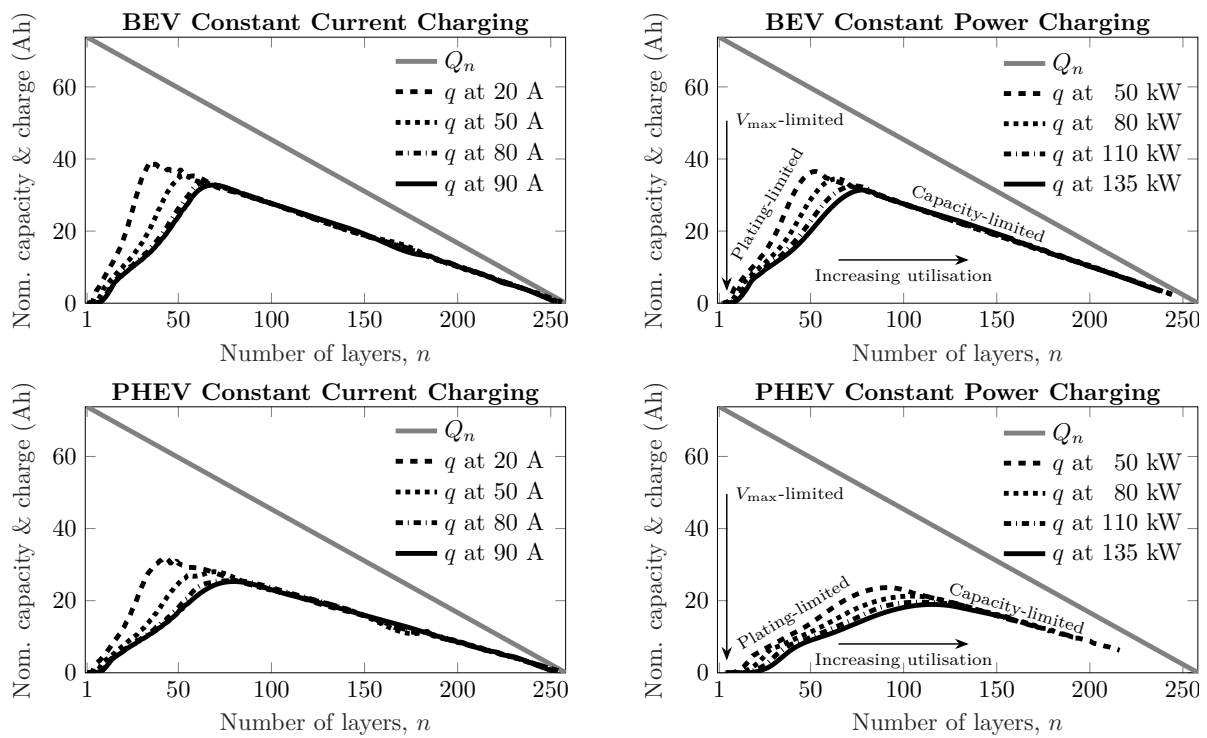


Figure 3.11^{§§} The right column shows nominal cell capacity and charge passed during CP charging. Rate capability and cell utilisation are positively correlated with n . With increasing power levels, the optimal layer configuration shifts to higher values of n . Similar behaviour is observed for galvanostatic charging (left column). Plotted for $T_{\text{init}} = T_{\text{sink}} = 25^\circ\text{C}$.

^{§§}This figure was created by Ian D. Campbell who asserts copyright, with intellectual contributions from and the right to use asserted by Krishnakumar Gopalakrishnan.

From the results discussed thus far, it is evident that it is the thermal environment that governs the overall globally optimal layer configuration to be used for cell design in both acceleration and fast charging studies and across both vehicular platforms. For all charging powers simulated, $n_{\text{opt}}^{\text{fastchg}}$ is the highest for the coldest temperature combination $(T_{\text{init}}, T_{\text{sink}}) = (15, 5)^\circ\text{C}$. This is due to the slow rate of electrochemical reaction and diffusion at cold temperatures. The thinner electrodes from using higher layer count enable fast charging without saturating the surface of the electrode particles. For the fast charging scenarios considered here, the optimal number of layers to use is 89 for the BEV cell and 153 for the PHEV cell. The globally optimal layer choice to be used for cell design is therefore the higher of the two values corresponding to acceleration and fast charging cases. Therefore, this model-based design framework recommends choosing 89 layers for the cells to be used in the BEV platform and 153 layers for those to be used in the PHEV platform.

3.7 Conclusions

A methodology to design the number of layers within pouch cells so as to maximise their energy density whilst simultaneously being capable of high charge-acceptance rate at the plating boundary has been developed. The proposed methodology may be employed by designers of xEV powertrains to mitigate the inefficiencies that plague the iterative experimental designs for each powertrain in a vehicle manufacturer's product portfolio. The methodology discussed in this chapter also paves the way to incorporate common module designs for packs through layer optimisation. By suitably changing the number of layers within a cell, while keeping the exterior module geometry unchanged, shall lead to cost reduction and lower the time for derivative product designs.

A mathematical procedure to adapt the standard galvanostatic-driven P2D model to accept direct power inputs has been elucidated. This reformulation is based on a quadratic boundary condition for the discretised solid-phase charge conservation equation, coupled with a positivity constraint on the cell's terminal voltage and an algebraic residual equation. A key numerical aspect of the PBMs used in this work is the incorporation of a hybrid pseudo-spectral/Finite Volume scheme, wherein the solid phase diffusion equation is solved in the Chebyshev domain while a finite volume discretisation is employed for rest of the axial-direction PDEs. This hybrid combination helps to achieve fast simulation runs without sacrificing model fidelity.

The methodology proposed here for pouch cells may be considered for application to cells of other form factors with suitable modifications. While considering the cylindrical form factor, instead of a discrete set of layers, the electrode sheets are wound into one continuous jelly roll and placed inside a cylindrical can. A suitable mathematical curve such as the logarithmic spiral could be employed wherein the number of turns could be used as a proxy for the layer count. The optimisation problem is also simplified to a certain extent since the cylindrical can's dimensions have already been standardised across the automotive battery industry. However, certain additional challenges could arise in directly translating the assumptions of the cooling methodology employed. For instance, a three dimensional discretisation of the thermal grid is not uncommon for cylindrical form factors, which requires careful considerations for bidirectionally coupling to the electrochemical model. Any differences in power densities at the interior of the core versus the extremities of the electrode spirals need to be accounted for.

This concludes the design-oriented aspects of the thesis. Next, chapter 4 deals with the aspects of analysing the computational bottlenecks present in one of the notable Reduced Order Models (ROMs) and proposes a mitigation strategy for them.

4

Computational Analysis and Numerical Reformulation of the DRA^{*}

4.1	Analysis of the Computational Bottlenecks of the DRA	138
4.2	Improved DRA for Battery Modelling	144
4.3	Golyandina-Usevich Algorithm	146
4.4	Customisations for Battery Modelling	147
4.5	Simulation Results and Discussion	148

^{*}This chapter is based on the journal publication – Krishnakumar Gopalakrishnan, Teng Zhang and Gregory J. Offer. “A Fast, Memory-Efficient Discrete-Time Realization Algorithm for Reduced-Order Li-Ion Battery Models”. *Journal of Electrochemical Energy Conversion and Storage* 14.1 (Feb. 2017), p. 011001. ISSN: 2381-6872. All intellectual ideas in the aforementioned article are original contributions of this thesis author. All text, tables, figures and captions therein were contributed solely by this thesis author. Copyright clearance for non-commercial verbatim reproduction of the content (such as in this thesis) has been secured through the publication agreement with the copyright holder ASME (see appendix B). The contents in this chapter may be, in full or in part, included verbatim from the said publication. This author wishes to express his thankfulness to Teng Zhang, co-author of this article, for checking my calculations and providing valuable feedback that helped to refine the manuscript for that journal publication.

THIS chapter presents an analysis and critical evaluation of a computational bottleneck present in a popular physics-based Reduced Order Model (ROM) framework of lithium-ion batteries and proposes an alternative numerical reformulation to mitigate it. From the literature review presented in chapter 2, it may be recalled that transcendental transfer functions of the cell's electrochemical field variables (except for ionic concentration and potential in the electrolyte) was obtained by Smith *et al.* [47] through linearisation of the underlying Pseudo Two-Dimensional (P2D) model equations. Lee *et al.* [48, 49] extended the aforementioned approach so as to obtain these missing electrolyte-specific transfer functions through a multi-modal EigenFunction expansion employing a Sturm-Liouville approach [174].

In order to arrive at a Linear Time-Invariant (LTI) state-space representation of the system (see eq. (2.1)) for embedded implementation, Lee *et al.* devised the Discrete-Time Realisation Algorithm (DRA), a numerical procedure to systematically transform all transcendental transfer functions to the time domain. A special property of the DRA is that it retains the physical nature of the original Doyle-Fuller-Newman (DFN) equations until the very last step wherein the matrices governing the system's dynamics are generated. This yields a one-dimensional discrete-time ROM of the cell that is entirely based upon fundamental physical principles. The ROM thus obtained could then be used to compute the time-evolution of all the internal electrochemical quantities of the DFN model. Prima facie it appears that this model could be directly implemented for embedded vehicular applications, for example, as the plant model for state estimation tasks. However, a comprehensive analysis of the procedure reveals a critical issue that must be first tackled before implementation aspects can be considered.

The unresolved issue in Lee *et al.* is the excessively high computational requirements associated with the DRA, which becomes a crippling bottleneck since the procedure needs to be repeated for multiple States of Charge (SOCs) and temperatures. This computational bottleneck arises from forming a large Block-Hankel matrix in memory upon which a Singular Value Decomposition (SVD) is performed. Under certain conditions as discussed in section 4.1.1, owing to the large size of the Block-Hankel matrix, the DRA computation is rendered intractable. This issue has been acknowledged by the original authors themselves in [5, 49]. In this chapter, this computational bottleneck is analysed and an improved

scheme is proposed[†]. Section 4.1 discusses an analytical evaluation of the massive computing requirements of the original DRA method. Redundancies and inefficiencies in this step are enumerated and the high computational costs are deemed as unnecessary. In section 4.2, a fast computational approach is presented which significantly reduces both the memory and computational time of the ROM workflow. Section 4.5 summarises the results obtained from applying the new workflow presented in section 4.2, by comparing and contrasting the much smaller computational requirements of the new method with the original DRA scheme. The improved modelling accuracy achieved by this proposed method when deployed under resource-constrained computing environments, is also highlighted.

4.1 Analysis of the Computational Bottlenecks of the DRA

The ROM proposed by Lee *et al.* aims for the simplified representation of the Pseudo Two-Dimensional (P2D) volume-averaged P2D implementation of the continuum model proposed by Doyle, Fuller and Newman [15, 16].

The block diagram in fig. 4.1 depicts this thesis author's summary presentation of the overall modelling workflow in Lee *et al.*. Firstly, the governing Partial Differential Algebraic System (PDAE) equations of the DFN model (see table 1.1) are linearised about an operating point of SOC and temperature. Then, closed-form Laplace domain transcendental transfer functions of all the internal physical quantities ($\phi_s, \phi_e, c_s, c_e, j$) at different cell locations, are derived using applied current as the input. A detailed treatment of this analytical derivation is presented in Lee *et al.* [48]. The authors proposed a novel Discrete-Time Realisation Algorithm (DRA) scheme [175] in order to transform these transcendental transfer functions to standard state-space representation. Sublevel-1 of fig. 4.1 shows a breakout view of the DRA procedure and illustrates the steps involved in this computation. At the heart of this numerical method is the classical subspace identification approach known as Ho-Kalman algorithm [176], whose computation steps are shown via the exploded view in sublevel-2 of fig. 4.1. Then, the Markov parameters (unit-pulse response) of this Single Input Multiple

[†]In the views of this thesis author, it is difficult to succinctly summarise the mathematical derivations involved in the long sequence of modelling steps of the DRA *i.e.*, obtaining transcendental transfer functions followed by the Ho-Kalman algorithm for state-space realisation. Extraction of salient equations from published works do not have the ability to convey the essence of the method in a standalone manner, and risks the introduction of a slew of new notation and symbols. Therefore, this chapter needs to be viewed as a continuum to the basic DRA presentation, a detailed presentation of which is available in the textbook by Plett [5].

4.1 Analysis of the Computational Bottlenecks of the DRA

Output (SIMO) linear system of battery transfer functions are computed[‡]. They form the entries of a Block-Hankel matrix [177], wherein each block element is a column vector of the set of Markov parameters at a given time-step as shown in eq. (4.1).

$$H = \begin{bmatrix} g_1 & g_2 & \cdots & g_n \\ g_2 & g_3 & & \\ \vdots & & \ddots & \vdots \\ g_n & \cdots & g_{2n-1} & \end{bmatrix} \quad (4.1)$$

where g_k represents the Markov parameter of the system at time-index k . Each entry g_k is a column vector for SIMO systems. For the lithium ion battery application proposed by Lee *et al.* [48], the Markov parameters of the system correspond to transcendental transfer functions of each of the following quantities to the applied current

1. Solid phase potential
2. Electrolyte potential
3. Solid phase concentration
4. Electrolyte concentration
5. Molar flux density
6. Overpotential
7. solid-electrolyte potential difference

at four different spatial locations — the two current collectors and the two separator interfaces.

A key computation in the Ho-Kalman algorithm is the Singular Value Decomposition (SVD) of this Block-Hankel matrix. A wide separation in the magnitude drop between successive singular values serves as a guide for the modeller in choosing a suitable reduced order to represent the entire dynamics of the system. The analyses of this thesis author, presented in section 4.1.2 and section 4.1.3 reveal major inefficiencies in both the Block-Hankel formation and the SVD computation steps which hinder the entire reduced-order modelling workflow.

[‡]A ubiquitous concept in linear systems and control theory, Markov parameters represent the discrete-time unit pulse response of a linear system.

4.1 Analysis of the Computational Bottlenecks of the DRA

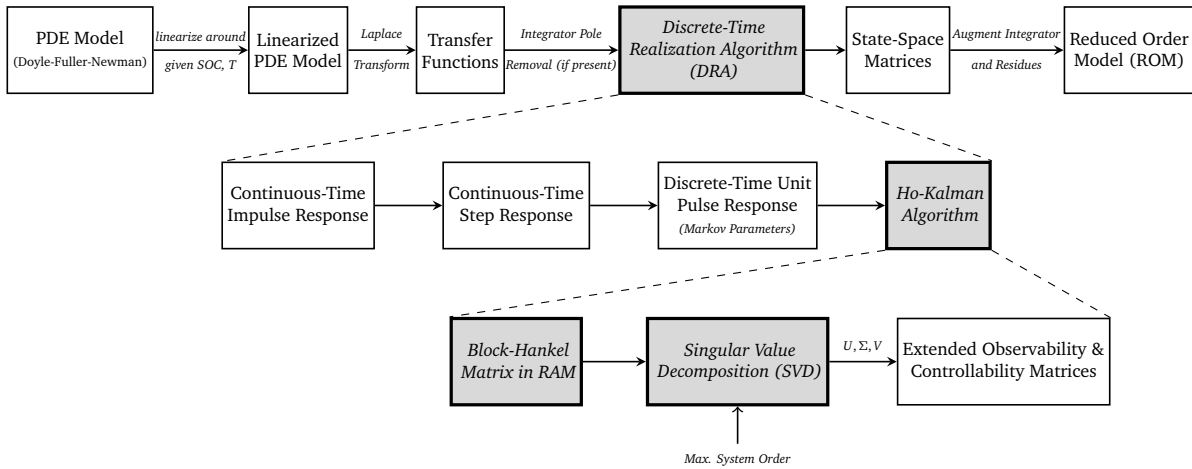


Figure 4.1 Reduced Order Model (ROM) workflow using classical Discrete-Time Realisation Algorithm (DRA). The shaded blocks represent computational bottlenecks.

4.1.1 Size of the Block-Hankel Matrix

Large Block-Hankel matrices can occur in DRA computation due to the following reasons.

1. For a given duration of Markov-parameter recording, if a high sample-rate ROM is desired, the emulation frequency in the DRA scheme has to be proportionately increased to accurately compute the continuous-time step and pulse responses in fig. 4.1. This implies that the total number of time-samples N for each Markov parameter will have to be scaled linearly to capture the desired duration of the unit-pulse response. However, the size of the Block-Hankel matrix has a *quadratic* dependence on the Markov parameter length.
2. The recorded sample size N could also become large if the Markov parameters of just one of the transfer functions decay very slowly. In Li-ion batteries, diffusion within the solid particle is typically the slowest process. For the cell modelled in Lee *et al.*, the unit-pulse response of surface concentration of Li adjacent to the positive current collector requires approximately 16000 samples before reducing to an appreciably low value, as shown in fig. 4.2.
3. For a battery modelling problem consisting of multiple transfer functions, the number of entries in the Block-Hankel matrix also scales linearly with the number of transfer functions. Thus, if more cell variables (*e.g.* concentrations and potentials at other spatial

locations within the cell) are to be studied, then the size of the transfer function vector and that of the Block-Hankel matrix increases correspondingly.

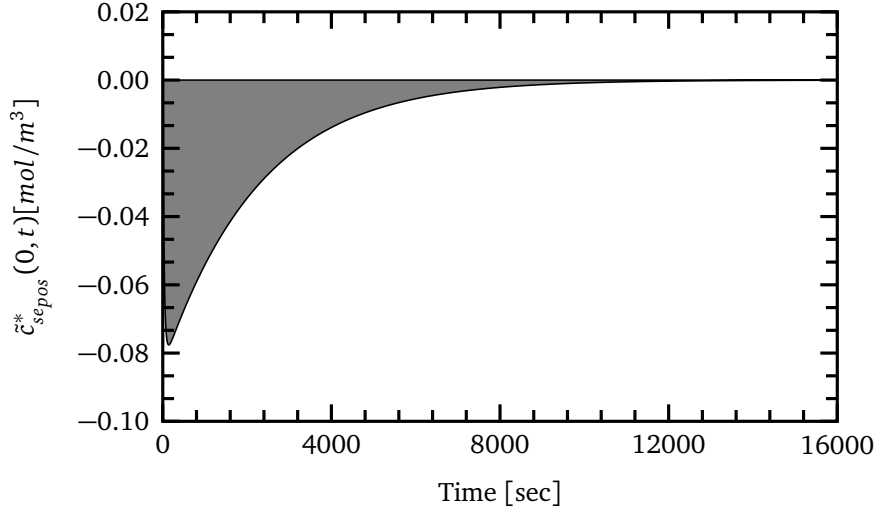


Figure 4.2 Time evolution of Markov parameters of pole-removed transfer function corresponding to surface concentration of Li in the solid particle adjacent to positive current collector.

Considering the combined influence of these effects, if x transfer functions are to be modelled and N time-samples of each Markov parameter are to be captured, the corresponding size of the Block-Hankel matrix H is

$$\text{Size}(H) \sim \mathcal{O}(xN^2) \text{ entries} \quad (4.2)$$

This has a significant computational impact as shown in section 4.1.2 and section 4.1.3.

4.1.2 Classical DRA — Memory (RAM) Requirements

Lee *et al.* [48] modelled 28 transfer functions representing various electrochemical variables at the current collector and separator interfaces. Each Markov parameter is a 28 element column vector. 16000 time-samples were obtained at a sample-rate of 1 Hz, allowing sufficient time for the Markov parameters of the slowest dynamics *i.e.*, solid surface concentration to settle to an acceptably low magnitude. The Block-Hankel matrix thus formed has 8000 blocks, each block consisting of 28 elements *i.e.*, has $8000 \times 28 = 224000$ rows and 8000 columns. Hence, the overall number of elements in the Block-Hankel matrix is $224000 \times 8000 = 1.79 \times 10^9$. Using double-precision arithmetic, its storage requirement can be estimated to be ≈ 27 GB.

Computing the SVD results in the formation of three more large matrices in memory – i) matrix of output singular vectors U , ii) matrix of input singular vectors V , and iii) the diagonal singular-value matrix Σ . With 8000 Hankel-blocks, approximately 81 GB of Random Access Memory (RAM) is required for holding these three output matrices generated by a full SVD. However, the intermediate operational memory usage during the SVD computation is often much higher than the combined size of all the matrices. As these large matrices must be repeatedly handled for each operating point of SOC and temperature, the high memory demand of the classical DRA remains a persistent issue.

4.1.3 Classical DRA – CPU Operation Count

The most widely used numerical algorithm for computing the full SVD of a generic dense matrix $A \in \mathbb{R}^{m \times n}$, $m \geq n$ is the two-stage Golub-Kahan-Reinsch method [178]. In the first stage, $A \in \mathbb{R}^{m \times n}$ is reduced to an upper bidiagonal form. In the second stage, SVD of this upper bidiagonal matrix $B \in \mathbb{R}^{m \times n}$ is computed using an iterative procedure such as the Demmel-Kahan method [178]. If stage I of the SVD computation employs R-Bidiagonalisation [178], then the overall process is referred to as R-SVD. This is the fastest known full SVD computation method that may be applied to this battery modelling problem. The DGESVD algorithm, originally implemented in LAPACK [179], employs this method. This has been ported to many numerical computation packages such as MATLAB, GNU Octave and Scilab. Several numerical libraries such as NAG and Intel MKL also use the DGESVD codes due to its acclaimed stability, robustness and versatility. The MATLAB implementation ‘svd’ is also based upon DGESVD and hence this can be considered as the de-facto baseline SVD code.

The operation count for computing the singular values and vectors of a generic dense matrix $A \in \mathbb{R}^{m \times n}$, $m \geq n$ using the R-SVD method is $4m^2n + 22n^3$ [178]. Markov parameters of x transfer functions and N time-samples yields a Block-Hankel matrix with $m = xN$ rows and $n = N$ columns. Hence,

$$\begin{aligned} \text{CPU Operation Count} &= 4(xN)^2N + 22N^3 \\ &= 2N^3(11 + 2x^2) \end{aligned} \quad (4.3)$$

Thus the Central Processing Unit (CPU) operation count scales as $\mathcal{O}(N^3)$ with the number of Markov time-samples N and as $\mathcal{O}(x^2)$ with the number of transfer functions x being modelled.

4.1 Analysis of the Computational Bottlenecks of the DRA

The ROM computed in Lee *et al.* uses 28 transfer functions wherein the Markov parameters are collected for 16 000 s with a sampling interval of 1 s. Thus, the CPU operation count for performing this computation is approximately $\mathcal{O}(16000^3) \approx 4 \times 10^{12}$ floating point operations.

4.1.4 Summary Effect of Computational Bottlenecks

The computational bottleneck in a classical DRA implementation arises due to the requirement of capturing a large number of Markov parameters, which in turn leads to growth in Block-Hankel size. In the case of battery modelling, this can arise in the following real-life scenarios:

1. Electrochemical variables at additional locations of interest within the cell (*e.g.* middle of electrode or separator domain) might need to be modelled. This increases the number of transfer functions and hence the number of Markov parameters.
2. High frequency load cycles necessitate higher sample-rates to obtain a high fidelity model. This leads to a correspondingly higher number of Markov parameters.
3. In cells with large particle sizes and small diffusion coefficients, a large set of Markov parameters is needed to capture the full system dynamics.

Lack of specialised computing infrastructure necessitates early truncation of the Markov parameters in the ROM workflow. The resulting errors in the singular value computation lead to significant modelling errors in the physical variables of the cell. Thus, in practice, the computational bottlenecks of classical DRA manifest as modelling errors when implemented in a resource-constrained computing environment. Furthermore, this tedious computation has to be repeated for multiple SOCs and temperatures.

The foregoing analysis clearly demonstrates that the high memory and CPU demands in a classical DRA implementation severely hamper the scope and applicability of the reduced order modelling process. This implies that the modelling workflow is not accessible to research groups without specialised computing infrastructure and its universal appeal is rendered questionable. The shaded blocks in fig. 4.1 depict the hierarchical propagation of the classical DRA's computational bottleneck throughout the ROM workflow.

4.2 Improved DRA for Battery Modelling

Collecting a large Markov parameter set is inevitable due to the fundamental physics of the cell dynamics as established in section 4.1.4. Hence, in order to circumvent the high computational demands of the classical DRA, the second step in the process *i.e.*, forming the Block-Hankel matrix, is critically examined with the following scientific rationale.

1. The unit-pulse responses of most battery transfer functions (other than those of rate-limiting steps such as solid diffusion) decay relatively quickly. Hence it is inefficient to record the Markov parameters of the full system for the entire duration needed to capture the slowest dynamics.
2. The Block-Hankel matrix is essentially redundant information since its entries are simply the Markov parameters arranged in a repeating special structure. Thus, it is wasteful to construct this huge matrix. If the SVD operation can be performed on a virtual Hankel matrix, the memory requirements can be drastically reduced.
3. The matrix of singular values Σ is diagonal and hence, sparse. It is redundant to hold all the non-diagonal entries (zeros) in memory.
4. It is not necessary to perform a *full* SVD operation in order to achieve order reduction. When an upper bound on desired system order can be decided a priori, it is sufficient to compute a *truncated* SVD yielding the first few dominant triplets of U , Σ and V .

Thus, forming the large Block-Hankel matrix and computing its SVD is identified as an avoidable bottleneck in the classical DRA method. This can be tackled since forming the Block-Hankel matrix is an idiosyncrasy of the algorithm used and does not arise from any fundamental physical limits. Facilitated by an efficient SVD implementation, this thesis author proposes an improved DRA that serves as a drop-in replacement in the ROM workflow.

4.2.1 Candidate Schemes for Block-Hankel SVD

Generic SVD routines such as `DGESVD` do not take advantage of the anti-diagonal structural symmetry of Block-Hankel matrices. Since it is sufficient to obtain the first few leading eigentriplets for order reduction, iterative algorithms such as the Jacobi and Lanczos schemes

(see [178]) emerge as attractive candidates for computing these dominant singular values and vectors. In order to ensure accessibility to the large community of battery researchers and to encourage widespread adoption of the fast reduced order modelling framework, the author of this thesis considered only freely available open-source numerical libraries that exist in the public domain, especially those with permissive licensing terms. Otherwise the gains achieved by an efficient SVD computation for implementing DRA on non-specialised computing hardware would be offset by commercial licensing terms, usage restrictions and monetary considerations associated with using proprietary codes. Among these open-source candidate algorithms, the Jacobi scheme [178] is available through the xGESVD routine in the LAPACK suite [179]. FORTRAN 77 codes for the implicitly restarted Arnoldi and Lanczos schemes (see nu-TrLan [180]) are available as part of the ARPACK [181] library.

The practical drawback of most SVD implementations, both open-source and proprietary, is that they require the entire matrix as input argument. Since operating upon the Block-Hankel matrix requires constructing it in the first place, the memory bottlenecks discussed in section 4.1.2 are not ameliorated. An example is the svds routine – an economy size SVD implementation in MATLAB. Albeit this is a commercial implementation of the Arnoldi codes, any potential benefits of using an iterative scheme is nullified by the memory penalty. Owing to reasons enumerated in section 4.2, the chosen SVD algorithm needs to be able to handle the computation without actually forming the huge block-Hankel matrix in memory.

4.2.2 SVD Operation on a Virtual Block-Hankel Matrix

The pioneering work by Larsen, PROPACK [182], based on his earlier work [183] implements a numerically stable Lanczos SVD computation designed specifically for large and sparse matrices. In addition to the ability to operate on the matrix as a whole, the PROPACK codes possess a unique flexibility of accepting input arguments in a functional form. A key highlight of the Lanczos SVD scheme is that it does not strictly require the matrix itself, but only the product of the matrix and its transpose with an arbitrary vector. This feature has been effectively exploited in the PROPACK suite. Therefore, these multiplication routines can be supplied as input arguments instead of forming the large Block-Hankel matrices in memory. Furthermore, this package includes sophisticated schemes such as Gram-Schmidt partial re-orthogonalisation [184] to compensate for numerical round-off errors in the basic

Lanczos bidiagonalisation and ensures orthogonality of the input and output singular vectors. The PROPACK suite is available as both Fortran 77 and MATLAB codes distributed under a permissive BSD license. Version 1.1 of the MATLAB implementation of the PROPACK suite was used by this thesis author.

For the ROM workflow, in order to use PROPACK's unique feature *viz.* its flexibility to accept functional form inputs, the key is to use an algorithm that effectively exploits the affine structure of the Block-Hankel matrix without actually forming it in memory. Recent research in a specialised time-series technique known as Singular Spectrum Analysis (SSA) [185] has yielded efficient methods for achieving this goal. Korobeynikov [186] proposed an algorithm that employs the Fast Fourier Transform (FFT) for implementing this matrix-vector product by embedding the Markov parameters into the column vectors of a circulant matrix. This is suitable for applications wherein the Hankel matrix is composed of scalar entries such as that formed by the Markov parameters of a Single Input Single Output (SISO) transfer function. Golyandina, Usevich and colleagues [187, 188] extended this approach to a generic 2D-case for performing SSA on images. With this modification, this algorithm is rendered capable of handling the structure of Multi-level Block-Hankel matrices formed from the Markov parameters of a generic Multi Input Multi Output (MIMO) system. While the modified scheme does not construct the Block-Hankel matrix in memory, the operational rubrics of the Golyandina-Usevich algorithm in conjunction with PROPACK is such that they iteratively operate on a virtual Hankel matrix of equivalent size. The Golyandina-Usevich algorithm is briefly summarised in section 4.3.

4.3 Golyandina-Usevich Algorithm

The Golyandina-Usevich algorithm is used for computing the product of a Block-Hankel matrix with an arbitrary vector. The steps involved in this scheme are enumerated in Algorithm 3 of Golyandina *et al.* [188]. These steps are reproduced here in the context of the improved DRA for reduced order battery modelling.

1. Compute a 2-D FFT of Markov parameter matrix.
2. Form an augmented vector by zero-padding the arbitrary vector input from Lanczos iteration.

3. Perform a column-wise reshaping of this augmented vector to obtain a new matrix with the same dimensions of the Markov parameter matrix.
4. Compute the element-wise product of this newly created matrix with the 2-D FFT of Markov parameter matrix.
5. Reshape the resulting matrix back to a column vector.
6. Extract the first L elements from this vector, wherein $L = Kx$. K represents the desired block-Hankel size and x represents the number of transfer functions being modelled.

At the end of Step 6, the product of the Hankel matrix and arbitrary vector is obtained. This is reused as an input for the Lanczos scheme which generates a new arbitrary vector in the subsequent iteration. Thus, the steps 1–6 are run in a loop within the main Lanczos scheme. These same steps can also be used for computing the product of the transpose of the Hankel matrix and the arbitrary vector. The only change is to account for the different dimensions of the arbitrary vector input from the Lanczos scheme in step 2. As a practical implementation, software code representing steps 1–6 is written in a plain-text file and used as functional-form inputs by the PROPACK scheme which implements the Lanczos iteration.

4.4 Customisations for Battery Modelling

Specific considerations are required for incorporating the Golyandina-Usevich algorithm in the ROM workflow for Li-ion batteries. The classical DRA architecture is set up to handle SIMO systems, wherein all transfer functions are derived by considering only a single input *viz.* the applied battery current. Thus the Markov parameters form a 2D matrix wherein each row corresponds to individual battery transfer functions with columns representing unit-pulse response samples for each transfer function. The 2D moving-window illustrated in [188] for Block-Hankel matrix formulation has to be suitably reshaped to account for this structure. Step 3 of the algorithm deals with 2-D FFT computation of the Markov Parameter Matrix (MPM). In this thesis author's implementation, this is pre-computed since it remains invariant between iterations of the Hankel-vector product computation loop. This pre-allocation and a priori computation contributes to overall code efficiency.

4.5 Simulation Results and Discussion

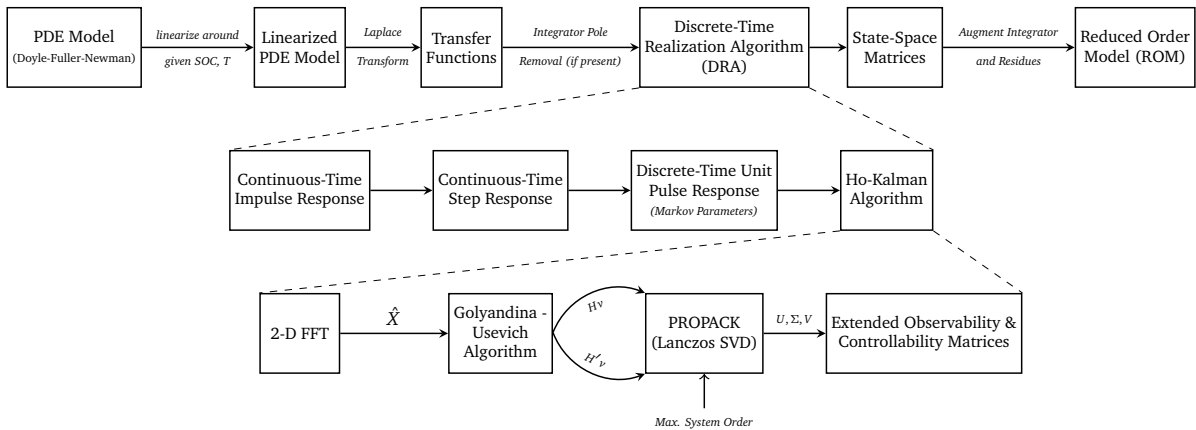


Figure 4.3 Reduced Order Model (ROM) workflow using improved Discrete-Time Realisation Algorithm (DRA).

Figure 4.3 shows the ROM workflow with the improved DRA wherein all computational bottlenecks highlighted by shaded blocks in fig. 4.1 have been eliminated. The strategy is to first employ the (suitably modified) Golyandina-Usevich algorithm for describing the matrix-vector multiplication routines. These two functions are then used as inputs to the PROPACK codes. Eigentriplets up to the desired upper bound on system order is then computed using a Lanczos SVD iteration. Figure 4.4 presents a comparison of singular values computed by both the traditional and new methodologies. It is evident that the two sets of singular values are identical. This proves that the new scheme can indeed serve as a drop-in replacement for the classical DRA.

4.5 Simulation Results and Discussion

This section provides a quantitative demonstration of the reduced computational demand of the improved DRA scheme by comparing it with the classical DRA implementation. The physical parameters of the cell are the same as those published in Fuller *et al.* [16]. Table 4.1 lists the parameters used in the ROM workflow (same as those employed by Lee *et al.* [48]).

Figure 4.5 shows a comparison of the memory usage of classical and improved DRA methods. It is evident that the SVD step in classical DRA consumes an overwhelming majority of the total memory demand, requiring ≈ 100 GB for a Hankel block size of 8000. This can be a limiting factor in modelling slow cell dynamics without access to a large memory workstation. The improved DRA method eliminates this bottleneck and the memory usage of

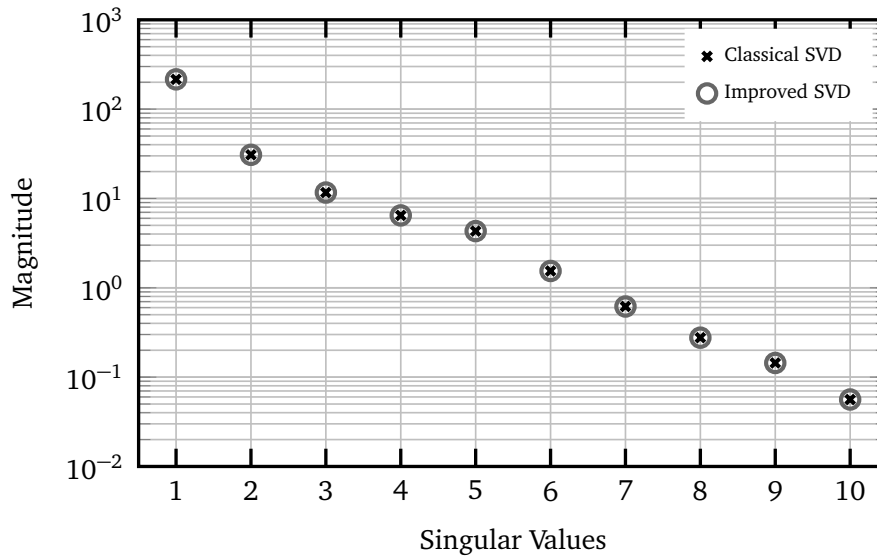


Figure 4.4 Comparison of singular values computed by the conventional and improved SVD methods. Using the new scheme results in identical singular values

Table 4.1 Parameters for ROM Computation

Initial Cell SOC	60 %
Hankel Block Size	8000
Discrete-Time Model Sample-Rate, T_s	1 s
Number of Electrolyte EigenModes	5
Continuous-Time Emulation Frequency, F_1	128 Hz
Desired Number of Singular Values	10

SVD step is negligible. Overall memory usage of the improved DRA is dominated by Markov parameter computation. Considering 10 GB of usable RAM, this means that 60000 Markov parameters (Hankel Block-size of 30000) can be captured.

Figure 4.6 shows a comparison of CPU times for computing the ROM at a single SOC and temperature for both the classical and the improved DRA methods[§]. Owing to the high operation count for the SVD computation (see eq. (4.3)), the classical DRA requires ≈ 40 min for a Hankel block size of 8000. Clearly, the overall CPU time for the classical DRA is almost exclusively spent for computing the SVD. The improved DRA method reduces the overall

[§] All computations reported in this chapter were performed on a dedicated high-RAM pool drawn from the compute cluster hosted at the Department of Mathematics at Imperial College London. The author of this thesis wishes to express his thankfulness to the relevant authorities for providing access to this facility. The resources borrowed were one core of a 4-core Intel[®] Xeon[®] E5-2637 v3 processor clocked at 3.50 GHz with 500 GB RAM.

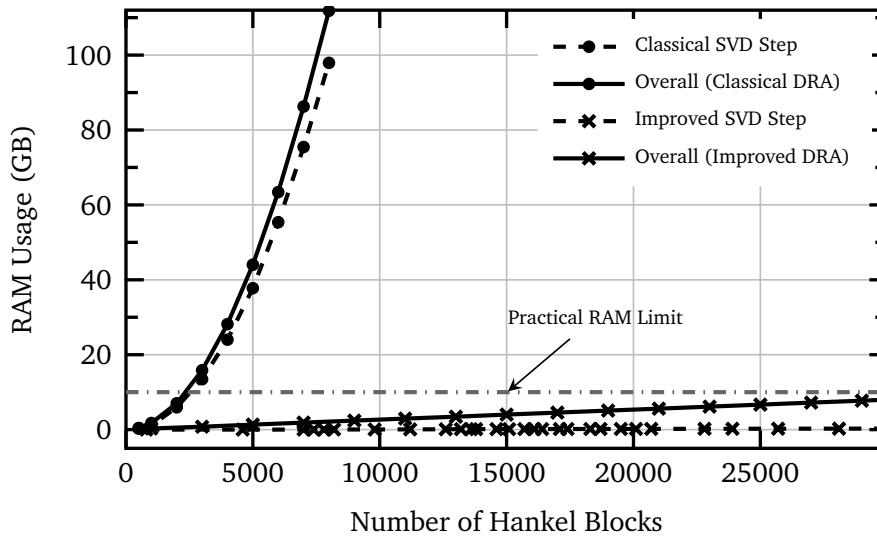


Figure 4.5 Memory usage of classical and improved DRA. Overall, RAM usage as well as the memory used only for SVD computation is illustrated.

computational time by two orders of magnitude, taking ≈ 40 s for the same block-size. In this case, the CPU time is evenly split between the SVD and Markov parameter computations.

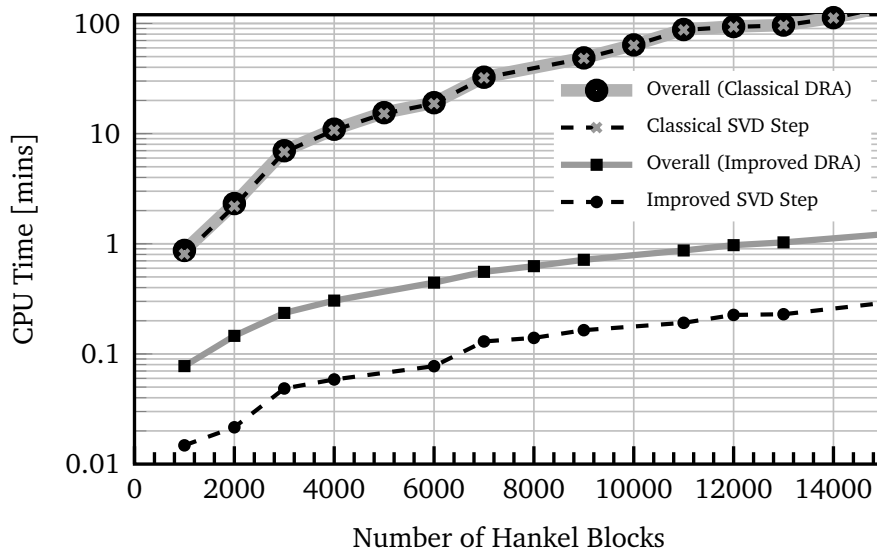


Figure 4.6 Computation times for classical and improved DRA schemes

From fig. 4.5, it is evident that if classical DRA is employed, a standard laptop with a nominal 10 GB RAM limit (dedicated for ROM workflow) cannot capture the full cell dynamics and hence is restricted to 2500 Hankel blocks. This necessitates early truncation

of Markov parameters at 5000 s. From fig. 4.2, the truncation residue at 5000 s for the unit-pulse response of solid surface concentration at positive current collector is $-0.0087 \text{ mol m}^{-3}$. The truncation errors in the MPM directly translate to errors in computed singular values, adversely affecting accuracy of simulated cell variables. It must be noted that the accuracy of simulation results reported here does not bear a causal relationship to the particular DRA scheme employed. In principle, when an upper bound on computational usage has not been enforced, the numerical operations of both the existing and proposed DRA schemes lead to similar error magnitudes for the modelled quantities. Instead, the accuracy comparison illustrated here primarily serves to demonstrate the practical usefulness of the improved DRA scheme when implemented in a commonplace computing environment.

Figure 4.7 shows a comparison of singular values obtained by the classical and improved SVD methods computed by imposing a RAM limit of 10 GB. Owing to early truncation of the MPM, the dominant singular values computed by the conventional method differ significantly from those computed by the improved SVD operating on untruncated data. With the same memory constraints, the improved DRA can handle up to 30000 Hankel blocks, allowing for capture of 60 000 s of Markov parameter data.

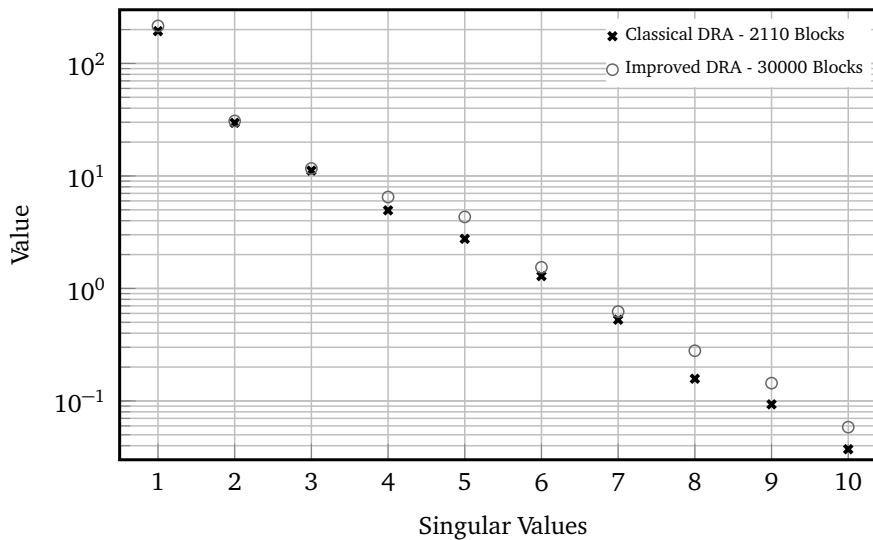


Figure 4.7 Comparison of singular values computed by conventional and improved SVD methods under a practical RAM limit of 10 GB

For comparative analysis of modelling accuracy under this memory constraint, a time-domain simulation of the ROMs obtained by classical and improved DRA methods is

performed. The input current profile corresponding to a Urban Dynamometer Driving Schedule (UDDS) drive cycle reported in Lee *et al.* [48] is used. Figure 4.8 depicts the time-evolution of the solid surface concentration at the positive electrode/separator boundary. For comparing the accuracy of the two ROMs, a COMSOL Multiphysics [189] simulation of the full-order pseudo-2D porous-electrode PDAE model is used as the reference. The ROM employing classical DRA diverges over time, and after 1500 s results in an error of 1120 mol m^{-3} . The ROM incorporating the new DRA workflow accurately tracks the COMSOL simulation trend-line.

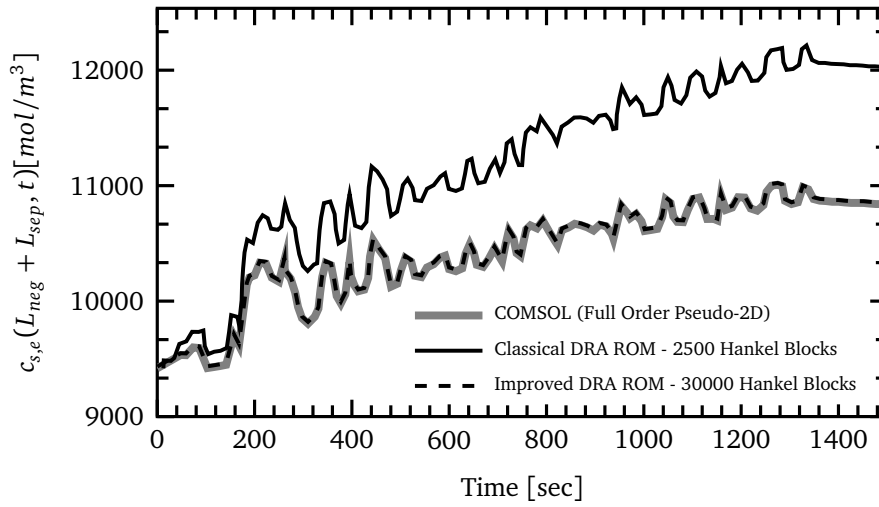


Figure 4.8 Time-domain simulation depicting solid surface concentrations at the boundary of positive electrode and separator. The simulation results from the P2D model implemented in COMSOL is used as the reference benchmark. The two ROMs were derived under a RAM limit of 10 GB. The performance of the improved DRA is significantly better than the classical DRA owing to the fact that its derivation could accommodate a larger number of Hankel blocks without exceeding the specified memory limit.

Table 4.2 provides a summary of the key simulation results. At a single operating point of SOC and temperature, for a Hankel block size of 8000, the ROM workflow incorporating the improved DRA is ≈ 100 times faster than that employing the classical DRA. Using the machine with specifications listed in the footnote[§], for 100 operating points (combinations of 10 SOC and temperature values), computing the ROM requires only 6 hours using the improved DRA, whereas the classical DRA consumes 666 hours (27 days). Furthermore, for the same block-size, the improved DRA is demonstrated to be superior in terms of memory efficiency, drastically reducing the memory requirement from 112 GB down to 2 GB. Finally,

the improved DRA demonstrates superior modelling accuracy when implemented even in moderately equipped computing environments such as laptops.

Table 4.2 Salient Results – Classical vs. Improved DRA

ROM Condition	Entity	Classical DRA	Improved DRA
8000 Hankel Blocks	Memory (overall)	111.80 GB	2.14 GB
	Memory (SVD step)	97.93 GB	0.03 GB
	CPU Time (overall)	39.78 min	0.63 min
	CPU Time (SVD step)	39.30 min	0.14 min
10 GB Memory Limit	Block Size	2500	30000
	Max. error in $c_{s,e_{\text{pos}}}(1,t)$	1120 mol m ⁻³	13 mol m ⁻³

This chapter concludes with the view that, although the bottlenecks in Lee *et al.* [48] revealed by this in-depth analysis have been effectively tackled in this chapter, owing to the circular dependency between the linearisation point and model parameters, the underlying model itself is not robust enough for immediate implementation. Furthermore, the model derivation is convoluted with the derivation being performed in the frequency domain and implementation in the time-domain. This thesis author is of the opinion that a simple, yet accurate model derived and implemented entirely in time-domain is the need of the hour for encouraging the automotive industry to adapt physics-based battery models onto on-board Battery Management Systems (BMSs) of electric vehicles. In the quest to fulfil this need, an analysis of the simplest time-domain Physics-Based Model (PBM) *viz.* the Single Particle Model (SPM) is presented next in chapter 5.

5

Performance Evaluation of State of the Art in Single Particle Modelling

5.1	SPM Model Development	155
5.2	Numerical Implementation	169
5.3	Desktop Simulation	178
5.4	Quadratic Approximation of Ionic Spatial Concentration	201
5.5	Conclusions	210

TAKING into account the relative strengths and weaknesses of all the physics-based reduced order modelling families in the literature considered (see chapter 2), the overarching simplicity of the Single Particle Model (SPM) coupled with its immediate potential to bring the power of physics-based predictions to an embedded environment is a strong motivation to pursue an in-depth exploration of its horizons. This chapter discusses the performance of multiple SPM variants, ranging from basic to sophisticated. The governing equations of the conventional SPM are first introduced and its baseline performance is evaluated. Next, an in-depth analysis of the basic SPM's drawbacks is performed. Various

published attempts to mitigate their current challenges towards implementability is presented and their inadequacies discussed. Owing to its simplicity and latent potential, a popular modelling strategy from the existing art that aims to enhance the performance of the basic SPM through incorporation of electrolyte dynamics, is chosen for further analysis. The chapter concludes with the author's critical comments on its relative merits that come to view through comparison against a benchmark model, whilst simultaneously identifying its critical weakness whose mitigation forms the focal point of the research discussed in chapter 6.

5.1 SPM Model Development

In order to establish a context for the author's work to be discussed in chapter 6, it is imperative to provide a holistic presentation of the basic SPM modelling art. The conventional SPM is the simplest of all time domain Physics-Based Models (PBMs). The rest of this section provides this author's digested summary of its modelling rubrics based upon the keen insights gained from perusing the vanguard literature in this topic [87, 92, 96] as well as their relevant derivative works.

5.1.1 Geometry

A description of the working principle of the cell was presented in section 1.1 and is not repeated here. The SPM aims to capture the electrochemical phenomena along the thickness l_j , $j \in \{\text{neg}, \text{pos}\}$ of each porous electrode by a representative spherical particle. Thus the two distinct solid phase porous regions of the cell *i.e.*, the negative and positive electrode regions, are idealised as two spheres of radii R_{neg} and R_{pos} respectively.

Figure 5.1 shows the geometrical origins of the basic SPM. In this arrangement, the spatial dimension along the axial thickness of each electrode degenerates to a single point which is represented by a sphere. Hence, the concentration of lithium within each electrode $c_{s,j}$, $j \in \{\text{neg}, \text{pos}\}$ is only a function of the radial position r_j , $j \in \{\text{neg}, \text{pos}\}$ and the time t . The surface area of each representative sphere is scaled appropriately, such that they are equivalent to the active area A_{elec} of the corresponding porous electrodes. Thus the SPM accounts for the reduced volume-fraction arising due to the microporous structure of the solid phase and hence, the storage capacity of the representative particles match that of the corresponding electrodes. The overarching assumption of the SPM modelling philosophy is that the electrochemical

performance of these representative electrodes are sufficient to model the voltage behaviour of the cell at its terminals. The SPM thus employs the coarsest possible spatial discretisation of the cell's thickness with the goal of minimising computational burden.

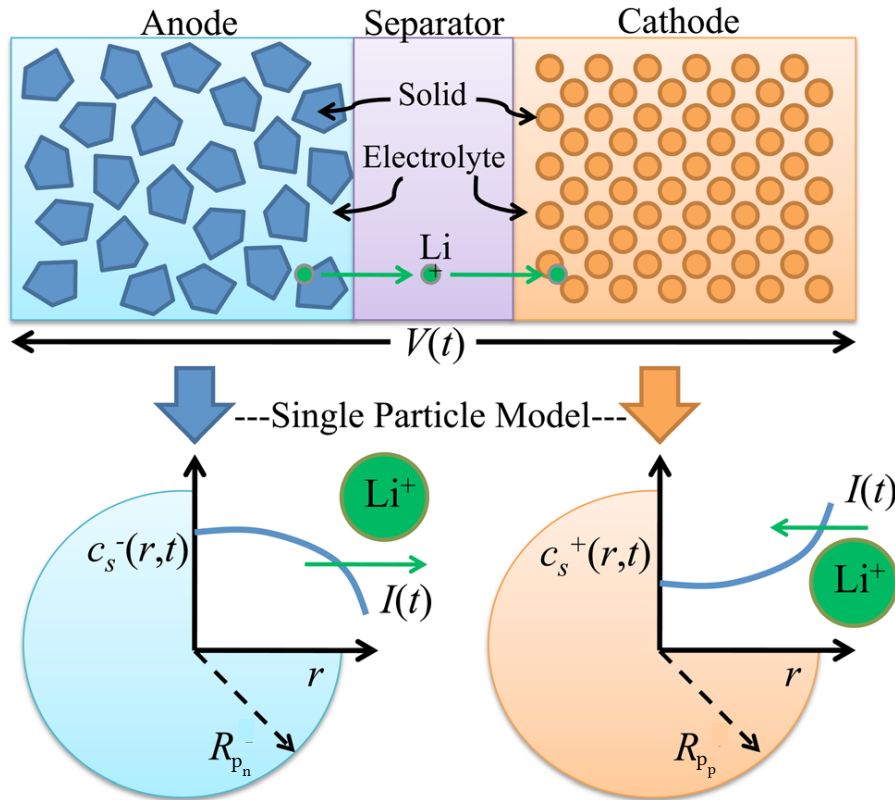


Figure 5.1 Schematic illustration depicting the geometrical origins of the basic SPM. The model is obtained through a degenerate spatial discretisation of one electrochemical layer of a pouch cell. The active material of each porous electrode is represented by one representative spherical particle, thus entirely eliminating the spatial dimension along the axial direction. Illustration adapted from Moura *et al.* [43].

5.1.2 Scope and Assumptions

Having described the geometrical representation of the model, it is imperative to establish its aims and scope. This section discusses the subset of physical phenomena that can be captured by the basic SPM and enumerates the inherent assumptions in model derivation. The validity of these assumptions and their effects on model accuracy shall be examined in the results presented in section 5.3.3. As a broad outline of its scope, the model attributes the cell polarisation to two dominant physics *viz.* reaction kinetics and solid phase transport phenomena *i.e.*, diffusion dynamics.

The SPM assumes that charge transfer happens throughout the surface of each representative spherical particle where intercalation occurs. The electronic conductivity of the solid phase is assumed to be high enough to ignore the spatial distribution of charge *i.e.*, the local volumetric current density is assumed to be uniform along the thickness of each porous electrode. This assumption is motivated from early calculations by Newman and Tobias [190] in their stand-alone analysis of current distributions in porous electrodes, wherein a volume-averaged molar flux was deemed sufficient throughout the thickness of the electrode. This uniform current density assumption implies that all of the particles in the electrode active material are in parallel. Solid phase diffusion dynamics within each electrode are therefore solved by assuming this averaged electrochemical reaction rate. In the simulation study by Smith and Wang [34], it is reported that soon after the beginning of discharge, solid phase concentration and ionic flux become nearly independent of spatial position, and that lithium diffusion in solid particles may be driven by an averaged molar flux at the surface.

Based on the discussion thus far, it is clear that the SPM does not attempt to model all physical processes within the cell. In particular, the model assumes instantaneous charge transport from one electrode to the other through the solution phase. This implies that electrolytic diffusion is sufficiently fast (relative to diffusion in the solid phase). Thus, mass transport phenomena in the electrolyte have been neglected in the basic SPM.

During the operation of the cell, the SPM assumes that the electrolyte concentration c_e remains constant at its equilibrium initial value $c_{e,0}$ throughout the cell thickness. Neglecting local concentration gradients in the solution phase, together with ignoring its mass transport phenomena, implies that the current in the electrolyte does not vary over space and time. Hence, in the conventional SPM there is no contribution of the solution phase to internal overpotentials *i.e.*, electrolyte dynamics have no influence on the cell's terminal voltage. The SPM also ignores any variations in material porosities in each electrode. Furthermore, all solid phase diffusivities and kinetic parameters are held constant. Finally, all thermal effects are assumed to be negligible and no degradation effects are attempted to be modelled in the basic SPM formulation.

These simplifying assumptions are made so as to facilitate the ease of implementing a PBM, without incurring the heavy computational cost that typically accompanies it. The impact of these assumptions on the accuracy of the model shall be examined in section 5.3.3

and later sections presents prior research that strives to straddle the fine balance between model sophistication and computational complexity.

5.1.3 Governing Equations

As discussed in section 5.1.2, the SPM captures the cell's dynamics arising due to diffusion and kinetics at the two representative spherical electrodes. It also accounts for the contribution of their equilibrium thermodynamics to the cell's Open Circuit Potential (OCP).

Solid Phase Diffusion

Conservation of Li^0 in the electrodes can be obtained by assuming that the movement of neutral atoms within the solid phase is primarily due to diffusion within particles. This diffusion phenomena is induced due to a concentration gradient that exists between the surface and interior/core of the solid phase particles. Based on the geometrical assumptions of the SPM as discussed in section 5.1.1 *i.e.*, owing to the lack of spatial discretisation in the axial direction x , the concentrations of Li^0 in the two electrodes $c_{s_j}(x, r, t)$, reduce to a function of the radial co-ordinate r and time t , and is denoted by $c_{s_j}(r, t)$, $j \in \{\text{neg, pos}\}$. To keep the notation tractable, this explicit spatio-temporal radial dependence is omitted, further simplifying the representation to c_{s_j} . We start with the derivation of the solid-phase diffusion equation eq. (1.3) in table 1.1, and then proceed to the simplifications of its boundary conditions facilitated by the SPM assumptions.

Diffusion in the solid phase can be modelled by applying classical Fickian dynamics [68] given by

$$\frac{\partial c_{s_j}}{\partial t} = \nabla \cdot (D_{s_j} \nabla c_{s_j}) \quad j \in \{\text{neg, pos}\} \quad (5.1)$$

The divergence of a vector field $\mathbf{F}(r, \theta, \phi)$ can be expressed in spherical co-ordinates as

$$\nabla \cdot \mathbf{F} = \frac{1}{r^2} \frac{\partial (r^2 F_r)}{\partial r} + \frac{1}{r \sin \theta} \frac{\partial (\sin \theta F_\theta)}{\partial \theta} + \frac{1}{r \sin \theta} \frac{\partial F_\phi}{\partial \phi} \quad (5.2)$$

where r denotes the radius, θ the polar angle, and ϕ the azimuthal angle. F_r , F_θ and F_ϕ denote the corresponding components of the vector field \mathbf{F} .

The co-ordinate origin at each electrode is aligned with the centre of its representative spherical particle. Due to symmetry in the polar and azimuthal axes, the divergence becomes

a function of only the radial position. Equation (5.2) therefore reduces to

$$\nabla \cdot \mathbf{F} = \frac{1}{r^2} \frac{\partial (r^2 F_r)}{\partial r} \quad (5.3)$$

Applying the Right-Hand Side (RHS) of the divergence operator of eq. (5.3) in eq. (5.1) yields

$$\frac{\partial c_{s_j}}{\partial t} = \frac{1}{r^2} \frac{\partial}{\partial r} \left(r^2 D_{s_j} \nabla c_{s_j} \right) \quad (5.4)$$

As per the assumption of uniform diffusivity in the solid phase, eq. (5.4) becomes

$$\frac{\partial c_{s_j}}{\partial t} = \frac{D_{s_j}}{r^2} \frac{\partial}{\partial r} \left(r^2 \nabla c_{s_j} \right) \quad (5.5)$$

Applying the gradient operator of eq. (5.5) along the radial direction r ,

$$\frac{\partial c_{s_j}}{\partial t} = \frac{D_{s_j}}{r^2} \frac{\partial}{\partial r} \left(r^2 \frac{\partial c_{s_j}}{\partial r} \right). \quad (5.6)$$

Equation (5.6) represents a mass-balance equation describing solid phase diffusion in each electrode and is identical to the governing equation eq. (1.3) from table 1.1. The potential at each electrode depends on the solid phase surface concentration c_{s,surf_j} *i.e.*, the Li^0 concentration $c_{s_j}(r, t)$ evaluated at $r = R_{p_j}$, $j \in \{\text{neg}, \text{pos}\}$ where R_{p_j} represents the equivalent radius of each representative spherical particle.

Due to spherical symmetry, flux at the centre of the particle is considered to be zero.

$$\left. \frac{\partial c_{s_j}}{\partial r} \right|_{r=0} = 0 \quad (5.7)$$

Diffusion in the solid phase is driven by concentration gradients induced due to intercalation flux density at the particle surface *i.e.*, the surface of each particle experiences a pore-wall flux density driven by reaction kinetics. Based on the SPM geometry discussed in section 5.1.1, the spatial dependence of this molar flux density $j_{n_j}(x, t)$ is eliminated and it can therefore be represented as $j_{n_j}(t)$, $j \in \{\text{neg}, \text{pos}\}$. For the sake of brevity, its explicit temporal dependence is also omitted resulting in a simplified notation j_{n_j} . Hence, at the particle surface

$$D_{s_j} \left. \frac{\partial c_{s_j}}{\partial r} \right|_{r=R_{p_j}} = -j_{n_j} \quad (5.8)$$

The sign convention chosen here is such that pore-wall flux leaving the particle surface is considered to be negative.

Charge conservation in solid phase is applied to evaluate the RHS in eq. (5.8), a detailed derivation of which is presented in Domenico *et al.* [96]. In summary, by assuming a uniform charge density throughout the thickness of each electrode (see section 5.1.2), we get

$$j_{n_j}(t) = \pm \frac{I(t)}{A l_j a_{s_j} F} \quad j \in (\text{neg}, \text{pos}) \quad (5.9)$$

Substituting eq. (5.9) in eq. (5.8)

$$D_{s_j} \left. \frac{\partial c_{s_j}}{\partial r} \right|_{r=R_{p_j}} = \mp \frac{I}{A l_j a_{s_j} F} \quad j \in (\text{neg}, \text{pos}) \quad (5.10)$$

wherein the load current $I(t) > 0$ for discharge, whose explicit time-dependence has been omitted in eq. (5.10) for being consistent notation with the Left-Hand Side (LHS). The positive and negative signs apply to the negative and positive electrode respectively as indicated by the ordered pair $j \in (\text{neg}, \text{pos})$. It should be noted that the term involving the Faraday constant in the RHS of eq. (5.9) is nF , where n is the number of electrons transferred during the reaction. However, since this thesis only discusses lithium-ion chemistries where $n = 1$, this is implicitly conveyed and shall be omitted for all potential occurrences.

The cell's State of Charge (SOC) can be obtained from the bulk concentration of lithium in either the negative or positive electrode. By convention, the negative electrode is used.

$$z(t) = \frac{3}{c_{s,\text{max}_{\text{neg}}}} \int_0^{R_{p_{\text{neg}}}} r^2 c_{s_{\text{neg}}}(r, t) dr \quad (5.11)$$

Given an initial cell SOC $z(0) = z_0$ at rest, the equilibrium concentration of Li^0 in the two individual electrodes can be computed as

$$c_{s_j}(r, 0) = c_{s,\text{max}_j} \left[z_0 \left(\theta_{100\%_j} - \theta_{0\%_j} \right) + \theta_{0\%_j} \right] \quad (5.12)$$

where $\theta_{100\%_j}$ and $\theta_{0\%_j}$ are the electrode stoichiometries at 100 % SOC and 0 % SOC respectively.

Equation (5.6), its corresponding boundary conditions (5.7) and (5.10) along with initial condition (5.12), provide the complete description of time-domain evolution of lithium in the conventional SPM for a given applied current profile $I(t)$. Considerations for efficient numerical simulation of this system is presented next.

Further Reduction in Dimensionality

A naive approach to numerically solving the solid phase diffusion equation is to discretise each of the two representative particles in the radial direction r . Given the elaborate simplifications made to remove spatial resolution from the axial direction, the efficacy of using a radial discretisation is rendered questionable, particularly within the scope of embedding the model in an online simulation and state-estimation environment. Since diffusion in each spherical particle is modelled by the well-known Fickian dynamics [68], several attempts have been made to obtain an approximate analytical solution for the solid phase concentration in both electrodes. In a dimensionless analysis study, Zhang and White [191] provide a comparative evaluation of the various approximation methods for solid phase diffusion, a summary of which is presented in table 5.1.

Table 5.1 Summary of approximation methods for solid phase diffusion

Approximation Method	Introduced by
Duhamel's superposition	Doyle, Fuller & Newman [15, 16]
Diffusion length	Wang <i>et al.</i> [192]
Corrected Diffusion length	Wang and Srinivasan [193]
Polynomial approximation	Subramanian <i>et al.</i> [78, 98]
Pseudo steady-state	Liu [81]

In the aforementioned study, the computational burden *i.e.*, storage requirements and Central Processing Unit (CPU) times of Duhamel's superposition method was found to be excessively high to warrant further interest in it. The original diffusion length method proposed by Wang *et al.* is valid only after the diffusion layer builds up to its steady state, and hence leads to significant errors in transient conditions. Although Wang and Srinivasan introduced an empirical correction factor to the diffusion length to extend its validity to short-time scale operations, this affected the convergence of the method for steady state conditions. The pseudo steady state solution proposed by Liu uses a finite integral transform technique to eliminate the radial dependence of solid phase concentration. However, this method uses

computations involving infinite summations, exponential and trigonometric quantities, which in this thesis author's view, makes it less attractive for online implementations.

The literature on polynomial methods by Subramanian *et al.* [78] provide detailed derivations of the 2nd and 4th order polynomial approximations. The 2nd order solution was found to have poor performance for transient behaviour, similar to that of the original diffusion length method. However, higher order polynomial approximations were found to provide acceptable levels of performance for both transient and steady state conditions and shall therefore be examined further.

The polynomial approximation method describes the dynamic evolution of the volume averaged concentration

$$c_{s,avg_j}(t) = \frac{1}{\Omega} \int_{\Omega} c_{s_j}(r, t) d\Omega \quad (5.13)$$

as a function of the applied load current $I(t)$. Here, Ω represents the volume of the spherical particle. For notational brevity, $c_{s,avg_j}(t)$ is shortened to \bar{c}_{s_j} whilst also dropping its explicit time dependence.

The 4th order polynomial approximation assumes that the solid phase concentration $c_{s_j}(r, t)$ is a quartic function of the radial co-ordinate r .

$$c_{s_j}(r, t) = a(t) + b(t) \left(\frac{r}{R_{p_j}} \right)^2 + d(t) \left(\frac{r}{R_{p_j}} \right)^4 \quad (5.14)$$

The detailed derivation of the coefficients $a(t)$, $b(t)$ and $c(t)$ is provided in Subramanian *et al.* [78]. Eqs. (5.15)–(5.17) summarise the governing equations obtained by applying the 4th order polynomial approximation of eq. (5.14) to the system of equations given by eqs. (5.6), (5.7) and (5.10).

$$\frac{d}{dt} \bar{c}_{s_j} + 3 \frac{j_{n_j}}{R_{p_j}} = 0 \quad (5.15)$$

$$\frac{d}{dt} \bar{q}_j + 30 \frac{D_{s_j}}{R_{p_j}^2} \bar{q}_j + \frac{45}{2} \frac{j_{n_j}}{R_{p_j}^2} = 0 \quad (5.16)$$

$$35 \frac{D_{s_j}}{R_{p_j}} (c_{s, surf_j} - \bar{c}_{s_j}) - 8D_{s_j} \bar{q}_j = -j_{n_j} \quad (5.17)$$

where $\bar{q}_j(t)$ represents the volume averaged concentration flux, that defines the average change of concentration with respect to the radial position r .

As per eq. (5.9), the interfacial flux density is proportional to the applied current. Hence eq. (5.15) implies a simple linear relationship between the applied current and the rate of evolution of average Li^0 concentration within each spherical particle. This further implies that the SOC of the cell has a linear rate-dependence on the externally applied current. Furthermore, due to the elimination of radial discretisation, the computation of SOC, given by eq. (5.11), reduces to the task of first computing the ratio of bulk (average) concentration to surface concentration and then adjusting it to account for the useable stoichiometry limits for the relevant electrode. Thus, the cell's SOC can be computed as

$$z = \frac{\frac{\bar{c}_{s,\text{neg}}}{c_{s,\text{maxneg}}} - \theta_{0\%\text{neg}}}{\theta_{100\%\text{neg}} - \theta_{0\%\text{neg}}} \quad (5.18)$$

where $\bar{c}_{s,\text{neg}}$ is obtained by solving eq. (5.15) for the negative electrode.

In the views of this author, this 4th order polynomial approximation proposed by Subramanian *et al.* [78] strikes an acceptable balance between the three modelling pivots – i) computational complexity, ii) mathematical tractability, and iii) numerical accuracy and has therefore been adopted for all SPM simulations presented in this work.

At the end of this dimension-reduction step, spatial dependence is completely eliminated, yielding a zero-order (in space) physical model whose dynamics are described by the Differential Algebraic Equation (DAE) system of eqs. (5.15)–(5.17).

Equilibrium Thermodynamics

The equilibrium potential of a porous electrode is a thermodynamic property that depends on the extent of lithiation in the outermost interstitial sites near the Solid-Electrolyte Interphase (SEI) layer. This surface stoichiometry θ_j for an electrode is obtained by computing the surface concentration (using eq. (5.17)) and dividing by the maximum lithiation capacity of that electrode.

$$\theta_j = \frac{c_{s,\text{surf}_j}}{c_{s,\text{max}_j}} \quad (5.19)$$

Although based upon the theoretical foundation laid out by the Nernst equation, owing to a multitude of complex phase transitions, the potential of porous electrodes (with respect to metallic lithium) is usually given as empirical functions of its surface stoichiometry [4, 8].

$$U_j(t) = \mathcal{U}_j(\theta_j(t)) \quad (5.20)$$

where the empirical relationships \mathcal{U}_j are typically high order polynomials or rational functions that are fitted to relaxation data from Galvanostatic Intermittent Titration Technique (GITT) experiments on half-cells [14, 194].

In the SPM, the cell's OCP is obtained by subtracting the negative electrode equilibrium potential U_{neg} from its positive electrode counterpart U_{pos} , as shown in eq. (5.21).

$$U_{\text{ocp}} = U_{\text{pos}} - U_{\text{neg}} \quad (5.21)$$

Even though the concept of OCP is defined only in equilibrium conditions when no current flows, the individual electrode potentials themselves form a significant component of the cell's terminal voltage $V(t)$.

Reaction Kinetics

In the SPM, the reaction kinetics in each spherical electrode is modelled using the Butler-Volmer expression (see eq. (1.7)).

$$j_{n_j} = j_{0_j} \left[\exp\left(\frac{(1-\alpha)F\eta_j}{RT}\right) - \exp\left(\frac{-\alpha F\eta_j}{RT}\right) \right] \quad (5.22)$$

where

$$j_{0_j} = k_{r_j} c_e^{1-\alpha} c_{s,\text{surf}_j}^\alpha (c_{s,\text{max}_j} - c_{s,\text{surf}_j})^{1-\alpha} \quad (5.23)$$

The equilibrium rate of forward and backward reactions at both electrodes is assumed to be equal. With charge transfer coefficient $\alpha = 0.5$, eq. (5.22) simplifies to

$$j_{n_j} = 2k_{r_j} \sqrt{c_e c_{s,\text{surf}_j} (c_{s,\text{max}_j} - c_{s,\text{surf}_j})} \sinh\left(\frac{F\eta_j}{2RT}\right) \quad (5.24)$$

The expression for overpotential η_j for the basic SPM can be obtained by rearranging eq. (5.24), substituting for j_{n_j} from by eq. (5.9) whilst using the initial electrolyte concentration $c_{e,0}$ and is given by

$$\eta_j(t) = \frac{2RT}{F} \sinh^{-1} \left(\frac{\pm I(t)}{2A l_j a_{s_j} F k_{r_j} \sqrt{c_{e,0} c_{s,\text{surf}_j} (c_{s,\text{max}_j} - c_{s,\text{surf}_j})}} \right) \quad (5.25)$$

Cell Terminal Voltage

The terminal voltage of the cell under applied load is obtained by subtracting the potential of the negative electrode from its positive counterpart.

Starting from the definition of the overpotential of each electrode

$$\eta_{\text{pos}} = \phi_{s,\text{pos}} - \cancel{\phi_{e,\text{pos}}}^0 - U_{\text{pos}} \quad (5.26)$$

$$\eta_{\text{neg}} = \phi_{s,\text{neg}} - \cancel{\phi_{e,\text{neg}}}^0 - U_{\text{neg}} \quad (5.27)$$

Within each electrode domain, the contribution of electrolyte potential is neglected (see sections 5.1.1 and 5.1.2 for a brief discussion on the exclusion of electrolyte dynamics).

Subtracting eq. (5.27) from eq. (5.26),

$$\eta_{\text{pos}} - \eta_{\text{neg}} = \underbrace{\phi_{s,\text{pos}} - \phi_{s,\text{neg}}}_{V_{\text{cell}}} - U_{\text{pos}} + U_{\text{neg}} \quad (5.28)$$

whose rearrangement yields

$$V_{\text{cell}} = \eta_{\text{pos}} - \eta_{\text{neg}} + U_{\text{pos}} - U_{\text{neg}} \quad (5.29)$$

In the basic SPM, eq. (5.29) is used to compute the cell's terminal voltage under load. Although their explicit time-dependence notation is omitted in the notation here, it is worth reminding that all quantities in eq. (5.29) are indeed continuous functions of time.

State Space Representation

For control oriented applications, it is imperative to have a classical state space representation that collates all intermediate equations and definitions presented thus far into a single system

of equations that describes the evolution of solid concentration and terminal voltage over time, expressed as a response to the external current input $I(t)$. However, the non-linearities in the equation for terminal voltage *i.e.*, eq. (5.29) imply that it is not possible to represent the SPM in the form of a classical Linear Time-Invariant (LTI) system of eq. (2.1). Instead, the SPM can be summarised by a system of linear state equations together with the single non-linear output equation.

Rearranging eqs. (5.16) and (5.17), the state equation is obtained as

$$\frac{d}{dt} \begin{pmatrix} \bar{q}_{\text{pos}} \\ \bar{q}_{\text{neg}} \\ \bar{c}_{\text{s,pos}} \\ \bar{c}_{\text{s,neg}} \end{pmatrix} = \underbrace{\begin{pmatrix} -30 \frac{D_{\text{s,pos}}}{R_{\text{p, pos}}^2} & 0 & 0 & 0 \\ 0 & -30 \frac{D_{\text{s,neg}}}{R_{\text{p,neg}}^2} & 0 & 0 \\ 0 & 0 & 0 & 0 \\ 0 & 0 & 0 & 0 \end{pmatrix}}_A \begin{pmatrix} \bar{q}_{\text{pos}} \\ \bar{q}_{\text{neg}} \\ \bar{c}_{\text{s,pos}} \\ \bar{c}_{\text{s,neg}} \end{pmatrix} + \underbrace{\begin{pmatrix} \frac{45}{2} \frac{1}{R_{\text{p, pos}}^2 A l_{\text{pos}} a_{\text{s, pos}} F} \\ \frac{45}{2} \frac{-1}{R_{\text{p,neg}}^2 A l_{\text{neg}} a_{\text{s, neg}} F} \\ \frac{3}{R_{\text{p, pos}} A l_{\text{pos}} a_{\text{s, pos}} F} \\ \frac{-3}{R_{\text{p,neg}} A l_{\text{neg}} a_{\text{s, neg}} F} \end{pmatrix}}_B I(t) \quad (5.30)$$

which corresponds to the classical LTI form

$$\dot{\mathbf{x}} = A \mathbf{x} + B \mathbf{u} \quad (5.31)$$

where $\mathbf{x} = [\bar{q}_{\text{pos}} \ \bar{q}_{\text{neg}} \ \bar{c}_{\text{s,pos}} \ \bar{c}_{\text{s,neg}}]^T$, $x \in \mathbb{R}^{4 \times 1}$ is the state vector. The scalar system input $\mathbf{u} \in \mathbb{R}$ is the applied current $I(t)$. The system matrix $A \in \mathbb{R}^{4 \times 4}$ and input matrix $B \in \mathbb{R}^{4 \times 1}$ are also shown in eq. (5.30).

For state estimation and controller design purposes, it is important to keep the number of elements in the state vector as small as possible by eliminating redundant variables. For instance, Di Domenico *et al.* [96] noted that with output voltage as the only measured quantity, the observability of the four-state model of eq. (5.30) is adversely affected. To tackle this issue, a state-reduction approach was proposed by Di Domenico *et al.* [96], which hinges upon the principle of material balance.

The total number of moles of lithium in the system is given by

$$n_{\text{Li}} = \frac{\varepsilon_{\text{s,pos}} l_{\text{pos}} A}{\frac{4}{3} \pi R_{\text{p, pos}}^3} \int_0^{R_{\text{p, pos}}} 4\pi r^2 c_{\text{s, pos}}(r, t) dr + \frac{\varepsilon_{\text{s,neg}} l_{\text{neg}} A}{\frac{4}{3} \pi R_{\text{p, neg}}^3} \int_0^{R_{\text{p, neg}}} 4\pi r^2 c_{\text{s, neg}}(r, t) dr \quad (5.32)$$

Upon considering only the bulk concentration as per the dimensionality reduction procedure outlined in section 5.1.3, eq. (5.32) reduces to

$$n_{\text{Li}} = \frac{\varepsilon_{\text{s,pos}} l_{\text{pos}} A}{\frac{4}{3} \pi R_{\text{p, pos}}^3} \bar{c}_{\text{s,pos}} \int_0^{R_{\text{p, pos}}} 4\pi r^2 dr + \frac{\varepsilon_{\text{s,neg}} l_{\text{neg}} A}{\frac{4}{3} \pi R_{\text{p, neg}}^3} \bar{c}_{\text{s,neg}} \int_0^{R_{\text{p, neg}}} 4\pi r^2 dr \quad (5.33)$$

$$= \varepsilon_{\text{s,pos}} l_{\text{pos}} A \bar{c}_{\text{s,pos}} + \varepsilon_{\text{s,neg}} l_{\text{neg}} A \bar{c}_{\text{s,neg}} \quad (5.34)$$

Assuming no loss of cycleable lithium or other degradation mechanisms, the total number of moles of lithium in the system is conserved *i.e.*, $\frac{dn_{\text{Li}}}{dt} = 0$. Substituting this into eq. (5.33),

$$0 = \frac{d}{dt} \varepsilon_{\text{s,pos}} l_{\text{pos}} A \bar{c}_{\text{s,pos}} + \frac{d}{dt} \varepsilon_{\text{s,neg}} l_{\text{neg}} A \bar{c}_{\text{s,neg}} \quad (5.35)$$

$$\frac{d}{dt} \bar{c}_{\text{s,pos}} = -\frac{d}{dt} \bar{c}_{\text{s,neg}} \quad (5.36)$$

As per eq. (5.36), the time evolution of the bulk concentration of one electrode can be obtained as a function of the other. Furthermore, Di Domenico *et al.* [96] show that the diffusion dynamics of the bulk concentrations can be algebraically related through their stoichiometric factors as

$$\bar{c}_{\text{s,pos}}(t) = c_{\text{s,max,pos}} \left[\frac{\bar{c}_{\text{s,neg}}(t) - \theta_{0\% \text{neg}} c_{\text{s,max,neg}}}{(\theta_{100\% \text{neg}} - \theta_{0\% \text{neg}}) c_{\text{s,max,neg}}} (\theta_{100\% \text{pos}} - \theta_{0\% \text{pos}}) + \theta_{0\% \text{pos}} \right] \quad (5.37)$$

Hence, it is possible to eliminate the bulk concentration of any one of the electrodes from the state-equation to arrive at a three-state description of the model dynamics. In extant lithium-ion chemistries, owing to its proclivity for lithium deposition during charging, the negative electrode is considered to be the limiting electrode (See Arora *et al.* [27]). Hence it is retained in the state vector, thereby leading to the final form of the state dynamics of the

conventional SPM as

$$\frac{d}{dt} \begin{pmatrix} \bar{q}_{\text{pos}} \\ \bar{q}_{\text{neg}} \\ \bar{c}_{\text{s,neg}} \end{pmatrix} = \underbrace{\begin{pmatrix} -30 \frac{D_{\text{s,pos}}}{R_{\text{p, pos}}^2} & 0 & 0 \\ 0 & -30 \frac{D_{\text{s,neg}}}{R_{\text{p,neg}}^2} & 0 \\ 0 & 0 & 0 \end{pmatrix}}_A \begin{pmatrix} \bar{q}_{\text{pos}} \\ \bar{q}_{\text{neg}} \\ \bar{c}_{\text{s,neg}} \end{pmatrix} + \underbrace{\begin{pmatrix} \frac{45}{2} \frac{1}{R_{\text{p, pos}}^2 A l_{\text{pos}} a_{\text{s, pos}} F} \\ \frac{45}{2} \frac{-1}{R_{\text{p,neg}}^2 A l_{\text{neg}} a_{\text{s, neg}} F} \\ \frac{-3}{R_{\text{p,neg}} A l_{\text{neg}} a_{\text{s, neg}} F} \end{pmatrix}}_B I(t) \quad (5.38)$$

The measured variable $y \in \mathbb{R}$ is the cell's terminal voltage $V(t)$ and is expressed as a non-linear scalar function of the state vector and the load current.

$$y = h(\mathbf{x}(t), u(t)) \quad (5.39)$$

The output equation given by eq. (5.39) includes a non-zero direct feedthrough dependency of the voltage on the input current, thereby modelling the resistive component of the cell's impedance. The full expression for output voltage is given by expanding eq. (5.29) as

$$V_{\text{cell}}(t) = \frac{2RT}{F} \sinh^{-1} \left(\frac{-I(t)}{2Al_{\text{pos}}a_{\text{s, pos}}Fk_{\text{r, pos}} \sqrt{c_{\text{e,0}}c_{\text{s, surf, pos}}(t) (c_{\text{s, max, pos}} - c_{\text{s, surf, pos}}(t))}} \right) - \frac{2RT}{F} \sinh^{-1} \left(\frac{I(t)}{2Al_{\text{neg}}a_{\text{s, neg}}Fk_{\text{r, neg}} \sqrt{c_{\text{e,0}}c_{\text{s, surf, neg}}(t) (c_{\text{s, max, neg}} - c_{\text{s, surf, neg}}(t))}} \right) + \mathcal{U}_{\text{pos}}(c_{\text{s, surf, pos}}(t)) - \mathcal{U}_{\text{neg}}(c_{\text{s, surf, neg}}(t)) \quad (5.40)$$

wherein the solid phase surface concentration at each electrode $c_{\text{s, surf}_j}$ is obtained from its corresponding bulk concentration $c_{\text{s, avg}_j}$ by rearranging eq. (5.17) and is given by

$$c_{\text{s, surf, pos}} = \bar{c}_{\text{s, pos}} + \frac{8R_{\text{p, pos}}}{35} \bar{q}_{\text{pos}} + \frac{R_{\text{p, pos}}}{35D_{\text{s, pos}}Al_{\text{pos}}a_{\text{s, pos}}F} I(t) \quad (5.41)$$

$$c_{\text{s, surf, neg}} = \bar{c}_{\text{s, neg}} + \frac{8R_{\text{p, neg}}}{35} \bar{q}_{\text{neg}} - \frac{R_{\text{p, neg}}}{35D_{\text{s, neg}}Al_{\text{neg}}a_{\text{s, neg}}F} I(t) \quad (5.42)$$

where $I(t) > 0$ for discharge.

Given the initial SOC of the cell $z(0)$, the initial bulk concentration of the negative electrode at equilibrium $c_{s,\text{neg}}(0)$ is obtained by eq. (5.12). The initial value of the mean radial concentration flux in both electrodes is zero *i.e.*, $q_j(0) = 0$. Therefore, the initial state vector is $[0 \ 0 \ c_{s,\text{neg}}(0)]^T$. Thus, the system of equations given by eqs. (5.37)–(5.42) form a complete state-space representation of the conventional SPM. This state-space model can be simulated as a standalone Initial Value Problem (IVP) or embedded as the plant model in control-oriented applications such as for dynamic state estimation.

5.2 Numerical Implementation

The equations presented in section 5.1 are well-known, self-sufficient and fully descriptive so as to implement the basic SPM. Although discrete-time numerical implementation of circuit-oriented cell models has been considered [11, 195–197], there has been no such treatment of this critical aspect in the SPM modelling literature. Since this thesis has a strong focus towards enabling the use of PBMs in an embedded environment, at least the numerical aspects of implementing these equations need to be discussed. The finer details and practical engineering considerations of real-time programming, in particular the integration of the cell model into the pack, interaction with upstream components and other such aspects of a typical vehicular drivetrain controller, are beyond the scope of this academic work. Nevertheless, the discussion here aims to lower the barrier to real-time implementation and is a unique contribution in the implementation context of cell models.

5.2.1 Continuous-time Implementation

Analytical solution

Although not explicitly given in SPM literature, using LTI system theory, the analytical solution for continuous-time state equation (eq. (2.1)) with current input* is given by

$$\mathbf{x}(t) = e^{A(t-t_0)}\mathbf{x}(t_0) + \int_{t_0}^t e^{A(t-\tau)}B\mathbf{u}(\tau) d\tau \quad (5.43)$$

*The analytical closed form solution cannot be obtained for constant voltage operation. This is because the boundary flux is implicitly determined by the non-linear Butler-Volmer equation eq. (1.7) and needs to be solved numerically with some variant of a Newton-type iteration scheme.

With a standard IVP, $t_0 = 0$

$$\mathbf{x}(t) = e^{At}\mathbf{x}(0) + \underbrace{\int_0^t e^{A(t-\tau)}\mathbf{B}\mathbf{u}(\tau) d\tau}_{\text{convolution integral}} \quad (5.44)$$

The matrix exponential e^{At} is known as the state-transition matrix and is defined as

$$e^{At} \triangleq \mathcal{L}^{-1}\{(sI - A)^{-1}\} \quad (5.45)$$

although several methods exist for its efficient numeric computation [198].

The analytical solution given by eq. (5.44) can be applied to obtain the matrix-vector state equation eq. (5.38) of the SPM. Once the state variables are obtained at a given time-step, after evaluating the surface concentrations as per eq. (5.41) and eq. (5.42), they may be substituted into the output equation of eq. (5.40) to obtain the cell's terminal voltage for that time-step.

Numerical considerations for continuous time implementation

The procedure described thus far has a practical limitation. The input current $I(t)$ to the cell has been defined as a continuous quantity. Although for the purpose of characterising the cell's behaviour, it is possible to use pre-determined continuous-functions as load profiles (e.g. sinusoidal waveforms for virtual Electrochemical Impedance Spectroscopy (EIS) testing), it is desirable to evaluate the model's response to typical real-life conditions. In a vehicular application, only *samples* of cell current measured by sensors at discrete-time intervals are reported to the Battery Management System (BMS). A Zero Order Hold (ZOH) operation is used at the model's input *i.e.*, the level of current is assumed to be held constant between two successive measurements.

It is tedious to hand-compute the convolution integral of eq. (5.44). However, state of the art adaptive-time solvers employing numerical schemes such as Dormand-Prince, Runge-Kutta, Collocation and Backward Differentiation Formula are available to efficiently handle such Ordinary Differential Equations (ODEs). Since lithium concentrations vary smoothly over time without abrupt discontinuities, a standard non-stiff solver of moderate order shall suffice. An example line of code using MATLAB's ode45 solver for this time integration is

```
[~, x_new] = ode45(@(t,x) stateEqn(x,Ik,spm_params), t_span, x_old);
```

Since the direction of applied current is susceptible to sudden reversals, (*e.g.* due to acceleration and braking events in a vehicular application), the solver needs to be stopped and re-started every sample period. Algorithm 5.1 shows the sequence of operations for a desktop simulation of the continuous time SPM on a digital computer. The source code listing of an example implementation in MATLAB is provided in listing A.1.

In the author's view, the continuous time SPM algorithm has limited practical use. Computing the convolution integral or deploying ODE solver codes onto a microcontroller is challenging and introduces substantial computational burden. Although the continuous time model can be used for desktop simulation, more sophisticated PBMs are already available for this task. Therefore, for online deployment in state estimation and control tasks, a discrete-time version of the model suitable for real-time implementation is needed.

5.2.2 Conceptual Overview of Real-Time Processing

The equations in section 5.1.3 are derived in continuous time form. In particular, the state equation given by eq. (5.38) describes the continuous time dynamic evolution of quantities such as the bulk concentration and rate of mean radial flux. However, a typical embedded controller such as that used in a vehicular BMS operates in discrete-time [3]. This implies that *samples* of voltage, current and temperature measurements are obtained at a periodic time interval T_s . The updating of solution variables are performed between two successive data acquisition events from the sensors.

Execution of control-oriented reduced-order PBMs such as the SPM and their associated computations are modular sub-tasks of a vehicular BMS. A single BMS often provides a whole host of other auxiliary functionality such as cell balancing, protection, diagnostics and data-logging [13]. Although thermal management tasks are typically delegated to dedicated controllers, the BMS software routines often handle data exchanged between various subsystems on the vehicular communication bus. While some of these tasks such as book-keeping and diagnostics can be performed at a low execution-rate, others such as cell measurements and model-related computations need to be performed with high priority.

Figure 5.2 shows an example of a plausible implementation of a BMS software in an embedded microcontroller. The vast array of functionality performed by the BMS can be

Algorithm 5.1 Continuous-time SPM

Require: Load profile ▷ e.g. a csv file of t vs. C-rate
Require: SPM parameter set ▷ e.g. stored in a struct `params`
User data: $z[1]$, $t_{f,user}$, $t_{f,condition}$, cell capacity I_{IC} , sample rate T_s ▷ $t_{f,condition} \in \{\max, \min\}$
Ensure: $z[1]$, $V_{cell}[1]$ within limits ▷ index $[k = 1] \triangleq$ time ($t = 0$)

- 1: **procedure** SIMULATESPM
- 2: $t_{f,desired} = \begin{cases} \max(t_{f,user}, t_{f,profile}), & \text{if } t_{f,condition} == \max; \\ \min(t_{f,user}, t_{f,profile}), & \text{otherwise.} \end{cases}$ ▷ may terminate early due to cut-off violations
Note: Flexible end time. Extrapolate last C-rate from profile until $t_{f,desired}$ if necessary.
- 3: $N_{max} \leftarrow \left\lceil \frac{t_{f,desired}}{T_s} \right\rceil + 1$ ▷ max iterations assuming no cut-offs
- 4: Allocate storage of size $\mathbb{R}^{N_{max} \times 1}$ for each simulation variable
- 5: Compute $\bar{c}_{s,neg}[1]$ as per eq. (5.12)
- 6: $I[1] \leftarrow I_{IC} \times \text{C-rate}[1]$, $\mathbf{x}[1] \leftarrow [0 \ 0 \ \bar{c}_{s,neg}[1]]^T$ ▷ C-rate[1] from profile
- 7: $V_{cell}[1] \leftarrow \text{COMPUTECELLVOLTAGE}(\mathbf{x}[1], I[1], \text{params})$ ▷ from direct feedthrough
- 8: **for** $k \leftarrow 2 : N_{max}$ **do**
- 9: $I[k] \leftarrow$ interpolate from profile using ZOH
- 10: Solve continuous-time equation eq. (5.38) ▷ solver IC set to $x[k - 1]$
- 11: $\mathbf{x}[k] \leftarrow$ last time-entry vector of soln. matrix ▷ from an adaptive solver e.g. MATLAB's `ode45`
- 12: Compute $z[k]$ as per eq. (5.18)
- 13: $V_{cell} \leftarrow \text{COMPUTECELLVOLTAGE}(\mathbf{x}[k], I[k], \text{param})$
- 14: **if** $z[k]$ or $V_{cell}[k]$ exceeded cut-off limits **then**
- 15: $k \leftarrow k - 1$ ▷ data from last step is invalid
- 16: $break;$
- 17: **end if**
- 18: **end for**
- 19: **end procedure**
- 20: **subroutine** COMPUTECELLVOLTAGE(\mathbf{x} , I , `params`)
- 21: Compute $c_{s,surf,neg}$ as per eq. (5.42) ▷ consider saturating i.e., $c_{s,min,neg} \leq c_{s,surf,neg} \leq c_{s,max,neg}$
- 22: Compute $\bar{c}_{s,pos}$ as per eq. (5.37)
- 23: Compute $c_{s,surf,pos}$ as per eq. (5.41)
- 24: Compute V_{cell} as per eq. (5.40)
- 25: **return** V_{cell} ▷ resume suspended line in SIMULATESPM

grouped and managed as two separate processes — i) a background thread, and ii) a foreground thread. The background thread runs continuously within the main loop sequentially processing instructions. Figure 5.2a shows an example illustration of typical background tasks that a BMS handles. All high-priority tasks are triggered by an interrupt and the supervisory

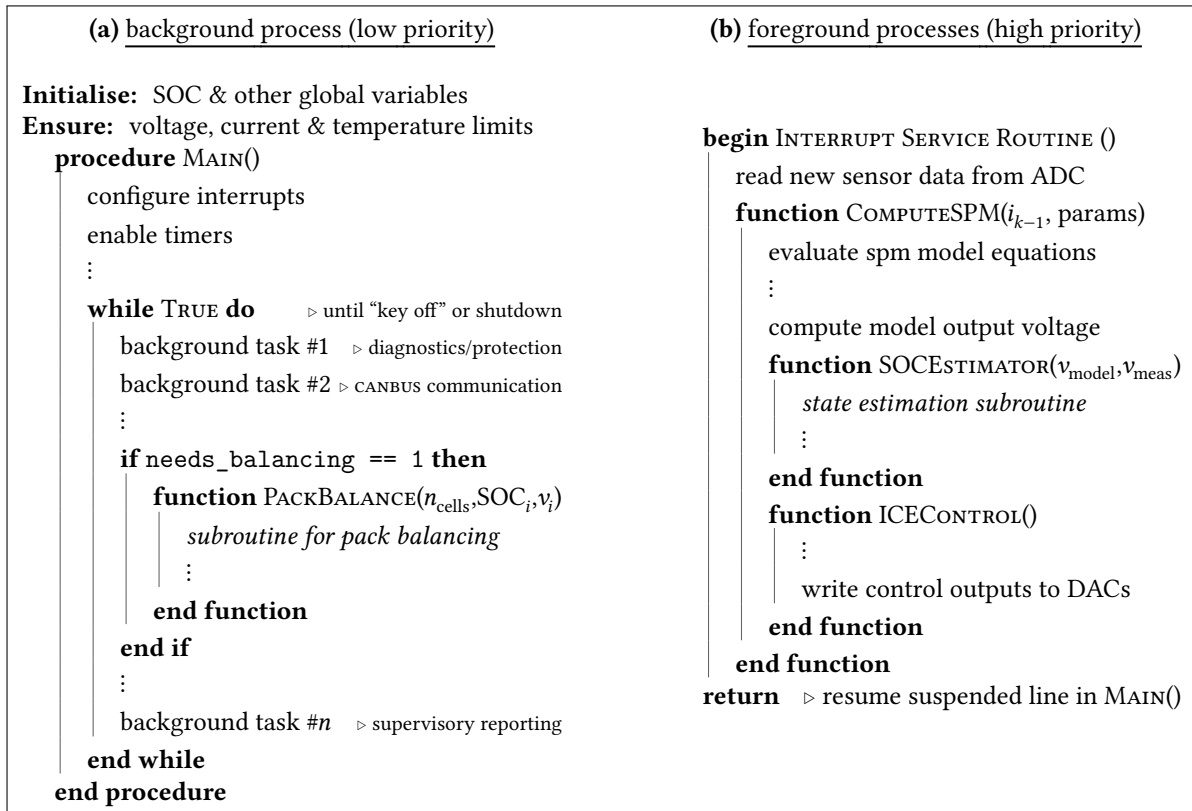


Figure 5.2 Overview of the real-time software implementation of a typical BMS. Through an interrupt-driven architecture for time-critical tasks as state estimation and control, the same processor can be efficiently utilised by employing its idle CPU cycles for background tasks such as diagnostics, fault logging and book-keeping.

control loop suspends the presently executing background task for later resumption. As shown in fig. 5.2b, a typical example of such an interrupt driven process is the evaluation of the SPM model equations and computation of control outputs and is discussed next.

Figure 5.3 depicts an exploded view of the timing aspects of the INTERRUPT SERVICE ROUTINE that was briefly presented in fig. 5.2b. Upon the expiry of an on-chip timer calibrated against a baseline precision-clock, hardware interrupts are raised by one or more Analog to Digital Converters (ADCs) associated with voltage/current sensors mounted on cells. The ISR disables the interrupt and reads the samples of data from the ADCs into software. At the end of this process, the ISR rearms the interrupts and simultaneously sends and acknowledgement to the appropriate sensor which reloads its timer. The SPM model equations are then evaluated in software and the resulting computational variables such as voltage and concentrations are employed in other pertinent tasks such as state estimator subroutines. If the BMS also

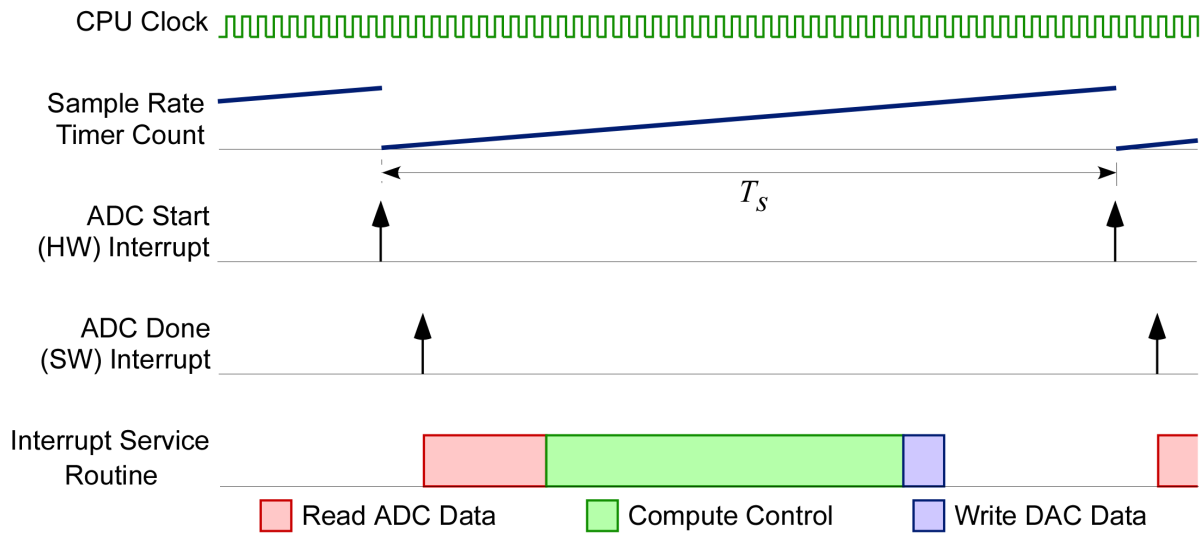


Figure 5.3 Timing diagram of a real-time software loop of a BMS. The sequence of events within one sample period T_s in relation to the base clock of the controller is shown. Particular emphasis is placed on depicting the handling of Interrupt Service Routine (ISR) requests pertinent to cell models. Other background tasks performed by the CPU are de-emphasised. Moreover, the integration of the BMS software loop within the larger scope of a master vehicular controller is not shown. Illustration adapted from Southward [199].

performs control tasks *e.g.* regulating the coolant’s flow rate or Internal Combustion Engine (ICE) state-toggling such as in the hysteresis control of a series hybrid drivetrain, these control outputs are written to the relevant Digital to Analog Converters (DACs).

5.2.3 Sample Delay Considerations

Figure 5.4 shows a vertically compressed view of all CPU activities across a larger time horizon. The CPU’s load factor is the ratio of time spent in foreground requests to its idling time. While a high load factor is beneficial in terms of efficient usage of resources, it adversely affects the power efficiency of the chip.

For Li-ion cell modelling, a sampling interval of $T_s = 1\text{ s}$ is commonly used, thus aiming to capture the cell dynamics below 500 mHz [†]. The CPU’s clock used is of several MHz, a vast majority of which is spent in background tasks or in sleep mode. Furthermore, a low-latency ISR code is employed in the tasks of reading the ADC value, evaluating the model equations and writing any control outputs to the DAC. Using a simplified PBM such as the SPM helps in achieving a low-latency throughput for the ISR.

[†]In the ideal case, according to the Nyquist sampling theorem. In practice, the frequency range is smaller.

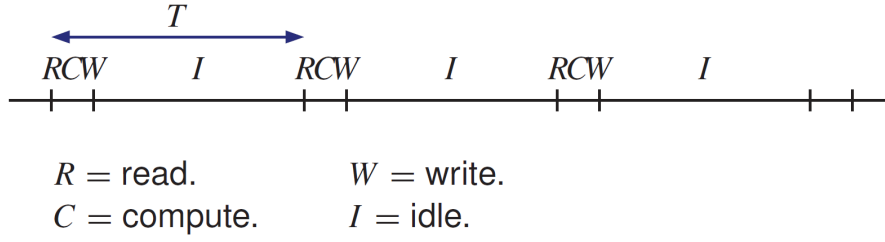


Figure 5.4 A compressed timeline of CPU execution cycles showing details of activities within each sample interval. The execution sequence is shown over a larger horizon so as to illustrate the proportion of ‘activity time’ relative to the ‘idle time’. The vast majority of the CPU cycle is spent in idling or background tasks. The servicing of the ISR occupies a relatively small fraction of each CPU cycle. Diagram reproduced from Plett [200].

The overall implication of such a scheme is that any *delays* owing to the sample and hold process at the model input and outputs can be neglected. In conventional sampled-data systems, control delays may be analysed by considering a multiplicative factor of $e^{-s\lambda}$ in the Laplace domain transfer function of the system. Delay parameters of $\lambda = 0.5T_s$ or $\lambda = 1T_s$ are commonly employed as conservative estimates. However, owing to the small CPU load factors, in this thesis this delay term is omitted for discrete-time formulation of the SPM.

5.2.4 Discrete-Time SPM Formulation

Due to the sampling and ZOH operations at the ADC input to the system, the input to the SPM is transformed from a simple continuous time signal to discrete-time sequences *i.e.*, $u(t) \mapsto u[k]$ and $y(t) \mapsto y[k]$, where $k = 0, 1, \dots, \infty$ is the sample index corresponding to the continuous time instant $t_k = kT_s$. The continuous time plant model represented by the ODE system of eq. (5.38) is therefore replaced by a discrete-time process and modelled by a *difference* equation which is to be determined.

Consider the general continuous-time solution given by eq. (5.43). Let $t_0 = kT_s$ and $t = (k + 1)T_s$, where $k = 0, 1, \dots, \infty$. Therefore,

$$x(t_0) = x(kT_s) \quad \equiv x[k] \quad (5.46)$$

$$x(t) = x((k + 1)T_s) \equiv x[k + 1] \quad (5.47)$$

Substituting these relationships into eq. (5.43) yields

$$\mathbf{x}[k + 1] = e^{AT_s} \mathbf{x}[k] + \int_{kT_s}^{(k+1)T_s} e^{A((k+1)T_s - \tau)} \mathbf{B} \mathbf{u}(\tau) d\tau. \quad (5.48)$$

With the ZOH scheme discussed here, $u(\tau)$ remains constant from kT_s to $(k+1)T_s$, and is equal to $u(kT_s)$ *i.e.*, $u[k]$. Consider a change-of-variable definition for the dummy variable of integration τ as $\eta = (k+1)T_s - \tau$. Thus, $\tau = (k+1)T_s - \eta$. Hence, $d\tau = -d\eta$. Substituting these into eq. (5.48),

$$\mathbf{x}[k+1] = e^{AT_s}\mathbf{x}[k] + \left[\int_{T_s}^0 e^{A\eta} B \right] u[k] - d\eta \quad (5.49)$$

Reversing the order of integration leads to

$$\mathbf{x}[k+1] = e^{AT_s}\mathbf{x}[k] + \left[\int_0^{T_s} e^{A\eta} B d\eta \right] u[k] \quad (5.50)$$

Equation (5.50) represents a discrete-time state-space representation of the dynamics of the system whose generic representation is given by the difference equation

$$\mathbf{x}[k+1] = A_d \mathbf{x}[k] + B_d u[k] \quad (5.51)$$

where $A_d = e^{AT_s}$ and $B_d = \int_0^{T_s} e^{A\eta} B d\eta$. If the continuous-time system matrix A is invertible, a closed form expression for B_d is obtained as

$$B_d = A^{-1}(A_d - I_n)B \quad (\text{if } A^{-1} \text{ exists}) \quad (5.52)$$

For the continuous time system matrix A of the SPM, its determinant is zero.

$$\begin{vmatrix} -30 \frac{D_{s,\text{pos}}}{R_{p,\text{pos}}^2} & 0 & 0 \\ 0 & -30 \frac{D_{s,\text{neg}}}{R_{p,\text{neg}}^2} & 0 \\ 0 & 0 & 0 \end{vmatrix} = 0 \quad (5.53)$$

and hence is not invertible. This necessitates an explicit evaluation of the integral in eq. (5.50) for computation of the discrete-time input matrix B_d .

Since the only non-zero entries of the matrix lie along its main diagonal *i.e.*, its modes are decoupled, the matrix exponential reduces to a diagonal matrix whose elements are simply the scalar exponentials of the original entries. The discrete-time input matrix B_d can be obtained

by evaluating eq. (5.55).

$$A_d = e^{AT_s} = \exp \left(\begin{bmatrix} -30 \frac{D_{s,pos}}{R_{p,pos}^2} & 0 & 0 \\ 0 & -30 \frac{D_{s,neg}}{R_{p,neg}^2} & 0 \\ 0 & 0 & 0 \end{bmatrix} T_s \right) = \begin{bmatrix} e^{-30 \frac{D_{s,pos}}{R_{p,pos}^2} T_s} & 0 & 0 \\ 0 & e^{-30 \frac{D_{s,neg}}{R_{p,neg}^2} T_s} & 0 \\ 0 & 0 & 1 \end{bmatrix} \quad (5.54)$$

$$B_d = \int_0^{T_s} e^{A\eta} B d\eta = \int_0^{T_s} \left(\begin{bmatrix} e^{-30 \frac{D_{s,pos}}{R_{p,pos}^2} \eta} & 0 & 0 \\ 0 & e^{-30 \frac{D_{s,neg}}{R_{p,neg}^2} \eta} & 0 \\ 0 & 0 & 1 \end{bmatrix} \cdot \begin{bmatrix} \frac{45}{2} \frac{1}{R_{p,pos}^2 A l_{pos} a_{s,pos} F} \\ \frac{45}{2} \frac{-1}{R_{p,neg}^2 A l_{neg} a_{s,neg} F} \\ \frac{-3}{R_{p,neg} A l_{neg} a_{s,neg} F} \end{bmatrix} \right) d\eta \quad (5.55)$$

$$B_d = \begin{bmatrix} \frac{1 - \exp\left(-30 \frac{D_{s,pos}}{R_{p,pos}^2} T_s\right)}{\frac{3}{4} \frac{D_{s,pos} A l_{pos} a_{s,pos} F}{R_{p,pos}^2}} \\ \frac{1 - \exp\left(-30 \frac{D_{s,neg}}{R_{p,neg}^2} T_s\right)}{-\frac{3}{4} \frac{D_{s,neg} A l_{neg} a_{s,neg} F}{R_{p,neg}^2}} \\ \frac{-3 T_s}{R_{p,neg} A l_{neg} a_{s,neg} F} \end{bmatrix} \quad (5.56)$$

The discrete-time matrix-vector system presented in eq. (5.54) and eq. (5.56) have not been presented in existing literature, but is vital to understanding the implementation of the SPM in digital controllers. Although, simpler alternatives such as Forward Euler methods are available to approximate the time-derivative of the state vector, they suffer from problems such as a growth in the rate of local truncation error per time-step [201], necessitating the use of very high sample rates, which increases the burden on the embedded controller. The matrix exponential approach is superior in terms of accuracy and stability across a wide range of sample rates.

For a pre-determined sample-rate, the matrix exponential and hence the A_d and B_d matrices can be computed offline on a desktop and stored into the non-volatile memory of the embedded controller to be loaded onto RAM during operation. The vectorised implementation of the state dynamics presented here is highly efficient and directly amenable for use in classical state-vector algorithms. For the cell's terminal voltage computation, the basic structure and form of the output equation given by eq. (5.39) remains intact, except that the

continuous time variables $(\mathbf{x}(t), u(t))$ need to be replaced by their discrete-time counterparts in the corresponding equation set *i.e.*, eqs. (5.40)–(5.42). The discrete-time output function h_d is evaluated *after* updating the state vector (through eq. (5.51)).

$$y[k + 1] = h_d(\mathbf{x}[k + 1], u[k + 1]) \quad (5.57)$$

The complete sequence of steps for implementing the discrete-time variant of the SPM is given in algorithm 5.2. In particular, it can be seen that the discrete-time system and input matrices, A_d and B_d can be easily pre-computed from the parameter set using the matrix exponential approach. In MATLAB, this can be achieved by passing the arguments of the matrix exponential to the ‘expm’ command. The vectorised implementation of the discrete-time state equation given in line 11 of algorithm 5.2 is a set of efficient linear algebra operations consisting of simple matrix-vector product and vector-addition routines.

This thesis strives for an inclusive approach by taking into account that some battery researchers whose focus is on fundamental aspects of lithium ion cells *e.g.* those specialising in electrochemistry, might not be familiar with the nuances of the matrix exponential and discrete-time matrix computations (in line 7 of algorithm 5.2). Therefore, a snippet of MATLAB code clarifying the computation of the discrete-time system and input matrices, A_d and B_d is given in code snippet 5.1. A full code listing of an example discrete-time SPM implementation in MATLAB is provided in listing A.2.

Thus, a discrete-time model of the basic SPM is now available for implementation in an embedded BMS. Further analysis of discrete-time issues such as aliasing, quantisation noise, signal pre-conditioning and discrete Fourier analysis lies in the specialised engineering domain of signal processing and falls outside the scope of the thesis. The results of the basic SPM are presented next in section 5.3.

5.3 Desktop Simulation

In this section, the performance of the basic SPM is discussed through desktop simulation and by comparison against a standard Doyle-Fuller-Newman (DFN) benchmark model incorporating the full Pseudo Two-Dimensional (P2D) dynamics.

Algorithm 5.2 Discrete-time SPM

Require: Load profile ▷ e.g. a csv file of t vs. C-rate

Require: SPM parameter set ▷ e.g. stored in a struct `params`

User data: $z[1]$, $t_{f,user}$, $t_{f,condition}$, cell capacity I_{IC} , sample rate T_s ▷ $t_{f,condition} \in \{\max, \min\}$

Ensure: $z[1]$, $V_{cell}[1]$ within limits ▷ index $[k = 1] \triangleq$ time ($t = 0$)

- 1: **procedure** SIMULATESPM
- 2: $t_{f,desired} = \begin{cases} \max(t_{f,user}, t_{f,profile}), & \text{if } t_{f,condition} == \max; \\ \min(t_{f,user}, t_{f,profile}), & \text{otherwise.} \end{cases}$ ▷ may terminate early due to cut-off violations
Note: Flexible end time. Extrapolate last C-rate from profile until $t_{f,desired}$ if necessary.
- 3: $N_{max} \leftarrow \left\lceil \frac{t_{f,desired}}{T_s} \right\rceil + 1$ ▷ max iterations assuming no cut-offs
- 4: Allocate storage of size $\mathbb{R}^{N_{max} \times 1}$ for each simulation variable
- 5: Compute $\bar{c}_{s,neg}[1]$ as per eq. (5.12)
- 6: $I[1] \leftarrow I_{IC} \times \text{C-rate}[1]$, $\mathbf{x}[1] \leftarrow [0 \ 0 \ \bar{c}_{s,neg}[1]]^T$ ▷ C-rate[1] from profile
- 7: Compute A_d and B_d ▷ as per eq. (5.54) and eq. (5.56)
- 8: $V_{cell}[1] \leftarrow \text{COMPUTECELLVOLTAGE}(\mathbf{x}[1], I[1], \text{params})$ ▷ from direct feedthrough
- 9: **for** $k \leftarrow 2 : N_{max}$ **do**
- 10: $I[k] \leftarrow$ interpolate from profile using ZOH
- 11: $x[k] \leftarrow A_d x[k-1] + B_d u[k-1]$ ▷ eq. (5.51)
- 12: Compute $z[k]$ as per eq. (5.18)
- 13: $V_{cell} \leftarrow \text{COMPUTECELLVOLTAGE}(\mathbf{x}[k], I[k], \text{param})$
- 14: **if** $z[k]$ or $V_{cell}[k]$ exceeded cut-off limits **then**
- 15: $k \leftarrow k - 1$ ▷ data from last step is invalid
- 16: $break;$
- 17: **end if**
- 18: **end for**
- 19: **end procedure**
- 20: **subroutine** COMPUTECELLVOLTAGE($\mathbf{x}, I, \text{params}$) ▷ uses discrete-time variants of eqs *i.e.*, at index k
- 21: Compute $c_{s,surf,neg}$ as per eq. (5.42) ▷ consider saturating *i.e.*, $c_{s,min,neg} \leq c_{s,surf,neg} \leq c_{s,max,neg}$
- 22: Compute $\bar{c}_{s,pos}$ as per eq. (5.37)
- 23: Compute $c_{s,surf,pos}$ as per eq. (5.41)
- 24: Compute V_{cell} as per eq. (5.40)
- 25: **return** V_{cell} ▷ resume suspended line in SIMULATESPM

```

% Returns A_d and B_d matrices
A_cts = [-30*Ds_pos/(R_pos^2), 0, 0; ...
         0, -30*Ds_neg/(R_neg^2), 0; ...
         0, 0, 0];

% A_d = e^{AT_s} (see eq. (5.54))
A_disc = expm(A_cts*Ts); % expm command computes the matrix exponential

B_cts = [ (45/2)/(R_pos^2*a_pos*L_pos*F*A); ...
         (-45/2)/(R_neg^2*a_neg*L_neg*F*A); ...
         (-3/(R_neg*a_neg*L_neg*F*A))];

% B_d = \int_0^{T_s} e^{A\eta} B d\eta (see eqs. (5.55)–(5.56))
B_disc = nan(size(B_cts));
B_disc(1) = B_cts(1)*(exp(A_cts(1,1)*Ts)-1)/A_cts(1,1);
B_disc(2) = B_cts(2)*(exp(A_cts(2,2)*Ts)-1)/A_cts(2,2);
B_disc(3) = B_cts(3)*Ts;

```

Code snippet 5.1 Computation of discrete-time matrices A_d and B_d in MATLAB

5.3.1 Cell Parametrisation[‡]

Table 5.2 lists the simulation parameters of an Lithium Cobalt Oxide (LCO) cell whose positive and negative electrodes are LiCoO_2 and LiC_6 respectively. The electrolyte in this system consists of LiPF_6 salt in a solution of Ethylene Carbonate (EC)/Dimethyl Carbonate (DMC)/Ethyl Methyl Carbonate (EMC) in a 1:1:1 ratio. The standard set of DFN parameters have been extensively described and documented in literature. The detailed characterisation of the physical properties of lithium-ion cells falls outside the scope of this thesis. Here, the vast majority of electrochemical parameters *viz.* the geometric, thermodynamic, kinetic and transport properties of the cell have been sourced from Subramanian *et al.* [137]. The significance of each of the parameters in the context of the modelling assumptions discussed in section 5.1.2 is examined.

The simulation parameters that are applicable exclusively to the P2D model are shown as highlighted text in table 5.2. It can be seen that only a subset of the isothermal DFN model's parameters are required for the SPM. In particular, there is no requirement to estimate any of the electrolyte-related parameters in each electrode region. Furthermore, the properties

[‡]Some contents in this section overlap with section 3.4.1 and represents a joint effort with Ian D. Campbell.

5.3 Desktop Simulation

Table 5.2 Parameters for isothermal simulation of the P2D and SPM implementations of an LCO cell (with LiCoO_2 - LiC_6 electrode pair and LiPF_6 electrolyte). Highlighted entries represent parameters exclusive to P2D model. $j \in \{\text{pos, sep, neg}\}$.

System Conditions		Other Constants	
Lower cutoff cell voltage, V_{\min} (V)	^a 2.50	Faraday constant, F (C m^{-1})	96487
Upper cutoff cell voltage, V_{\max} (V)	^b 4.30	Universal gas constant, R ($\text{J mol}^{-1} \text{K}^{-1}$)	8.314
Cell-level Parameters			
Cell temperature, T_{cell} (K)			^c 298.15
<i>Init.</i> electrolyte conc., $c_{e,0}$ (mol m^{-3})			^c 1000
Overall active surface area, A (m^2)			ⁱ 2.053
Thermodynamic, Kinetic, Geometric and Transport Parameters			
Parameter	Pos	Sep	Neg
Bruggeman coefficient, brugg_j	^c 4	^c 4	^c 4
Intrinsic electrolyte diffusivity, D ($\text{m}^2 \text{s}^{-1}$)	^d 3.22×10^{-10}	^d 3.22×10^{-10}	^d 3.22×10^{-10}
Intrinsic electrolyte conductivity, κ (S m^{-1})	— see table note <i>e</i> & section 5.3.2 —		
Li^+ transference number, t_+	^c 0.363	^c 0.363	^c 0.363
Intrinsic electronic conductivity, σ_j (S m^{-1})	^c 100.00	—	^c 100.00
Thickness, l_j (m)	^c 72×10^{-6}	^c 25×10^{-6}	^f 88×10^{-6}
Electrolyte volume fraction, ε_j	^c 0.385	^c 0.724	^c 0.485
Filler vol. fraction, ε_{fj}	^c 0.025	—	^c 0.033
Particle radius, R_{pj} (m)	^c 2×10^{-6}	—	^c 2×10^{-6}
Specific interfacial surface area, a_{sj} ($\text{m}^2 \text{m}^{-3}$)	^g 885×10^3	—	^g 723.6×10^3
Electrode diffusivity, D_{sj} ($\text{m}^2 \text{s}^{-1}$)	^c 1×10^{-14}	—	^c 3.9×10^{-14}
Stoichiometry, 0% SOC, $\theta_{\min,j}$	^h 0.9917	—	^h 0.0143
Stoichiometry, 100% SOC, $\theta_{\max,j}$	^c 0.4955	—	^c 0.8551
Max concentration, $c_{\text{s,max},j}$ (mol m^{-3})	^c 51 554	—	^c 30 555
Reaction rate coefficient, $k_{\text{r},j}$ ($\text{m}^{2.5} \text{mol}^{-0.5} \text{s}^{-1}$)	^c 2.33×10^{-11}	—	^c 5.03×10^{-11}
Open circuit potential, U_j (V)	^k see table note	—	^m see table note
Spatial Discretisation			
Parameter	Pos	Sep	Neg
Nodes, through-thickness (axial), $N_{\text{a},j}$	15	15	15
Nodes, within spherical particle (radial), $N_{\text{r},j}$	10	—	10

^a Ref. [74] ^b Set to ≈ 100 mV above the cell's OCP at 100 % cell SOC ^c Ref. [137] ^d Computed at $T_{\text{cell}} = 298.15$ K using coefficients from table II in Ref. [202]

^e Computed at $T_{\text{cell}} = 298.15$ K using coefficients from table III in Ref. [202] at $c_{e,0} = 1000$ mol m^{-3}

^f Set up for capacity balance of electrodes such that $l_{\text{neg}} = 1.22 \times l_{\text{pos}}$ here (see section 3.5.6) ^g Computed as per eq. (5.61)

^h Obtained as residual stoichiometries after a C/500 simulated discharge from 100 % cell SOC to 2.7V

ⁱ Chosen so that current density for the electrochemical layer is 29.23 A m^{-2} for 60 A applied current (see section 3.4.1)

$$^k \mathcal{U}(\theta_{\text{pos}}) = \frac{-4.656 + 88.669\theta_{\text{pos}}^2 - 401.119\theta_{\text{pos}}^4 + 342.909\theta_{\text{pos}}^6 - 462.471\theta_{\text{pos}}^8 + 433.434\theta_{\text{pos}}^{10}}{-1 + 18.933\theta_{\text{pos}}^2 - 79.532\theta_{\text{pos}}^4 + 37.311\theta_{\text{pos}}^6 - 73.083\theta_{\text{pos}}^8 + 95.96\theta_{\text{pos}}^{10}} \quad (5.58)$$

$$^m \mathcal{U}(\theta_{\text{neg}}) = 0.7222 + 0.1387\theta_{\text{neg}} + 0.029\theta_{\text{neg}}^{0.5} - \frac{0.0172}{\theta_{\text{neg}}} + \frac{0.0019}{\theta_{\text{neg}}^{1.5}} + 0.2808e^{(0.9-15\theta_{\text{neg}})} - 0.7984e^{(0.4465\theta_{\text{neg}}-0.4108)} \quad (5.59)$$

of the separator material which are necessary in the DFN model are also not considered in the SPM computations. A brief enumeration of the additional P2D-specific parameters in the context of parametrisation requirements is provided here.

- a. brugg_j ($\times 3$)** The empirical Bruggeman coefficient helps to define the effective values of conductivity and diffusivity of the electrolyte. Although an identical value (4) is used in table 5.2, in principle all three regions can have different values of brugg and need to be parametrised separately.
- b. D ($\times 1$)** The intrinsic electrolyte diffusivity of a typical electrolyte consisting of LiPF_6 salt in an organic solvent was experimentally characterised and provided as a table of polynomial coefficients by Valøen and Reimers [202]. Evaluating this polynomial at a cell temperature of 298.15 K results in an intrinsic diffusivity of $3.22 \times 10^{-10} \text{ m}^2 \text{ s}^{-1}$. Since this is a material property independent of the region within the cell, it needs to be parametrised only once.
- c. κ ($\times 1$)** Like the diffusivity, the intrinsic electrolyte conductivity is also a material property and its value is independent of the region within the cell. Unlike the diffusivity, the electrolyte conductivity is a strong function of its ionic concentration. Thus, the polynomial proposed by Valøen and Reimers [202] needs to be evaluated at $T_{\text{cell}} = 298.15 \text{ K}$ and has to be updated during the simulation as salt concentration within the electrolyte changes over time. A discussion on the choice of initial concentration is provided in section 5.3.2.
- d. t_+^0 ($\times 1$)** The cationic transference number measures the relative mobility of the Li^+ ion in the organic solvent and is independent of the region within the cell. Hence, this intrinsic property is to be parametrised only once (per solvent).
- e. σ_j ($\times 2$)** The intrinsic conductivity of the solid phase depends on the material used in the porous electrodes. Although a simplified assumption of equal conductivity is used for the two electrodes, in practice, this property needs to be characterised for each of the two electrodes.

Neglecting Arrhenius-type temperature dependence of physical properties and their corresponding activation energies, the basic SPM facilitates the ability to afford physics-based modelling capabilities with *eight* fewer parameters than the equivalent isothermal P2D model. With the naive assumption of equal parametrisation effort per physical property, this implies a **20 %** reduction in parametrisation requirements for the basic SPM when compared to its DFN counterpart. However, considering the fact that parametrising the electrolyte's transport properties requires apparatus and infrastructure typically available only in specialised chemical/materials science labs, the reduction in parametrisation overhead for system-level engineering stakeholders is more pronounced.

Prima facie, it may seem that electrolyte porosities and filler volume fractions do not influence the SPM model. However, they do have an indirect bearing on arriving at a critical parameter *viz.* the solid phase volume fraction ε_{s_j} . This parameter is required to compute the specific interfacial surface area of the electrodes a_{s_j} *i.e.*, the effective electrode area exposed to reaction and is an important entity in the SPM model equations presented in section 5.1.3. The solid phase volume fractions are also required in simulating the P2D model owing to the need for computing the effective electronic conductivities of the electrodes (see eq. (1.6)). They are calculated as

$$\varepsilon_{s_j} = 1 - \varepsilon_j - \varepsilon_{f_j} \quad (5.60)$$

where ε_j and ε_{f_j} are the electrolyte and filler volume-fraction within the respective electrode regions. Using the values from table 5.2 results in $\varepsilon_{s, \text{pos}} = 0.590$ and $\varepsilon_{s, \text{neg}} = 0.482$ for the positive and negative electrodes respectively. The specific interfacial surface areas are then calculated as

$$a_{s_j} = \varepsilon_{s_j} \frac{4\pi R_{p_j}^2}{\frac{4}{3}\pi R_{p_j}^3} = \frac{3\varepsilon_{s_j}}{R_{p_j}} \quad (5.61)$$

As discussed in the assumptions made during model derivation (see section 5.1.2) and consistent with the assumed model geometry, the parameters not covered by the SPM pertain to those describing electrolyte dynamics and distribution of electronic charge along the axial thickness direction of the cell. Properties such as the intrinsic diffusivities and conductivities of the electrolyte as well as the transference number of Li^+ in the organic solvent are thus completely redundant for SPM simulation. The assumption of uniform charge density along the through-thickness length of each electrode implies that the intrinsic

electronic conductivities of the two electrodes do not play any role in the model dynamics. The porosities and Bruggeman coefficients in table 5.2 serve as modifying factors of the intrinsic conductivities and diffusivities (see table 1.1) leading to an effective value within each region of the electrochemical layer. Thus, their relevance is also rendered void for the basic SPM simulation. The thickness of the separator material only plays a role in electrolyte behaviour. By the model geometry presented in section 5.1.1, this parameter also falls outside the scope of the basic SPM.

The thicknesses of the electrodes are optimised for equal loading *i.e.*, to achieve a balance in their individual capacities to store Li atoms. The thickness of the positive electrode is chosen as the value from Subramanian *et al.* [137]. The thickness of the negative electrode region is then computed with the goal of equalising the volume of active material in each electrode for every electrochemical layer in a pouch cell.

$$A_{\text{elec, pos}} \epsilon_{\text{s, pos}} l_{\text{pos}} = A_{\text{elec, neg}} \epsilon_{\text{s, neg}} l_{\text{neg}} \quad (5.62)$$

In a lithium-ion pouch cell, the electrodes are designed such that the layers can be overlaid on top of one another and finally encapsulated in a pouch. Geometrical considerations then imply that the cross-sectional area (or face area) of the two electrodes must be the same. However, due to the consideration of avoiding plating at the edges due to microscopic malformations, the design is done such as to have a small overhang of the negative electrode layer (< 2 mm) with respect to the positive electrode layer [149] (see fig. 3.7). Nevertheless, the active surface area is just the common overlap area between the two electrodes, and hence A_{elec} is equal to the cross-sectional area of the positive electrode.

Thus, eq. (5.62) reduces to $\frac{l_{\text{neg}}}{l_{\text{pos}}} = \frac{\epsilon_{\text{s, pos}}}{\epsilon_{\text{s, neg}}} = 1.22$, yielding $l_{\text{neg}} = 72 \mu\text{m}$.

At first, it may be surprising to note that the values of the particle radius R_p , used in both the P2D and SPM remain identical. However, it is important to note that the P2D equations of the DFN model are cast in a normalised form *i.e.*, already set up to account for the overall capacity of the cell under consideration implicitly through usage of a current density (per unit area) for its simulation. Furthermore, this explains why increasing the number of discretisation nodes does not increase the modelled capacity, but instead merely serves to improve the simulation accuracy owing to the enhanced spatial resolution.

The overall active surface area $A = nA_{\text{elec}}$ is the combined cross-sectional area of all layers (n is the number of electrochemical (pos, sep, neg) triplets) stacked into the pouch cell. In both the P2D and SPM models, this parameter serves to scale the external load current down to the current density experienced by each electrochemical layer. A value of $\approx 30 \text{ A m}^{-2}$ was reported in the results section of Subramanian *et al.* [137]. When considering a 60 Ah pouch cell with 10 mm exterior thickness and using the parameters reported in [137], this results in a cross-sectional area of 2.053 m^2 (see section 3.4.1). Considering the equalisation of capacity loading, with the newly chosen thickness value of the negative electrode, the 1C-rate capacity of the cell has been revised to 29.23 A m^{-2} .

On simulating the P2D model with a trickle bleeding type discharge corresponding to a current of $C/500$ and logging the data every 1 ms, after reaching 2.7 V^{\S} , the remnant concentrations in the two electrodes were noted. The corresponding residual stoichiometry values are reported in table 5.2.

Since only isothermal cell behaviour is considered, table 5.2 omits the activation energies for the various diffusivities and conductivities of materials (see section 5.3.2 for further thermal considerations). For this reason, table 5.2 does not include other material properties such as specific heats, and thermal conductivities. No properties of the current collectors appear in the isothermal model equations for both the P2D and SPM models and hence are omitted. All other electrochemical properties, *viz.* stoichiometries at 100 % SOC, maximum concentrations, diffusivities, reaction rate coefficients and OCP of the two electrodes remain invariant between the P2D and SPM models.

5.3.2 Simulation Setup

For reproducibility of results, it is important to discuss the system-level parameters influencing simulation setup.

The lower cut-off voltage of the cell is chosen to be 2.5 V . This is deliberately kept lower than the voltage corresponding to the cell's 0 % *i.e.*, 2.7 V . If set above 2.7 V even at infinitesimally small discharge currents, the cell would cut-off before achieving complete discharge. Choosing a value lower than 2.7 V means that the cell gets a chance to recover

^{\S}From manufacturer datasheets for LCO chemistries, this value is considered to correspond to 0 % SOC.

its terminal voltage, despite spikes in highly dynamic load currents that might bring the voltage below this threshold momentarily. If a low-enough value is not chosen, a system-level shutdown shall be initiated despite possessing the ability to continue to operate after recovery of terminal voltage. In this case, choosing a cut-off voltage of 2.5 V does not damage the cell since checks are in place to monitor the SOC and trigger cut-off in the event of charge depletion (see algorithms 5.1 and 5.2). Northrop *et al.* [74] use this value, although no specific explanation is given for this choice.

The upper cut-off voltage of the cell is chosen at 4.3 V *i.e.*, ≈ 100 mV higher than the equilibrium OCP at 100 % SOC. There are several reasons for this smaller margin at the upper end of the voltage spectrum.

- safety** li-ion cells are less tolerant to overcharging and can pose fire hazards.
- degradation** overcharging li-ion cells can lead to plating and accelerate other degradation mechanisms.
- low C-rates** charging C-rates are typically lower than discharge C-rates.
- CCCV charging** For on-board chargers, taper charging (such as in a Constant Current Constant Voltage (CCCV) profile) is activated, which ensures that charging current drops off rapidly, leading to a lower overvoltage towards the upper SOC range.
- low probabilities** The only charging event when an electrified vehicle is in motion is during regenerative braking. The vehicular BMS manages the operating window such that the starting SOC is much lower than the overvoltage that could be caused due to braking. Furthermore, during operation, net discharge events occur more frequently than regenerative braking events.

For both the P2D model and the SPM model, the cell temperature is kept constant at its initial value of 25 °C (298.15 K). This might imply to the reader that the operation of the lithium ion cell is assumed to be isothermal. While this is not true in general, for the C-rates considered here ($< 5C$), typical in a Battery Electric Vehicle (BEV) application particularly for the short-duration transient loads studied, it is certainly a valid zeroth order coarse approximation of the cell's thermal condition. Detailed modelling of thermal dynamics is not within the

scope of this thesis, as the primary goal is to obtain a PBM incorporating electrochemical principles amenable for embedded application. Hence, the thermal dependence of parameters through an Arrhenius-type relationship is also not considered. Future work could include performing thermally coupled simulations *i.e.*, incorporating thermally dependent parameters and simplified heat generation expressions *e.g.* a lumped thermal model could be employed for both the SPM and P2D and their performances may be compared.

To understand the parametrisation of initial concentration, the expression for electrolyte conductivity needs to be examined. As discussed in section 5.3.1, the intrinsic conductivity of a specific type of electrolyte is a material property that depends on the local concentration of Li^+ ions and temperature. In the characterisation of the electrolyte by Valøen and Reimers [202], the best fit expression for electrolyte conductivity was obtained as

$$\begin{aligned} \kappa_j(c_e, T, x, t) = & 10^{-4}c_e(x, t)(-10.5 + 0.668 \times 10^{-3}c_e(x, t) + 0.494 \times 10^{-6}c_e(x, t)^2 \\ & + (0.074 - 1.78 \times 10^{-5})c_e(x, t) - 8.86 \times 10^{-10}c_e(x, t)^2)T(t) \\ & + (-6.96 \times 10^{-5} + 2.8 \times 10^{-8}c_e(x, t))T(t)^2 \end{aligned} \quad (5.63)$$

Figure 5.5 shows a surface plot of the electrolyte conductivity as a function of initial concentration $c_{e,0}$ and cell temperature T_{cell} . For the modelling task at hand, relevant aspects

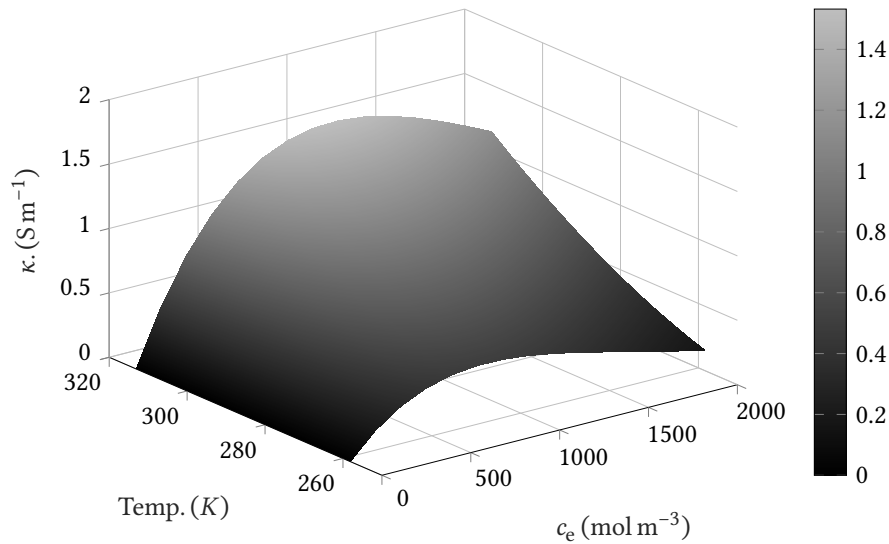


Figure 5.5 Electrolyte conductivity as a function of cell temperature and initial concentration.

of this material property can be better understood through the simplifications afforded by the simulation conditions applicable here. At equilibrium initial condition, c_e is uniform over the axial space x . Secondly, only isothermal cell behaviour is considered *i.e.*, $T(t) = T_{\text{cell}}(0) = T_{\text{cell}}$. Hence, eq. (5.63) reduces to

$$\begin{aligned} \kappa_j = 10^{-4}c_{e,0} & \left(-10.5 + 0.668 \times 10^{-3}c_{e,0} + 0.494 \times 10^{-6}c_{e,0}^2 \right. \\ & \left. + (0.074 - 1.78 \times 10^{-5})c_{e,0} - 8.86 \times 10^{-10}c_{e,0}^2 \right) T_{\text{cell}} \\ & \left. + (-6.96 \times 10^{-5} + 2.8 \times 10^{-8}c_{e,0}) T_{\text{cell}}^2 \right)^2 \quad (5.64) \end{aligned}$$

As inferred from fig. 5.5, the electrolyte conductivity κ is a smooth function of c_e and T_{cell} . Thus eq. (5.64) can be effectively visualised through a parametric plot of κ versus c_e with T_{cell} as the variable parameter as seen in fig. 5.6. From fig. 5.6, it is evident that at $T_{\text{cell}} = 298.15\text{ K}$, the maximum value of electrolyte conductivity is attained at $c_e = 1000\text{ mol m}^{-3}$. It is advantageous to operate the cell around this salt concentration so as to minimise the cell's overall resistance. Hence, the initial concentration $c_{e,0}$ is chosen to be 1000 mol m^{-3} . It should be noted that while the electrolyte concentration in the P2D model exhibits both spatial and temporal variations during the simulation, in the SPM model, it remains constant throughout.

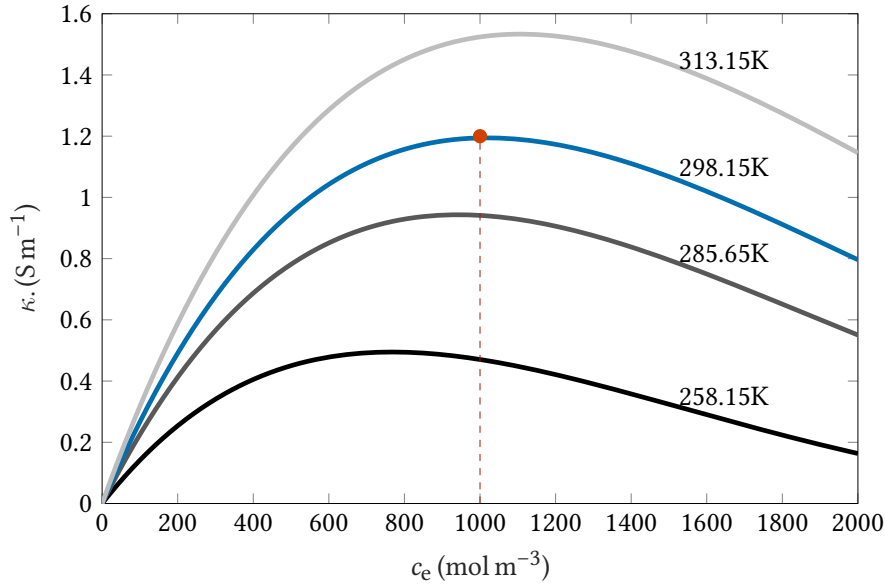


Figure 5.6 Electrolyte conductivity versus equilibrium concentration at various cell temperatures. At $T_{\text{cell}} = 298.15\text{ K}$, the maximum value of electrolyte conductivity corresponds to a salt concentration of 1000 mol m^{-3} .

The reduction in parametrisation requirements discussed in section 5.3.1 is only one of the factors contributing to the simplicity and ease of simulation. As discussed in section 5.1.1, an important computational requirement that is present in the P2D model, but completely eliminated from the SPM is the requirement of discretisation. As reported in table 5.2, with 15 nodes per region along the axial direction and with 10 shells per electrode in the radial direction, the P2D model under simulation achieves mesh independence to a tolerance of $\approx 2\%$ for the range of C-rates considered. For higher C-rates, coupling a thermal model is of higher importance than incorporating further meshing refinements. The discretisation-related parameters are specific to the P2D model and are highlighted accordingly in table 5.2.

Capacity Characterisation

First, it must be established that incorporating the parameters presented in table 5.2 into the SPM model equations results in a cell with *identical* capacity as the DFN model. This is to ensure the validity of comparisons in further simulations. Using the values of per-layer C-rate as discussed in section 5.3.1, and the overall active surface area from table 5.2, the cell under simulation has a capacity of 60 Ah.

Present literature in battery modelling, both for the DFN model and for the SPM, do not discuss any aspect of capacity characterisation. In particular, parameters such as the geometric surface area of cells and even their 1C-rate are often not listed in publications. This practice can be attributed to the fact that all one-dimensional and Pseudo Two-Dimensional models operate on a per-layer basis, using an applied current *density*. Many a time, researchers assume a unit surface area for the cell. This implicit normalisation is amenable to those studies which strive to make numerical comparisons between models through simulation. However, it leads to a lack of clarity on the actual capacity of the cells being modelled. Furthermore, when comparing with experimental data from a real cell, such works resort to ad hoc techniques such as empirical curve-fitting for obtaining the surface area. Often the source of such parametrisation is not made clear. Section 3.4.1 documents the details of obtaining the overall surface area of cells and arriving at the C-rate per layer of the specific cell under consideration. Since the DFN model does not explicitly model the cell capacity, a brief explanation is provided on how a simple *numerical* characterisation can be used for determining cell capacity given a *complete* parameter list.

For experimental capacity characterisation of cells, the standard practice is to apply a very small discharge current beginning at 100 % SOC, logging the charge passed using a high-precision coulomb counter until the cell hits the voltage corresponding to 0 % SOC as specified in the manufacturer's datasheet. In order to decouple the effect of the cell's dynamics from its capacity, it is required to apply an infinitesimal bleeding current (tending towards, but not reaching 0 A).

Current sensors in battery cycler equipment use high-precision (typically 15–18 bit) ADCs and are able to offer high Signal to Noise Ratios (SNRs) except at ultra-low currents. The main difficulty with using very low C-rates is that it drastically slows down the characterisation procedure. Using a discharge current of $C/100$ *i.e.*, 0.6 A in this case, results in a characterisation time of 100 h or $\approx 4^{1/4}$ days (excluding soak-times and other set-up related activities). Furthermore, for accurate coulomb-counting, a high data logging rate is needed, producing large file sizes and corresponding difficulties in post-processing them. Considering moderate buffer-sizes used in data logging modules of typical cell-cycler software (shared between channels), and to avoid excessively large wait-times for characterisation, discharge currents of $C/20$ – $C/25$ are usually deemed sufficient.

In order to validate that the choice of model parameters result in an intended capacity of 60 Ah, an analogous procedure is carried out by means of computer simulation. A characterisation simulation beginning at 100 % SOC with a discharge current of 0.6 A was performed[¶]. If the assumed cell capacity is indeed consistent with the model parameters, then this corresponds to a C-rate of 1/100. Therefore, both the P2D and SPM should run for exactly 100 hours before cut-off due to charge depletion.

Capacity validation through computer simulation is not bound by the limitations of the experimental approach discussed earlier. Using 64-bit IEEE floating point arithmetic, quantities as low as $\mathcal{O}(10^{-16})$ can be safely computed, nullifying any SNR issues. Table 5.3 summarises the key data from this simulation run. For accurate coulomb counting, the data logging interval is set to 50 ms. Both models ran close to 100 hours. The small deviations from this expected termination time can be attributed to the fact that the current is not arbitrarily small with the pragmatic goal of obtaining results in a reasonable time.

[¶]All computations were performed on a 64-bit Hewlett-Packard Z840 workstation with a 16-core Intel® Xeon® E5-2640 v3 (Haswell) processor clocked at 2.60 GHz with 128 GB DDR4 RAM at 1866 MT/sec.

Table 5.3 Simulation data for capacity characterisation of P2D and SPM models. The P2D model is considered as the reference benchmark. The modelling error is defined as $\varepsilon_v = V_{\text{cell}_{\text{p2d}}} - V_{\text{cell}_{\text{spm}}}$

Parameter	Value	Units
Data-logging interval	50.00	ms
Combined CPU time with warm cache	12.22	min
Total RAM used	603.90	MB
P2D run-time	99.94	h
SPM run-time	99.90	h
P2D discharge capacity	59.96	Ah
SPM discharge capacity	59.94	Ah
Worst case error, $\varepsilon_{v_{\text{max}}}$	-94.30	mV
Mean error, μ_{ε_v}	-3.00	mV
RMS error, $\varepsilon_{v_{\text{RMS}}}$	8.20	mV
MAE error, $\varepsilon_{v_{\text{MAE}}}$	3.20	mV
Standard deviation of error, σ_{ε_v}	7.60	mV

As seen in table 5.3, even the *combined* CPU time to simulate both the P2D and SPM models is two orders of magnitude lower than real-time. The only issue that remains to be addressed is that of considerable memory and storage requirements due to high-rate data-logging for accurate coulomb counting. For a standard computer workstation, this places only a minor demand on its CPU. For comparable volume of data to be logged, the reliability and ruggedness of a dedicated workstation far exceeds that of real-time cell cyclers, thereby establishing numerical simulation as an amenable method for characterisation of cell capacity. A major disadvantage of simulation based capacity validation is its extreme sensitivity to parameters such as the maximum concentration of the electrodes and their stoichiometries, which are generally difficult to characterise. In this context, the experimental procedure of high-precision coulomb counting assumes a practical significance as it requires no knowledge of the cell's parameters other than the manufacturer's datasheet.

Figure 5.7 shows the voltage response of the SPM and P2D models, which overlap almost entirely. It is clear that both the P2D and SPM models achieve a run-time of 100 hours. This represents the first visualisation of results produced by the SPM model equations discussed in section 5.1.3 and its numerical implementation from section 5.2.

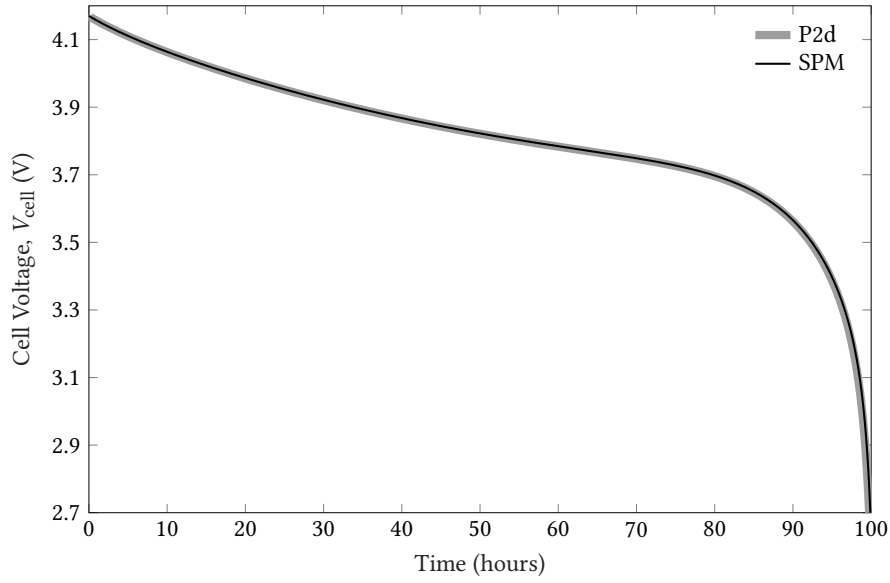


Figure 5.7 Voltage response of P2D and SPM models to a discharge current input of 0.6 A. Both models achieve their charge depletion point after ≈ 100 h confirming that their modelled capacities match. Key simulation data for this characterisation run is shown in table 5.3.

The voltage error is defined as

$$\varepsilon_v = V_{\text{cell}_{\text{p2d}}} - V_{\text{cell}_{\text{spm}}} \quad (5.65)$$

The absolute maximum error is of $\mathcal{O}(100)$ mV, which occurs towards the end of discharge. Although this represents the worst case upper bound on the error, this is not strictly representative of the overall error behaviour as evidenced by the standard deviation of the error vector. The mean and Root Mean Square (RMS) error values indicate an accuracy of $\mathcal{O}(10)$ mV. It should be noted that throughout the simulation, the voltage response of the SPM remains slightly above that of P2D, thereby leading to a negative value for the mean voltage error. For continuous quantities such as time-domain simulation outputs of physical variables, the Mean Absolute Error (MAE) is a suitable error metric and is defined as

$$\varepsilon_{\text{MAE}} = \frac{\sum_{i=1}^n |\varepsilon_i|}{n} \quad (5.66)$$

Here, the numerical value of MAE is consistent with the order of magnitude of the RMS and mean error metrics as well as with the standard deviation of the error vector.

Thus, a common foundation for further simulations has been established by confirming that the two models indeed simulate a cell with a capacity of 60 Ah. With the cell parametrisation discussed, simulation setup presented and capacities validated, the simulation results are fully reproducible and are presented next in section 5.3.3.

5.3.3 Simulation Results

Constant current discharge

The left column of fig. 5.8 shows the time-domain voltage response of the basic SPM for various constant discharge currents. The voltage response of the P2D model is also overlaid on these plots and is used as a reference benchmark for comparisons. It is difficult to use a common time-scale for the horizontal axes of the plots since the run-times differ by two orders of magnitude for the C-rates considered.

Since these comparisons have to be done across multiple C-rates, each yielding different magnitudes in voltage responses, it is helpful to use a relative error metric such as the percentage error, defined as

$$\hat{\epsilon}_v(\%) = 100 \frac{V_{\text{cell}_{\text{p2d}}} - V_{\text{cell}_{\text{spm}}}}{V_{\text{cell}_{\text{p2d}}}} \quad (5.67)$$

It is to be noted that, in all cases, the P2D model terminates faster than the SPM either due to hitting lower cut-offs of either terminal voltage or SOC (see fig. 5.9). Consequently, the error vector is defined only for the common time-region before cut-off.

In fig. 5.8, the column on the right shows the percentage error in the voltage response of the SPM with respect to the P2D model. At very low C-rates below $\approx 0.5C$, the voltage-response performance of the SPM is acceptable. However, the performance degradation is rapid above this C-rate. It is clear that the error in the SPM response is monotonic and unidirectional. This indicates that the source of the error is due to unmodelled dynamics. In particular, as discussed in the modelling assumptions of section 5.1.2, the SPM ignores the electrolyte dynamics. Thus, the overpotential in the electrolyte is not modelled, which results in the terminal voltage of the SPM being always higher than its P2D counterpart.

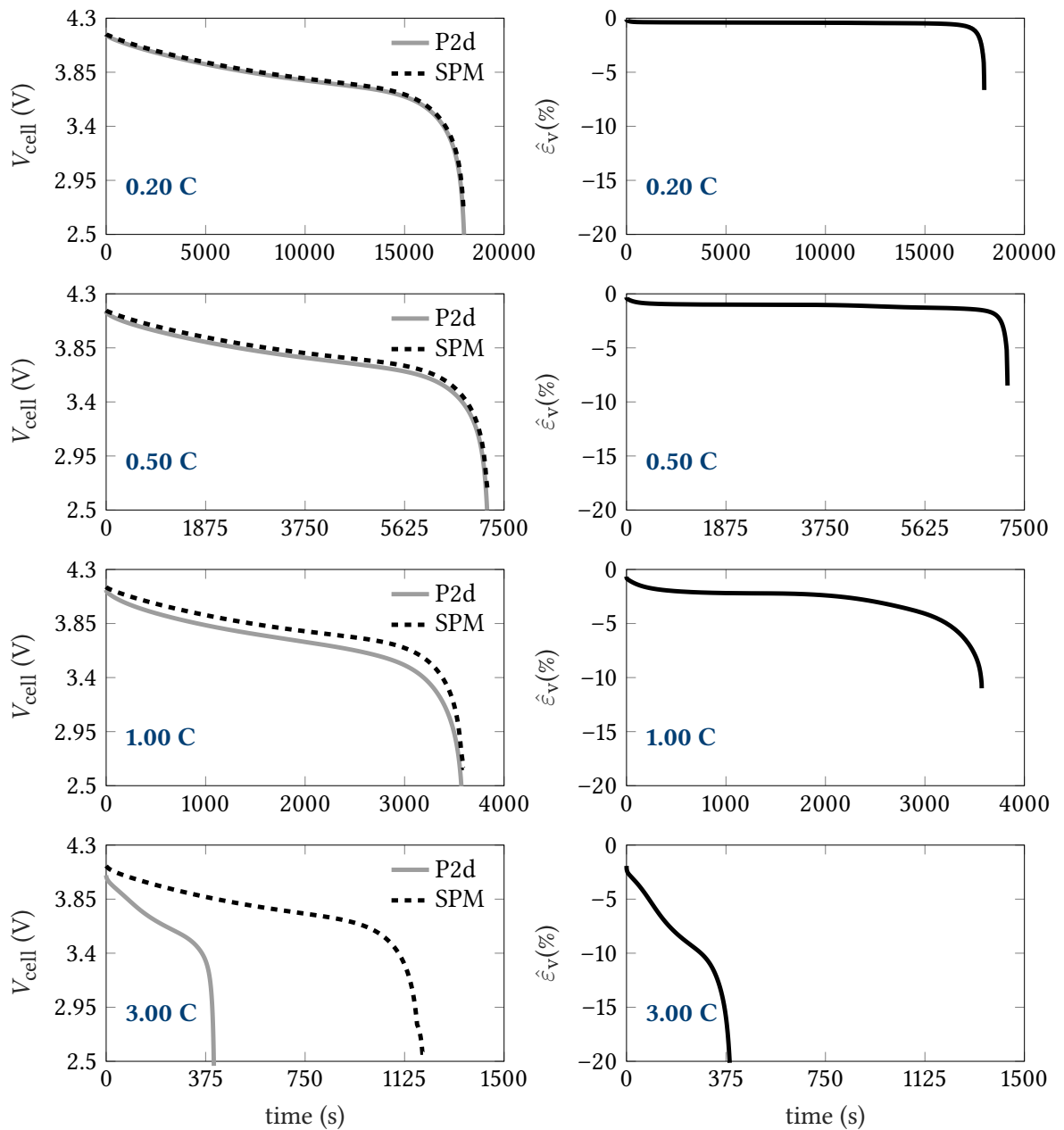


Figure 5.8 Voltage responses of the P2D and SPM models to various constant discharge rates. The left column shows the time-domain voltage response of the SPM plotted against the benchmark P2D response. The column on the right shows the percentage voltage error of the SPM with respect to the P2D model. The performance of the SPM degrades considerably at discharge currents above just 0.5C.

Figure 5.9 shows the time-evolution of SOC computed by the P2D and the SPM models for various discharge currents. Since the SOC of a cell is already a normalised quantity by definition, the difference between the two models can be directly used for comparison across

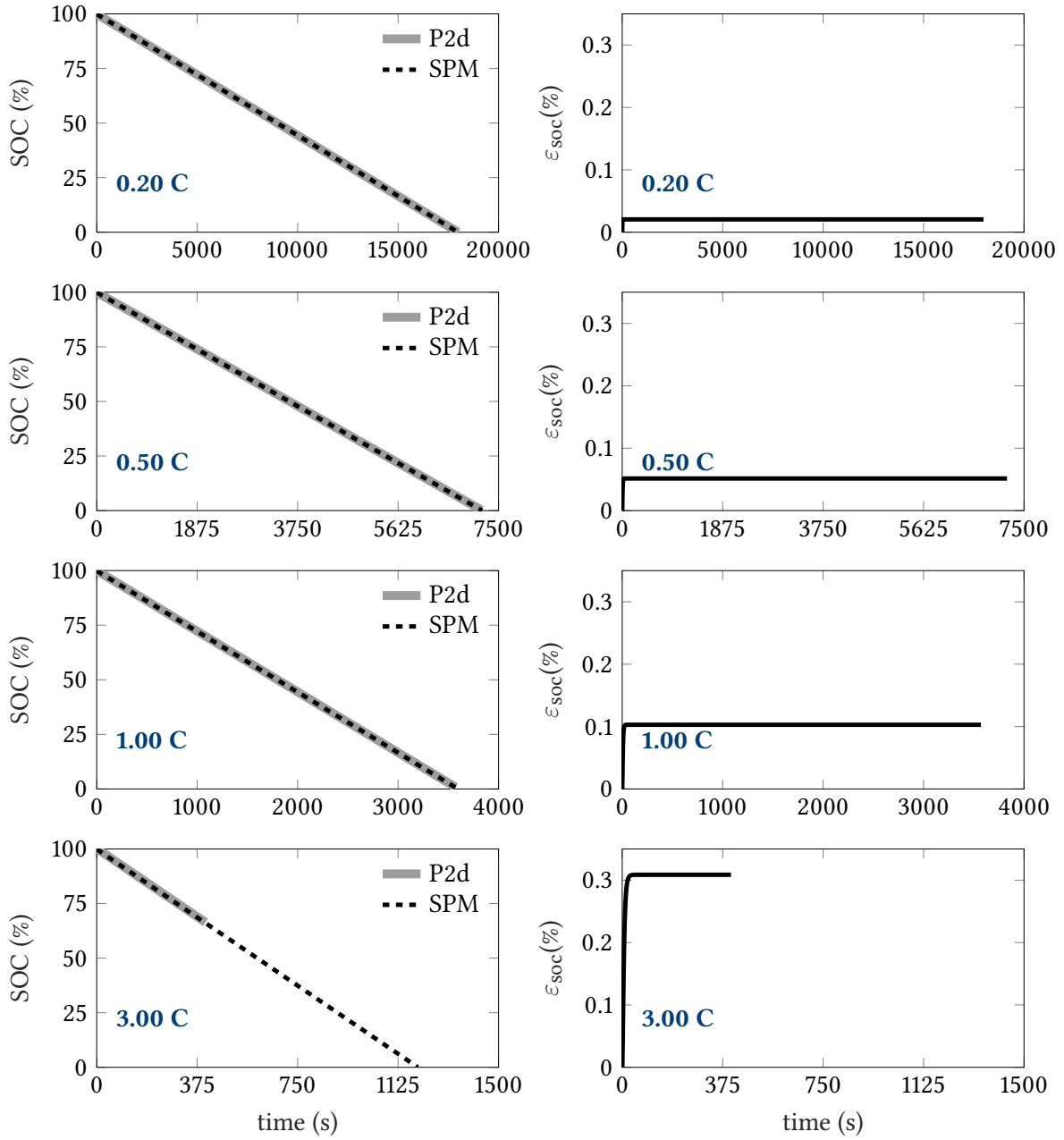


Figure 5.9 Plots in the left column depict the time evolution of SOC computed by the P2D and SPM models for various constant discharge rates. The column on the right shows the error of the SOC computed by the SPM with respect to that computed by the P2D model *i.e.*, $\epsilon_{\text{soc}} = z_{\text{p2d}} - z_{\text{spm}}$. In this case, the basic SPM remains quite accurate even at moderate currents such as 3C.

multiple C-rates. The SOC error is defined as

$$\epsilon_{\text{soc}} = z_{\text{p2d}} - z_{\text{spm}} \quad (5.68)$$

and like the error in the terminal voltage, remains unidirectional over time, and defined only until one of the models hits cut-off. Table 5.4 shows a summary of various error metrics used to quantify the performance of the basic SPM for various discharge rates.

Table 5.4 Summary of error metrics of the basic SPM for terminal voltage and SOC in constant current discharge simulations.

C-rate	$\hat{\epsilon}_v$ (%)		ϵ_{soc} (%)	
	abs. max.	MAE	abs. max.	MAE
0.2	6.64	0.49	0.02	0.02
0.5	8.49	1.17	0.05	0.05
1.0	11.00	2.95	0.10	0.10
3.0	56.53	9.22	0.31	0.30

A quick perusal of table 5.4 reveals a discrepancy that invokes surprise at first glance. Whilst the performance of the SPM is quite poor in terms of terminal voltage prediction, it is worth noting that its SOC prediction capabilities remain quite accurate even at moderate discharge currents of about 3C and therefore, warrants a brief explanation.

Referring to eq. (5.18), it is seen that the SOC of the cell is directly proportional to the bulk (average) concentration in the negative electrode. Hence the plots of fig. 5.9 also represent the solid phase concentration with a constant scaling factor. As per the assumptions listed in section 5.1.2, the only transport phenomena modelled in the SPM is solid phase diffusion. However, for computation of the terminal voltage, the electrolyte overpotential contribution has been omitted (see eqs. (5.26) and (5.27)). This explains why the voltage accuracy suffers, while the open-loop SOC computation remains accurate. The high accuracy of SOC (and hence, solid-phase concentration) computation also validates the usage of the 4th order polynomial approximation in the place of Fick's law for modelling solid-phase diffusion.

However, the discrepancy in accuracies of terminal voltage and SOC computed by the basic SPM leads to an important implication. Even at moderate C-rates, the basic SPM *cannot* be effectively used in the design of SOC observers. This is because, the measured voltage maps to a vastly different operating point when using the SPM as the plant model, leading to strong deviations of the estimated SOC.

Constant current charge

The CCCV charging profile is a widely adopted standard charging strategy for charging lithium ion cells [3]. In the constant current phase, a charging rate of 1C is used as an accepted baseline, although faster charging strategies are presently being actively sought after.

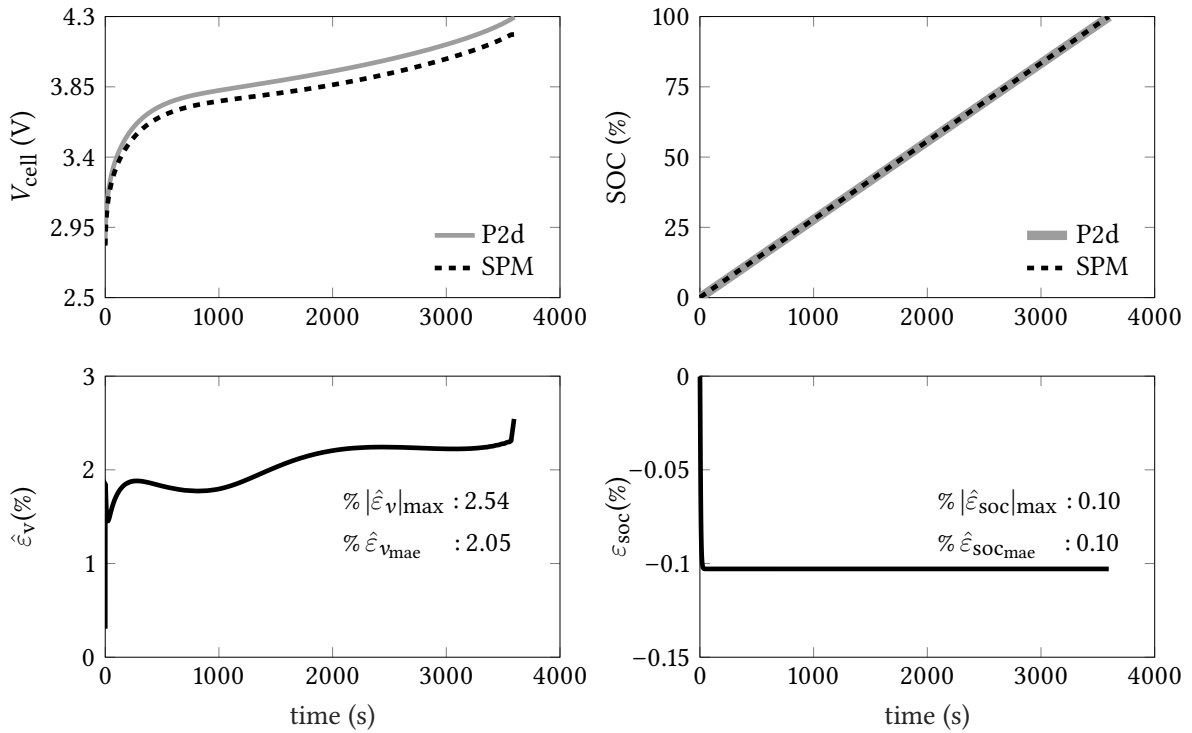


Figure 5.10 Time evolution of voltage and SOC (top row) of the P2D and SPM models upon charging with a constant current of 1C, *i.e.*, 60 A starting at 0 % SOC. The bottom row shows the percentage in terminal voltage and SOC respectively of the SPM with respect to the P2D model.

The top row of fig. 5.10 shows the evolution of terminal voltage and SOC of the P2D and SPM models under an applied charging current of 1C *i.e.*, 60 A. The constant-voltage charging phase is not shown. The bottom row shows the corresponding errors of the SPM model with respect to the reference P2D benchmark. The corollary behaviour of the constant current discharge behaviour is observed here. The terminal voltage of the SPM remains below the P2D model throughout. This is expected since, to account for the electrolyte voltage drop modelled in the P2D dynamics, a higher terminal voltage needs to be applied. The voltage error is thus unidirectional and remains positive (opposite to that observed for the corresponding discharge case). Similarly, the SOC plots overlap very closely, thereby validating the underlying polynomial approximation of solid phase diffusion. It is striking to

note that the error in SOC remains exactly around the same magnitude ($\approx 0.1\%$) in both the charging and discharging cases.

Dynamic input profile

For automotive applications, it is important to characterise the performance of the cell model under dynamic load conditions. Several standard vehicular drivecycles have been defined and adopted by regulatory agencies across the world. These drivecycles describe the profile of the vehicle's speed as a function of time. The profile of speed versus time of drivecycles is typically available in intervals of 1 s, and is therefore consistent with the sample interval used for the simulation (see table 5.2).

The Urban Dynamometer Driving Schedule (UDDS) is one such well-known drivecycle, originally introduced by the United States Environmental Protection Agency that represents city driving conditions which can be applied to a typical mid-sized passenger vehicle. world. Figure 5.11 shows the UDDS drivecycle wherein the vehicle's speed has been converted to SI units for use in further computations. One complete drivecycle runs for 1369 s. As seen in fig. 5.11, the UDDS profile is highly dynamic consisting of many sets of rapid acceleration and braking events. Hence, this drivecycle is chosen to provide representative results of the model's performance to dynamic inputs.

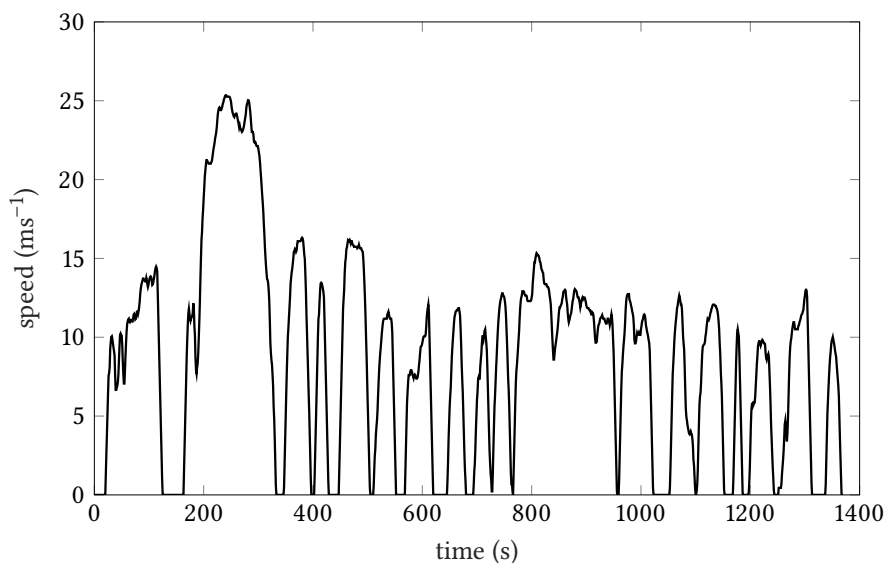


Figure 5.11 Profile of speed versus time for the UDDS drivecycle

In an all-electric drivetrain wherein lithium ion batteries provide the propulsion power, the speed profile can be suitably converted to a corresponding current profile experienced by the cell through the application of basic governing equations from vehicle dynamics (see section 3.5.2). Therefore, from the cell's perspective, traversal of the drivecycle then corresponds to the following events. During acceleration phases, the cell experiences a sharp discharge spike of current. Similarly, assuming that regenerative braking is employed, each deceleration event corresponds to a charging current. Thus a current versus time dynamic load profile can be obtained. To briefly summarise the conversion process used here, the computed power profile of the cell is divided by its nominal voltage and suitably scaled so that the peak of the current profile corresponds to a discharge current of 3C. Considering that all the braking energy cannot be recovered due to losses at the wheels, brake discs and other mechanical components, a regenerative braking factor of 85 % (the fraction of recoverable power) is assumed for the charging scenario.

Figure 5.12 shows the simulation results obtained by applying the UDDS current input profile (top row) to both the P2D and SPM models. The simulation is started at 50 % cell SOC. This is representative of the median point for the operating window of SOC swing for both BEVs and Plug-in Hybrid Electric Vehicles (PHEVs) [30]. Although regenerative braking is employed, due to the reduced occurrence of braking events as well as considering efficiencies of the drivetrain, as with any drivecycle, the UDDS profile also results in a net-discharge. The cell's SOC at the termination of the UDDS run is ≈ 6 % lower than its starting value.

The voltage output from the models is plotted in the middle row of fig. 5.12. The bottom row shows the evolution of the cell's SOC over time. Consistent with the error trends observed in the constant current discharge and charge simulations, the error in terminal voltage is high whereas that in SOC is low. In this work, the voltage error metrics are reported directly in units of mV for the dynamic simulation run. Furthermore, it is a standard practice to report the RMS error for such dynamic load profiles and is therefore included in the summary of error metrics reported in table 5.5.

Table 5.5 Summary of error metrics of the basic SPM with UDDS input profile.

Error metric	ϵ_v (mV)	ϵ_{SOC} (%)
Abs. max.	97.37	0.21
MAE	19.38	0.04
RMS	25.88	0.06

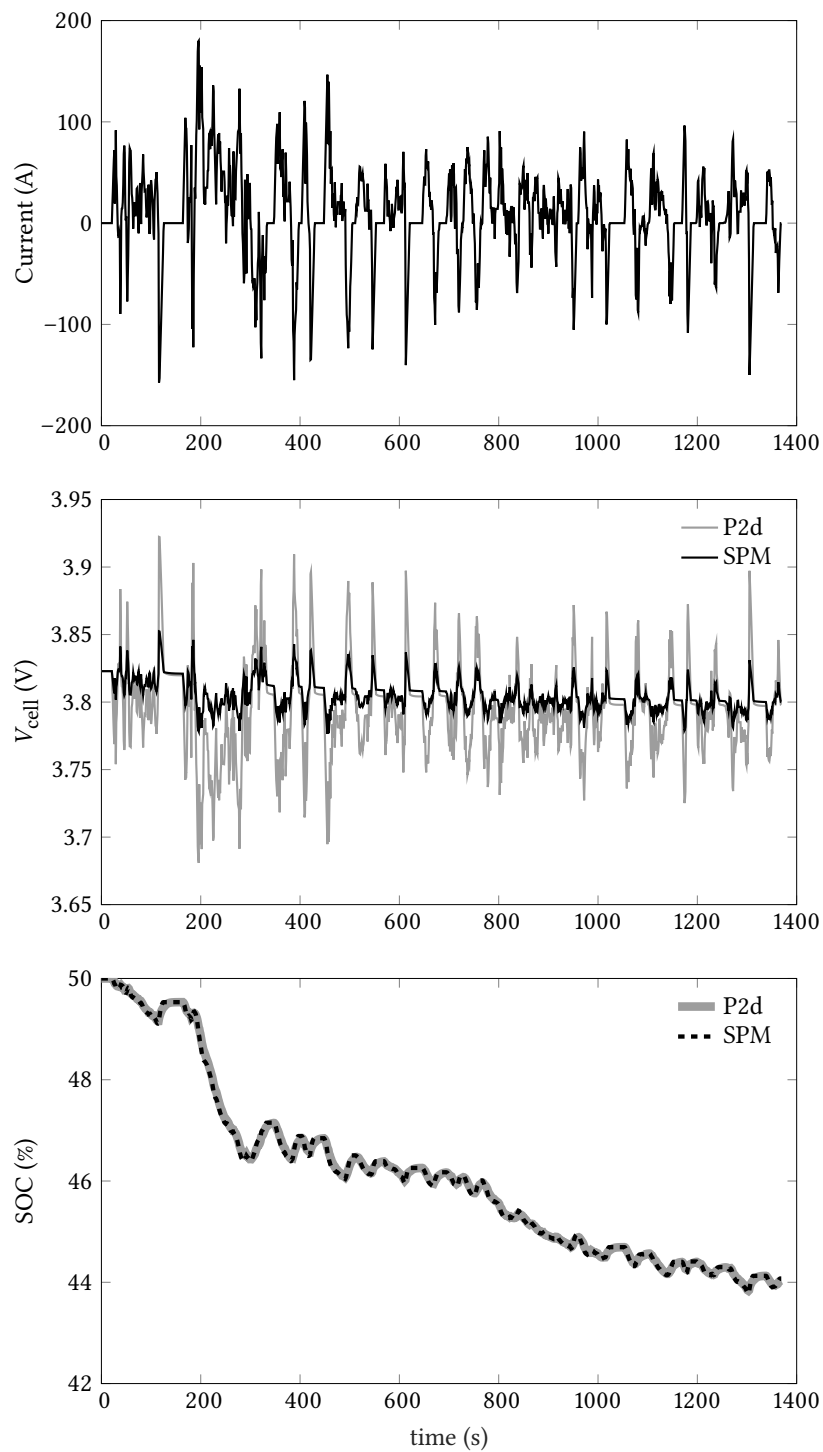


Figure 5.12 Simulation results for a UDDS current profile. The voltage prediction performance of the SPM to dynamic loads is poor while its SOC computation accuracy is high.

5.4 Quadratic Approximation of Ionic Spatial Concentration

As evidenced by the results from constant current charge, discharge and dynamic simulation runs presented in section 5.3, the basic SPM suffers from poor voltage accuracy. The prior art discussed in section 2.3.2 aim to tackle this issue through inclusion of electrolyte dynamics using various state of the art methods. However, they lack in providing an in-depth analysis and expository illustration of the fundamental deficiency of the standard P2D dynamics, which is uncovered later in section 6.1.1. This is facilitated through the introduction of the quadratic approximation model of ionic spatial concentration in this section[‡]. The quadratic approximation model is notable since it serves as the baseline reference for inclusion of electrolyte dynamics into an SPM.

5.4.1 Model derivation

The schematic in fig. 5.13 shows the definition of the co-ordinate systems used in deriving the polynomial approximation of the electrolyte concentration profile. The three regions {neg, sep, pos} are abbreviated to { n , s , p } respectively in all mathematical expressions. The globally defined x co-ordinate starts at the negative current collector interface ($x = 0$) and terminates at the positive current collector interface ($x = l_{\text{tot}}$, where $l_{\text{tot}} = l_n + l_s + l_p$). Three local co-ordinate systems z valid only within their respective regions are also defined. In particular, it must be noted that the direction of the local z_{pos} co-ordinate axis is opposite to that of the other two local co-ordinate axes as well as the global co-ordinate axis.

A standard quadratic expression is chosen a priori for approximating the electrolyte concentration profile within each region.

$$c_{e,n}(z, t) = a_2(t)z^2 + a_1(t)z + a_0(t) \quad 0 \leq z \leq l_n \quad (5.69)$$

$$c_{e,s}(z, t) = a_5(t)z^2 + a_4(t)z + a_3(t) \quad 0 \leq z \leq l_s \quad (5.70)$$

$$c_{e,p}(z, t) = a_8(t)z^2 + a_7(t)z + a_6(t) \quad 0 \leq z \leq l_p \quad (5.71)$$

[‡]The mathematical derivations here represents the author's digested summary of literature, and is particularly based upon a portion of Deng *et al.* [83]

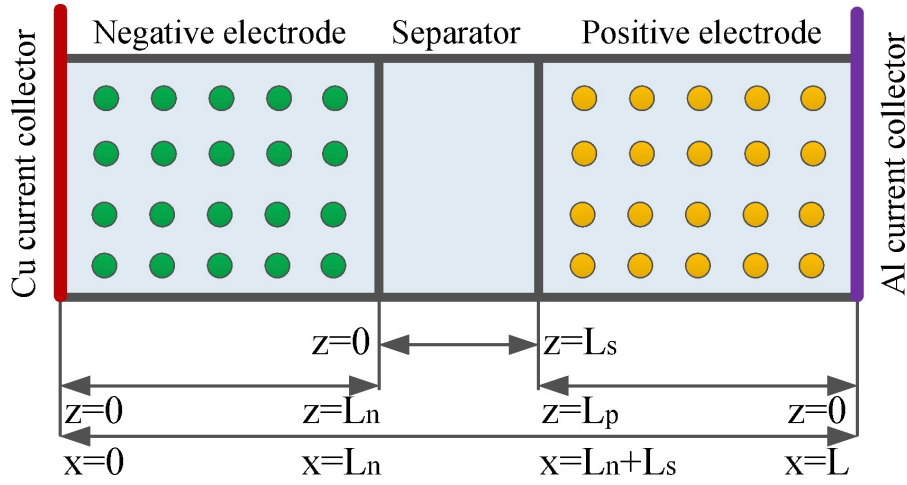


Figure 5.13 Schematic diagram of the electrochemical sandwich consisting of a) negative electrode, b) separator, and c) positive electrode depicting the co-ordinate system used in deriving the quadratic approximation profile. The global spatial co-ordinate is $x \in \{0, L\}$, where $L = l_{\text{tot}} = l_{\text{neg}} + l_{\text{sep}} + l_{\text{pos}}$. Local co-ordinate systems z specific to each region are also defined. It should be noted that the positive electrode's local co-ordinate axis direction is reversed with respect to the global co-ordinate axis. Illustration reproduced from Deng *et al.* [83].

The time-dependent coefficient vector $\vec{a}(t) = [a_0(t) \ a_1(t) \ \dots \ a_8(t)]^T$ is to be determined**. Applying boundary conditions of the electrolyte diffusion equation from the DFN model (refer eq. (1.4)) to eqs. (5.69)–(5.71), it is clear that $a_1 = 0$ and $a_7 = 0$. Thus, eqs. (5.69)–(5.71) become

$$c_{e,n} = a_2 z^2 + a_0 \quad 0 \leq z \leq l_n \quad (5.72)$$

$$c_{e,s} = a_5 z^2 + a_4 z + a_3 \quad 0 \leq z \leq l_s \quad (5.73)$$

$$c_{e,p} = a_8 z^2 + a_6 \quad 0 \leq z \leq l_p \quad (5.74)$$

with the coefficient vector being modified to $\vec{a} = [a_0 \ a_2 \ \dots \ a_6 \ a_8]^T$.

Table 5.6 lists the equations and boundary conditions for phenomena describing electrolyte diffusion and charge balance within the separator domain.

Equation (5.75) and eq. (5.76) are obtained by applying the pertinent electrolyte equations of the DFN model (eq. (1.4) and eq. (1.5) respectively) to the separator region. Applying the

**Hereafter, the explicit time-dependence of the coefficients is omitted. Similarly, the spatio-temporal dependence of the electrolyte concentration $c_{e,j}$ is also dropped from the notation.

5.4 Quadratic Approximation of Ionic Spatial Concentration

Table 5.6 Electrolyte-specific governing equations and boundary conditions of the Doyle-Fuller-Newman (DFN) model within the separator domain.

Region	Governing equations	Boundary conditions ($l_{\text{neg}} := l_n, l_{\text{sep}} := l_s, l_{\text{pos}} := l_p$)
Separator $\delta \in \{\text{sep}\}$	$\varepsilon_\delta \frac{\partial c_e}{\partial t} = D_{\text{eff},\delta} \frac{\partial^2 c_e}{\partial x^2}$	$c_e \Big _{x=l_n^-} = c_e \Big _{x=l_n^+}, \quad D_{\text{eff},n} \frac{\partial c_e}{\partial x} \Big _{x=l_n^-} = D_{\text{eff},s} \frac{\partial c_e}{\partial x} \Big _{x=l_n^+} \quad (5.75)$ $c_e \Big _{x=(l_n+l_s)^-} = c_e \Big _{x=(l_n+l_s)^+}, \quad D_{\text{eff},s} \frac{\partial c_e}{\partial x} \Big _{x=(l_n+l_s)^-} = D_{\text{eff},p} \frac{\partial c_e}{\partial x} \Big _{x=(l_n+l_s)^+}$
	$\frac{I}{A} = \bar{\kappa}_{\text{eff},\delta} \left(\frac{\partial^2 \phi_e}{\partial x^2} + \frac{2RT}{F} (t_+^0 - 1) \frac{\partial^2 \ln c_e}{\partial x^2} \right)$	$\phi_e \Big _{x=l_n^-} = \phi_e \Big _{x=l_n^+}, \quad \kappa_{\text{eff},n} \frac{\partial \phi_e}{\partial x} \Big _{x=l_n^-} = \kappa_{\text{eff},s} \frac{\partial \phi_e}{\partial x} \Big _{x=l_n^+} \quad (5.76)$ $\phi_e \Big _{x=(l_n+l_s)^-} = \phi_e \Big _{x=(l_n+l_s)^+}, \quad \kappa_{\text{eff},s} \frac{\partial \phi_e}{\partial x} \Big _{x=(l_n+l_s)^-} = \kappa_{\text{eff},p} \frac{\partial \phi_e}{\partial x} \Big _{x=(l_n+l_s)^+}$

continuity and flux boundary conditions from eq. (5.75) at both separator interfaces,

$$a_2 l_n^2 + a_0 = a_3 \quad (\text{continuity at neg/sep interface}) \quad (5.77)$$

$$a_5 l_s^2 + a_4 l_s + a_3 = a_8 l_p^2 + a_6 \quad (\text{continuity at sep/pos interface}) \quad (5.78)$$

$$2a_2 l_n D_{\text{eff},n} = a_4 D_{\text{eff},s} \quad (\text{flux b.c. at neg/sep interface}) \quad (5.79)$$

$$(2a_5 l_s + a_4) D_{\text{eff},s} = -2a_8 l_p D_{\text{eff},p} \quad (\text{flux b.c. at sep/pos interface}) \quad (5.80)$$

The negative sign in eq. (5.80) is due to the specific choice of the co-ordinate system used for the positive electrode region (see fig. 5.13). Due to this, fluxes at the separator/positive electrode interface have opposing directions. Let $Q_{e,j}$ denote the number of moles of Li^+ ions in the electrolyte per unit cross-sectional area within each region $j \in \{\text{neg}, \text{sep}, \text{pos}\}$. This is computed as the product of *a*) the porosity and *b*) spatial integral of the concentration function *i.e.*, $Q_{e,j} = \varepsilon_j \int_0^l c_{e,j}(z) dz$. Applying this to eqs. (5.72)–(5.74),

$$Q_{e,n} = \varepsilon_n \left(\frac{1}{3} a_2 l_n^3 + a_0 l_n \right) \quad (5.81)$$

$$Q_{e,s} = \varepsilon_s \left(\frac{1}{3} a_5 l_s^3 + \frac{1}{2} a_4 l_s^2 + a_3 l_s \right) \quad (5.82)$$

$$Q_{e,p} = \varepsilon_p \left(\frac{1}{3} a_8 l_p^3 + a_6 l_p \right) \quad (5.83)$$

At this stage, $Q_{e,j}(t)$ are unknown. Since these are time-dependent functions, the derivation naturally progresses towards seeking a set of ODEs that describe a relationship for their time evolution. Transforming the 2nd order ODEs of eq. (1.4) (for electrodes) and eq. (5.75)

5.4 Quadratic Approximation of Ionic Spatial Concentration

(for separator) to their respective local co-ordinates and integrate once along the thickness of each region. Performing this sequence of steps for the negative electrode region

$$\begin{aligned}
 \varepsilon_n \int_0^{l_n} \left(\frac{\partial}{\partial t} c_{e,n}(z, t) \right) dz &= \int_0^{l_n} \left(\frac{\partial}{\partial z} \left(D_{\text{eff}_n} \frac{\partial c_{e,n}}{\partial z} \right) + (1 - t_+^0) a_{s,n} j_n \right) dz \\
 \varepsilon_n \frac{\partial}{\partial t} \int_0^{l_n} c_{e,n}(z, t) dz &= \int_0^{l_n} \left(\frac{\partial}{\partial z} \left(D_{\text{eff}_n} \frac{\partial c_{e,n}}{\partial z} \right) + (1 - t_+^0) a_{s,n} j_n \right) dz \\
 \frac{\partial}{\partial t} \left(\varepsilon_n \int_0^{l_n} c_{e,n}(z, t) dz \right) &= \int_0^{l_n} \left(\frac{\partial}{\partial z} \left(D_{\text{eff}_n} \frac{\partial c_{e,n}}{\partial z} \right) + (1 - t_+^0) a_{s,n} j_n \right) dz \\
 \underbrace{\frac{d}{dt} Q_{e,n}(t)} &= D_{\text{eff}_n} \frac{\partial c_{e,n}}{\partial z} \Big|_{z=l_n} + (1 - t_+^0) a_{s,n} \int_0^{l_n} j_n dz
 \end{aligned}
 \tag{5.84}$$

transposing integration & differentiation operations in the LHS
 apply time-derivative operator to the whole LHS
 apply integral to the RHS

Performing the identical sequence of operations starting from (eq. (5.75)) for the separator and (eq. (1.4)) for the positive electrode yields

$$\frac{d}{dt} Q_{e,s}(t) = D_{\text{eff}_s} \frac{\partial c_{e,s}}{\partial z} \Big|_{z=l_s} \tag{5.85}$$

$$\frac{d}{dt} Q_{e,p}(t) = D_{\text{eff}_p} \frac{\partial c_{e,p}}{\partial z} \Big|_{z=l_p} + (1 - t_+^0) a_{s,p} \int_0^{l_p} j_p dz \tag{5.86}$$

In order to evaluate the integral term in the RHS of eq. (5.84) and eq. (5.86), the solid phase charge conservation equation (eq. (1.6)) is integrated along the local co-ordinate axis of the negative electrode and positive electrode respectively.

$$\int_0^{l_n} j_n dz = \frac{I}{a_{s,n} AF} \tag{5.87}$$

$$\int_0^{l_p} j_p dz = \frac{-I}{a_{s,p} AF} \tag{5.88}$$

Substituting eqs. (5.87)–(5.88) into eqs. (5.84)–(5.86) respectively,

$$\frac{d}{dt} Q_{e,s} = D_{\text{eff}_s} \frac{\partial c_{e,s}}{\partial z} \Big|_{z=l_s} - \cancel{(1 - t_+^0) a_{s,n}} \frac{I}{\cancel{a_{s,n}} AF} \tag{5.89}$$

$$\frac{d}{dt} Q_{e,p} = D_{\text{eff}_p} \frac{\partial c_{e,p}}{\partial z} \Big|_{z=l_p} - \cancel{(1 - t_+^0) a_{s,p}} \frac{-I}{\cancel{a_{s,p}} AF} \tag{5.90}$$

5.4 Quadratic Approximation of Ionic Spatial Concentration

which leads to the general expressions for the cross-sectional molar density of Li^+ ions in each of the three regions as

$$\frac{d}{dt} Q_{e,n} = D_{\text{eff}_n} \left. \frac{\partial c_{e,n}}{\partial z} \right|_{z=l_n} + (1 - t_+^0) \frac{I}{AF} \quad (5.91)$$

$$\frac{d}{dt} Q_{e,s} = D_{\text{eff}_s} \left. \frac{\partial c_{e,s}}{\partial z} \right|_{z=l_s} \quad (5.92)$$

$$\frac{d}{dt} Q_{e,p} = D_{\text{eff}_p} \left. \frac{\partial c_{e,p}}{\partial z} \right|_{z=l_p} - (1 - t_+^0) \frac{I}{AF} \quad (5.93)$$

Substituting the assumed quadratic expressions for electrolyte concentrations in each of the three regions eqs. (5.72)–(5.74) in the above system *i.e.*, eqs. (5.91)–(5.93)

$$\frac{d}{dt} Q_{e,n} = 2a_2 l_n D_{\text{eff}_n} + (1 - t_+^0) \frac{I}{AF} \quad (5.94)$$

$$\frac{d}{dt} Q_{e,s} = 2a_5 l_s D_{\text{eff}_s} \quad (5.95)$$

$$\frac{d}{dt} Q_{e,p} = 2a_8 l_p D_{\text{eff}_p} - (1 - t_+^0) \frac{I}{AF} \quad (5.96)$$

The initial ionic concentration in the electrolyte is identical in all three regions of the cell, assuming equilibrium starting conditions *i.e.*, $c_{e,0_j} = c_{e,0}$, $j \in \{n,s,p\}$. Hence the initial number of moles of Li^+ per unit area in each of the three regions is given by

$$Q_{e,n}(0) = \varepsilon_n c_{e,0} l_n \quad (5.97)$$

$$Q_{e,s}(0) = \varepsilon_s c_{e,0} l_s \quad (5.98)$$

$$Q_{e,p}(0) = \varepsilon_p c_{e,0} l_p \quad (5.99)$$

and the initial coefficient vector which satisfies the system equations is obtained as

$$\begin{bmatrix} a_0(0) \\ a_2(0) \\ a_3(0) \\ a_4(0) \\ a_5(0) \\ a_6(0) \\ a_8(0) \end{bmatrix} = \begin{bmatrix} c_{e,0} \\ 0 \\ c_{e,0} \\ 0 \\ 0 \\ c_{e,0} \\ 0 \end{bmatrix} \cdot \quad (5.100)$$

5.4 Quadratic Approximation of Ionic Spatial Concentration

The system of three ODEs, (5.94)–(5.96) together with eqs. (5.97)–(5.99) representing the initial conditions, form an IVP. Eqs. (5.77)–(5.83) represent a square system of seven linear algebraic equations with seven unknown coefficients which must be solved at each time-step. These algebraic constraints coupled with the aforementioned IVP form a DAE system.

There are now two choices for proceeding with solution of the system. The naive approach would be to solve the DAE using advanced DAE solvers specially designed to handle index-1 semi-explicit systems such as DASSL [203] and DASPK [204]. For start-stop type of input currents with discontinuities, the consistent initialisation of algebraic conditions and derivatives is numerically challenging. All DAE solvers typically use adaptive time-stepping algorithms. The feasibility of using such a complex scheme for real-time computation is questionable. On the other hand, the overall system can be viewed as composed of two numerical subsystems – *a*) an independent ODE system, and *b*) an independent algebraic system. Each system is executed back to back in succession using solutions from the other system from the previous time-step.

To clarify the sequence of operations, in order to bootstrap the model, it is required to compute $Q_{e,j}(t)$ in all three regions. The ODE system is integrated for one time-step by retaining the coefficients at their initial value. The $Q_{e,j}(t)$ thus solved is substituted into the algebraic system to yield the updated value of the coefficient vector $\vec{a}(t = t_k)$. This new value of the coefficient vector is substituted back into the ODE system and the process continues. Although the continuous simulation of the overall DAE is not accomplished, this scheme is pragmatic from an engineering viewpoint. This is because, the periodic pauses needed to update the intertwined sub-systems translate naturally into fixed time-steps and is well-suited for a BMS controller operating at a fixed sample rate. This is also an effective workaround to mitigate the complexities of having to implement and solve DAEs in real time.

The simulation results of the quadratic approximation scheme and the analysis of its strengths and weaknesses is presented next in section 5.4.2.

5.4.2 Numerical implementation, simulation results and analysis

Numerical implementation

From an analysis point of view, the quadratic approximation model for computing the spatio-temporal evolution of electrolyte concentration can be simulated as an independent subsystem, and hence can be implemented numerically as a standalone module as shown in algorithm 5.3. In practice, this modular code is embedded as a subroutine within the main SPM loop (see algorithm 5.2).

Algorithm 5.3 Quadratic approximation model for spatio-temporal electrolyte concentration

Require: Load profile ▷ e.g. a csv file of t vs. C-rate
Require: Electrolyte model parameter set ▷ e.g. stored in a struct `ceparams`
User data: t_f , sample rate T_s , $c_{e,init}$

- 1: **function** QUADRATICELECTROLYTEMODEL
- 2: Set $Q_{e,init}$ as per eqs. (5.97)–(5.99)
- 3: $\vec{a}[1] \leftarrow$ values from eq. (5.100)
- 4: $V_{cell}[1] \leftarrow$ COMPUTECELLVOLTAGE($\mathbf{x}[1]$, $I[1]$, `params`) ▷ from direct feedthrough
- 5: **for** $k \leftarrow 2 : N_{max}$ **do**
- 6: $I[k] \leftarrow$ interpolate from profile using ZOH
- 7: Solve continuous-time state equations—eqs. (5.94)–(5.96) ▷ Using $\vec{a}[k-1]$
- 8: $Q_{e_j}[k] \leftarrow$ last time-entry vector of soln. matrix ▷ if using an adaptive solver
- 9: $\vec{a}[k] \leftarrow$ solution of *linear* system of equations—eqs. (5.77)–(5.83) ▷ Using $Q_{e_j}[k-1]$
- 10: Compute c_e as per eqs. (5.72)–(5.74) ▷ Quadratic polynomial expressions for concentration
- 11: **end for**
- 12: **end function**

Simulation results

Figure 5.14 shows the spatial distribution of Li^+ ions in electrolyte along the thickness of the cell at various snapshots of time obtained by simulation of the P2D and the quadratic approximation models using a 1C discharge current. The P2D model's response is considered as the reference benchmark. During the initial transient phase, the concentration profile within each electrode region exhibits a characteristic inflection point. During this phase, the concentration profile computed by the parabolic profile exhibits a large deviation in terms of percentage error at each spatial location. However, with the passage of time, as a Quasi-Steady

5.4 Quadratic Approximation of Ionic Spatial Concentration

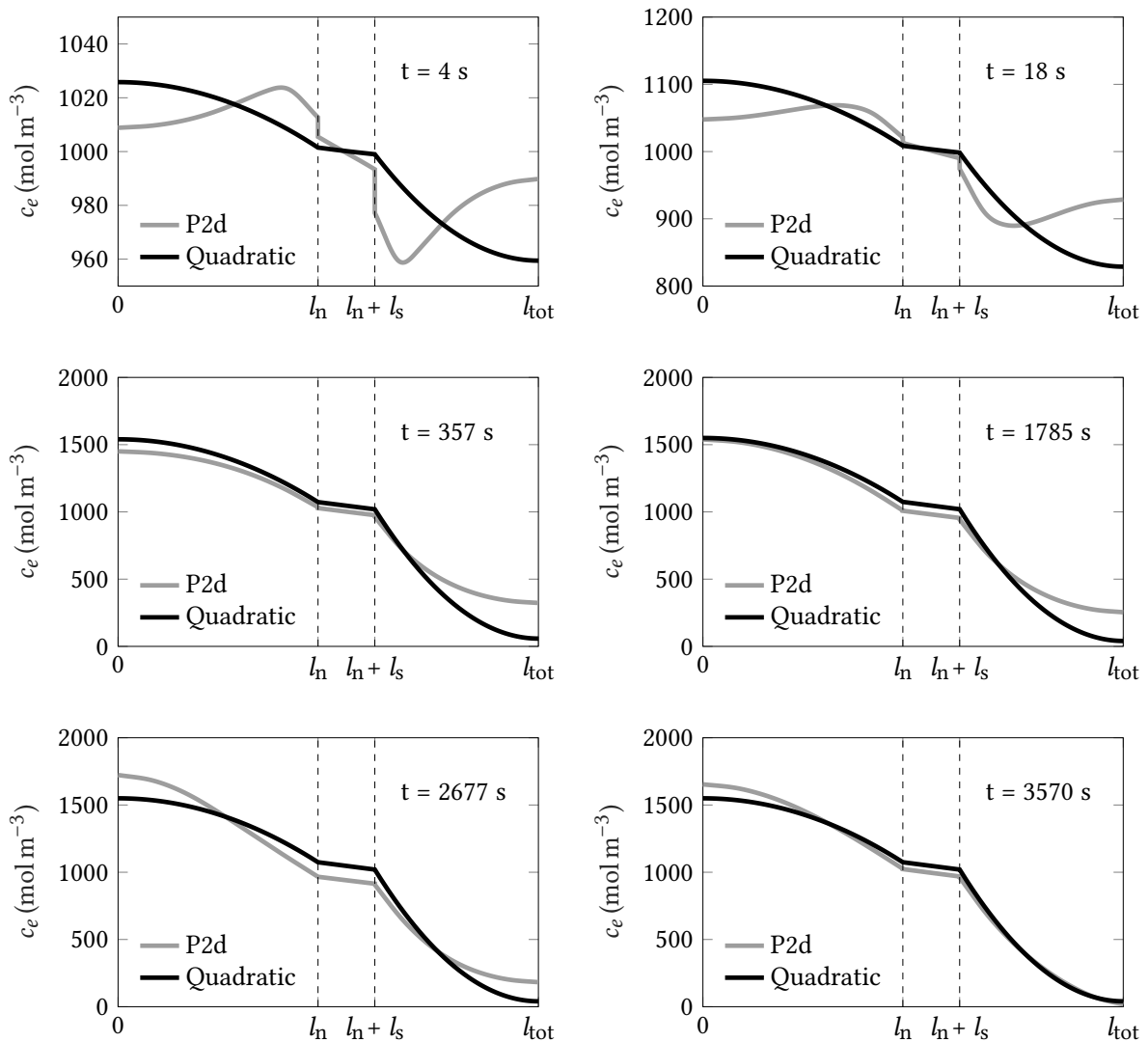


Figure 5.14 Spatial distribution of ionic concentration in electrolyte along cell thickness at various snapshots of time for a 1C discharge. The concentration profile obtained from simulating the P2d model is used as the reference. The performance of the quadratic model is quite poor during the initial transient duration, but improves over time as a quasi-steady state is reached.

State (QSS) is established, this inflection point flattens out, and the quadratic approximation becomes closer to the true concentration value at each spatial location. Similar trends in behaviour is exhibited for discharge and charging at higher C-rates and these results are therefore omitted here in the interest of keeping the discussion succinct.

It is important to note that while having a spatial concentration profile is useful, as seen in eq. (2.4), it is the values of concentration at the *current collector interfaces* that are most influential in computation of the electrolyte overpotential and hence, in the voltage accuracy

5.4 Quadratic Approximation of Ionic Spatial Concentration

of the enhanced SPM. Thus, it is important to obtain this alternative perspective of time-evolution of the electrolyte concentration at the two current collectors.

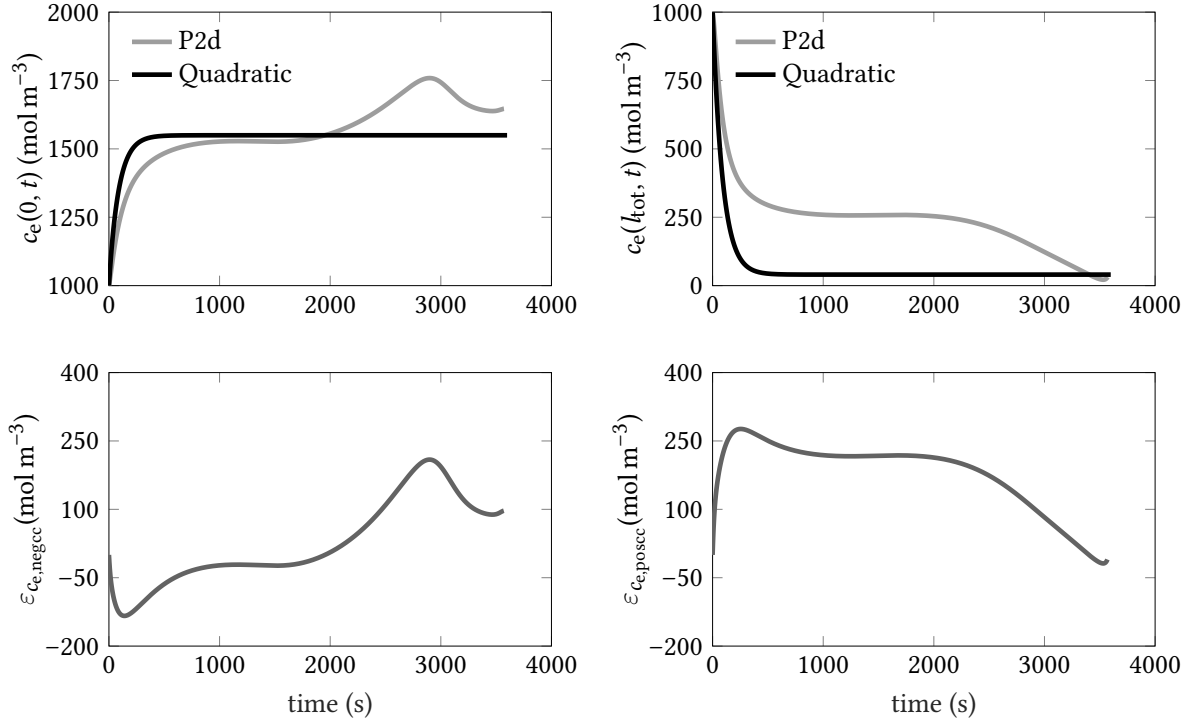


Figure 5.15 Evolution of ionic concentration over time at the two current collector interfaces for a 1C discharge (top row). The time evolution of the corresponding error variables is shown in the bottom row of plots.

Figure 5.15 shows the time evolution of ionic concentration in the electrolyte at the two current collector interfaces computed by the P2D and quadratic approximation models for a 1C discharge current. The concentration values computed by the P2D model is considered as the reference benchmark. At the negative electrode–current collector interface, the ionic concentration exhibits a few oscillations of small amplitude owing to the complex interactions of the ionic phase with the porous electrode and the charge transfer process at the electrode–electrolyte boundary. The concentration evolution predicted by the quadratic approximation model is rather simplistic and is unable to capture this intricate time-evolution pattern. This is because the governing equation predicting time evolution of concentration in the quadratic approximation model is that given by the *first-order* ODE of eq. (5.94) (with a proportional mapping from $Q_{e,n}$ to $c_e(0, t)$). Following system theory, the step response of a first order ODE is that of an exponential rise to a final settling value, which is exactly the shape seen in the top-left plot of fig. 5.15.

The ionic concentration evolution at the positive current collector does not exhibit major oscillations and even has a subtle monotonicity to its response. However, the classical first order response predicated by the quadratic approximation model falls short of representing its complete dynamics. Errors of similar magnitude are present in the ionic concentration at both current collector interfaces, with a maximum absolute error of $\approx 250 \text{ mol m}^{-3}$.

5.5 Conclusions

This chapter dealt with the in-depth analysis of – *a)* the basic SPM and *b)* an electrolyte-enhanced SPM employing the quadratic spatial approximation model for ionic concentration. Simulation results for the basic SPM reveal that while its SOC computation is of acceptable accuracy even at moderate C-rates, it suffers from poor performance in the prediction of terminal voltage at currents above 0.5C. This renders the model unusable as the plant model for state estimation tasks since the voltage measured from the model in a feedback estimator shall map to a distant SOC operating point.

The assumptions and governing equations of the popular quadratic approximation model for the spatial profile of ionic concentration was presented. Simulation results reveal that while its spatial profile computation for a galvanostatic operation is of acceptable accuracy, the temporal performance of the model is mediocre. In particular, the time evolution of ionic concentration at the current collector interfaces computed by the model fail to capture the intricacies in the temporal evolution exhibited by the P2D model's profile.

This chapter concludes with a view that accuracy of the quadratic approximation model needs to be improved upon before deployment in applications involving highly dynamic load profiles such as a vehicular BMS. In chapter 6, causal factors of the lacklustre performance of the quadratic approximation model is analysed in the context of developing an improved representation of electrolyte spatial dynamics through system identification.

6

Implementing a New Electrolyte Model for Augmentation of the Basic SPM

6.1	Performance Analysis: Quadratic Approximation Model	212
6.2	A New Electrolyte Model through System Identification	216
6.3	Brief Introduction to System Identification	219
6.4	Overview of Black Box System Identification	220
6.5	Introduction to Electrolyte Time-Evolution Subsystems	223
6.6	Design of Persistent Excitations	223
6.7	Investigation of Linearity and Time Invariance	228
6.8	Transfer Function Identification Procedure	234
6.9	Performance Analysis of System Id Model: Ionic Concentration	246
6.10	Composite SPM Model with Electrolyte Dynamics	255
6.11	Conclusions	266

6.1 Performance Analysis: Quadratic Approximation Model

BASED upon the insights gained from the extensive analyses performed in chapter 5, this chapter presents the thesis author's attempts to surpass the performance of the current pinnacle in modelling art through the development of a new electrolyte model. In particular, this chapter describes the attempts towards arriving at an accurate description of the spatio-temporal evolution of the electrolyte concentration in a lithium ion cell for real-time applications. The performance of the quadratic approximation model which was introduced in chapter 5 is analysed through the novel application of a symbolic regression framework. This helps to expose the issue of equation deficiency in the underlying Doyle-Fuller-Newman (DFN) model and questions its suitability for the purpose of reduced order modelling of the electrolyte concentration dynamics with a pre-assumed equation structure. Although this framework did not ultimately yield the desired outcomes, it did nevertheless facilitate a comprehensive analysis of the strengths and weaknesses of the quadratic approximation model which has not been performed in existing literature. Next, the author's unique contribution to the art of single particle modelling *viz.* a novel time-evolution model of electrolyte concentration evolutions through the technique of system identification is presented. The results of the new approach is compared against the baseline quadratic approximation model as well as the benchmark Pseudo Two-Dimensional (P2D) model. Finally, the new model equations are incorporated into an electrolyte-enhanced Single Particle Model (SPM) and the improved performance of the newly developed composite model is quantified.

6.1 Performance Analysis: Quadratic Approximation Model

In the author's analysis of the quadratic approximation model, the origin and nature of its sub-optimal performance can be explained as per the following rationale. The quadratic approximation model uses a bottom-up approach wherein the final simplified model structure is pre-assumed and then the physics are made to fit within this framework. Given that the top-down approach to electrolyte modelling *i.e.*, accounting for all physical phenomena and then simplifying them yields mathematically intractable and overly complex models (see section 2.3.2 for a detailed discussion), this approach seems to be a pragmatic alternative to enhancing the SPM with electrolyte dynamics. However, a detailed look at this model from an alternate viewpoint is necessary for further analysis.

6.1.1 Symbolic regression using Multi-Gene Genetic Programming

The question boils down to whether a quadratic approximation is indeed the *best* model structure that can be assumed a priori for the spatial profile of ionic concentration in the electrolyte. This author embarked on a journey to find suitable alternate model structures *i.e.*, a single family of curves that can capture both the transient and Quasi-Steady State (QSS) behaviour exhibited by the ionic concentration. The open-source MATLAB toolbox GPTIPS2 [205] uses the state-of-the-art Multi-Gene Genetic Programming (MGGP) approach for symbolic data mining and is ideally suited for such symbolic regression tasks (fitting a mathematical equation structure, and not merely obtaining best-fit coefficients to a pre-assumed curve as in classical numerical regression, to a given data).

In employing the MGGP approach, it is important to recognise that the key criteria that restricts *a)* the choice of gene-sequence depth, as well as *b)* the choice in number of parent mutations, is the total number of unknown symbolic coefficients required to be solved in the assumed model structure. There are a total of *seven* linear equations available from the physics of the DFN model (see eqs. (5.77)–(5.83)). Hence, in order to guarantee a solution the assumed family of curves cannot consist of more than seven coefficients. Furthermore, for a unique solution, the number of coefficients must be *exactly* seven. Yet another restriction on the choice of locus of feasible curves arises due to the fact that the behaviour of ionic concentration in the negative and positive electrode regions are similar in complexity*, and hence need to be mathematically described by an identical family of curves.

Upon a close inspection of the spatial concentration profile from the P2D simulation results shown in fig. 5.14, it is evident the electrolyte approximation functions within the electrode regions is of higher complexity* than the approximation function suitable for use in the separator region. Based on the results of the quadratic model, it is clear that at least two coefficients are required within the electrode regions *i.e.*, $n_{c,elec} \geq 2$. There exists an inhibiting factor that prevents the use of a lower order function within the separator. As per the simulation results of the P2D model, the time-domain change of number of moles per square meter in the separator is non-zero. Since the time-derivative of a linear approximation

*The concept of complexity of curves used here is not based on a precise mathematical definition such as that employed by Neumann-Coto and Arenas [206], but is loosely used to simply convey an empirical sense of their curvature. However, the analysis here applies to the more rigorous definition as well.

6.1 Performance Analysis: Quadratic Approximation Model

applied to eq. (5.95) is zero, this straight-line equation is immediately ruled out. Among the non-polynomial mathematical curves tried (such as trigonometric, hyperbolic, power series among others), none could obtain the relatively simple shape of the separator function without being forced to reduce the contribution from one of the coefficients to below machine precision. This necessitates the retention of the quadratic approximation function used thus far (with no missing terms) *i.e.*, $n_{c,sep} = 3$. Thus, the overall number of coefficients in the best possible approximation shall be $2n_{c,elec} + n_{c,sep} = 2 \cdot 2 + 3 = 7$, which is the total number of electrolyte-specific physical constraints available from the DFN model. Hence it can be concluded that the quadratic approximation model does indeed make the *best* use of all of the available physical equations. The final question that remains to be answered is, with these coefficient limitations, whether the quadratic equation structure is indeed the optimal one. This was investigated through the MGGP approach described next.

The GPTIPS2 toolbox uses a variety of heuristic algorithms from the theory of MGGP to hypothesise a suitable equation structure for the data to be fitted. The dataset consisted of electrolyte concentration at the three cell regions captured at various snapshots of time. Both transient and QSS data were fed into this symbolic data mining process and a single all-encompassing family of curves capable of capturing the electrolyte concentration behaviour was sought for. However, the constraints in the number of coefficients that can be employed results in a restriction of the depth of gene mutations as well as the number of parent/seed populations. The best equation set (without strictly enforcing the aforementioned hard constraints, yet minimising the distance to the constraint vector) that the symbolic regression approach yielded was

$$c_{e,n}(z, t) = a_2(t) \cosh z^2 + a_1(t) \sinh z + a_0(t) \quad 0 \leq z \leq l_n \quad (6.1)$$

$$c_{e,s}(z, t) = a_5(t)z^2 + a_4(t)z + a_3(t) \quad 0 \leq z \leq l_s \quad (6.2)$$

$$c_{e,p}(z, t) = a_8(t) \cosh z^2 + a_7(t) \sinh z + a_6(t) \quad 0 \leq z \leq l_p \quad (6.3)$$

Although eqs. (6.1)–(6.3) fit the transient and QSS profiles well, they violate the constraint on the number of coefficients available resulting in an under-determined system of equations. Both the least-squares and least-norm solution of this system were tried. However, the results were inferior to that produced by the baseline quadratic approximation method.

6.1 Performance Analysis: Quadratic Approximation Model

Next, an attempt was made to obtain different mathematical structures for the transient phase and QSS phase both of which respect the constraint on number of coefficients allowed. The symbolic regression outputs for this approach are shown in table 6.1.

Table 6.1 Best fit expressions for the transient and Quasi-Steady State approximation functions for the electrolyte functions obtained by the MGGP approach.

Transient Function	Quasi-Steady State Function	Region
$c_{e,n_{\text{trans}}} = a_1(t)z^6 \ln z^6 + a_0(t)$	$c_{e,n_{\text{QSS}}} = a_1(t) \sinh z^2 + a_0(t)$	$0 \leq z \leq l_n$
$c_{e,s_{\text{trans}}} = a_4(t)z^2 + a_3(t)z + a_2(t)$	$c_{e,s_{\text{QSS}}} = a_4(t)z^2 + a_3(t)z + a_2(t)$	$0 \leq z \leq l_s$
$c_{e,p_{\text{trans}}} = a_6(t)z^6 \ln z^6 + a_5(t)$	$c_{e,p_{\text{QSS}}} = a_6(t) \sinh z^2 + a_5(t)$	$0 \leq z \leq l_p$

Although the equations from table 6.1 produced a markedly improved response during the transient phase, the performance during the QSS phase was merely at par to the baseline quadratic approximation model. This raised the prospect of employing a blended approach, wherein a model changeover between the transient and QSS was contemplated. However, since there is no precise definition of what constitutes the transient phase of the electrolyte concentration response, this approach required some ad hoc timing criteria for correctly transitioning between the two MGGP equation sets. Further complications arise during dynamic input conditions, wherein the concentration profiles are mostly in a state of flux and could linger for longer durations at the contiguous boundary between transient-like and QSS-like behaviours. In the interest of reproducibility across different cell-chemistries and corresponding parameter sets, the proposed blended model transition approach was not further pursued.

Overall, the long and arduous process of symbolic regression was not a definitive success in this case mainly due to the limitation of equation deficiency of physical constraints. Perhaps if yet another Physics-Based Model (PBM) *i.e.*, an alternative to the widely prevalent DFN model, can be used as the baseline, a few more physical governing equations could possibly be made available. This can perhaps result in a less restrictive gene-set for coefficient determination and consequently pave the way for a successful implementation through this hitherto unexplored route of MGGP-based equation synthesis.

In conclusion, the quadratic model for electrolyte concentration approximation makes the best use of the available physical equations. Given the constraints with respect to physical

equations discussed here, it is also deemed to be the optimum family of a priori chosen curves capable of modelling the *spatial* profile of ionic concentration. Notwithstanding these merits, the *temporal* performance of the quadratic approximation approach is sub-optimal as seen in fig. 5.15. The author of this thesis addresses this specific issue with a completely different approach that shall be discussed next in section 6.2.

6.2 A New Electrolyte Model through System Identification

Having performed a comprehensive analysis of the state of the art in SPM modelling with electrolyte dynamics, this section presents the author's unique contribution to the field. Firstly, the scope of the contribution is identified. The methodology adopted and corresponding results are presented thereafter.

6.2.1 Scope and motivation

This subsection is intended as a capstone summary helping to briefly recount the discussion so far and to provide a context for the author's work in the wider realm of the SPM modelling art. In the same vein as the discussion in section 2.3.2, the scope of the proposed enhancement to the SPM concerns entirely with improving the electrolyte subsystem since it has already been established in section 5.3.3 that the simplified representation of the solid-phase subsystem through a fourth order polynomial approximation method for diffusion of Li^0 in the solid particle is of sufficiently high accuracy.

Inspecting the electrolyte domain, the contribution of electrolyte overpotential to terminal voltage consists of *a*) diffusion overpotential *b*) time-dependent ohmic losses that originates from differential concentration gradients (that is indirectly dependent upon concentration). Once electrolyte concentration at each time-step is available, eq. (2.4) proposed by Prada *et al.* [99] may be used for the electrolyte overpotential computation. Hence, the accurate determination of spatio-temporal values of electrolyte concentration merits focus.

There exists a subtle detail in the use of eq. (2.4) which is discussed here upfront before proceeding ahead to the refined context of the author's work. The intrinsic conductivity of electrolyte κ is a function of the ionic concentration (refer section 5.3.2). If the ionic concentration at the corresponding current collectors are used for evaluating κ_{neg} and κ_{pos} ,

6.2 A New Electrolyte Model through System Identification

this would lead to a lopsided computation of the overpotential in electrolyte. Furthermore, under this scheme, the computation of electrolyte conductivity shall be rendered ambiguous since it is unclear which separator interface shall be chosen for the separator's ionic concentration. Although this has not been discussed clearly in literature, the author of this thesis chose to use the mean concentration within each cell region, defined as

$$\bar{c}_{e,j}(t) = \frac{1}{l_j} \int_0^{l_j} c_{e,j}(z, t) dz = \frac{Q_{e,j}(t)}{\varepsilon_j l_j} \quad (6.4)$$

though other measures of central tendency might be equally valid. Hence, the results of this section have the associated variability in them depending on how the electrolyte concentration computations are used in evaluating the intrinsic conductivity of electrolyte.

As the ionic concentration has both a direct and indirect contribution in eq. (2.4), its spatio-temporal computation is a critical aspect. As discussed in section 5.4, the quadratic approximation is a widely used spatio-temporal model for electrolyte concentration which makes the best use of available physical constraints. As established in the results of section 5.4.2, while the spatial performance of the quadratic approximation approach is acceptable, its time-domain performance, particularly at the crucial locations of the current collector interfaces is mediocre at best.

The *scope* of the author's work is to obtain suitable alternate expressions for improving the computation of **time evolution** of the electrolyte concentration whilst retaining the quadratic approximation approach for describing its spatial profile. Such an approach is motivated by the keen observation that the baseline quadratic approximation model has a natural 'pause' in its model description. To clarify, eqs. (5.77)–(5.83) form a tightly coupled square system *i.e.*, a set of seven linear equations in seven unknowns. In this system, the time evolution of $Q_{e,j}$ are described through a separate system of first order Ordinary Differential Equations (ODEs) given by eqs. (5.94)–(5.96). In a practical implementation, these ODEs are solved independently in a decoupled manner *i.e.*, by using the coefficients obtained from the linear system of eqs. (5.77)–(5.83) in the previous time-step. The author's hypothesis is that by taking advantage of the natural break in the operational sequence which involves two separate computations between two nearly independent subsystems, it must be possible to replace the under-performing time-evolution ODEs from the baseline quadratic approximation with a superior alternate model.

6.2.2 Selection of Methodology – Background and Rationale

This section presents the background and thought process in systematically arriving at the choice of the methodology that was adopted for the new time-evolution model of the electrolyte concentration dynamics.

Based upon the experience gained in dealing with the literature presented in section 2.3.2, it is the author's view that, owing to the complex behaviour of electrolyte, a naive top-down approach *i.e.*, including all the physics upfront followed by a systematic simplification, might only yield a model that is mathematically intractable for adoption in an embedded Battery Management System (BMS) environment. The baseline quadratic approximation method has proven that a bottom-up approach *i.e.*, pre-assuming a simplified structure for the final model and adapting its coefficients to physical constraints yields a viable candidate for describing electrolyte dynamics and for later inclusion in the conventional SPM.

Upon a closer examination of the rubrics of the baseline quadratic approximation model, it comes to light that the natural 'pause' discussed towards the end of section 6.2.1 permeates to a level more than merely having to operate sequentially on two pseudo-decoupled subsystems – it goes to the extent of rendering the operating philosophy of fitting physical equations semi-void. To clarify this statement and to substantiate the claim, while there is no doubt that the linear algebraic equations of eqs. (5.77)–(5.83) do incorporate physical principles from the DFN model, the same does not hold true for the ODEs of eqs. (5.94)–(5.96). In fact, all the boundary conditions from the DFN model have been exhausted by this stage (refer section 5.4.2). Although eqs. (5.91)–(5.93) are derived from the DFN model, the coefficients of the diffusivities in the Right-Hand Side (RHS) of the next set of equations *i.e.*, eqs. (5.94)–(5.96), merely involve substitutions of the spatial derivatives of the assumed quadratic expression.

Herein lies the weakness of the baseline quadratic approach. Unlike the spatial algebraic equations, which are tightly bound by the continuity and flux boundary conditions at the separator interfaces, there is no equality constraint on the spatial derivative, which is free to grow or shrink without any explicitly imposed bounds. The onus of being accurate is therefore on the spatial derivative evaluation which in-turn depends on the correctness of the quadratic functions (eqs. (5.72)–(5.74)) themselves. It is not feasible to quantify the magnitude of error introduced in the time-evolution of concentration given a small-signal perturbation in the

coefficients of the quadratic spatial computation *i.e.*, the implicit coupling between them is not transparent. Since the quadratic approximation itself is not perfect *i.e.*, does not capture the spatial gradient *exactly* as the P2D model as seen in fig. 5.14, the internal coupling of coefficients leads to errors in time-evolution computation.

The author's approach is to therefore break this detrimental coupling between spatial derivative of concentration and its temporal evolution counterpart. Inspired by the fact that the quadratic approximation model had almost achieved the desired goals with

- a) a bottoms-up approach *i.e.*, assuming some model structure a priori, and
- b) not bound by any physical considerations due to the exhaustion of governing equations

led the author to broach a suitable modelling concept that exhibits these common traits, yet of a completely different nature and hitherto unexplored in physics-based battery modelling in general and electrolyte modelling in particular – *black-box system identification*.

6.3 Brief Introduction to System Identification

An in-depth coverage of the topic of system identification is well beyond the scope of this thesis. However, keeping in mind the interests of the battery modelling community who might not be familiar with this subject area, a brief overview of the core ideas that are essential for tackling the specific problem at hand is presented. For readers further interested in this topic, the author suggests the textbook by Ljung [207] for a comprehensive theoretical treatment of the foundation topics in system identification.

System identification aims to provide a mathematical model of the input-output mapping of the system[†] under consideration. The three categories of system identification are:

- a. **White box** wherein underlying physical equations are completely known. The numerical value of coefficients of governing equations are then to be parametrised from input-output data.

[†]The precise definition of what constitutes a 'system' is detailed in Ljung's textbook. However, for all practical purposes, in this thesis the word 'system' stands for any unknown entity whose terminal behavioural model is being sought for – primarily from input-output data.

- b. Black box** wherein no governing equations are available for the system under consideration. The model formulation is facilitated by a rich set of system theory which proceeds by exciting the system with input waveforms with certain desirable properties and correlating characteristics from the response to draw conclusions about viable mathematical structures capable of emulating the terminal behaviour of the system under generalised inputs. Black box system identification was employed for the specific problem under consideration in this thesis and hence all future descriptions will pertain to this class.
- c. Grey box** is a hybrid of the two approaches wherein a part of the model's governing physics is known a priori *e.g.* the structure of a well-defined subsystem that is part of a large, complex system may be known ahead of time, where the task is to characterise the full system. Grey box system identification tasks can often be reduced to a single sub-problem of black box system identification by removal of the known physics and tackling them separately.

6.4 Overview of Black Box System Identification

Black-box system identification techniques are composed of the following – *a)* non-parametric methods, and *b)* parametric methods.

6.4.1 Non-parametric methods

Non-parametric methods do not seek a pre-assumed mathematical structure for the system. They aim to directly estimate the very kernel of what characterises every system *viz.* the Markov parameters in the time-domain and the Frequency Response Function (FRF) in the frequency domain, thereby requiring *infinite* number of data points for their representation. Major non-parametric system identification methods include

- Identification in time domain
 - Direct estimation of the system's Markov parameters through statistical correlation of its response to an unit-pulse input.
- Identification in frequency domain *i.e.*, of the FRF
 1. Direct estimation through input-output statistical cross-correlation.
 2. Empirical Transfer Function Estimate (ETFE) using Discrete Fourier Transforms (DFTs) of input and output sequences.

3. Smoothed periodogram estimates using Welch's method.
4. Blackman-Tukey Estimate using standard filter windows in digital signal processing (such as Hamming, Hanning, Bartlett, Boxcar etc.).

6.4.2 Parametric methods

Parametric methods aim to fit specific input-output data to some family of well-known mathematical constructs that are and widely applicable to a large variety of inputs. It is important to recognise that, in contrast to white-box system identification, the salient coefficients/properties of these mathematical structures *do not*, in any way correspond to physical properties of the system under consideration. Major parametric system identification methods use

- Transfer-function based frequency domain model structures
 1. Output Error (OE) model
 2. Auto Regressive with Exogenous Inputs (ARX) model
 3. Auto Regressive with Moving Average and Exogenous Inputs (ARMAX) model
 4. Box-Jenkins (BJ) model
- State-space time-domain model structures
 1. Ho-Kalman realisation
 2. Eigensystem Realisation Algorithm (ERA) realisation
 3. Deterministic and stochastic *subspace* structures

6.4.3 Investigation of suitable system identification methodology

Among the various system identification techniques mentioned, the non-parametric methods have some serious drawbacks. As outlined in section 6.2.2, the author is inspired by the trait of having a pre-assumed model structure that brought the baseline quadratic approximation closer to a successful realisation. The non-parametric methods do not conform to this philosophy. Furthermore, the requirement of infinite number of data samples in order to fully quantify the system dampens its feasibility for implementation in resource constrained environments. The author is of the opinion that resorting to truncation of the characteristic sequence shall only yield a sub-optimal solution. Hence non-parametric methods are ruled out for applying to the task at hand.

6.4 Overview of Black Box System Identification

While parametric state-space identification is a feasible alternative, these methodologies are tedious and error-prone. For instance, applying the Ho-Kalman algorithm requires construction of large-sized Block-Hankel matrices followed by a Singular Value Decomposition (SVD) operation. The ERA uses the identical set of operations of the Ho-Kalman procedure, except that certain blocks in the Hankel matrices are chosen at random for deletion for obtaining better estimates in low Signal to Noise Ratio (SNR) environments and for capturing slowly decaying phenomena with long time constants. The subspace methods are mathematically involved, requiring a profound understanding of concepts from linear algebra such as projections to orthogonal subspaces. The system under consideration is presented in section 6.5 and after linearity considerations, refined in section 6.7.2. It is composed of two independent Single Input Single Output (SISO) subsystems. However, the inflection point in the complexity-performance trade-off in state-space identification is achieved only when dealing with Multi Input Multi Output (MIMO) systems that suggest strong cross-coupling among its internal states or at least some degree of coupling among the various inputs and outputs. Furthermore, the impulse responses of the system(s) under consideration do not have long tails since they are characterised by relatively short time constants. Owing to these reasons, it was decided that state space identification methods shall not be adopted here.

Owing to a cornucopia of well-established technical know-how readily available in the systems engineers toolkit, transfer function based model structures are naturally amenable for control-oriented applications. However, there exists an apparent discrepancy to its usage for this case, that must be addressed first. Transfer function methods are a frequency domain technique and hence, the resulting model descriptions have mathematical structures radically different from the time-domain model equations of the conventional SPM within which they are to be embedded. This conundrum is resolved by closely inspecting the model's scope and its tractability for conversion to time domain as explained next.

It is worth remembering that, as per section 2.2.1, for the reduced order modelling of the *entire cell*, all frequency domain model groups were considered as out of scope of this thesis specifically due to the overhead of conversion from frequency to time domain for implementation and other associated difficulties. The blanket exclusion nature of this statement is to be revisited considering the specific scope of the problem at hand. The body of literature on frequency domain Reduced Order Models (ROMs) discuss obtaining physics-based *transcendental* transfer functions for *all* electrochemical quantities of the coupled

6.5 Introduction to Electrolyte Time-Evolution Subsystems

Partial Differential Algebraic System (PDAE) system of table 1.1 through a top-down approach. However, the frequency domain system identification methods are concerned with obtaining standard *rational* transfer functions for a much narrower scope *viz.* the time-evolution subsystem, through a bottom-up approach. Such rational transfer functions are to be obtained for SISO systems for which an approximation-free effortless conversion already exists in classical control theory and is presented in section 6.8.7. In view of their overwhelming simplicity and familiarity to control engineers, after considering these arguments that circumvent their only apparent impediment to adoption, *transfer function* based system identification was chosen for tackling the problem at hand. The steps leading to the identification procedure is presented next.

6.5 Introduction to Electrolyte Time-Evolution Subsystems

The first order ODEs of eqs. (5.94)–(5.96) in the baseline quadratic approximation model for electrolyte concentration describe the time-evolution of the overall number of moles of Li^+ in each of the three regions of the cell $Q_{e,j}$. Through system identification, the author seeks to obtain the two rational transfer functions of $Q_{e,\text{neg}}$ and $Q_{e,\text{pos}}$ to the applied current I in the frequency domain *i.e.*, $\frac{Q_{e,n}(s)}{I(s)}$ and $\frac{Q_{e,p}(s)}{I(s)}$. Based on the DFN model, the total moles of Li^+ per unit area in the separator $Q_{e,s}$ is not a function of the exogenous applied current. Therefore, the baseline quadratic approximation ODE is retained for computing its time-evolution.

6.6 Design of Persistent Excitations

In order to successfully apply any system identification technique, the input signal must be carefully designed to be persistently exciting [207]. Narendra and Annaswamy [208, 209] were among the earliest researchers to provide a detailed treatment of the desirable properties of persistent excitation and their implication to the quality of the identification output. A practical method to achieve persistent excitation is to subject the system under consideration to a sequence of well-characterised input signals that are capable of exciting its hypothesised modes. For this task, the author of this thesis chose to use the data-quality guidance provided by The Mathworks Inc. [210] and performed an iterative refinement until the identification procedure resulted in a generalisable model.

Before discussing the shape characteristics of the input sequence, its magnitude must be established. The various specially prepared input sequence families do not share a common definition for their magnitudes. A guiding principle in system identification is that it is important to have the input signal's magnitude to be representative of standard operating conditions if the system is linear. Although standardised drive cycle profiles are available, from which a speed to current mapping can be performed, it is impossible to predict a priori, the specific amplitudes of currents that the cell may undergo under real-life load conditions. Without further deterministic information, the author of this thesis chose to interpret magnitude as being the peak amplitude of the input current profile. As seen in fig. 5.12, the representative Urban Dynamometer Driving Schedule (UDDS) drivecycle input profile corresponds to a peak of $3C$ *i.e.*, 180 A. Following the standard principles of system identification, it is desirable for the inputs to the system to lie along some measure of central tendency. This is to enable the identified system to generalise well *i.e.*, not deviate too far from the truth when subject to inputs that are far away from the central measure. Yet another consideration is not to saturate the identified model by choosing input magnitude to be too close to the peak of the expected operating range. Taking into account all aforementioned considerations, the peak amplitude of the input current was fixed at $2C$ *i.e.*, $2/3^{\text{rd}}$ of the UDDS profile's peak current amplitude.

6.6.1 Training current profile

Since not much prior information is available about the poles and zeros of the electrolyte subsystem(s) in question, a wide variety of special waveforms with a sampling interval of 1 s were used for the current perturbation used in this system identification task. The specific input sequence consisted of

1. Random Binary Signal (RBS) (0–199 s)
2. 'Chirp' *i.e.*, a swept cosine signal from 0–100 mHz (200–799 s)
3. Periodic Random Binary Signal with a period of 200 s and 2 such periods (800–1199 s)

thereby helping to obtain a wide-sense persistent excitation. The swept cosine signal is designed to excite the low frequency (DC) modes of the electrolyte subsystem and helps to capture the system's response to constant and other systematically varying input profiles. The two RBSs are intended to target the poles and zeros of the electrolyte subsystem that

would typically be excited by highly dynamic input profiles. The periodicity in one of the RBSs was introduced to draw out any repeated real pole or complex conjugate poles in the system that might otherwise appear to be a single real pole. The presence of both low and high frequency spectra in the combined training set presents a high degree of confidence to capture the relevant dynamics of the electrolyte subsystem. The input current profile used for this system identification task is plotted in fig. 6.1.

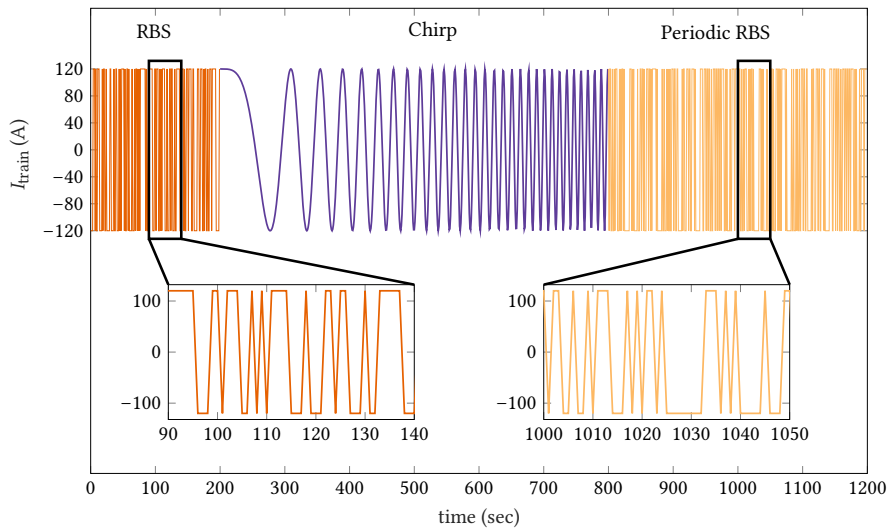


Figure 6.1 Input current profile used as the training set for system identification. The sequence consists of *a*) a Random Binary Signal, *b*) a chirp or swept cosine signal (0–100 mHz), and *c*) a periodic Random Binary Signal thereby covering both low and high frequency spectra while incorporating the potential to excite any periodic modes in the system to be identified.

6.6.2 Validation current profile

For the purposes of identification, the P2D model is considered as the true system. First, the current profile from the training set is applied to the P2D model. Its simulation results, in particular the numerically solved concentration values at each spatially discretised node in each of the three regions per time-step is integrated over the thickness of the respective regions and multiplied with their respective porosities to obtain the number of moles of Li^+ per unit area in each of the three regions $Q_{e,j}$. Only the quantities $Q_{e,n}$ and $Q_{e,p}$ are chosen as the outputs for system identification and a transfer function model is fitted as per the evaluation procedure discussed in section 6.8.

As with any classical curve fitting (numerical regression) procedure, system identification is also prone to overfitting the training data. In general, the ‘best’ transfer function that

identifies the given system is the lowest order model that not only minimises the training error, but also minimises the error on a previously unseen validation dataset. In the absence of an independent validation dataset, the training error can be made arbitrarily small by increasing the number of poles and zeros of the transfer function models without any bounds. However, such a model shall not have truly identified the dynamics of the system and shall not generalise well to real-world datasets outside the training realm. Hence, having an independent validation current profile for the task at hand is of paramount importance. The validation profile visualised in fig. 6.2 consists of the following sequence

1. Periodic Random Gaussian Signal (RGS) with 4 periods of 200 s each (0–799 s)
2. Pseudorandom Binary Signal (PRBS) for emulating white noise *i.e.*, with a flat power spectra across the frequency spectrum (800–999 s)
3. Multi-sine signal *i.e.*, a signal consisting of sinusoids at various fundamental frequencies added together (1000–1199 s)

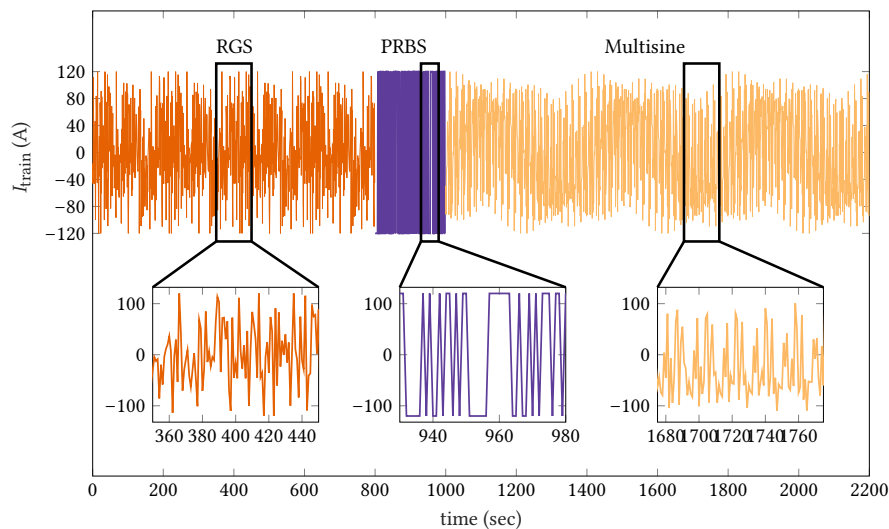


Figure 6.2 Input current profile used as validation set for system identification. The sequence consists of *a*) a Random Gaussian Signal, *b*) a Pseudorandom Binary Signal, and *c*) a multisine waveform. The overall sequence is intended to emulate the flat power spectrum of white noise (with the PRBS) and excite any poles and zeros within 3σ spread of the RGS mean. The multisine signal is composed of sinusoids with fundamental frequencies from 100 mHz up to the Nyquist frequency. Its amplitude variation across the frequency spectrum increases the probability to capture the system’s modes that were possibly missed by the preceding two waveforms.

The MATLAB code used for generating the training and validation input profiles is given in code snippet 6.1.

```

% Needs matlab's system identification toolbox
clear; close all; clc; format short g;
warning('off','Ident:dataprocess:idinput7'); % suppress sysid warnings
I_1C = 60; % Amps
range = 2*[-I_1C I_1C]; % peak-peak swing is  $\pm 2C = 40$  A
NumCh = 1; % no of channels (used by sysid toolbox for multichannel id)
Ts = 1; % sampling interval

%% Random Binary Input Signal (RBS)
N = 200; % samples per quantum of each waveform
u1 = idinput(N,'rbs',[],range); % 'idinput' from sysid toolbox
%% Chirp Signal (swept cosine)
t_chirp_start = 0;
t_chirp_end = 3*N*Ts; %
t = linspace(t_chirp_start,t_chirp_end,3*N);
f0 = 0;
f1 = 1e-1; %  $f_1 = 100$  mHz is the max chirp frequency
u2 = max(range)*chirp(t,f0,t(end),f1)';
%% Periodic Random Binary Input Signal (Periodic RBS)
bin_seq_Period = N; % seconds
bin_seq_Period_N = ceil(bin_seq_Period/Ts); % samples
bin_NumPeriod = 2;
u3 = idinput([bin_seq_Period_N,NumCh,bin_NumPeriod],'rbs',[],range);
%% Random Guassian Signal (RGS)
rgs_Period = N; % seconds
rgs_Period_samples = ceil(rgs_Period/Ts);
rgs_NumPeriod = 4;
u4 = idinput([rgs_Period_samples,NumCh,rgs_NumPeriod],'rgs',[],range/2);
%% PseudoRandom Binary Signal (PRBS)
prbs_Period = N; % seconds
prbs_Period_samples = ceil(prbs_Period/Ts);
u5 = idinput(N,'prbs',[],range);
%% Multisine signal (sum of sines)
samples_per_Period = 2*N;
NumPeriod = 3;
[u6,freq] = idinput([samples_per_Period 1 NumPeriod],'sine',[],range);

%% Split into training and validation data sets
I_load_train = [u1;u2;u3];
I_load_validate = [u4;u5;u6];

```

Code snippet 6.1 Generation of training and validation input current profiles in MATLAB

6.7 Investigation of Linearity and Time Invariance

The transfer function identification techniques listed in section 6.4 work best for Linear Time-Invariant (LTI) systems. At first glance, this seems to be overly restrictive for the system(s) at hand. When treated as a single macroscopic entity, a lithium ion battery, exhibits overall non-linear characteristics, particularly due to strong non-linearities in *a*) the Butler-Volmer reaction kinetics (see eq. (1.7)), and *b*) the Open Circuit Potentials (OCPs) of the two electrodes (see eq. (5.58) and eq. (5.58)). However, we are dealing with a much narrower scope *i.e.*, the systems under consideration are just the two sub-system entities (one per electrode) that transform the applied current at a particular time-step to the overall moles per unit area of Li^+ ions in the corresponding electrode region of the electrolyte at that same instant. Therefore, it is the linearity and time-invariance of these *subsystems* that must be investigated.

6.7.1 Time-invariance of the electrolyte time-evolution subsystems

A test for time-invariance is prescribed in the lecture notes on system identification by Plett [211]. The steps involved therein are reproduced here after being suitably adapted to the notation of the subsystems at hand.

1. Apply input $u_1(t) = I(t)$ to the system and measure the outputs $Q_{e,n_1}(t)$ and $Q_{e,p_1}(t)$.
2. Apply a delayed version of the input by τ seconds *i.e.*, $u_2(t) = I(t - \tau)$ to the system and measure the outputs $Q_{e,n_2}(t)$ and $Q_{e,p_2}(t)$.
3. If $Q_{e,n_2}(t) = Q_{e,n_1}(t - \tau)$ and $Q_{e,p_2}(t) = Q_{e,p_1}(t - \tau)$ for all possible delays τ , as well as for all choice of input signals $I(t)$, then the systems are time-invariant.

For the systems at hand, it is not strictly required to apply this prescriptive test. Unless a fundamental change in the underlying reaction phenomena/chemistry occur that alter the performance over time, these systems can be treated as time-invariant. Factors that induce time-dependent shift in the behaviour of lithium ion batteries are degradation phenomena such as thickening of Solid-Electrolyte Interphase (SEI) layer, dendrite growth or mechanical fatigue in electrodes which in-turn affect electrolytic diffusion and conductivity. Yet another cause of time-dependent behavioural change is the drift in parameter values. However, these phenomena are typically one or more orders of magnitude slower than the P2D dynamics.

6.7 Investigation of Linearity and Time Invariance

This separation of time-scales imply that, in practice they can be decoupled. Therefore, separate models can be identified for the faster and slower processes. A suitable model-blending approach can then be considered to cover all processes across time-scales. Although the concepts developed here for the fast electrolyte dynamics can be suitably adapted to such slow phenomena, their study falls outside the scope of this thesis and is left as an exercise for future work. Thus, the overall battery system, and hence by extension, the two subsystems considered are deemed to be time-invariant. However, in the interest of completeness, this author systematically applied the aforementioned test procedure with every combination arising from the choice of ten time-delay values and the following six current profiles – *a*) constant current 1C discharge, *b*) constant current 3C discharge, *c*) constant current 1C charge, *d*) UDDS input profile with peak amplitude of 3C, *e*) training profile used in system identification (see fig. 6.1), and *f*) validation profile used in system identification (see fig. 6.2). Finally, these tests were repeated for a choice of five different initial States of Charge (SOCs) – 90 %, 70 %, 50 %, 30 % and 10 %[‡].

Figure 6.3 demonstrates the time-invariance of the subsystems considered at an initial SOC of 50 % for a time-delay of 130 s using the highly dynamic system identification training sequence that was synthesised by this thesis author (see fig. 6.1). The applied current profile $u_1(t)$ (top row of the central column) produces the outputs $Q_{e,n_1}(t)$ and $Q_{e,p_1}(t)$ shown in the top left and top right plots respectively. When the delayed version of this input sequence $u_2(t) = u_1(t - \tau)$ (middle row, middle column) is applied, it results in the outputs $Q_{e,n_2}(t)$ and $Q_{e,p_2}(t)$ to its left and right respectively. Following the steps of the test procedure, subtracting these outputs from the correspondingly delayed versions of their original counterparts result in zero residuals, thereby proving time-invariance of these subsystems under these representative test conditions. The residual sequences in the bottom row of plots are of $\mathcal{O}(10^{-15})$ and arise due to numerical round-offs that occur when operating close to the noise floor of the machine's floating point units.

Similar to the case demonstrated here, all tests for time-invariance for all permutations of the chosen operating conditions passed successfully *i.e.*, the delayed version of the original output signals accurately matched with the responses to the corresponding delayed

[‡]The number of moles of Li^+ per unit area in the electrolyte does not depend on the electrode's SOC. However, different starting point of SOC's were considered to have a wide variety in the length of the recorded data until cut-offs were hit. *e.g.* starting at 90 % SOC could mean that for a current spike early in the profile, upper cut-off voltage shall be hit sooner leaving a smaller set of logged simulation data.

6.7 Investigation of Linearity and Time Invariance

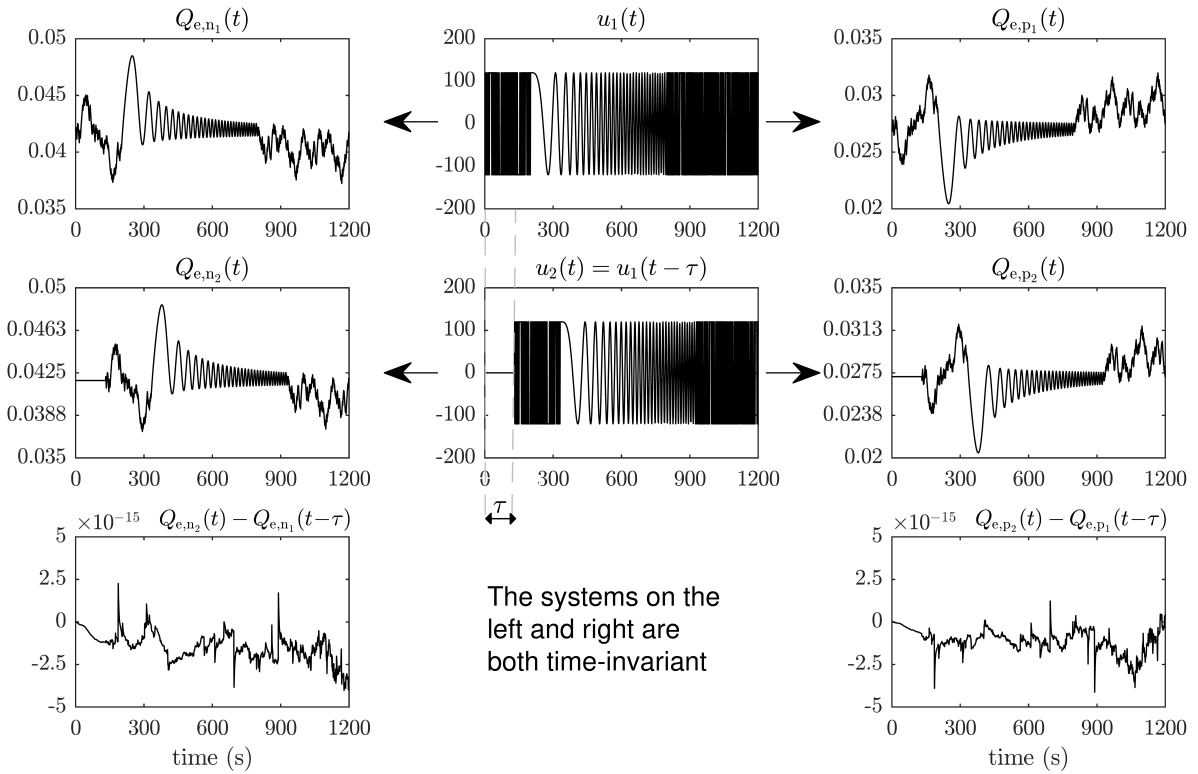


Figure 6.3 Demonstration of time-invariance of the subsystems considered. The applied current profile $u_1(t)$ is the system identification training sequence from fig. 6.1 (top row of the central column). The top left plot shows the response $Q_{e,n_1}(t)$, while that on the top right shows $Q_{e,p_1}(t)$. The second row of the middle column shows the same input sequence delayed by $\tau = 130$ s. Application of this current profile $u_2(t) = u_1(t - \tau)$ results in the outputs $Q_{e,n_2}(t)$ and $Q_{e,p_2}(t)$ to its left and right respectively. Subtracting these from the correspondingly delayed versions of the original outputs result in zero residuals, thereby proving time-invariance of these subsystems. The jitter shown in the bottom row of plots is $\mathcal{O}(10^{-15})$ in magnitude and are due to the numerical roundoffs that occur when operating close to the noise floor of the machine's floating point units.

input (down to machine precision), thereby confirming the time-variance of the subsystems considered in the system identification problem, which enables us to proceed further.

6.7.2 Linearity analysis of the electrolyte time-evolution subsystems

De-biasing of input signals

In the analyses of linearity of systems, it is a recommended practice to de-bias the output and input quantities about their mean operating conditions. The input signal in this case is the applied load current $I(t)$, which can be both positive (during discharge) and negative (during charge). The mean of the training profile is -1.167 A and that of the validation profile

6.7 Investigation of Linearity and Time Invariance

is -0.3273 A. Clearly, the mean values are dependent upon the actual current profile used. The appropriately de-biased signal *i.e.*, $\tilde{I}(t) = I(t) - \bar{I}(t)$ is to be used for training and validation data sets in the system identification procedure. For the purpose of linearity analysis, it is a standard practice to simply apply a step change in input (from zero) and measure the output responses, thereby bypassing the de-biasing requirements.

For the output signals, bias values can be pre-computed analytically and accounted for. The overall number of moles of Li^+ per unit area in any region within the cell cannot be physically negative. Even though under high C-rates, ion depletion at localised spatial locations (such as the current collectors) is certainly possible, the entire thickness of any region cannot become devoid of ions at any point in time since the cell shall instantaneously cease to work. Thus, for a typical well-designed cell operating within the manufacturer prescribed C-rate limits, the output signals under consideration operate in a small window about their initial values. In the author's simulations, even at $\pm 5\text{C}$, the overall number of moles of Li^+ in any cell region exhibited a maximum change of less than 15 % from its initial value. Thus, the de-biased output variables for system identification $\tilde{Q}_{e,j}(t)$ can be obtained by subtracting their respective initial values $Q_{e,j}(0)$ (see eq. (5.97) and eq. (5.99)) from $Q_{e,j}(t)$

$$\tilde{Q}_{e,n}(t) = Q_{e,n}(t) - Q_{e,n}(0) \quad (6.5)$$

$$\tilde{Q}_{e,p}(t) = Q_{e,p}(t) - Q_{e,p}(0) \quad (6.6)$$

which implies that the transfer functions to be identified have to be modified to be $\frac{\tilde{Q}_{e,n}(s)}{\tilde{I}(s)}$ and $\frac{\tilde{Q}_{e,p}(s)}{\tilde{I}(s)}$ respectively. This does not affect the time-invariance proved in section 6.7.1 since the initial values $Q_{e,j}(0)$ are merely constants and hence not time-dependent.

Test for linearity

Similar to the test for time invariance described in section 6.7.1, a test for linearity is also prescribed in the lecture notes on system identification by Plett [211]. The steps involved therein are reproduced here after being suitably adapted to the notation of the subsystems at hand. This is essentially a recipe for testing the superposition principle.

1. Apply input profile $I_1(t)$ to the system and obtain outputs $\tilde{Q}_{e,n_1}(t)$ and $\tilde{Q}_{e,p_1}(t)$.
2. Apply a different profile $I_2(t)$ to the system and obtain outputs $\tilde{Q}_{e,n_2}(t)$ and $\tilde{Q}_{e,p_2}(t)$.

6.7 Investigation of Linearity and Time Invariance

3. Now apply an input profile $I_3(t) = \alpha I_1(t) + \beta I_2(t)$ and obtain a corresponding set of outputs $\tilde{Q}_{e,n_3}(t)$ and $\tilde{Q}_{e,p_3}(t)$.
4. If $\tilde{Q}_{e,n_3}(t) = \alpha \tilde{Q}_{e,n_1}(t) + \beta \tilde{Q}_{e,n_2}(t)$ and $\tilde{Q}_{e,p_3}(t) = \alpha \tilde{Q}_{e,p_1}(t) + \beta \tilde{Q}_{e,p_2}(t)$ for all possible $\{\alpha, \beta\}$ and for all choice of input signals $\{I_1(t), I_2(t)\}$, then the systems are linear.

As in the time-invariance test, the same set of five different initial SOCs[‡] – 90 %, 70 %, 50 %, 30 % and 10 %, was retained for these linearity tests. For each test run, a pseudo-random number generator was used to select the values of $\{\alpha, \beta\}$ from the set of real numbers \mathbb{R} (not restricted to the set of integers \mathbb{Z}) in the closed interval spanning $[-1.25, 1.25]$. Negative values are acceptable for both the scaling coefficients since the resulting composite input $I_3(t)$ can be either positive or negative. The composite signal $I_3(t)$ was obtained by taking a random combination of any two of the following current profiles – *a*) step input with a constant current 1C discharge, *b*) step input with a constant current discharge at C/5, *c*) step input with a constant current 1C charge, and *d*) step input with a constant current charge at C/5.

The scaling factors α and β were restricted to the range $[-1.25, 1.25]$ in consideration of limiting the peak applied current to within a $\pm 3C$ window – the operating condition for most Battery Electric Vehicles (BEVs), so that the isothermal assumption for the model shall remain valid. This peak current corner case occurs when the pseudo-random generator chooses both scaling factors at the selected range's limits for the 1C constant current discharge or charging cases. The limited range of the scaling factors are also motivated by the fact that most real-world systems remain linear only within a certain operating window. In particular, care must be taken to ensure that the cell's SOC during the linearity test remains within its physical limits for any initial SOC. Furthermore, localised saturation or depletion of ions for extended durations must be avoided. Hence it can be concluded that, with the chosen range for the scaling factors, if the two subsystems under consideration remain linear everywhere below a peak current of $\pm 3C$ in the isothermal case, then the linearity tests are considered as passed. Future extensions to undertake a temperature-dependent system identification exercise can potentially use a first-order Taylor expansion about this operating window. The discussion thus far has fully established all the conditions for conducting the test for linearity.

Figure 6.4 illustrates one instance of a linearity test wherein constant currents and integer scaling factors are used for the sake of illustration. The plots in the left column deal with the electrolyte time-evolution subsystem in the negative electrode region. Similarly, the plots

6.7 Investigation of Linearity and Time Invariance

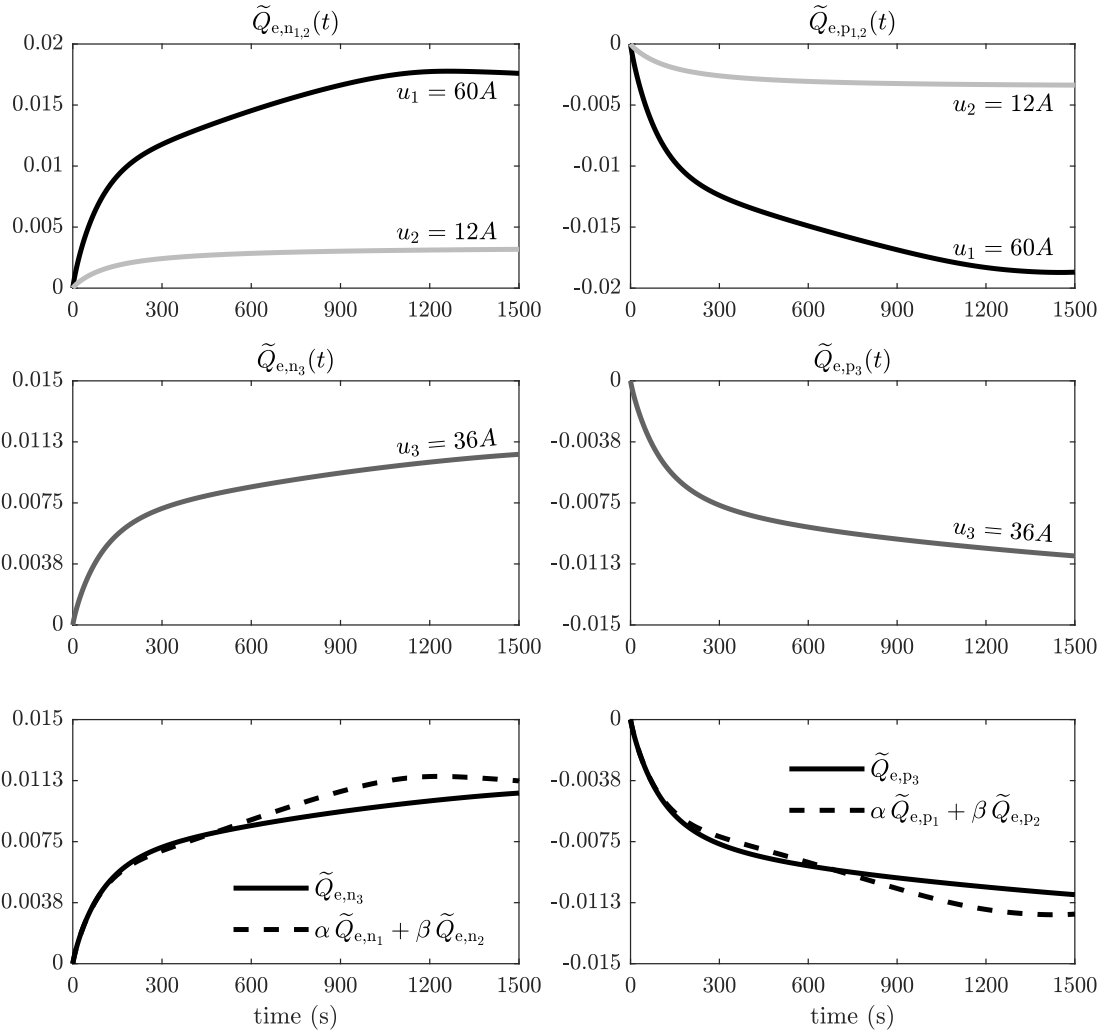


Figure 6.4 Illustration of one instance of linearity tests for the subsystems under consideration. For this visualisation, constant current inputs are used throughout. The top row of plots shows $\tilde{Q}_{e,n}$ and $\tilde{Q}_{e,p}$ for two step inputs $I_1(t) = 60\text{ A}$ and $I_2(t) = 12\text{ A}$ *i.e.*, discharge with 1C and C/5 currents respectively. The second row of plots shows \tilde{Q}_{e,n_3} and \tilde{Q}_{e,p_3} for $I_3 = 36\text{ A}$, where $I_3 = \alpha I_1 + \beta I_2$ with $(\alpha, \beta) = (1, -2)$. The last row of plots overlays these quantities with the manually computed linear combination of their two preceding responses. Had these sequences overlapped exactly, the systems would have been exactly linear. Despite exhibiting deviations over the considered horizon, the transient responses in both electrode regions do follow the superposition principle. Even past the transient, maximum error in both cases is an order of magnitude lower than the individual outputs. Hence, the two systems are deemed to be *approximately* linear.

in the right column deal with the corresponding subsystem in the positive electrode region. A discharge current of 1C *i.e.*, 60 A is first applied and the corresponding outputs \tilde{Q}_{e,n_1} and \tilde{Q}_{e,p_1} are obtained. Secondly, a discharge current of C/5 *i.e.*, is applied and the corresponding outputs \tilde{Q}_{e,n_2} and \tilde{Q}_{e,p_2} are obtained. These set of responses are plotted in the top row of

fig. 6.4. Now, a third value of input current I_3 , computed as a linear combination of the previous input currents *i.e.*, $I_3 = \alpha I_1 + \beta I_2$ is applied. For illustrative purposes, the integer set $(\alpha, \beta) = (1, -2)$ was chosen for the scaling coefficients, which implies $I_3 = 12$ A. The corresponding outputs \tilde{Q}_{e,n_3} and \tilde{Q}_{e,p_3} are plotted in the middle row. As per the test for linearity, if these signals are equal to the signal generated by manually computing the linear combination of the preceding two outputs, then the system is linear.

The plots in the third row show \tilde{Q}_{e,n_3} and \tilde{Q}_{e,p_3} overlaid with their respective linear combination signals. For the subsystem in the negative electrode region, the transient performance matches precisely until ≈ 450 s, whereas that for the positive electrode region exhibits a good matching for approximately the first 250 s. However, for the horizon considered the two overlaid plots do not overlap exactly. Hence, the systems are not truly linear. However, the exhibited behaviour is quite close to linearity, with the maximum absolute error in each region being $\mathcal{O}(10^{-4})$ even past the initial transient, which is an order of magnitude lower than its individual components. This behaviour was exhibited for all test instances considered. Considering that for dynamic simulation runs, the transient performance is paramount to the good performance of the model, in conjunction with the aforementioned low error metric, these subsystems can be considered to be *approximately* linear.

Based on the analysis presented here, LTI behaviour for the two subsystems is assumed, which facilitates in proceeding with the actual system identification procedure.

6.8 Transfer Function Identification Procedure[§]

6.8.1 The transfer operator and its model form

In a classical system identification task, the discrete-time transfer functions for the systems under consideration need to be determined. These discrete-time transfer functions are based on Z-transforms in the frequency domain. However, for the purpose of working in time-domain, an analogous linear operator q that performs a forward shift on its input *i.e.*, $qu[k] \mapsto u[k + 1]$. Similarly, applying the backward shift operator q^{-1} on the input yields its value at the previous time-step *i.e.*, $q^{-1}u[k] \mapsto u[k - 1]$.

[§]The early stages of this section presents this author's digested summary of the theoretical framework adapted from a subset of content from the lecture notes on system identification by Plett [211–213].

6.8 Transfer Function Identification Procedure

In a generic LTI system wherein measurements are corrupted by noise, the system dynamics are represented by the transfer operator $G(q)$ [¶] that acts on the applied input $u[k]$, whereas the noise dynamics are represented by the disturbance operator $H(q)$ that acts to filter (or shape) an assumed white noise input $e[k]$. The overall output can be written as the linear combination

$$y[k] = G(q)u[k] + H(q)e[k] \quad (6.7)$$

where $G(q) = \frac{B(q)}{A(q)}$ and $H(q) = \frac{C(q)}{D(q)}$ are the transfer operators describing the dynamics of the system and disturbance respectively.

$A(q), B(q), C(q)$ and $D(q)$ are rational polynomials in q . The two transfer operators $G(q)$ and $H(q)$ can be represented by

$$G(q) = q^{-n_k} \frac{b_1 q^{-1} + \dots + b_{n_b} q^{-n_b}}{1 + a_1 q^{-1} + \dots + a_{n_a} q^{-n_a}} \quad (6.8)$$

$$H(q) = q^{-n_l} \frac{c_1 q^{-1} + \dots + c_{n_c} q^{-n_c}}{1 + d_1 q^{-1} + \dots + d_{n_d} q^{-n_d}} \quad (6.9)$$

where (n_k, n_l) are the number of transport delay samples, (n_b, n_c) the number of feedforward coefficients and (n_a, n_d) , the number of feedback coefficients in $G(q)$ and $H(q)$ respectively. Thus, the system identification task becomes one that of estimating the

1. number of transport delay samples n_k
2. number of feedforward coefficients (zeros) n_b
3. zeros themselves b_1, b_2, \dots, b_{n_b}
4. number of feedback coefficients (poles) n_a
5. pole locations $a_1, a_2 \dots a_{n_a}$
6. coefficients of the noise filter $H(q)$ [¶].

for each of the two transfer operators $G_1(q)$ and $G_2(q)$ *i.e.*, the electrolyte time-evolution subsystems in the negative and positive electrode region respectively.

[¶]The term transfer operator in the time domain mathematically corresponds to the term transfer function in the frequency domain. Mathematically, $G(q) = G(z)|_{z=q}$.

[¶]In the ARMAX estimation of non-linear dynamics, the noise-filter is capable of returning non-zero coefficients even if the identification data set is obtained from a *noise-free* simulation of the P2D model as is the case here. However, as a first-order approximation, in the interest of simplicity and considering that this work serves as an introduction to the application of system identification to SPMs, this thesis author errs on the side of making the linearity assumption, which is valid only for low C-rates, whilst acknowledging that this limitation could be relaxed by incorporating the coefficients of the noise-filter $H(q)$ in the future. For the rest of this work, only the coefficients of the linear plant dynamics $G(q)$ are estimated.

6.8.2 Estimation of transport delay

The transport delay n_k can be estimated visually by inspecting the step response of the systems under consideration.

In fig. 6.4, step inputs of $I_1 = 60$ A, $I_2 = 12$ A, and $I_3 = 36$ A were applied to the two subsystems. Inspecting closely all the responses *i.e.*, \tilde{Q}_{e,n_1} , \tilde{Q}_{e,n_2} and \tilde{Q}_{e,n_3} in the negative electrode region, and \tilde{Q}_{e,p_1} , \tilde{Q}_{e,p_2} and \tilde{Q}_{e,p_3} in the positive electrode region, it is clear that all these outputs start exactly at zero. Therefore, there is no delay term to be considered for the transfer operators *i.e.*, $n_k = 0$ for both subsystems.

6.8.3 Choice of model structure

Among the transfer-function model structures mentioned in section 6.4.2, the ARX model structure is too simplistic to consider. Despite the fact that its numerical computation involves only basic linear algebra operations, that can be efficiently handled on modern computing systems, it is considered to produce poor estimates of the system's poles and zeros. In the absence of contributions from the noise-term, the all-encompassing model structure used by the Box-Jenkins approach is deemed to be unnecessary for the problem at hand. Therefore, the two model structures considered were ARMAX and OE for the coefficient determination.

6.8.4 Starting guesses for coefficient orders

At first, the training profile of fig. 6.1 is de-biased (through mean removal) and applied as the input current profile in a P2D simulation beginning at 50 % SOC. The outputs of this simulation are suitably post-processed as per the following sequence of steps.

1. The concentrations solved at various node locations within each electrode are numerically integrated over the corresponding electrode thicknesses using trapezoidal rule.
2. The resulting integral value is multiplied with the porosity of the corresponding electrode region to obtain $Q_{e,n_{\text{train}}}(t)$ and $Q_{e,p_{\text{train}}}(t)$.
3. These quantities are then de-biased by subtracting their initial values to obtain $\tilde{Q}_{e,n_{\text{train}}}(t)$ and $\tilde{Q}_{e,p_{\text{train}}}(t)$.

6.8 Transfer Function Identification Procedure

The same procedure is repeated for the validation current profile of fig. 6.2 to obtain $\tilde{Q}_{e,n_{\text{val}}}(t)$ and $\tilde{Q}_{e,n_{\text{val}}}(t)$. These data sets are used for all subsequent sub-tasks involved in this system identification exercise.

To facilitate a smaller search window for the coefficient determination in parametric transfer function methods, a hand-estimation of coefficient order through non-parametric methods may be first considered. This coarse estimate acts as a feeder to aid the faster convergence of the non-linear optimisation algorithms used in parametric methods. In this work, a basic spectral analysis using a Hanning window implemented using the MATLAB command `spa` is applied to time-domain data to transform it into frequency response data.

Figure 6.5 shows the Bode plots of the frequency response to the training set in the negative electrode (left column) and positive electrode (right column) regions of the cell. It is important to note that these Bode diagrams obtained by such non-parametric methods only represent an approximation of the physical dynamics intended to help in initial estimates of the system behaviour. Some preliminary understanding of the various characteristics of the system can be gleaned from these Bode diagrams. The first visually striking feature is the similarity in the general shape of the approximate frequency characteristics in the negative and positive electrode regions, both in the magnitude response and in the phase response. This confirms the author's assumptions of equal 'complexity' in the symbolic regression search discussed in section 6.1.1. This is also congruent with the physical behaviour of the electrolyte in these two regions.

Finite DC gain

By visual extension of the frequency responses towards lower frequencies, it is clear that the DC gains of both the systems are finite and below unity. This behaviour can clearly be seen in the time-domain responses of fig. 6.4. For the plotted time-horizon, this effect is most visible for the case of the 12 A constant current input, wherein the responses of both regions settle to a finite value after an initial transient. Finally, the finiteness of the DC gain helps to narrow down the search window for the parametric model structures. In particular, this fact indicates that the model structures to be trialled must not have any integrator terms (or poles at the origin of the complex plane).

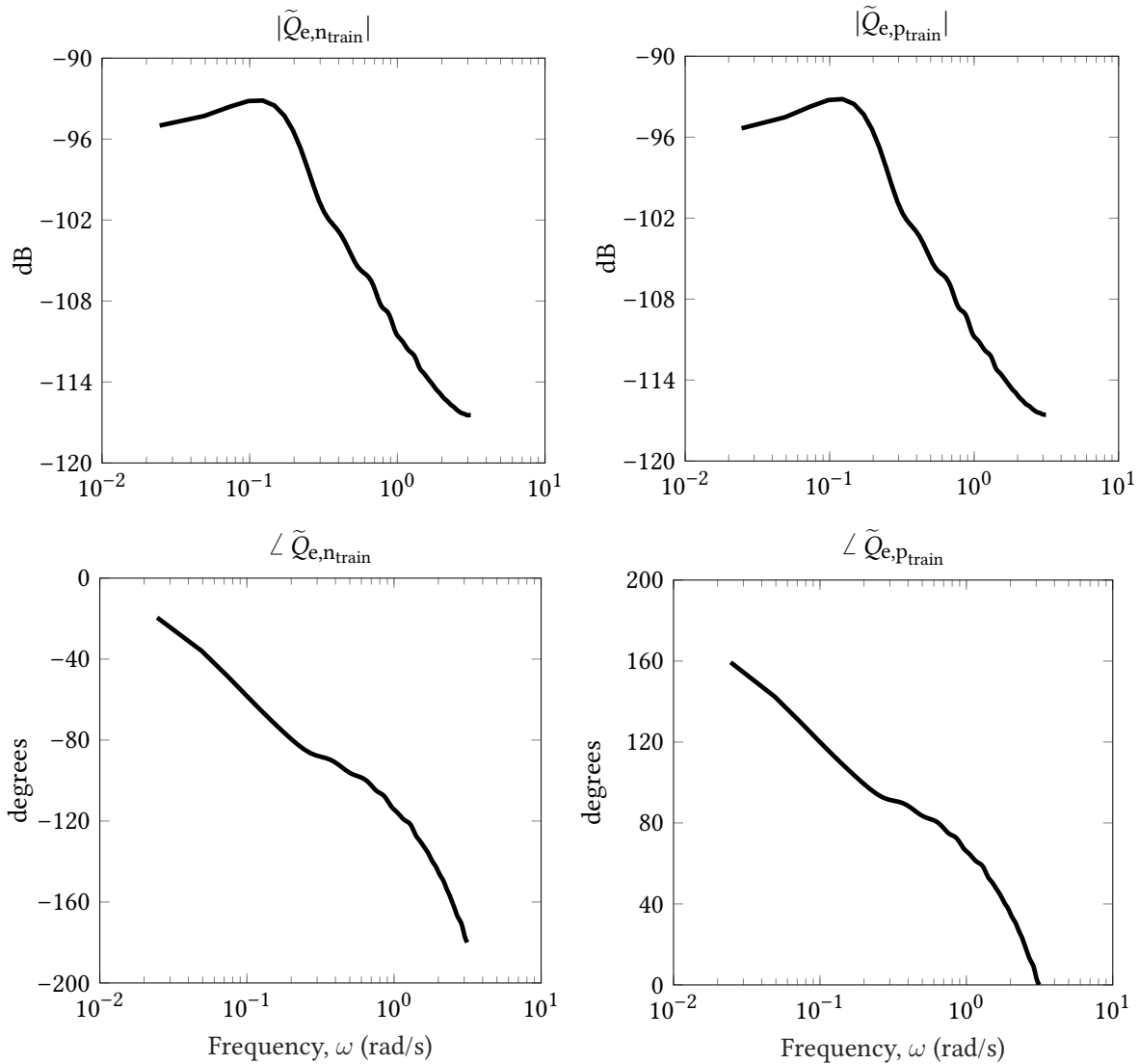


Figure 6.5 Bode plots showing the estimated frequency response for the two subsystems under consideration. The frequency response data was obtained through a spectral analysis *i.e.*, by computing the ratios of spectra of the de-biased input and output sequences. The sequences were smoothed using a Hanning window before computing the ratio.

Resonance and model order

First order transfer functions do not exhibit characteristic peaks or resonances in their frequency responses. However, for the Bode magnitude plots in fig. 6.5, a pronounced resonance around 0.15 rad s^{-1} is observable. This has an enormous impact — it presents an important clue that the first order time-evolution ODEs of eq. (5.94) and eq. (5.96) are inadequate to represent the system dynamics.

Estimation of number of poles and zeros

The high-frequency roll-off in the slopes of the Bode magnitude plots in fig. 6.5 provide clues on the number of poles in the system. The corner frequency ω_c in both cases appear to be around 0.15 rad s^{-1} . The high-frequency slope of both systems is $\approx 20 \text{ dB per decade}$, which implies that they have at-least one more pole than the number of zeros if using a continuous time transfer function. For the corresponding z-domain transfer function, this implies $n_a \geq n_b$. Looking at the phase plot of the two electrode regions, it can be hypothesised that there exists at-least one zero in these continuous-time systems around the $0.3\text{--}0.4 \text{ rad s}^{-1}$ frequency range. The discrete-time sampling process adds an additional zero to the system.

Based on this preliminary analysis, the estimates are $n_k = 0, n_b \geq 2, n_a \geq 3$. Only asymptotic approximations to corner frequencies can be estimated from the Bode plots. Furthermore, the estimated locations are not used in the parametric system identification algorithms and is of much less importance than the model order estimates. With this initial understanding, the parametric system identification procedure is carried out.

6.8.5 Refinement of coefficient orders using deterministic criteria

The initial estimate of coefficient orders in section 6.8.4 was performed based only on a visual inspection of the Bode magnitude plots. Owing to the fact that the frequency response data is the result of a crude ratio of spectra, there is a high probability of missing vital information on the number and locations of poles and zeros. Hence only a lower bound on the coefficient orders are available until this point. Next, a set of deterministic criteria is used to widen and refine the coefficient order range.

Although the ARX structure is deemed to be too simplistic (see section 6.8.3), owing to the fact that only linear algebra operations are involved, as opposed to numerical optimisation routines employed in the OE, ARMAX and Box-Jenkins structures, certain deterministic criteria can be incorporated for coefficient order selection. This can serve as a refinement of the initial number of coefficients guessed from the Bode magnitude plots of fig. 6.5.

For any model structure used, its error can be defined as

$$\varepsilon[k] = y[k] - \hat{y}_m[k] \quad (6.10)$$

6.8 Transfer Function Identification Procedure

where $y[k]$ are true measurements and

$$\hat{y}_m[k] = G(q)u[k] \quad (\text{eq. (6.7) with } H(q) \text{ set to } 0)$$

are model outputs obtained using the assumed transfer operator $G(q)$ (to be determined).

The number of numerator and denominator coefficients in $G(q)$ as well as their values are to be determined. This set of unknowns can be collected into a parameter vector θ . Thus, as per eq. (6.10), the error sequence is parametrised by θ , and its notation is amended to $\varepsilon[k; \theta]$.

For an input-output data set consisting of N samples, a generic cost function that may be applied for all the four model structures *viz.* ARX, ARMAX, OE and Box-Jenkins is

$$V_N(\theta) = \sum_{k=1}^N L(\varepsilon[k; \theta]) \quad (6.11)$$

where $L(\cdot)$ is a positive-valued scalar loss function.

In a typical system identification task, the sum of squares of the error sequence is used as the typical loss function, thereby yielding

$$V_N(\theta) = \sum_{k=1}^N \varepsilon^2[k; \theta] \quad (6.12)$$

The vector $\hat{\theta}$ that minimises this cost function is desired

$$\hat{\theta} = \arg \min_{\theta} V_N(\theta) \quad (6.13)$$

For the ARX model structure, eq. (6.12) reduces to a standard quadratic optimisation problem which may be solved analytically using least squares linear algebra. However, for robustness against estimation bias, instead of the standard Ordinary Least Squares (OLS) estimates, the Instrumental Variable (IV) estimation method [207] was used for this model order selection task. Applying this to the ARX model structure, two deterministic model order criteria have been defined – *a)* Akaike's Information Criterion (AIC), and *b)* Rissanen's Minimum Description Length (MDL) [207].

In the AIC, the optimal number of parameters \hat{d} in θ is obtained by minimising the modified log likelihood cost function

$$V_{N,\text{mod}}(\theta) = \ln V_N(\theta) + \frac{2d}{N}, \quad N \gg d \quad (6.14)$$

In the MDL criterion, the cost function in eq. (6.14) is modified to

$$V_{N,\text{mod}}(\theta) = V_N(\theta) \left(1 + \frac{d \ln N}{N} \right) \quad (6.15)$$

For the two subsystems at hand, both criteria converged to the same choices for the coefficient orders, yielding $n_a = 4$, $n_b = 4$ and $n_k = 0$. Therefore, these values were used as the starting points for the non-linear optimisation algorithms used in determining the exact pole and zero locations for the discrete-time transfer functions which is described next.

6.8.6 Final transfer function coefficients – Nonlinear optimisation

For the ARMAX and Box-Jenkins model structures, eq. (6.12) results in a non-linear cost function which is minimised iteratively using quasi-Newton approaches. The theoretical foundation of standard non-linear optimisation methods such as L-BFGS and Levenberg-Marquardt are well established whose detailed explanation is out of the scope of this thesis. Although state of the art methods are not covered, the interested reader may consult the textbook by Scales [214] for an introductory overview of this topic.

The final model structures (for both the positive electrode and negative electrode time-evolution subsystems) in the z-domain are given by

$$G(z) = \frac{b_1 z^{-1} + \dots + b_{n_b} z^{-n_b}}{1 + a_1 z^{-1} + \dots + a_{n_a} z^{-n_a}} \quad (6.16)$$

wherein the coefficients in the numerator and denominator are to be determined.

The number of coefficients obtained from section 6.8.5 was used as the initial guess for the coefficient orders in the non-linear optimisation. For the initial guesses for the numerical values of the coefficients $(a_1, a_2, \dots, a_{n_a})$ and $(b_1, b_2, \dots, b_{n_b})$, a randomised multi-start algorithm was used. For the two transfer functions identified, no distinction is made between whether the ARMAX structure or Box-Jenkins structure was used to arrive at the coefficients. Since the output magnitudes of $\tilde{Q}_{e,n}$ and $\tilde{Q}_{e,p}$ are of $\mathcal{O}(10^{-3})$, a constant scaling factor of $k = 1000$ is used to bring the order of magnitude of output data values to unity. A well-chosen scaling factor is often vital to the convergence of non-linear optimisation algorithms. Since the system is linear, this constant gain shall not fundamentally change the dynamics of the

6.8 Transfer Function Identification Procedure

system and can be accounted for by using the reciprocal scaling factor of 0.001 in numerical implementations. The identification procedure was carried out using MATLAB's System Identification Toolbox [215].

Table 6.2 A sample of results showing the coefficients of four discrete-time transfer functions identified for the electrolyte time-evolution subsystem in the negative electrode region. Only those models that yielded similar errors (within 0.5 %) across both input datasets were retained. The fourth order model from case C (shaded in grey) performed the best across both training and validation profiles and is chosen as the final model. The 95 % confidence bounds on the coefficients were at least one order of magnitude lower than their mean values reported here.

Case	Numerator				Denominator				Training accuracy (%)	Validation accuracy (%)
	b_1	b_2	b_3	b_4	a_1	a_2	a_3	a_4		
A	0.0026	-0.0025			-1.922	0.923			95.11	95.13
B	0.0028	-0.0052	0.0025		-2.833	2.669	-0.836		99.14	98.54
C	0.0028	-0.0075	0.0066	-0.0019	-3.577	4.767	-2.801	0.612	99.73	99.28
D	0.0026	0.0026	-0.0024	-0.0024	0.060	-1.906	-0.058	0.907	95.12	95.14

Table 6.2 shows the results obtained by applying the aforementioned non-linear identification routines to the time-evolution subsystems in the negative electrode region. The coefficient orders tried in the system identification procedure were informed by the inferences from the bode magnitude plots as well as that obtained by applying the deterministic AIC and MDL criteria. Only those models that yielded similar errors (within 0.5 %) across both input datasets were retained.

As discussed in section 6.8.4, a first order transfer function cannot capture all the dynamics of the subsystems under consideration. Therefore, the lowest order tried in the identification procedure was two (case A in table 6.2). As higher order models were tried, the system accuracy improves steadily as seen in cases B and C. However in order to avoid overfitting, the *lowest* order model that produces the highest matched accuracy across both training and validation profiles must be chosen.

Case D illustrates the importance of the initial values used in the non-linear optimisation algorithms. Despite using an identical number of coefficients as case C, the optimisation algorithm converges to a radically different set of zeros and poles resulting in a percentage error comparable to that of the simple second order case. The fourth order model from case C (shaded grey in table 6.2) performs the best across both training and validation profiles and is

6.8 Transfer Function Identification Procedure

chosen as the final model. The number of numerators and denominators match exactly that predicted by the deterministic criteria given in section 6.8.5. A similar selection procedure was applied for the identification of the transfer function corresponding to $\tilde{Q}_{e,p}$ in the positive electrode region.

The final identified transfer functions (for the scaled output) are

$$\frac{\tilde{Q}_{e,n}(z)}{\tilde{I}(z)} = \frac{0.002842z^{-1} - 0.00753z^{-2} + 0.006595z^{-3} - 0.001906z^{-4}}{1 - 3.577z^{-1} + 4.767z^{-2} - 2.801z^{-3} + 0.6118z^{-4}} \quad (6.17)$$

$$\frac{\tilde{Q}_{e,p}(z)}{\tilde{I}(z)} = \frac{-0.002809z^{-1} + 0.007139z^{-2} - 0.005944z^{-3} + 0.001614z^{-4}}{1 - 3.464z^{-1} + 4.444z^{-2} - 2.495z^{-3} + 0.515z^{-4}} \quad (6.18)$$

Figure 6.6 shows a comparison of the $\tilde{Q}_{e,n}$ output for *a*) the P2D model, and *b*) the identified transfer function of eq. (6.17) using the training current profile of fig. 6.1. The transfer function of eq. (6.17) was obtained by scaling the output of the training profile to be of order $\mathcal{O}(1)$ by a factor of 1000. Therefore, for final implementation and comparison purposes, the raw output produced by applying the transfer function needs to be scaled back by its reciprocal. If the system is linear, then this scaling factor shall have no impact on the frequency-dependent dynamics of the subsystem. The output predicted by the identified transfer function is virtually indistinguishable from the ‘true’ output computed by post-processing the P2D model with an RMS error of $5.70 \times 10^{-6} \text{ mol m}^{-2}$ and a MAE of $19.19 \times 10^{-6} \text{ mol m}^{-2}$. This high accuracy of the transfer function prediction justifies the linearity assumption for the subsystem. Figure 6.7 presents the same comparison using the validation input profile for the subsystem in the positive electrode region. The accuracy of the identified transfer function for this independent data set is clearly illustrated.

The poles of eq. (6.17) are located at (0.9969, 0.9870, 0.9106, 0.6829) while those of eq. (6.18) lie at (0.9967, 0.9880, 0.8952, 0.5842) on the Z-plane *i.e.*, close to each other. This confirms the hypothesis that these two sub-systems exhibit similar dynamics. The slight differences in the pole locations could be attributed to the variations in the physical parameters pertaining to the two electrode regions. The numerator coefficients of eq. (6.17) and eq. (6.18) are also close to each other except that their signs are opposite to each other. This is to be expected, since as seen in the step response plots of fig. 6.4, $\tilde{Q}_{e,n}$ and $\tilde{Q}_{e,p}$ evolve in time in opposite directions. This is also explained by the fact that, for a given applied current, a decrease in the number of

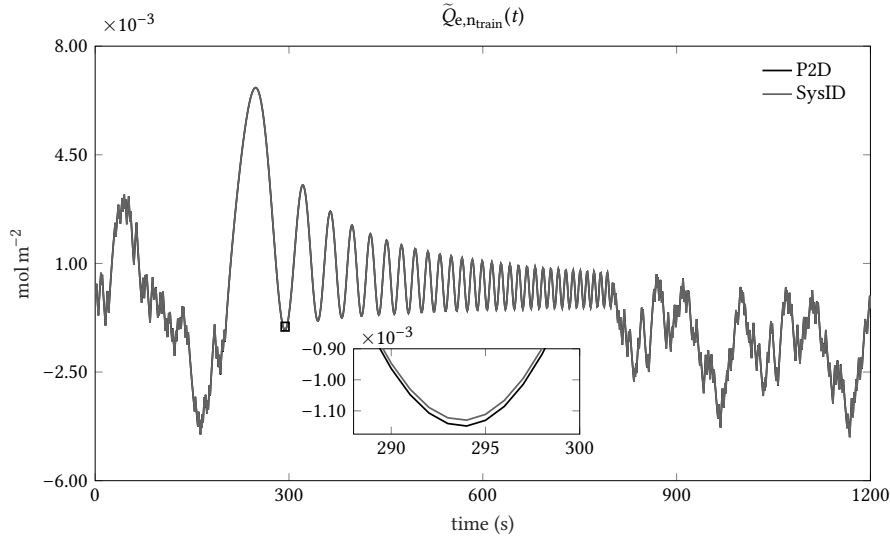


Figure 6.6 Time-evolution of $\tilde{Q}_{e,n}$ computed using the P2D model and the identified transfer function of eq. (6.17) (scaled by 0.001) with the synthetic training input profile of fig. 6.1. The output predicted by the identified transfer function closely matches the ‘true’ output obtained by a high-fidelity P2D simulation with an RMS error of $5.70 \times 10^{-6} \text{ mol m}^{-2}$ and a MAE of $19.19 \times 10^{-6} \text{ mol m}^{-2}$. Note that the transfer function in eq. (6.17) was originally obtained by scaling the output by 1000. The transfer function output is multiplied by the reciprocal of the same scaling factor to obtain the predicted response shown here, thereby once again justifying the linearity assumption for this subsystem.

ions in the negative electrode has to be accompanied by an increase in the positive electrode and vice-versa (the values of the changes are not exactly equal owing to the presence of the separator). The identified transfer functions are thus consistent and deemed to be suitable for representing the electrolyte time-evolution in these regions.

6.8.7 Numerical implementation of identified transfer functions

The concept of deploying a Z-domain transfer function may seem incongruous to the one of the major goals of this thesis *viz.* time-domain implementation of ROMs in an embedded environment such as a BMS. While the majority of the models is derived and implemented entirely in time-domain, only the two time-evolution subsystems of the electrolyte seems to deviate from this trajectory. However, an explanation for this is provided in section 6.4.3. In particular, it was mentioned that an approximation-free conversion to time-domain from Z-domain exists, that mitigates this perceived drawback for these two sub-systems. This conversion is amenable for discrete-time implementation without any other modifications.

6.8 Transfer Function Identification Procedure

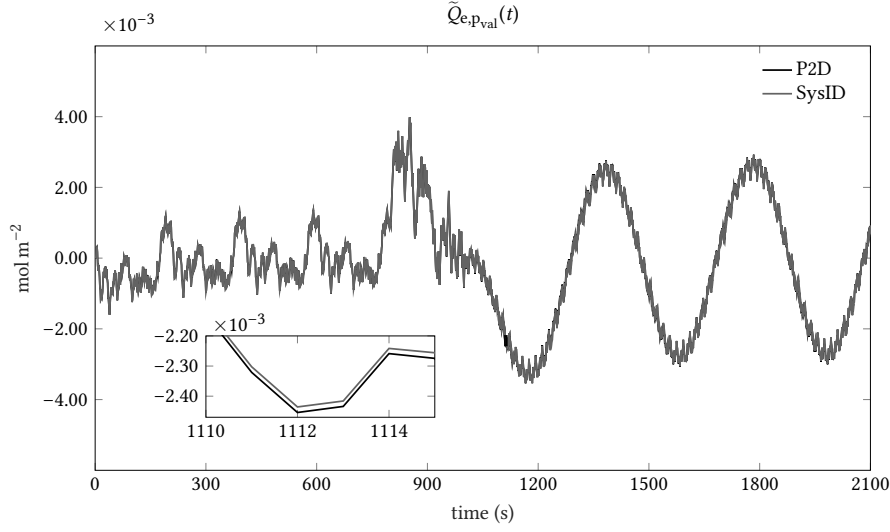


Figure 6.7 Time-evolution of $\tilde{Q}_{e,p}$ computed using the P2D model and the identified transfer function of eq. (6.18) (scaled by 0.001) with the synthetic validation input profile of fig. 6.2. The output predicted by the identified transfer function closely matches the ‘true’ output obtained by a high-fidelity P2D simulation with an RMS error of $12.07 \times 10^{-6} \text{ mol m}^{-2}$ and a MAE of $31.59 \times 10^{-6} \text{ mol m}^{-2}$. Note that the transfer function in eq. (6.18) was originally obtained by scaling the output by 1000. The transfer function output is multiplied by the reciprocal of the same scaling factor to obtain the predicted response shown here, thereby once again confirming the linearity of this subsystem.

Starting from the generic structure of the identified transfer functions (see eq. (6.8)),

$$\begin{aligned}
 G(z) &= \frac{b_1 z^{-1} + \dots + b_{n_b} z^{-n_b}}{1 + a_1 z^{-1} + \dots + a_{n_a} z^{-n_a}} && \left. \begin{array}{l} \text{Replace with analogous} \\ \text{transfer operator } q = z \end{array} \right\} \\
 G(q) &= \frac{b_1 q^{-1} + \dots + b_{n_b} q^{-n_b}}{1 + a_1 q^{-1} + \dots + a_{n_a} q^{-n_a}} && \left. \begin{array}{l} \text{in time domain} \\ \text{Apply the definition} \\ \text{of } G(q) \text{ on the LHS} \end{array} \right\} \\
 \frac{y[k]}{u[k]} &= \frac{b_1 q^{-1} + \dots + b_{n_b} q^{-n_b}}{1 + a_1 q^{-1} + \dots + a_{n_a} q^{-n_a}} && \left. \begin{array}{l} \text{Cross-multiply} \\ \text{Expand on both sides} \end{array} \right\} \\
 (1 + a_1 q^{-1} + \dots + a_{n_a} q^{-n_a}) y[k] &= (b_1 q^{-1} + \dots + b_{n_b} q^{-n_b}) u[k] && \left. \begin{array}{l} \text{Apply the definition} \\ q^{-p} x[k] = x[k-p] \\ \text{Rearrange to obtain} \\ \text{the final expression} \end{array} \right\} \\
 y[k] + a_1 q^{-1} y[k] + \dots + a_{n_a} q^{-n_a} y[k] &= b_1 q^{-1} u[k] + \dots + b_{n_b} q^{-n_b} u[k] \\
 y[k] + a_1 y[k-1] + \dots + a_{n_a} y[k-n_a] &= b_1 u[k-1] + \dots + b_{n_b} u[k-n_b] \\
 y[k] &= -a_1 y[k-1] - \dots - a_{n_a} y[k-n_a] \\
 &\quad + b_1 u[k-1] + \dots + b_{n_b} u[k-n_b] \tag{6.19}
 \end{aligned}$$

We thus obtain a simple algebraic expression (a difference equation) that computes the output at the given time-step given past inputs and outputs. This is a highly memory-efficient implementation since, at any given time-step, only the previous n_a (four) output samples and n_b (four) input samples need to be ‘remembered’ (stored). This concludes all the aspects (derivation and implementation) of this author’s new model for the electrolyte time-evolution subsystem. The performance of this model for computation of electrolyte concentration needs to be evaluated, which is performed next.

6.9 Performance Analysis of System Identification Model: Ionic Concentration in Electrolyte

To demonstrate that a suitable advancement of the field has indeed been achieved through this system identification exercise, a comparison with the existing state of the art in reduced order electrolyte modelling is warranted. Secondly, to comprehend its extent of validity and performance boundaries, the newly developed ROM must also be pitted against the full-order P2D model. This section aims to provide such a comparative discussion for two types of inputs – *a*) constant current inputs *b*) dynamic load profiles

6.9.1 Constant current inputs

Figure 6.8 shows the spatial distribution of ionic concentration in the electrolyte along cell thickness for a 1C discharge beginning at 100 % SOC. The spatial concentration computed by each of the three approaches – i) the P2D model, ii) the quadratic approximation model and iii) the newly developed system identification model(s).

During the initial phase of discharge, the P2D model exhibits a characteristic inflection point near the separator interfaces that diffuses out over time until a QSS. This is due to the fact the reaction front is initially established close to the separator, and as surface concentration of lithium in particles near separator is depleted, the reaction starts moves further into the electrode thickness. Neither of the two ROMs under consideration here could successfully capture this characteristic inflection. This is explained by the fact that both of them use the standard quadratic approximation profile for the *spatial* profile, which means that only one apex point is possible per electrode, which is pinned to their separator interfaces by design.

6.9 Performance Analysis of System Id Model: Ionic Concentration

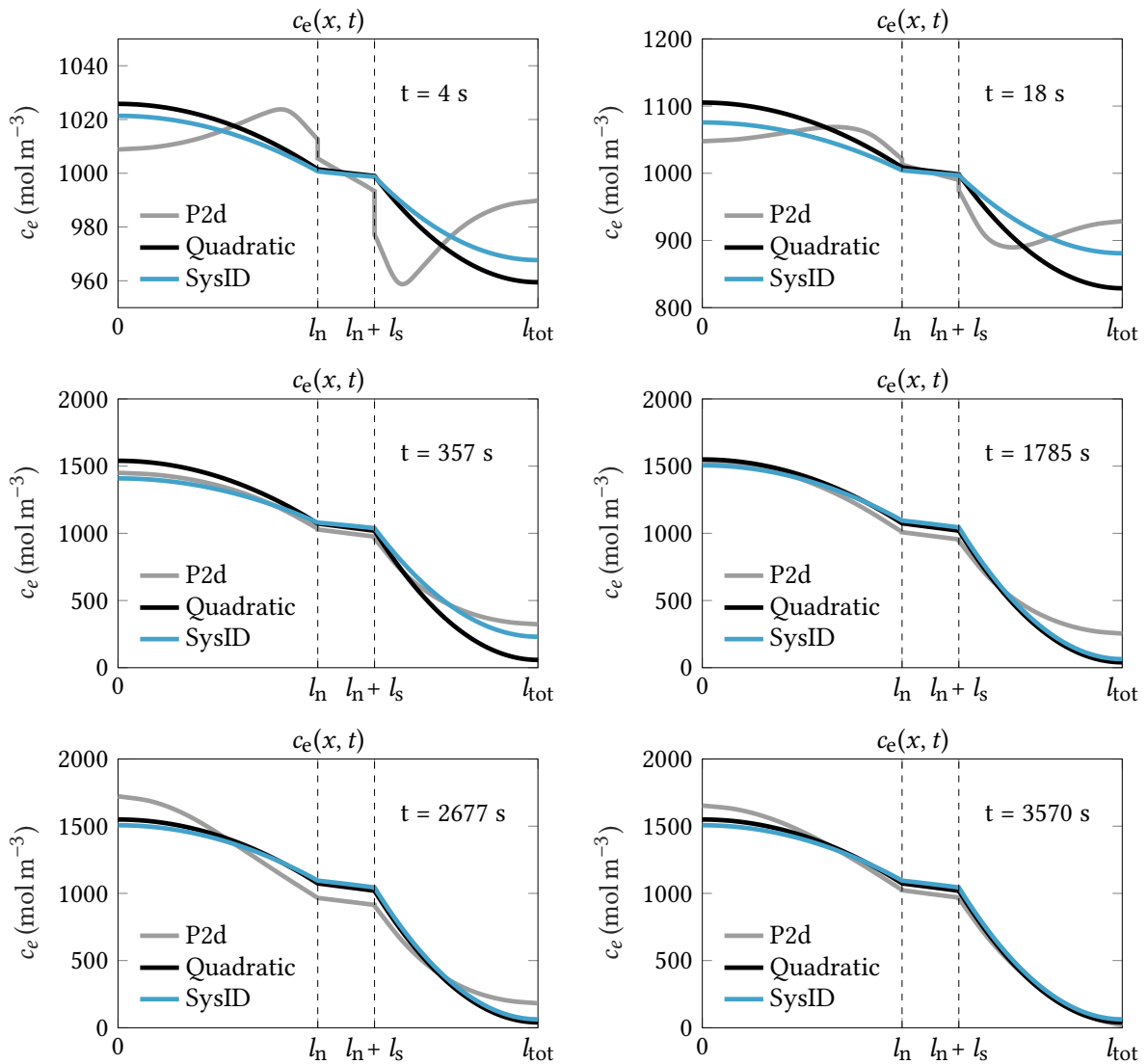


Figure 6.8 Spatial distribution of ionic concentration in electrolyte along cell thickness at various snapshots of time computed by each of the three models for a 1C discharge. The concentration profile computed by the P2D model is used as the benchmark reference. The system identification model performs noticeably better than the quadratic approximation model during the initial transient while delivering a similar performance as a QSS is reached.

During the transient portion of discharge (approximately up to 357 s as shown in fig. 6.8), the locus of the concentration profile computed by the newly developed system identification model(s) lies closer to the P2D model than that computed by the quadratic approximation model. After the initial transition phase, it appears that the concentration profile predicted by both the ROMs converge to the P2D model's concentration profile.

6.9 Performance Analysis of System Id Model: Ionic Concentration

To obtain a quantifiable perspective on the accuracy of the newly developed model, it is desirable to plot the temporal evolution of the concentration, particularly at the two current collector interfaces. The behaviour of the baseline quadratic approximation model in this regard was established in section 5.4.2. Therefore it is important to ascertain whether a noteworthy improvement was achieved using the model arrived at using the system identification procedure.

Figure 6.9 shows time-evolution of ionic concentrations at the current collector interfaces of the negative and positive electrodes for a 1C discharge. Concentration profiles computed by the three approaches – i) P2D model, ii) quadratic approximation model and the iii) newly developed system identification model(s) are overlaid in the top row of plots, wherein the left hand side corresponds to the current collector interface at the negative electrode while the right hand side corresponds to that at the positive electrode. The plots in the bottom row of fig. 6.9 show the time-evolution of the absolute value of their errors. The concentration error of each of the two ROMs is defined with respect to the benchmark P2D model *i.e.*, $\varepsilon_{c_{e,j}}(t) = c_{e,j,ROM} - c_{e,j,p2d}(t)$. The absolute value of the error is plotted so that the magnitude of the error can be visualised better, aiding immediate comparisons based on the plots.

For both current collectors, the newly developed system identification model outperforms the quadratic approximation model during the transient phase. At the negative electrode/current collector interface, the error of the system identification model remains strictly below that of the quadratic approximation model until ≈ 650 s and remains comparable to it until ≈ 1600 s. Beyond this time, the quadratic approximation model has a slightly better accuracy, although the system identification model still remains at a comparable distance from it. After ≈ 2000 s, both models yield the same response shape. For the positive electrode/current collector interface, the error of the system identification model remains below that of the quadratic approximation model until ≈ 3300 s.

Figure 6.10 shows a zoomed version of the time-evolution of the ionic concentration at the two current collectors, wherein the first 300 s after application of the load current is plotted. The significant improvement in accuracy achieved by the newly developed system identification model(s) is clearly demonstrated. At both the current collectors, the concentration computed by the system identification model(s) closely track that of the benchmark P2D model.

6.9 Performance Analysis of System Id Model: Ionic Concentration

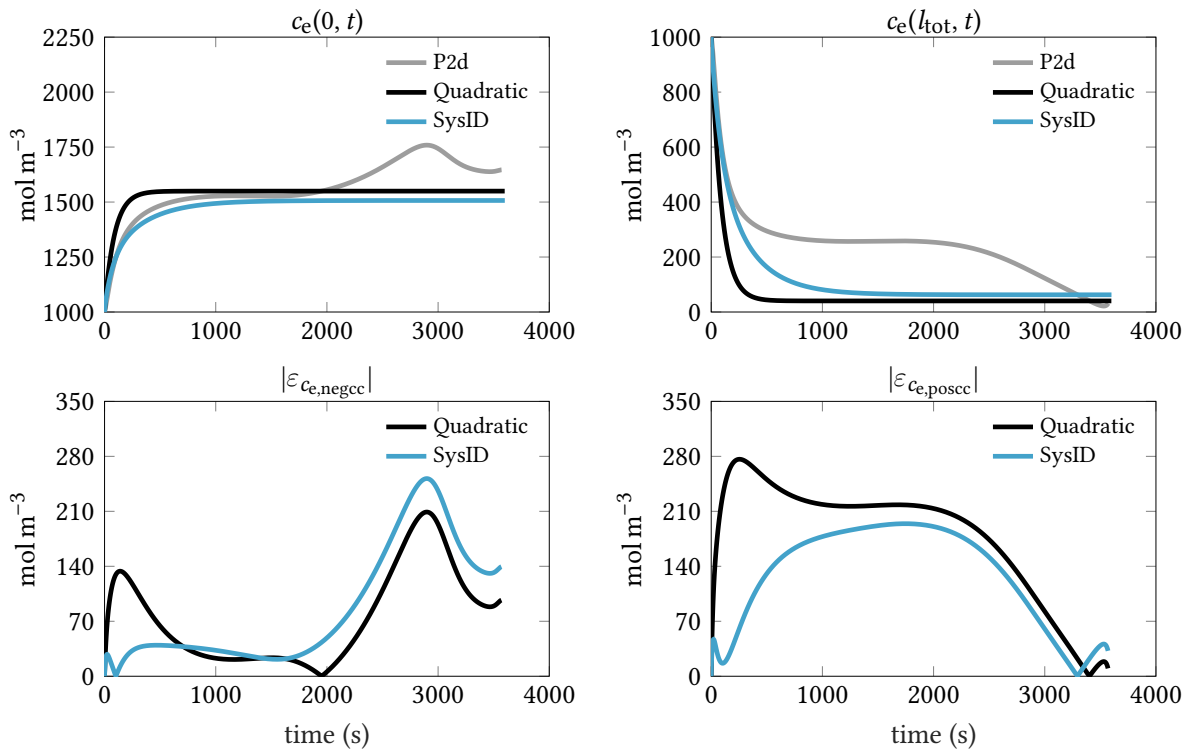


Figure 6.9 Evolution of ionic concentration over time at the two current collector interfaces for a 1C discharge for i) the P2D model, ii) the quadratic approximation model and iii) the newly developed system identification model(s) (top row). For the quadratic approximation and system identification models, the time evolution of their absolute error relative to the P2D benchmark is also shown (bottom row). At both current collectors, the transient performance of the system identification model is superior to the quadratic approximation model. At QSS, the quadratic approximation model is slightly more accurate than the system identification model.

The loss of fidelity exhibited past the initial transient phase warrants an explanation. It should be recalled that the natural decoupling of the temporal and spatial systems were taken advantage of in developing the system identification technique. This means that, for the spatial profile, the system identification model reverts to the same quadratic profile as the baseline quadratic approximation model. This explains why the two models have similar shape past the initial transient. During the transient phase when the QSS behaviour is yet to be established, it is reasonable to assume that the temporal dynamics are of paramount importance in governing the concentration profile evolution. After a QSS has been established with the reaction front diffusing out and a steady stream of ion-electron separation/recombination in place, it is hypothesised that the temporal dynamics have settled and the spatial configuration assumes importance.

6.9 Performance Analysis of System Id Model: Ionic Concentration

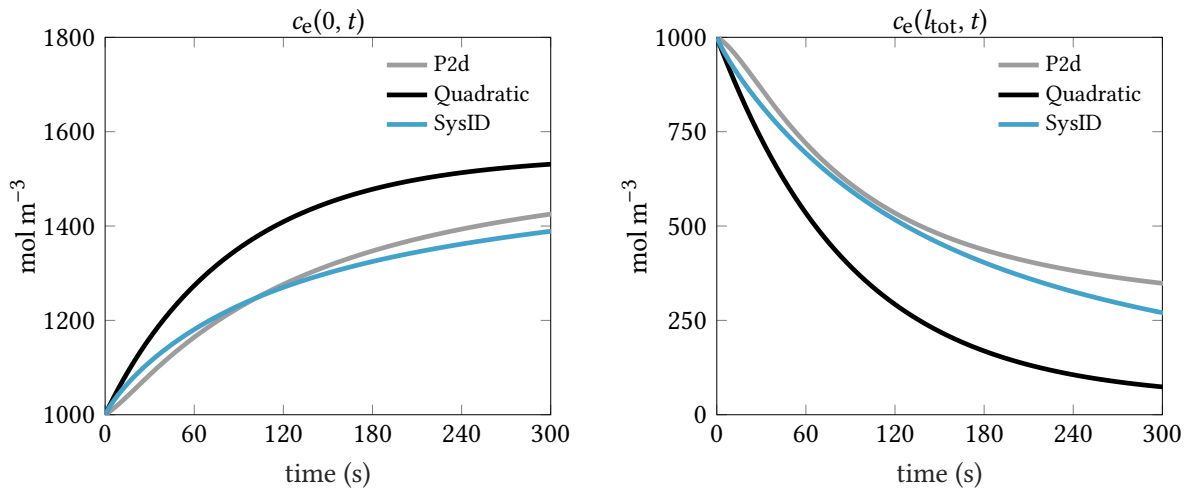


Figure 6.10 Transient phase of the temporal evolution of ionic concentration at the two current collector interfaces for a 1C discharge as computed by – i) the P2D model, ii) the quadratic approximation model, and iii) the newly developed system identification model(s). The significantly improved accuracy of the system identification model(s) relative to the state of the art quadratic approximation model is clearly demonstrated.

With a sustained application of constant current past the initial transient, strong spatial gradients in the ionic concentration are established within the cell *i.e.*, the concentrations are far from the initial equilibrium value. This precisely exposes the realm where the system identification model exhibits its natural weakness. By following the theory of system identification, which necessitates bias removal, the training and validation profiles of fig. 6.1 and fig. 6.2 had nearly zero mean. This means that the currents were as equally positive as negative leading to a small-signal perturbation around the equilibrium value of the electrolyte concentration. While this profile is ideally suited to excite the system’s dynamics, it fails to capture the large signal behaviour. As a topic of future research, perhaps a spatially-coupled system identification could be attempted to handle this issue. Table 6.3 provides a summary of error statistics for the transient phase, thereby helping to compare the performance of the quadratic and system identification models against the benchmark P2D simulation results.

The main implication of these results is that the identified models are primarily suitable for transient *i.e.*, dynamic load profiles, which is typical of a real-life scenario in an electric/hybrid electric vehicular operation. Such a model is less suitable for sustained constant current application. This implies that a BMS in a vehicle undergoing a Constant Current Constant Voltage (CCCV) charging cannot rely on these identified electrolyte models. However, this

6.9 Performance Analysis of System Id Model: Ionic Concentration

Table 6.3 Summary of error statistics comparing the performance of quadratic approximation and system identification models. The input is a 1C constant current discharge applied for the first 30 minutes starting at 100 % cell SOC. The metric being compared is the absolute value of the concentration difference with respect to the P2D model at the two current collector interfaces.

Error statistic (mol m ⁻³)	$ \varepsilon_c $ at Neg/CC		$ \varepsilon_c $ at Pos/CC	
	Quadratic	SysID	Quadratic	SysID
Max	133.80	39.51	276.33	194.27
Mean	48.16	29.56	227.92	146.53
Median	25.60	30.17	218.96	173.14
Standard Deviation	36.94	8.22	29.71	55.79

exclusion does not seriously hamper the model's wider applicability since a simple coulomb-counting approach with a high-precision Analog to Digital Converter (ADC) is much more accurate than any other PBM in this particular scenario.

Although constant current discharge is not a practical use-case for vehicular batteries, performing this benchmark evaluation has helped in understanding the limits of the newly developed model. This study has also helped in providing a glimpse of its potential strength *viz.* significantly improved accuracy under dynamic load conditions, which is presented next.

6.9.2 Dynamic current inputs

To characterise the performance of the newly developed system identification electrolyte concentration model(s) under dynamic load conditions, the UDDS drivecycle was used. The details of this drivecycle such as its speed versus time data and its highly dynamic nature was discussed in section 5.3.3. The peak of the applied load current used corresponds to a discharge current of 180 A *i.e.*, 3C. A plot of this current profile was shown in the top row of fig. 5.12. This load profile was applied to the three models under consideration – *a)* P2D model, *b)* quadratic approximation model, and *c)* newly developed system identification model(s) – and the spatio-temporal evolution of ionic concentration in electrolyte computed by each of them was studied.

Since the load current is highly dynamic and continuously alternating between charging and discharging at various magnitudes throughout the profile duration, it is difficult to discern a specific pattern or trend within the spatial thickness of the cell. Hence, unlike the case

6.9 Performance Analysis of System Id Model: Ionic Concentration

of prolonged unidirectional current application wherein a clear reaction front that diffuses gradually out can be visualised (see fig. 6.8), little information can be gained from visualisation of spatial concentration profiles. Since the ionic concentrations at the two current collectors have a direct (and two-pronged) influence on the electrolyte overpotential (see eq. (2.4)), it is particularly important to characterise the accuracy at these two critical spatial locations.

Since a direct correspondence between the time-dependent dynamics of the load profile and that of the electrolyte concentration can be intuitively visualised, its values at the two current collector interfaces are examined. The plots in the top row of fig. 6.11 shows the time evolution of the ionic concentration at the two current collector locations for the UDDS current profile computed by each of the three models under consideration. The plots to the left pertain to the negative current collector location while that to the right correspond to the positive current collector location. The bottom row of plots show the absolute value of concentration error of the quadratic and system identification models relative to the P2D reference benchmark. As seen in fig. 6.11, the absolute error of the newly developed system identification models remain below that of the baseline quadratic approximation model throughout the drivecycle.

Based on the conclusions from the constant current input study of section 6.9.1, it is to be expected that the system identification model(s) exhibit a superior performance during the transient phase of the simulation. As seen in the initial duration of fig. 6.11, the absolute error of the system identification model is indeed lower than that of the baseline quadratic approximation model. Particular, when a sudden current spike is applied at ≈ 200 s, the quadratic approximation model is unable to cope and its absolute error deviates far away from its mean value. The absolute error of system identification model remains well controlled and even with this instantaneous load demand, its standard deviation is remarkably close to its median value as shown in table 6.4.

While the superior accuracy of the newly developed model during the transient phase was not surprising, the fact that its performance remains consistent throughout the entire time horizon is noteworthy. Despite being subject to incessant changes in load demands, the system identification model responds better than the quadratic approximation model well past the initial transient. Figure 6.12 shows a zoomed view of the ionic concentration in the electrolyte at the two current collector interfaces. To prove the improved performance of

6.9 Performance Analysis of System Id Model: Ionic Concentration

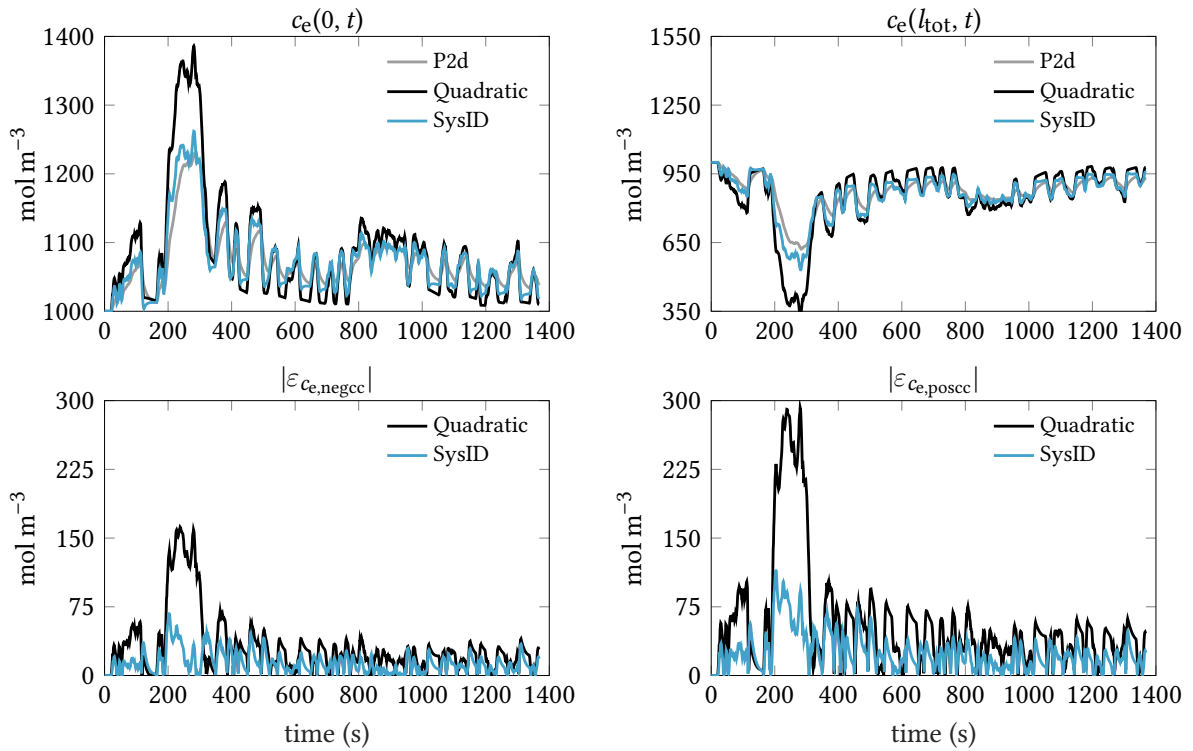


Figure 6.11 Evolution of ionic concentration over time at the two current collector interfaces with a UDDS input profile (see topmost plot of fig. 5.12) as computed by i) the P2D model, ii) the quadratic approximation model and iii) the newly developed system identification model(s) (top row). The plots on the left pertain to the negative electrode/current collector interface, while that on the right corresponds to the positive electrode/current collector interface. For the quadratic approximation and system identification models, their absolute error relative to the P2D benchmark is also shown (bottom row). The system identification model is considerably more accurate than the quadratic approximation model for the entire time horizon of the drivecycle.

Table 6.4 Summary of error statistics with a UDDS input current profile for the quadratic approximation and system identification models. The metric used is the absolute value of the concentration difference with respect to the P2D model at the two current collector interfaces.

Error statistic (mol m^{-3})	$ \epsilon_{c_e} $ at Neg/CC		$ \epsilon_{c_e} $ at Pos/CC	
	Quadratic	SysID	Quadratic	SysID
Max	307.27	190.04	292.20	114.44
Mean	66.38	54.98	55.15	25.02
Median	49.65	47.12	40.39	20.93
Standard Deviation	66.80	37.18	60.50	20.17

6.9 Performance Analysis of System Id Model: Ionic Concentration

the developed model well into the operation of the cell, a 50 s window beginning at $\approx 60\%$ of the overall profile duration is examined in detail. Although it exhibits some oscillations, the system identification model(s) reasonably track the ‘true’ concentrations computed by the P2D model. However, the baseline quadratic approximation model seems to suffer from a large bias with respect to the P2D model. It should also be noted that nearly every ‘kink’ in the two ROMs is identical. This could be attributed to the fact the spatial profile used in both of them is identical. Hence, it must be concluded that the difference in their amplitude arises from the improved calculation of coefficients $a_k(t)$ in eq. (5.69) and eq. (5.71) through the usage of more accurate $Q_{e,n}$ and $Q_{e,p}$ in the Left-Hand Side (LHS) of eq. (5.81) and eq. (5.83) respectively. Detailed error metrics of the two ROMs is shown in table 6.4.

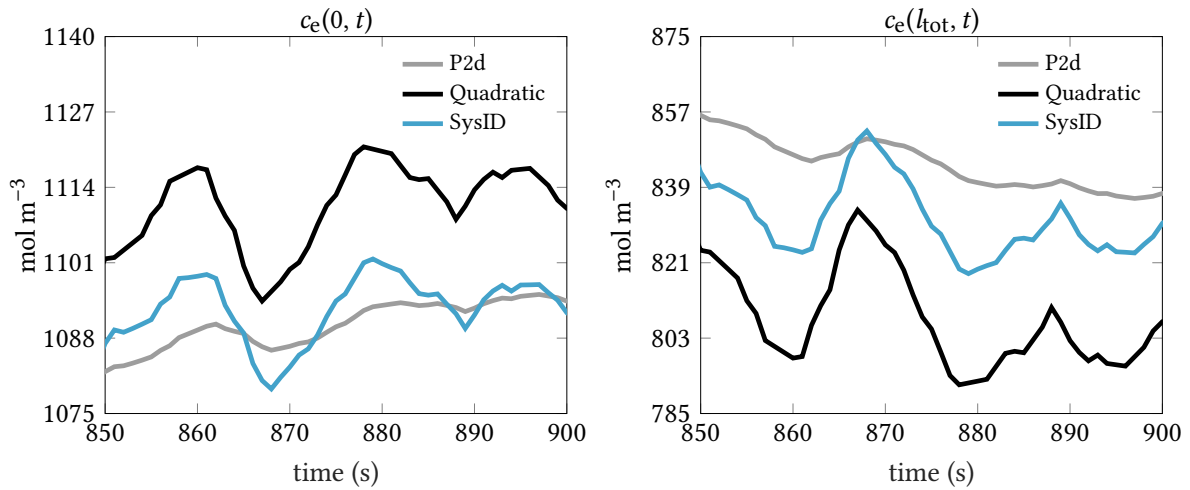


Figure 6.12 A zoomed view of the ionic concentration (showing a 50 s window beginning at $\approx 60\%$ of the overall profile duration) in the electrolyte at the two current collector interfaces for the UDDS profile of fig. 5.12 as computed by – i) the P2D model, ii) the quadratic approximation model, and iii) the newly developed system identification model(s). At both current collector interfaces, the system identification model(s) exhibits a reasonable tracking of the concentration profile computed by the benchmark P2D. The profile computed by the quadratic approximation model seems to suffer from offsets/bias issues that adversely affects its accuracy.

Based on the evidence presented thus far, it can be concluded that the time-evolution subsystem model(s) developed here using the system identification technique indeed represent an advancement of the field of reduced order electrolyte modelling. With this aspect thus tackled, it is imperative to explore the potential benefits of incorporating the discrete-time model(s) thus obtained into the conventional SPM and is discussed next.

6.10 Composite SPM Model with Electrolyte Dynamics

At this stage, it must be recalled that the purpose of developing the system identification electrolyte model was to mitigate the poor performance of the basic SPM at C-rates above 0.5C (see section 5.3.3). This sub-optimal performance was attributed to the lack of electrolyte dynamics in the basic SPM. The performance of the newly developed system identification model has been proved to be superior to the current state of the art. The next step is to embed this electrolyte model into the basic SPM so as to obtain a composite SPM. The performance of this composite model is evaluated to ascertain its suitability towards online implementation.

6.10.1 Computation of electrolyte overpotential

The missing component in the terminal voltage computation of the basic SPM is the contribution from the electrolyte overpotential term. This is the potential difference in the entire electrolyte *i.e.*, the electrolyte potential at the positive current collector interface with respect to that at the negative current collector interface.

As discussed in section 2.3.2, using the equation proposed by Prada *et al.* [99], the overpotential in the electrolyte is computed as

$$\begin{aligned} \phi_{e,\text{pos}} - \phi_{e,\text{neg}} = & (1 - t_+^0) \frac{2RT}{F} \ln \frac{c_{e,\text{pos/cc}}}{c_{e,\text{neg/cc}}} \\ & - \frac{I}{2A} \left(\frac{l_{\text{neg}}}{\kappa_{\text{eff,neg}}} + 2 \frac{l_{\text{sep}}}{\kappa_{\text{eff,sep}}} + \frac{l_{\text{pos}}}{\kappa_{\text{eff,pos}}} \right) \end{aligned} \quad (\text{eq. (2.4) revisited})$$

Equation (2.4) consists of two distinct terms – i) a diffusion overpotential due to concentration gradient in the electrolyte, and ii) an ohmic resistance term that is dependent upon a) the instantaneous value of applied current, b) the thicknesses of the three cell regions, and c) the effective ionic conductivity in each of the three regions.

The ohmic loss term of eq. (2.4) needs to be examined in closer detail. The dependence of this term on instantaneous load current and cell thicknesses can be accounted in a straightforward manner. However, there are ambiguities in computing the effective ionic conductivity in each of the three cell regions. The effective value of ionic conductivity in

6.10 Composite SPM Model with Electrolyte Dynamics

the electrolyte depends on its intrinsic conductivity, the Bruggeman constants and porosities of each of the three regions. The intrinsic electrolyte conductivity in-turn depends on the electrolyte concentration.

Ambiguities arise in interpreting the value of ionic concentration to be used for computation of electrolyte concentration. Since eq. (2.4) deals with overall potential drop across the entire length of the cell, the concentration used for computing electrolyte conductivity could, for example be that at the respective current collectors. This concept however introduces inconsistencies with the separator term. Using the separator concentration from one of the electrode interfaces introduces unequal weighting in this computation. If the ionic concentration at the midpoint of the separator is used, this scheme becomes inconsistent with that at the two current collectors. Another possibility for computing the effective conductivity in a cell region is to use the mean of the concentration in that region. However, since the mean is nothing but a simple statistical first moment is equally influenced by the entire concentration profile within each cell region. This is questionable given that the electrolyte overpotential across the entire cell thickness is most likely governed by the conductivities at the two current collector interfaces. Some form of weighted mean could be conjured, wherein the current collector locations are given the highest weight and the separator locations the least weight. However, finding the weights becomes yet another exercise and from the engineering perspective of computing these in real-time, seems to be in the realm of diminishing returns.

In published literature, only a cursory treatment has been accorded to the aforementioned ambiguities. In Prada *et al.* [99], the usage of initial concentrations is used to only introduce the concept of ohmic resistance in that article. However, the author of this thesis wishes to extend this concept further. In the simulations conducted by this thesis author, it became clear that the dependence on applied current was required in order to obtain reasonable accuracies. Computing mean of concentrations in cell regions for calculation of ionic conductivities led to a biased computation of overpotentials. Therefore, this author decided to use the value of initial concentration for the computation of ionic conductivities in the current-dependent contribution to electrolyte overpotential throughout the entire time horizon considered.

6.10 Composite SPM Model with Electrolyte Dynamics

Hence, as per the adopted scheme eq. (2.4) gets modified as

$$\phi_{e,\text{pos}}(t) - \phi_{e,\text{neg}}(t) = (1 - t_+^0) \frac{2RT}{F} \ln \frac{c_{e,\text{pos/cc}}(t)}{c_{e,\text{neg/cc}}(t)} - \frac{I}{2A} \left(\frac{l_{\text{neg}}}{\kappa_{\text{eff,neg}}(c_e(0))} + 2 \frac{l_{\text{sep}}}{\kappa_{\text{eff,sep}}(c_e(0))} + \frac{l_{\text{pos}}}{\kappa_{\text{eff,pos}}(c_e(0))} \right) \quad (6.20)$$

wherein the time-dependent terms are explicitly shown in the notation.

Using eq. (6.20) for electrolyte overpotential computation has an important implication. The two-pronged influence of the time-dependent electrolyte concentration on the electrolyte overpotential *viz.* *a)* a direct influence in the form of concentration dependent diffusion polarisation, and *b)* an indirect influence through its use in ionic conductivity calculations has now been reduced to just one. This implies the results from the system identification model are now required only in the first term of eq. (6.20).

In the light of the decision of use the (constant) initial concentration for the ohmic term, it is natural to question the gains from the circuitous route of the system identification exercise that was undertaken to obtain the improved electrolyte model. Therefore, it is imperative to quantify the relative weight of the concentration dependent diffusion resistance compared to the bulk solution resistance.

Figure 6.13 shows the contribution to the overall potential drop $\phi_{e,\text{pos}}$ and $\phi_{e,\text{neg}}$ in the electrolyte from each of the two terms in eq. (6.20) for a 1C discharge. The bulk solution resistance is constant owing to the fact that the initial electrolyte concentration is used in computing the effective ionic conductivities in the three regions of the cell. The gradient induced diffusion polarisation term, however has a stronger contribution in both the transient and steady state. The entire dynamics of the overall potential drop during the transient phase is governed by this concentration-dependent term, while its steady state contribution is in fact higher than the bulk solution resistance. The constant ohmic resistance term merely provides a non-zero offset for the electrolyte solution overpotential. In questioning whether the system identification exercise was indeed worthwhile, if the concentrations in the two current collectors had not been computed at each time-step, then this diffusion polarisation term would become zero. This is because, the numerator and denominator in eq. (6.20) would have to be retained at the initial concentration, leading to a unit ratio whose natural logarithm

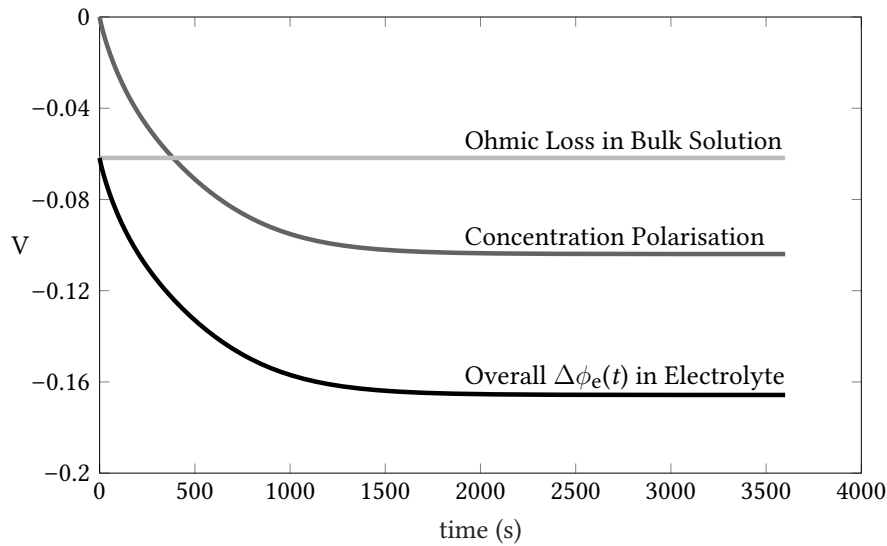


Figure 6.13 Contribution to the overpotential in the electrolyte from each of the two terms in eq. (6.20) for a 1C discharge. The bulk solution resistance is approximated as a constant value determined by the equilibrium initial concentration. The concentration dependent polarisation term governs the dynamic behaviour of the overall overpotential. Furthermore, this gradient-induced diffusion resistance has a strong contribution to the steady state, higher than the bulk solution resistance and cannot be neglected without introducing significant errors.

is zero. Therefore, it is clear that computing the concentrations at the two current collectors through system identification has indeed helped in improving the modelling accuracy.

Having established the relative importance of computing the diffusion-dependent polarisation overpotential, the next question that arises is whether the constant approximation for the bulk solution resistance is indeed appropriate. It also remains to be seen if the accurate computation of the ionic concentration through system identification (see section 6.9) has translated into a similarly accurate computation of electrolyte overpotential. This is answered by a comparing the electrolyte overpotential computed by the system identification model with that obtained from the P2D model.

Figure 6.14 shows a comparison of the electrolyte overpotential computed by the P2D and system identification models for a 1C discharge. There is a discrepancy in the initial offset of the overpotential value. However, this cannot be attributed to the use of the constant concentration approximation in the computation of ionic conductivities in eq. (6.20). This is because, at equilibrium the concentration used is exactly the initial concentration. Furthermore, at the instant of applying the current, diffusion gradients in the electrolyte have not yet been established. Hence, the contribution from the diffusion overpotential is zero,

6.10 Composite SPM Model with Electrolyte Dynamics

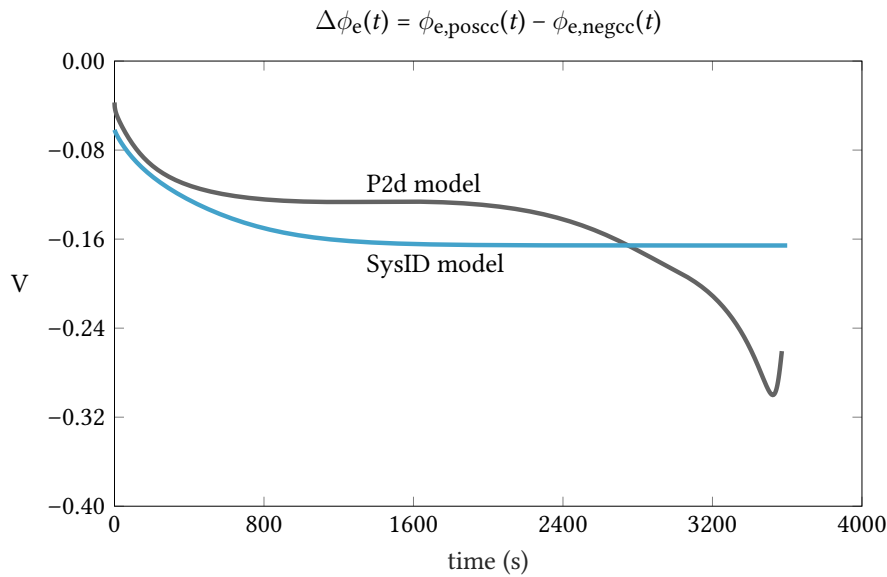


Figure 6.14 Comparison of electrolyte overpotential computed by the P2D model and the system identification model (using eq. (6.20)) for a 1C discharge. During the transient phase, the profile obtained by the system identification model closely matches that of the P2D model. The mismatch in the initial overpotential does not arise to the use of a constant concentration for the bulk resistance contribution, since at equilibrium this value is exact and not an approximation. Past the initial transient, accuracy of the system identification model degrades. This can be explained by its analogous behaviour for concentration computation in the Quasi-Steady State (see section 6.9.1) for constant current inputs.

which can also be seen in fig. 6.13. Thus, it can be concluded that this initial mismatch is due to the presence of some other unmodelled phenomena that affects the DC offset of electrolyte overpotential, and is not arising due to the approximations used by this author.

In fig. 6.14, the shape of the transient profile of overpotential computed by the system identification model closely matches that of the P2D model. This validates that the newly developed model does indeed capture the electrolyte dynamics sufficiently well during the initial transient. However, past the initial transient, the model's accuracy degrades and the resulting profile does not track the P2D model. This behaviour in overpotential is analogous to that exhibited in the spatio-temporal concentration study discussed in section 6.9.1 for constant current inputs, wherein it was deemed that this newly developed model is more suitable for dynamic loads. The same conclusion for electrolyte overpotential accuracy is reached from this constant current study. Nevertheless, even for constant current loads, using the newly developed model is better than having no electrolyte model whatsoever as in the basic SPM.

6.10 Composite SPM Model with Electrolyte Dynamics

Figure 6.15 shows a comparison of the electrolyte overpotential computed by the P2D and system identification models for a UDDS load profile. The input current corresponding to this load profile is shown in the top row of fig. 5.12. The system identification model is able to reasonably track the overpotential profile computed by the P2D model. Unlike the case of sustained unidirectional current input, the error in this case remains well-contained. The Mean Absolute Error (MAE) obtained for this profile was 15.88 mV with an Root Mean Square (RMS) error of 24.11 mV. This corresponds to 8.19 % and 12.44 % of the peak magnitude of the overpotential (193.86 mV).

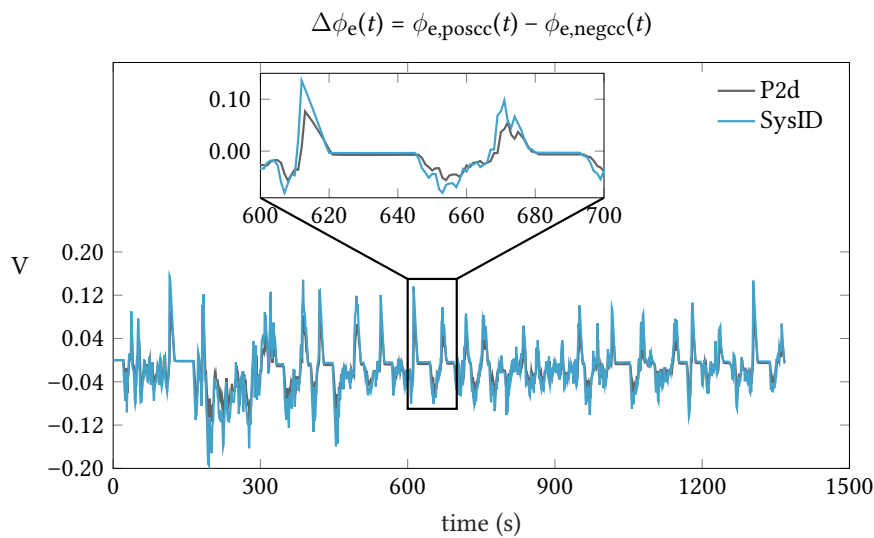


Figure 6.15 Comparison of electrolyte overpotential computed by the P2D model and the system identification model (using eq. (6.20)) for a UDDS load profile. The overpotential profile computed by the system identification model reasonably matches that obtained by the P2D model with a Mean Absolute Error (MAE) of 15.88 mV and a Root Mean Square (RMS) error of 24.11 mV.

Hence, it can be concluded that the electrolyte overpotential computation using the system identification model provides an acceptable performance for dynamic load profiles. The next step is to incorporate this electrolyte overpotential calculation into the basic SPM and to quantify the voltage accuracy of the resulting composite SPM.

6.10.2 Terminal voltage computation of composite SPM

In section 5.3.3, it was shown that in the basic SPM, the computation of the cell's SOC is of sufficient accuracy. However, its terminal voltage strongly deviates from the true value as computed by a P2D model. This mismatch between SOC and terminal voltage hinders the

6.10 Composite SPM Model with Electrolyte Dynamics

suitability of the basic SPM as the plant model in online state estimation applications. The discrepancy in terminal voltage is due to the lack of electrolyte overpotential contribution in its computation. Having obtained a suitable methodology to compute this (see section 6.10.1), it is now possible to refine the computation of the cell's terminal voltage.

Referring to eq. (5.26) and eq. (5.27), the reaction overpotential in each of the two porous electrode regions is given by

$$\eta_{\text{pos}} = \phi_{\text{s,pos}} - \phi_{\text{e,pos}} - U_{\text{pos}} \quad (6.21)$$

$$\eta_{\text{neg}} = \phi_{\text{s,neg}} - \phi_{\text{e,neg}} - U_{\text{neg}} \quad (6.22)$$

wherein the contribution from the electrolyte potential terms $\phi_{\text{e,pos}}$ and $\phi_{\text{e,neg}}$ are no longer to be neglected.

Subtracting eq. (6.22) from eq. (6.21)

$$\eta_{\text{pos}} - \eta_{\text{neg}} = \underbrace{\phi_{\text{s,pos}} - \phi_{\text{s,neg}}}_{V_{\text{cell}}} - \phi_{\text{e,pos}} + \phi_{\text{e,neg}} - U_{\text{pos}} + U_{\text{neg}} \quad (6.23)$$

whose rearrangement yields

$$V_{\text{cell}} = \eta_{\text{pos}} - \eta_{\text{neg}} + \underbrace{\phi_{\text{e,pos}} - \phi_{\text{e,neg}}}_{\Delta\phi_{\text{e}}} + U_{\text{pos}} - U_{\text{neg}} \quad (6.24)$$

Substituting for $\Delta\phi_{\text{e}}$ from eq. (6.20) in into eq. (6.24), and expanding each of its terms (see derivation of eq. (5.40) for details), the final expression for the cell's terminal voltage is obtained as

$$\begin{aligned} V_{\text{cell}}(t) = & \frac{2RT}{F} \sinh^{-1} \left(\frac{-I(t)}{2Al_{\text{pos}}a_{\text{s,pos}}Fk_{\text{r,pos}}\sqrt{c_{\text{e}}c_{\text{s,surf}_{\text{pos}}}(t)}(c_{\text{s,max}_{\text{pos}}} - c_{\text{s,surf}_{\text{pos}}}(t))} \right) \\ & - \frac{2RT}{F} \sinh^{-1} \left(\frac{I(t)}{2Al_{\text{neg}}a_{\text{s,neg}}Fk_{\text{r,neg}}\sqrt{c_{\text{e}}c_{\text{s,surf}_{\text{neg}}}(t)}(c_{\text{s,max}_{\text{neg}}} - c_{\text{s,surf}_{\text{neg}}}(t))} \right) \\ & + (1-t_+^0) \frac{2RT}{F} \ln \frac{c_{\text{e,pos/cc}}(t)}{c_{\text{e,neg/cc}}(t)} - \frac{I}{2A} \left(\frac{l_{\text{neg}}}{\kappa_{\text{eff,neg}}(c_{\text{e}}(0))} + 2 \frac{l_{\text{sep}}}{\kappa_{\text{eff,sep}}(c_{\text{e}}(0))} + \frac{l_{\text{pos}}}{\kappa_{\text{eff,pos}}(c_{\text{e}}(0))} \right) \\ & + \mathcal{U}_{\text{pos}}(c_{\text{s,surf}_{\text{pos}}}(t)) - \mathcal{U}_{\text{neg}}(c_{\text{s,surf}_{\text{neg}}}(t)) \quad (6.25) \end{aligned}$$

6.10 Composite SPM Model with Electrolyte Dynamics

All other expressions and computations of the basic SPM remain unchanged (see section 5.1 for the complete set of equations constituting the model). The final step is to show that the composite SPM thus obtained has an improved performance especially in those scenarios that the basic SPM performed poorly.

6.10.3 Validation of composite SPM: Terminal voltage accuracy

The final step in this model development effort is the validation phase. In particular, the voltage accuracy of the composite SPM is compared against the P2D model for standard input conditions. In order to compare and contrast the gains achieved by the composite SPM, the terminal voltage output of the basic SPM is also considered here.

Constant Current Inputs

The voltage accuracy of the newly developed composite SPM is first evaluated for the standard test case of 1C discharge current starting from a cell SOC of 100 %.

Figure 6.16 shows the terminal voltage output of various SPMs for a 1C discharge beginning at 100 % SOC (top plot). Since it does not account for electrolyte overpotentials, the voltage profile computed by the basic SPM lies above that of the benchmark P2D model. On the other hand, the composite SPM tends to over correct for the electrolyte overpotential so that its terminal voltage lies below the P2D output. Since the output of the two ROMs lie on either side of the P2D model, it is appropriate to use the absolute value of their errors with respect to the P2D benchmark to compare them. In the bottom plot, the percentage deviation of the absolute error of the two ROMs is shown. The statistics of this deviation is quantified in table 6.5 which additionally includes the performance metrics from the quadratic approximation SPM.

Table 6.5 Summary of statistics for the percentage absolute error in terminal voltage for the basic SPM and the composite SPM in constant current 1C discharge simulations.

Error Statistic for $ \hat{\epsilon}_v $	Basic SPM	Quadratic SPM	Composite SPM
Worst Case	10.67	5.83	4.05
Mean	2.92	1.79	1.54
RMS	3.27	2.31	1.65

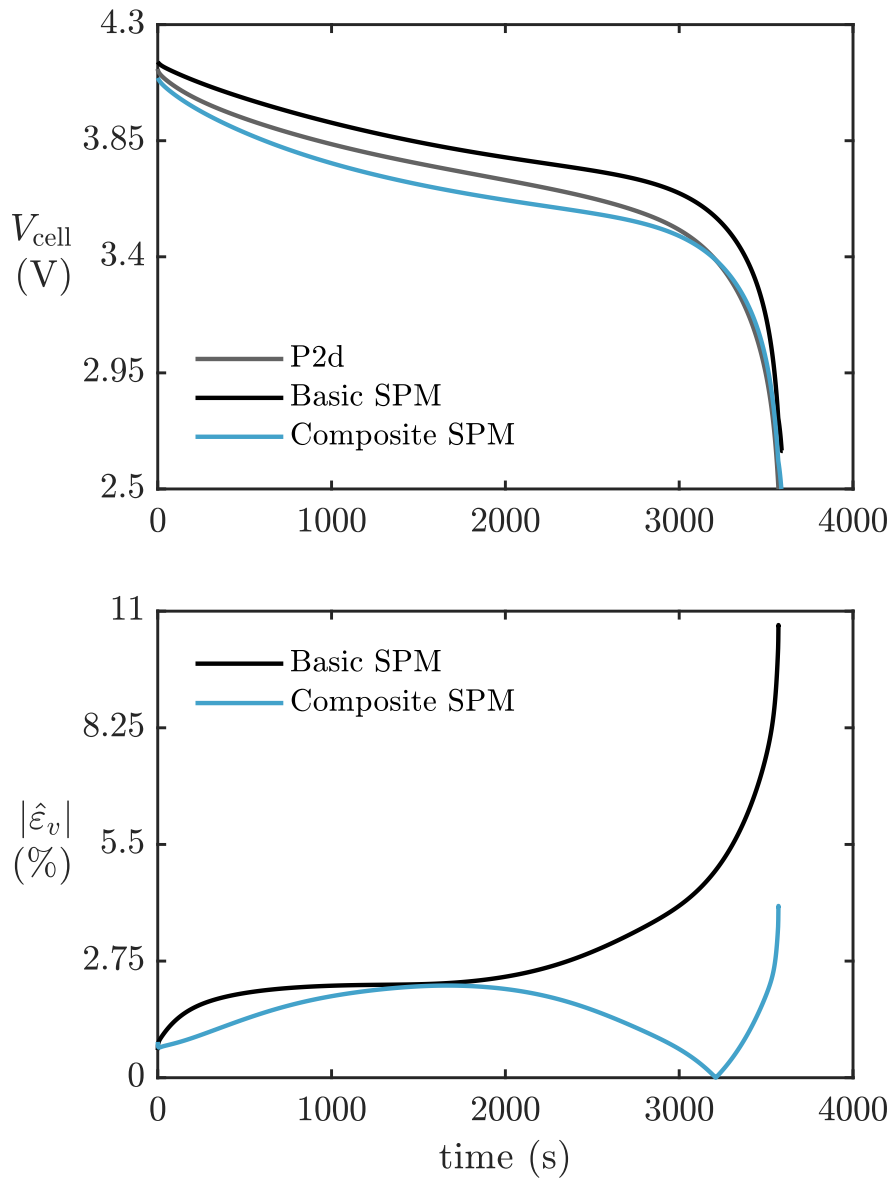


Figure 6.16 Voltage output of various SPMs for a 1C discharge beginning at 100 % SOC (top plot). Since it does not account for electrolyte overpotentials, the voltage profile computed by the basic SPM lies above that of the benchmark P2D model. On the other hand, the composite SPM tends to over correct for the electrolyte overpotential so that its terminal voltage lies below the P2D output. Since the two ROMs have outputs on either side of the P2D model, it is convenient to use the absolute error to compare them. In the bottom plot, the percentage deviation of the absolute error of the two ROMs is shown. The composite SPM performs significantly better with a peak absolute error of $\approx 4\%$ in contrast to nearly 11 % for the basic SPM.

In each of the error statistic considered, the composite SPM performs significantly better than the basic SPM for the 1C discharge case.

6.10 Composite SPM Model with Electrolyte Dynamics

One of the biggest drawbacks of the conventional SPM was its poor voltage accuracy at moderate C-rates above 0.5C (see table 5.4). The high accuracy achieved for the 1C rate seems to indicate that the composite SPM is indeed a viable solution for all high C-rates, especially given the backdrop of its methodical derivation steeped in system identification.

However, there exists a fundamental flaw in all models that use a priori assumptions of simplified spatial profiles for ionic concentration in the electrolyte. In the case of both the baseline quadratic and the system identification models, a parabolic profile spanning the entire thickness of each region within the cell was chosen a priori. However, no attempt to modify the profile upon encountering an ion starvation event at any spatial location.

This critical flaw is exposed by the sustained application of any higher current that induces an ion starvation at one of the electrodes during operation. Figure 6.17 depicts the ionic concentration in the electrolyte over time at both current collectors for a 2C discharge. The profiles computed by both the P2D and system identification models are plotted. For the system identification model, the current collector interface at the positive electrode experiences an ion starvation event at ≈ 150 s. The quadratic spatial profile used by this model does not account for such a reduction in the effective electrode thickness. All the boundary conditions and coefficients were formulated using the original electrode thickness. Therefore, beyond 150 s, the concentration becomes negative which is not physically meaningful. The author of this thesis has implemented a saturation mechanism in the code that detects an ion depletion event and prevents the concentrations from becoming negative.

Implementing this hard lower bound of zero for the ion concentration does not mitigate the problems associated with computing the electrolyte overpotential. Specifically, computational difficulties are encountered when computing the concentration dependent diffusion overpotential eq. (6.20). In the case of ion depletion at the positive current collector, the argument of the logarithmic term becomes zero which leads to a non-feasible computation ($-\infty$). Ion depletion at the negative current collector is equally detrimental to the computation. However, this scenario has a lower probability owing to the low C-rates during charging operation (see section 5.3.2). Furthermore, in the absence of the lower bound of zero for the concentrations, complex numbers are obtained from the logarithmic term, which lead to physically erroneous overpotential calculations. An alternative is to simply

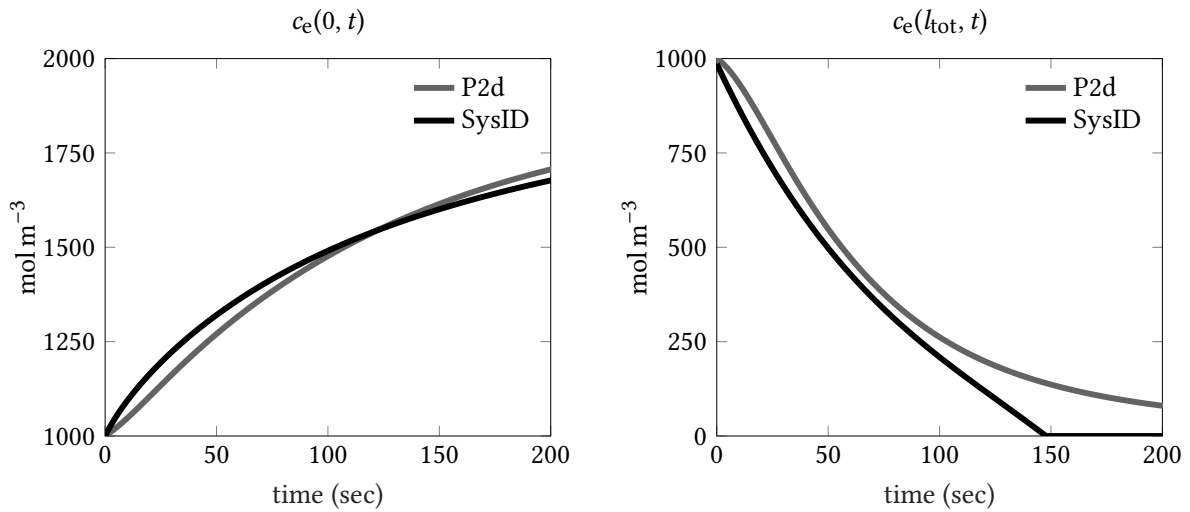


Figure 6.17 Time evolution of ionic concentration in electrolyte computed by the P2D and system identification models at – a) negative current collector interface (left plot), and b) positive current collector interface (right plot) for a constant current discharge at 120 A *i.e.*, 2C. In the system identification mode, ion starvation occurs at the positive current collector interface at ≈ 150 s. The quadratic spatial profile used by the system identification model spans the entire electrode region and does not account for ion depletion scenarios. In this thesis, the author has implemented a saturation mechanism in the computer code to prevent the ionic concentration from becoming negative. Despite this mitigating action, the computation of electrolyte overpotential using eq. (6.20) is problematic in such scenarios.

omit the diffusion impedance term. However, since this term is responsible for the large-signal dynamics of the overpotential (see fig. 6.13), omitting this and reverting to a simple ohmic resistance contribution shall lead to significant errors in the electrolyte overpotential, and consequently in the terminal voltage. Finally, setting the diffusion impedance to zero at the transition boundary of ion starvation is also not a feasible solution. This is because, the sudden inflection in the trajectory of the terminal voltage shall induce large errors in any state estimation algorithms that depend on the composite SPM as the plant model.

The difficulties encountered in electrolyte overpotential computations for ion depletion scenarios have not yet been discussed in the literature by the research community that use such quadratic approximation models. This thesis author therefore assumes that such a scenario had not been previously encountered for the parameter set and C-rate combinations used by those researchers. Despite the fact that this phenomenon might be an artefact of the idiosyncrasies of the parameter set used here, it is nevertheless questionable to not have mathematically adapted the parabolic profile to such events. The aspect of rendering the model robust to such vagaries is currently an open problem in the field and can be the subject

of future research. It can therefore be concluded that this composite SPM is *unsuitable* in its present form for sustained constant current discharge at higher C-rates. Despite this setback due to deficiencies in the mathematical formulation of the underlying spatial profile, the superior performance of the system identification model in the computation of ionic concentrations and overpotentials for *dynamic* conditions warrant such a study for the composite SPM.

Dynamic Load Conditions

In order to evaluate the performance of the composite SPM to dynamic inputs, the input profile corresponding to the UDDS drivecycle profile in fig. 5.12 with a peak current of 180 A *i.e.*, 3C was used.

Figure 6.18 shows the voltage output of the composite SPM for a UDDS input profile with a peak magnitude of 180 A *i.e.*, 3C (see fig. 5.12). The voltage profiles computed by the basic SPM and the benchmark P2D model is also overlaid (top plot). The percentage absolute error of the two ROMs relative to the P2D model is shown in the bottom plot. It is seen that the terminal voltage of the composite SPM is more accurate than the basic SPM (see table 6.6, which additionally includes the performance metrics from the quadratic SPM). For instance, the voltage profile computed by composite SPM matches the complex shape characteristics of the P2D model while remaining very close to it in magnitude.

Table 6.6 Summary of statistics for the percentage absolute error in terminal voltage for the basic SPM, quadratic approximation SPM and the composite SPM with UDDS input profile.

Error Statistic for $ \hat{\epsilon}_v $	Basic SPM	Quadratic SPM	Composite SPM
Worst Case	2.59	1.68	0.72
Mean	0.51	0.36	0.11
RMS	0.68	0.39	0.16

6.11 Conclusions

In summary, while the newly developed composite SPM is not considered robust for use in sustained discharge at high C-rates, it is indeed a suitable option for dynamic load profiles, even for those with high peak magnitudes of instantaneous charge or discharge. Such load

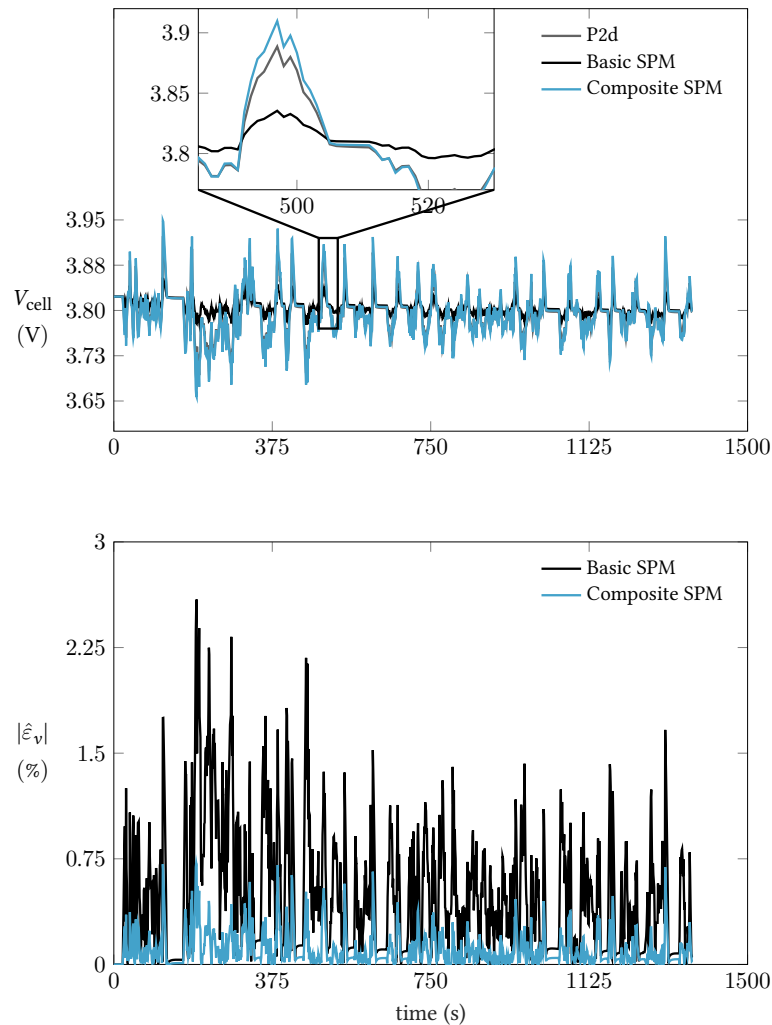


Figure 6.18 Voltage output of the composite SPM for a UDDS input profile with a peak magnitude of 180 A *i.e.*, 3C (see fig. 5.12). The voltage profiles computed by the basic SPM and the benchmark P2D model is also overlaid (top plot). The percentage absolute error of the two ROMs relative to the P2D model is shown in the bottom plot. The terminal voltage of the composite SPM is significantly more accurate than the basic SPM (see table 6.6).

profiles are typically encountered in vehicular applications, particularly in hybrid electric vehicles. Thus, a suitable time-domain ROM that can be directly implemented in discrete-time has been developed through system identification and its strengths and weaknesses have been quantified. The applicability of this model has been proven for real-life scenarios using a highly dynamic load cycle. Thus, this author concludes that the composite SPM developed here does indeed represent an advancement to the present modelling art. This model may now be used as the plant model in state estimation and control applications in a vehicular BMS. This concludes the chapter as well as all the implementation aspects of physics-based battery modelling discussed in this thesis.

7

Conclusions

7.1	Physics-Based Models as a Design Tool	269
7.1.1	Conclusions from the model-based design study	269
7.1.2	Future work informed by the optimal layer design framework	270
7.2	Analysis of Salient Physics-based Reduced Order Models	271
7.2.1	Conclusions from analysis of the DRA-based state-space ROM	272
7.2.2	Future outlook for the DRA-based hybrid state-space ROM	272
7.2.3	Conclusions from analysis of the SPM family of models	273
7.2.4	Proposed analysis routes for the SPM modelling family	275
7.3	Implementation Aspects of Basic and Composite SPM	276
7.4	Closing Remarks	278

IN this thesis, the deployment of physics-based computational modelling of lithium ion cells for electric vehicle applications has been rigorously examined with a three-pronged strategy *viz.* through their analysis, design and implementation. The Pseudo Two-Dimensional (P2D) implementation of the Doyle-Fuller-Newman (DFN) model was used as the backbone of all modelling efforts. Salient conclusions drawn from each of these aspects are presented in this chapter. Based upon the invaluable experience gained during the course of this research, and particularly from the findings presented herein, key areas in physics-based modelling that can benefit from further study in the future are also identified.

7.1 Physics-Based Models as a Design Tool

7.1.1 Conclusions from the model-based design study

Chapter 3 presented a computational framework to optimise the number of electrochemical layers within a pouch cell so as to maximise its usable energy while meeting specific power demands. In particular, this helped to construct a model-based deterministic approach to optimally design cells that can be subjected to fast-charging without the concerns of plating. In the context of electric vehicle applications, using this approach has the potential to alleviate the two immediate concerns of consumers *viz.* range anxiety and long charging times.

To facilitate immediate adoption by relevant stakeholders, the concepts developed in the optimisation framework of chapter 3 was realised in computer code and presented in the form of an open-source design toolbox, Battery Optimal Layer Design (BOLD). This toolbox was applied to the optimal layer design of an example cell from literature to obtain two sets of power-dependent optimal layer configurations for two drivetrains – a Battery Electric Vehicle (BEV) and a Plug-in Hybrid Electric Vehicle (PHEV). By suitably adapting the numerical values of parameters to a real-world cell, model-based cell designs can be obtained, which can potentially help to eliminate the current trend of over-engineering of cells using conservative empirical layer choices.

From a perspective of technical advancements to the underlying Physics-Based Model (PBM), the standard form of the P2D model has been suitably modified to facilitate a direct application of input power densities. This was achieved through reformulation of the boundary conditions on the solid-phase potential Partial Differential Equation (PDE). Although this innate power input capability has been claimed as purportedly developed in extant literature, its independent derivation and accessible documentation provided herein shall help other researchers to apply this in a straight-forward manner for vehicle drivecycles, acceleration tests and power-based charging protocols.

This investigation also revealed that the fast charging process determines the optimal layer configuration instead of either acceleration runs or drivecycle requirements. This may help to counter the current trend in publications which often rely primarily upon a drivecycle-based dynamic input current profile to evaluate various aspects of cell modelling such as predicting degradation and for advanced control and estimation algorithms. While validation

against such a dynamic input profile is certainly vital, for future advancements dealing with aspects of cell design or plating-related degradation, validation against fast-charging power profiles is deemed to be absolutely essential.

The study also provided important guidelines about the role of thermal environment on cell performance. It became clear that at very low temperatures, a high number of layers was required for satisfying a specific charging power level relative to that needed at moderate thermal environments such as room temperatures. A practical takeaway from this conclusion is that it suffices to use a low number of layers in vehicles to be sold in territories with perennial moderate temperature conditions.

Finally, this design study revealed that the speed at which lithium intercalates into the negative electrode during charging limits the charge-addition rate to the cell. Lowering the charging times of electric vehicles requires the use of higher charging powers. However, this necessitates a high number of layers to absorb the overpotentials and to provide adequate number of thermal conduction pathways (owing to the higher number of current collectors) to dissipate the additional heat generated. Consequently, this has a detrimental effect on the capacity and hence, the All-Electric Range (AER) of the vehicle.

7.1.2 Future work informed by the optimal layer design framework

As a direct inference of the final conclusion in section 7.1.1, assuming that the electric grid infrastructure is adequately equipped to cope with the surge in future power demands for charging of electric vehicles, the solid state diffusion at the negative electrode becomes the bottleneck. It is therefore important for future research to focus on the development of new materials for the negative electrode possessing much higher solid phase diffusion coefficients, particularly at low temperatures.

From a perspective of improving the framework itself, at the outset, it is clear that the plating threshold assessment can be made more accurate by incorporating the solid phase diffusion coefficient as function of State of Charge (SOC). In the interest of simplicity and to lay the foundation for such model-based cell designs, the scope of this work was intentionally narrowed down to solely focus on changing the layer configurations within cells. In doing so, certain assumptions were made that might have to be revisited and potentially relaxed before its application to real-world cell designs.

7.2 Analysis of Salient Physics-based Reduced Order Models

For instance, adherence to the specific type of cooling phenomena used *i.e.*, tab cooling, is one of the stronger assumptions used in this work. In this work, the benefits of employing this cooling mechanism has been enumerated, and it is desirable that future pack designs adopt it. However, the vast majority of the current generation of battery packs use surface-cooled designs. This means that temperature for all layers within the pouch shall not be the same, which further implies that it longer suffices to simulate just a single layer. Therefore, the framework needs to be suitably modified to handle multiple layer choices concurrently.

Furthermore, using surface cooling shall invalidate the assumption of small thermal gradients along the planar axis of the cell. This means that the lumped thermal model shall no longer be accurate to model the temperature evolution of the cell. Furthermore, the differential temperature evolution along the cross-sectional direction shall influence the transport and kinetic properties of the cell. This electrochemical-thermal coupling along the planar direction shall necessitate adding another spatial dimension to the underlying PBM, thereby rendering the presently used P2D model ineffective. With the aim of minimising the optimising run-times, future research may focus on how to suitably adapt the computational infrastructure that was proposed in this thesis to account for these considerations.

For real-world cell designs, it is prudent to examine the examine the role of variable porosities to achieve the balancing of active materials per layer. Since the computational framework developed in this thesis uses a modular approach, in the future the constant volume-fractions used in the methodology could simply be replaced by values informed by optimal porosity computations. For this purpose, researchers could investigate the feasibility of adapting a suitable scheme from the available pool of literature that have focussed on using model-based porosity optimisation [28, 29, 216]. Finally, experimental prototyping is an important step in any cell design and it is no exception here either. Therefore, experimentally applying the desired power levels to confirm the optimal layer choices predicted by the framework is an important step to be undertaken before its large-scale deployment.

7.2 Analysis of Salient Physics-based Reduced Order Models

Chapters 4 and 5 of this thesis primarily focussed on performing an in-depth analysis of two distinct Reduced Order Models (ROMs) from two distinct perspectives. In chapter 4, the hybrid ROM obtained by using the Discrete-Time Realisation Algorithm (DRA) is analysed

to investigate its *computational* bottlenecks. In chapter 5, an in-depth analysis of a niche selection of candidate models from the family of Single Particle Models (SPMs) is presented from the perspective of *modelling accuracy i.e.*, their ability to faithfully compute the system-level quantities of the cell such as its SOC and terminal voltage. Finally, the early portions of chapter 6 provides a thorough analysis of the bottlenecks of the quadratic approximation model for computing the spatial profile of ionic concentration in the electrolyte. The conclusions drawn from all aforementioned analyses are presented next. Topics that may be of interest to future researchers engaging with these ROMs are also proposed.

7.2.1 Conclusions from analysis of the DRA-based state-space ROM

In chapter 4, Singular Value Decomposition (SVD) of a large Block-Hankel matrix (≈ 27 GB) was identified as a computational bottleneck in applying the classical DRA scheme for the hybrid ROM discussed therein. It is concluded that this bottleneck arises due to slow dynamics of solid phase diffusion which leads to the aforesaid large sized Block-Hankel matrix.

To mitigate this bottleneck, an improved DRA scheme was presented, whose centrepiece is an iterative SVD algorithm. This algorithm was obtained as a combination of the Golyandina-Usevich and Lanczos algorithms discussed in chapter 4. The results of applying the improved DRA scheme demonstrate a significant performance improvement achieved by using the new method without trading-off model fidelity. At a single operating point of SOC and temperature, for a Hankel block size of 8000, the ROM workflow incorporating the improved DRA is approximately 100 times faster than that employing the classical DRA. On a standard computer workstation whose specifications are given in chapter 4, for 100 operating points (combinations of 10 SOC and temperature values), obtaining the ROM required only 6 hours using the improved DRA, whereas the classical DRA consumed 666 hours (≈ 27 days). Furthermore, for the same block-size, the improved DRA is demonstrated to be superior in terms of memory efficiency, drastically reducing the memory requirements from 112 GB down to 2 GB. Finally, the improved DRA demonstrates improved modelling accuracy even in moderately equipped computing environments such as standard consumer-grade laptops.

7.2.2 Future outlook for the DRA-based hybrid state-space ROM

The improved DRA method proposed in chapter 4 opens up the possibility of applying this hybrid ROM for physical quantities in other locations within the cell's geometry *e.g.* in the

7.2 Analysis of Salient Physics-based Reduced Order Models

middle of the electrode region, without being hindered by computational limitations that would have otherwise rendered it intractable. Furthermore, high sample-rate ROMs capable of handling highly dynamic load profiles can be deployed in future Battery Management System (BMS) applications. The proposed scheme also empowers the ROM framework to tackle other cell chemistries with slower diffusion coefficients or even those with completely different rate-limiting mechanisms, and therefore *prima facie*, appears to be promising.

Despite the benefits facilitated by the streamlining of the reduced order modelling workflow through the improved DRA, there exists a fundamental deficiency in this hybrid modelling approach that impedes its near-term adoption in state estimation tasks. This aspect was already discussed in chapter 2 and is reiterated here. The entries in the matrices of the final state space model depend on the linearisation point of SOC and temperature. This linearisation requirement adversely affects the usability of the model for state estimation tasks, wherein the SOC is in fact an unknown quantity and is to be estimated. This cyclic dependency between the linearisation point and the state-estimation entity renders this model questionable for use in a demanding application such as in embedded BMSs on-board electric vehicles. Therefore, the immediate future step is to analyse the stability of this internal feedback loop. Once this has been performed, researchers may consider to engage in the process of adapting the derivation of this hybrid state-space ROM approach to higher C-rates, in conjunction with the numerical benefits afforded by the improved DRA developed here.

7.2.3 Conclusions from analysis of the SPM family of models

Based upon the holistic evaluation of various ROMs in chapter 2, owing to its simplicity, the SPM family of models was identified as the most promising modelling candidate from an *implementation* perspective. Chapter 5 provided an in-depth analysis of the strengths and drawbacks of this modelling family.

Results from simulation of the basic SPM revealed that two contrasting aspects. Firstly, the SOC computation of the SPM was of acceptable accuracy even at moderate C-rates thereby validating the fourth order polynomial approximation approach for capturing solid phase diffusion dynamics. However, the basic SPM suffers from severe inaccuracies in computing the cell's terminal voltage at currents above 0.5C. This dichotomous behaviour, revealed through this analysis, has not been explicitly commented upon in present literature. In particular,

7.2 Analysis of Salient Physics-based Reduced Order Models

despite its overarching simplicity, it can be concluded that it is this contrasting aspect that renders the model unusable as the plant model for state estimation tasks. This is because, the voltage measured from the model in a feedback estimator shall map to a radically distant SOC operating point requiring excessively strong gain factors for correcting it adversely affecting the stability of estimators.

Several research efforts from literature that have attempted to tackle the voltage inaccuracies of the basic SPM through inclusion of electrolyte dynamics were also presented in chapter 5. A critical evaluation of each of the salient efforts revealed that a suitable approach that can successfully handle all possible operational scenarios is yet to be devised. In particular, the existing modelling approaches for electrolyte inclusion either made far-fetched assumptions that were easily violated or presented nearly intractable mathematical expressions that pushed the SPM closer in computational complexity to the P2D dynamics. The author's analysis of pertinent literature also revealed the possibility of re-using certain portions of existing work *e.g.* the electrolyte overpotential expression, whilst also arguing the need for a fresh approach to model other aspects of electrolyte dynamics such as the ionic concentration profile within the cell's thickness.

The final section of chapter 5 presented the assumptions and governing equations of the quadratic approximation model for the spatial profile of ionic concentration. The results obtained by simulating this model reveal that while its spatial profile computation for a galvanostatic operation is of acceptable accuracy, its temporal performance is mediocre. Particularly, the time evolution of ionic concentration at the current collector interfaces computed by the model fail to capture the intricacies in the temporal evolution exhibited by the P2D model's profile. Furthermore, the spatial profile uses the Quasi-Steady State (QSS) approximation which is violated during the initial transient. Hence, the most impactful conclusion from the foregoing analysis is that the basic quadratic approximation model is unsuitable for dynamic loads, thereby ruling it out for deployment in vehicular applications.

The initial portions of chapter 6 analysed the causal factor contributing to the mediocre performance of the quadratic approximation model. For this analysis, a genetic programming approach was employed to synthesise suitable alternative reduced order equations for modelling the spatial profile of the electrolyte concentration. The foregoing analysis helped to reveal that given the constraints and interior-point boundary conditions of the underlying

DFN model at the separator interfaces, the number of coefficients used in the quadratic spatial profile does indeed make the best use of all available equations. The genetic programming approach being able to synthesise suitable mathematical structures that can potentially capture the spatial profile accurately during both transient and steady state conditions. However, there is a shortfall in the number of equations in order to uniquely solve for these extra coefficients. The final conclusion that stems from this fact is that, by decoupling the spatial and temporal profiles of the electrolyte concentration dynamics, the performance of the present state of the art can indeed be improved upon.

7.2.4 Proposed analysis routes for the SPM modelling family

Albeit extensive, the analyses of SPMs performed in this thesis is by no means complete. It is more appropriate to say that this author chose to analyse SPMs from their implementation perspective, particularly their voltage and SOC accuracies in an open-loop implementation. However, a holistic evaluation covering other aspects are necessary before their deployment in a vehicular BMS can be considered. For instance, the observability of models must be proven before they can be employed in the feedback path of a state estimator. Even within the broad stream of observability analysis, there are several details that need to be meticulously handled of which some avenues for future exploration are identified.

In the simplification of the state-vector of the basic SPM proposed by Di Domenico [96], the bulk concentration in the two electrodes was assumed to be equal (see section 5.1.3). This allowed to eliminate the bulk concentrations of one of the two electrodes, thereby reducing the state vector to $\mathbb{R}^{3 \times 1}$. This assumption hinges on the assumption that there is no loss of cycleable lithium. However, such an assumption is valid only for a brand new cell. As the cell ages, owing to various phenomena such as parasitic side reactions and decomposition of the solid conductive matrix, this assumption shall no longer hold true. Therefore, analysis of models obtained by augmenting the basic or electrolyte-enhanced SPMs with equations describing degradation shall become critical. Not only does this force to retain both bulk concentrations in the state vector, the states from the degradation rate-equations appear in it, thereby enlarging it. In future studies, the effect of these augmented state variables on the observability of the system needs to be quantified.

7.3 Implementation Aspects of Basic and Composite SPM

In this thesis, only an *isothermal* analysis of various SPMs have been performed. While this is an important initial step to analyse the strengths and weaknesses of the state of the art incumbent SPM models by isolating the purely electrochemical aspects, the effect of temperature cannot be underplayed. It is well-known that the thermal conditions of the cell affects its electrochemical and vice-versa. Therefore, future works shall benefit from performing comprehensive analyses of coupled electrochemical-thermal SPMs. Considering the simplicity of SPMs, the lumped thermal model might be a suitable candidate for it be paired with. Finally, in addition to its influence on the accuracy of open-loop terminal voltage and SOC, the effect of temperature on the observability of the holistic model needs to be evaluated. Since the cell temperature is available as an additional measurement, it is likely to improve the model's observability. However, there is a trade-off since this comes at the cost of increased size of the state vector. It is also worthwhile to explore the inflection point of this trade-off to limit the model's fidelity at a sufficient level whilst reaping the maximum gains out of the additional temperature measurement.

Based upon the conclusion that the performance of any reduced order spatial profile model is hamstrung by the equation deficiencies in the underlying DFN model, it is worthwhile to reproduce the Multi-Gene Genetic Programming (MGGP) approach with a different PBM. For this future task, it is imperative to choose a model that provides additional interior-point conditions *i.e.*, not just at the separator, but perhaps a second order condition within an interior location at each electrode. Once such a suitable PBM has been identified, this thesis author is confident that the genetic programming approach shall indeed synthesise an accurate description of the electrolyte's spatio-temporal dynamics.

7.3 Implementation Aspects of Basic and Composite SPM

A driving impetus behind this thesis is to deliver ROMs amenable to embedded *implementation*. Large portions of chapter 5 and nearly the entirety of chapter 6 were devoted to this study. The conclusions that emerged from these implementation efforts are summarised here. Future areas of research are also identified in-line.

In chapter 5, the aspects of discrete-time implementation in a microcontroller were discussed. In particular, the computation of the discrete-time system and input matrices through

7.3 Implementation Aspects of Basic and Composite SPM

the matrix exponential approach is presented. A straightforward conclusion from the discrete-time implementation is that they run orders of magnitude faster than their continuous-time counterparts. This is owing to the fact that adaptive time-stepping integrators are not required and can be replaced by a simple matrix-vector multiplication scheme. This implementation detail provides necessary starting point for battery researchers to start coding the ROMs discussed herein. Future work in this direction shall benefit from including various real-world issues such as accounting for sample delays as well as implementing a progressive update scheme for the matrix entries to account for degradation effects. Important aspects of numerical implementation arise during the design of state estimators. Having a robust open-loop implementation of a discrete-time plant model shall facilitate easy implementation of such feedback algorithms.

Chapter 6 discussed the implementation aspects of ROM from a different perspective — that of formulating a new electrolyte enhanced composite SPM for embedded implementation. The temporal evolution of electrolyte dynamics in the two electrode regions were characterised through system identification techniques that have never been tried before in literature. The identified model structures are presented in the final form as discrete-time difference equations that can be readily incorporated into the discrete-time equations developed in chapter 5 for the basic SPM. The salient conclusion from this modelling effort is that, system identification is indeed a viable candidate for the derivation of ROMs of lithium ion batteries. The improved accuracy of electrolyte concentration dynamics relative to the state of the art quadratic approximation model corroborates the success of this strategy. Nevertheless, before widespread adoption of this technique can be advocated, certain aspects of this approach must be examined carefully. For instance, the assumptions of linearity and time-invariance must be revisited for higher magnitudes of charge and discharge currents. Thermal effects must also be incorporated into the overall system identification approach. Machine learning and system identification are two complementary approaches to the same task *i.e.*, identification of internal dynamics from terminal measurements. Future research could also explore this possibility and perhaps a combined system identification/machine learning strategy might metamorphose into the approach that powers future generation of surrogate ROMs for electric vehicle applications.

7.4 Closing Remarks

The feasibility of bringing PBMs of lithium batteries into electrified transportation has been studied in this thesis from a multi-dimensional perspective. Yet, there exists a common underpinning that connects these seemingly different routes to the enhancement of our extant knowledge — that of parametrising the underlying PBM. The number of parameters in any PBM is excessively large to the point of detracting potential adopters. Even without considering degradation effects, obtaining the physical, geometric, transport and kinetic parameters of a cell shall require access to specialised laboratory equipment that are sometimes exclusive to large scale research organisations. The studies discussed here shall assume real-world significance only upon a successful demonstration of a cost-effective parametrisation strategy. The author's contributions to an optimal 'Design of Experiments (DoE)' numerical procedure for identifying the parameters of an SPM is detailed in [217]. However, the broader task of parametrising a full-order PBM is well beyond the scope of this thesis or indeed any single researcher, and needs the concerted effort of the community as a whole to tackle it.

The next task in the journey to real-world implementation of the advancements brought about by this thesis is to experimentally validate them. However, this is contingent upon obtaining a successful parametrisation strategy, and should be embarked upon as soon as a robust procedure to identify the physical parameters is made available. Nevertheless, this author hopes that through the three-pronged approach to cell modelling presented in this thesis, the goal of bringing physics-based battery models to electrified transportation has been brought a step closer to realisation.

References

- [1] Martin Weiss, Pierre Bonnel, Rudolf Hummel, Alessio Provenza and Urbano Manfredi. “On-Road Emissions of Light-Duty Vehicles in Europe”. *Environmental Science & Technology* 45.19 (Oct. 2011), pp. 8575–8581. ISSN: 0013-936X. DOI: [10.1021/es2008424](https://doi.org/10.1021/es2008424) [cited on page 34].
- [2] H. Ibrahim, A. Ilinca and J. Perron. “Energy storage systems—Characteristics and comparisons”. *Renewable and Sustainable Energy Reviews* 12.5 (June 2008), pp. 1221–1250. ISSN: 1364-0321. DOI: [10.1016/J.RSER.2007.01.023](https://doi.org/10.1016/J.RSER.2007.01.023) [cited on page 34].
- [3] Davide Andrea. *Battery management systems for large lithium-ion battery packs*. Boston : Artech House, 2010, p. 290. ISBN: 9781608071050 [cited on pages 34, 94, 171, 197].
- [4] Thomas B. Reddy and David Linden. *Linden’s handbook of batteries*. 4th ed. New York: McGraw-Hill, 2011, p. 1457. ISBN: 9780071624213 [cited on pages 35, 36, 164].
- [5] Gregory L. Plett. *Battery Management Systems, Volume I: Battery Modeling*. 1st ed. Norwood, Massachusetts: Artech House, 2015, p. 346. ISBN: 978-1630810238 [cited on pages 35, 37, 39, 40, 137, 138].
- [6] D. Grazioli, M. Magri and A. Salvadori. “Computational modeling of Li-ion batteries”. *Computational Mechanics* 58.6 (Dec. 2016), pp. 889–909. ISSN: 0178-7675. DOI: [10.1007/s00466-016-1325-8](https://doi.org/10.1007/s00466-016-1325-8) [cited on page 37].
- [7] Krishnan S. Hariharan, Piyush Tagade and Sanoop Ramachandran. *Mathematical Modeling of Lithium Batteries : From Electrochemical Models to State Estimator Algorithms*. Green Energy and Technology. Cham: Springer International Publishing, 2017. ISBN: 9783319035277. DOI: [10.1007/978-3-319-03527-7](https://doi.org/10.1007/978-3-319-03527-7) [cited on page 37].
- [8] Christopher D. Rahn and Chao-Yang Wang. *Battery Systems Engineering*. Oxford, UK: John Wiley & Sons Ltd, Feb. 2013. ISBN: 9781118517048. DOI: [10.1002/9781118517048](https://doi.org/10.1002/9781118517048) [cited on pages 37, 61, 83, 164].
- [9] Henk J. Bergveld, Wanda S. Kruijt and Peter H. Notten. *Battery Management Systems : Design by Modelling*. Dordrecht : Springer Netherlands, 2002, p. 295. ISBN: 9789401708432. DOI: [10.1007/978-94-017-0843-2](https://doi.org/10.1007/978-94-017-0843-2) [cited on page 37].
- [10] Aden Seaman, Thanh-Son Dao and John McPhee. “A survey of mathematics-based equivalent-circuit and electrochemical battery models for hybrid and electric vehicle simulation”. *Journal of Power Sources* 256 (June 2014), pp. 410–423. ISSN: 0378-7753. DOI: [10.1016/J.JPOWSOUR.2014.01.057](https://doi.org/10.1016/J.JPOWSOUR.2014.01.057) [cited on page 38].
- [11] Gregory L. Plett. “Sigma-point Kalman filtering for battery management systems of LiPB-based HEV battery packs: Part 1: Introduction and state estimation”. *Journal of Power Sources* 161.2 (Oct. 2006), pp. 1356–1368. ISSN: 0378-7753. DOI: [10.1016/J.JPOWSOUR.2006.06.003](https://doi.org/10.1016/J.JPOWSOUR.2006.06.003) [cited on pages 38, 169].

- [12] Fengchun Sun, Xiaosong Hu, Yuan Zou and Siguang Li. “Adaptive unscented Kalman filtering for state of charge estimation of a lithium-ion battery for electric vehicles”. *Energy* 36.5 (May 2011), pp. 3531–3540. ISSN: 0360-5442. DOI: [10.1016/J.ENERGY.2011.03.059](https://doi.org/10.1016/J.ENERGY.2011.03.059) [cited on page 38].
- [13] Gregory L. Plett. *Battery Management Systems, Volume II: Equivalent-Circuit Methods*. Norwood, Massachusetts: Artech House, 2016. ISBN: 978-1-63081-027-6 [cited on pages 39, 103, 171].
- [14] M. Ecker, T.K.D. Tran, P. Dechent, S. Kabitz, A. Warnecke and Dirk U. Sauer. “Parameterization of a Physico-Chemical Model of a Lithium-Ion Battery: I. Determination of Parameters”. *Journal of the Electrochemical Society* 162.9 (June 2015), A1836–A1848. ISSN: 0013-4651. DOI: [10.1149/2.0551509jes](https://doi.org/10.1149/2.0551509jes) [cited on pages 39, 164].
- [15] Marc Doyle, Thomas F. Fuller and John S. Newman. “Modeling of Galvanostatic Charge and Discharge of the Lithium/Polymer/Insertion Cell”. *Journal of The Electrochemical Society* 140.6 (June 1993), pp. 1526–1533. ISSN: 00134651. DOI: [10.1149/1.2221597](https://doi.org/10.1149/1.2221597) [cited on pages 40, 138, 161].
- [16] Thomas F. Fuller, Marc Doyle and John S. Newman. “Simulation and Optimization of the Dual Lithium Ion Insertion Cell”. *Journal of The Electrochemical Society* 141.1 (Jan. 1994), p. 1. ISSN: 00134651. DOI: [10.1149/1.2054684](https://doi.org/10.1149/1.2054684) [cited on pages 40, 138, 148, 161].
- [17] Gregory L. Plett. *Lecture Notes 04 & 06: ECE5710 - Modeling, Simulation, and Identification of Battery Dynamics*. Colorado Springs, 2018. URL: <http://mocha-java.uccs.edu/ECE5710/ECE5710-Notes04.pdf>; <http://mocha-java.uccs.edu/ECE5710/ECE5710-Notes06.pdf> [cited on page 41].
- [18] Marcello Torchio, Lalo Magni, R B. Gopaluni, Richard D. Braatz and Davide M. Raimondo. “LIONSIMBA: A Matlab Framework Based on a Finite Volume Model Suitable for Li-Ion Battery Design, Simulation, and Control”. *Journal of The Electrochemical Society* 163.7 (2016), A1192–A1205. ISSN: 0013-4651. DOI: [10.1149/2.0291607jes](https://doi.org/10.1149/2.0291607jes) [cited on pages 41, 105, 125, 307].
- [19] Stefan H. Thomke. “Simulation, learning and R&D performance: Evidence from automotive development”. *Research Policy* 27.1 (May 1998), pp. 55–74. ISSN: 00487333. DOI: [10.1016/S0048-7333\(98\)00024-9](https://doi.org/10.1016/S0048-7333(98)00024-9) [cited on page 45].
- [20] Markus C. Becker, Pasquale Salvatore and Francesco Zirpoli. “The impact of virtual simulation tools on problem-solving and new product development organization”. *Research Policy* 34.9 (Nov. 2005), pp. 1305–1321. ISSN: 00487333. DOI: [10.1016/j.respol.2005.03.016](https://doi.org/10.1016/j.respol.2005.03.016) [cited on page 45].
- [21] Robert M. Spotnitz. “Battery modeling”. *The Electrochemical Society Interface* (2005), pp. 39–42. ISSN: 10648208. DOI: [10.1109/MC.2003.1250886](https://doi.org/10.1109/MC.2003.1250886) [cited on page 45].
- [22] M S. Islam and Craig A. J. Fisher. “Lithium and sodium battery cathode materials: computational insights into voltage, diffusion and nanostructural properties”. *Chemical Society Reviews* 43.1 (Dec. 2014), pp. 185–204. ISSN: 0306-0012. DOI: [10.1039/C3CS60199D](https://doi.org/10.1039/C3CS60199D) [cited on page 46].
- [23] Ying S. Meng and M E. Arroyo-de Dompablo. “First principles computational materials design for energy storage materials in lithium ion batteries”. *Energy & Environmental Science* 2.6 (June 2009), p. 589. ISSN: 1754-5692. DOI: [10.1039/b901825e](https://doi.org/10.1039/b901825e) [cited on page 46].

- [24] Austin D. Sendek, Qian Yang, Ekin D. Cubuk, Karel-Alexander N. Duerloo, Yi Cui and Evan J. Reed. “Holistic computational structure screening of more than 12 000 candidates for solid lithium-ion conductor materials”. *Energy & Environmental Science* 10.1 (2017), pp. 306–320. ISSN: 1754-5692. DOI: [10.1039/C6EE02697D](https://doi.org/10.1039/C6EE02697D) [cited on page 46].
- [25] Venkatasailanathan Ramadesigan, Paul W. Northrop, Sumitava De, Shriram Santhanagopalan, Richard D. Braatz and V. R. Subramanian. “Modeling and Simulation of Lithium-Ion Batteries from a Systems Engineering Perspective”. *Journal of the Electrochemical Society* 159.3 (Jan. 2012), R31–R45. ISSN: 0013-4651. DOI: [10.1149/2.018203jes](https://doi.org/10.1149/2.018203jes) [cited on pages 47, 83, 84, 120, 121].
- [26] John S. Newman. “Optimization of Porosity and Thickness of a Battery Electrode by Means of a Reaction-Zone Model”. *Journal of The Electrochemical Society* 142.1 (1995), p. 97. ISSN: 00134651. DOI: [10.1149/1.2043956](https://doi.org/10.1149/1.2043956) [cited on pages 47, 86].
- [27] Pankaj Arora, Marc Doyle and Ralph E. White. “Mathematical Modeling of the Lithium Deposition Overcharge Reaction in Lithium-Ion Batteries Using Carbon-Based Negative Electrodes”. *Journal of The Electrochemical Society* 146.10 (Oct. 1999), p. 3543. ISSN: 00134651. DOI: [10.1149/1.1392512](https://doi.org/10.1149/1.1392512) [cited on pages 48, 167].
- [28] Nansi Xue, Wenbo Du, Amit Gupta, Wei Shyy, Ann Marie Sastry and Joaquim R. Martins. “Optimization of a Single Lithium-Ion Battery Cell with a Gradient-Based Algorithm”. *Journal of The Electrochemical Society* 160.8 (May 2013), A1071–A1078. ISSN: 0013-4651. DOI: [10.1149/2.036308jes](https://doi.org/10.1149/2.036308jes) [cited on pages 48, 271].
- [29] Nansi Xue, Wenbo Du, Thomas A. Greszler, Wei Shyy and Joaquim R. Martins. “Design of a lithium-ion battery pack for PHEV using a hybrid optimization method”. *Applied Energy* 115 (Feb. 2014), pp. 591–602. ISSN: 03062619. DOI: [10.1016/j.apenergy.2013.10.044](https://doi.org/10.1016/j.apenergy.2013.10.044) [cited on pages 48, 49, 271].
- [30] Dragan Maksimovic. *Course Notes ECEN5017: Power Electronics for Electric Drive Vehicles*. 2012. URL: <http://ecee.colorado.edu/%7B~%7Ddecen5017/> [cited on pages 49, 91, 99, 113, 129, 199].
- [31] Changhong Liu and Lin Liu. “Optimal Design of Li-Ion Batteries through Multi-Physics Modeling and Multi-Objective Optimization”. *Journal of The Electrochemical Society* 164.11 (2017), E3254–E3264. ISSN: 0013-4651. DOI: [10.1149/2.0291711jes](https://doi.org/10.1149/2.0291711jes) [cited on page 49].
- [32] Ali Jokar, Barzin Rajabloo, Martin Désilets and Marcel Lacroix. “Review of simplified Pseudo-two-Dimensional models of lithium-ion batteries”. *Journal of Power Sources* 327 (Sept. 2016), pp. 44–55. ISSN: 0378-7753. DOI: [10.1016/J.JPOWSOUR.2016.07.036](https://doi.org/10.1016/J.JPOWSOUR.2016.07.036) [cited on pages 50, 51, 58].
- [33] Guodong Fan, Ke Pan and Marcello Canova. “A comparison of model order reduction techniques for electrochemical characterization of Lithium-ion batteries”. *54th IEEE Conference on Decision and Control (CDC)*. IEEE, Dec. 2015, pp. 3922–3931. DOI: [10.1109/CDC.2015.7402829](https://doi.org/10.1109/CDC.2015.7402829) [cited on pages 50, 51, 58].
- [34] Kandler Smith and Chao-Yang Wang. “Solid-state diffusion limitations on pulse operation of a lithium ion cell for hybrid electric vehicles”. *Journal of Power Sources* 161.1 (Oct. 2006), pp. 628–639. ISSN: 0378-7753. DOI: [10.1016/J.JPOWSOUR.2006.03.050](https://doi.org/10.1016/J.JPOWSOUR.2006.03.050) [cited on pages 53, 157].

- [35] Thanh-Son Dao, Chandrika P. Vyasarayani and John McPhee. “Simplification and order reduction of lithium-ion battery model based on porous-electrode theory”. *Journal of Power Sources* 198 (Jan. 2012), pp. 329–337. ISSN: 0378-7753. DOI: [10.1016/J.JPOWSOUR.2011.09.034](https://doi.org/10.1016/J.JPOWSOUR.2011.09.034) [cited on page 53].
- [36] Guodong Fan, Ke Pan, Marcello Canova, James Marcicki and Xiao G. Yang. “Modeling of Li-Ion Cells for Fast Simulation of High C-Rate and Low Temperature Operations”. *Journal of The Electrochemical Society* 163.5 (Feb. 2016), A666–A676. ISSN: 0013-4651. DOI: [10.1149/2.0761605jes](https://doi.org/10.1149/2.0761605jes) [cited on pages 53, 76, 77].
- [37] Guodong Fan, Xiaoyu Li and Marcello Canova. “A reduced-order electrochemical model of li-ion batteries for control and estimation applications”. *IEEE Transactions on Vehicular Technology* 67.1 (2018), pp. 76–91. ISSN: 00189545. DOI: [10.1109/TVT.2017.2738780](https://doi.org/10.1109/TVT.2017.2738780) [cited on page 53].
- [38] Wikipedia. *Padé approximant* — Wikipedia, The Free Encyclopedia. 2018. URL: https://en.wikipedia.org/wiki/Pad%C3%A9_approximant (visited on 03/12/2018) [cited on page 53].
- [39] Joel C. Forman, Saeid Bashash, Jeffrey L. Stein and Hosam K. Fathy. “Reduction of an Electrochemistry-Based Li-Ion Battery Model via Quasi-Linearization and Padé Approximation”. *Journal of The Electrochemical Society* 158.2 (Feb. 2011), A93. ISSN: 00134651. DOI: [10.1149/1.3519059](https://doi.org/10.1149/1.3519059) [cited on pages 53, 65].
- [40] James Marcicki, Marcello Canova, A. Terrence Conlisk and Giorgio Rizzoni. “Design and parametrization analysis of a reduced-order electrochemical model of graphite/LiFePO4 cells for SOC/SOH estimation”. *Journal of Power Sources* 237 (Sept. 2013), pp. 310–324. ISSN: 0378-7753. DOI: [10.1016/J.JPOWSOUR.2012.12.120](https://doi.org/10.1016/J.JPOWSOUR.2012.12.120) [cited on pages 53, 76].
- [41] Saeid Bashash, Scott J. Moura and Hosam K. Fathy. “Charge trajectory optimization of plug-in hybrid electric vehicles for energy cost reduction and battery health enhancement”. *Proceedings of the 2010 American Control Conference*. IEEE, June 2010, pp. 5824–5831. ISBN: 978-1-4244-7427-1. DOI: [10.1109/ACC.2010.5530497](https://doi.org/10.1109/ACC.2010.5530497) [cited on page 53].
- [42] Hector Perez, Niloofar Shahmohammadhamedani and Scott J. Moura. “Enhanced Performance of Li-Ion Batteries via Modified Reference Governors and Electrochemical Models”. *IEEE/ASME Transactions on Mechatronics* 20.4 (Aug. 2015), pp. 1511–1520. ISSN: 1083-4435. DOI: [10.1109/TMECH.2014.2379695](https://doi.org/10.1109/TMECH.2014.2379695) [cited on page 53].
- [43] Scott J. Moura, Miroslav Krstic and Nalin A. Chaturvedi. “Adaptive PDE Observer for Battery SOC/SOH Estimation”. *Volume 1: Adaptive Control; Advanced Vehicle Propulsion Systems; Aerospace Systems; Autonomous Systems; Battery Modeling; Biochemical Systems; Control Over Networks; Control Systems Design; Cooperativ*. ASME, Oct. 2012, pp. 101–110. ISBN: 978-0-7918-4529-5. DOI: [10.1115/DSCC2012-MOVIC2012-8800](https://doi.org/10.1115/DSCC2012-MOVIC2012-8800) [cited on pages 53, 156, 309].
- [44] Githin K. Prasad and Christopher D. Rahn. “Model based identification of aging parameters in lithium ion batteries”. *Journal of Power Sources* 232 (June 2013), pp. 79–85. ISSN: 0378-7753. DOI: [10.1016/J.JPOWSOUR.2013.01.041](https://doi.org/10.1016/J.JPOWSOUR.2013.01.041) [cited on pages 53, 58, 65].
- [45] Shifei Yuan, Lei Jiang, Chengliang Yin, Hongjie Wu and Xi Zhang. “A transfer function type of simplified electrochemical model with modified boundary conditions and Padé approximation for Li-ion battery: Part 1. lithium concentration estimation”. *Journal of Power Sources* 352 (June 2017), pp. 245–257. ISSN: 0378-7753. DOI: [10.1016/J.JPOWSOUR.2017.03.060](https://doi.org/10.1016/J.JPOWSOUR.2017.03.060) [cited on pages 53, 65].

- [46] Shifei Yuan, Lei Jiang, Chengliang Yin, Hongjie Wu and Xi Zhang. “A transfer function type of simplified electrochemical model with modified boundary conditions and Padé approximation for Li-ion battery: Part 2. Modeling and parameter estimation”. *Journal of Power Sources* 352 (June 2017), pp. 258–271. ISSN: 0378-7753. DOI: [10.1016/J.JPOWSOUR.2017.03.061](https://doi.org/10.1016/J.JPOWSOUR.2017.03.061) [cited on pages 53, 65].
- [47] Kandler A. Smith, Christopher D. Rahn and Chao-Yang Wang. “Control oriented 1D electrochemical model of lithium ion battery”. *Energy Conversion and Management* 48.9 (Sept. 2007), pp. 2565–2578. ISSN: 0196-8904. DOI: [10.1016/J.ENCONMAN.2007.03.015](https://doi.org/10.1016/J.ENCONMAN.2007.03.015) [cited on pages 54, 65, 137].
- [48] James L. Lee, Andrew Chemistruck and Gregory L. Plett. “One-dimensional physics-based reduced-order model of lithium-ion dynamics”. *Journal of Power Sources* 220 (Dec. 2012), pp. 430–448. ISSN: 0378-7753. DOI: [10.1016/J.JPOWSOUR.2012.07.075](https://doi.org/10.1016/J.JPOWSOUR.2012.07.075) [cited on pages 55, 56, 62, 66, 137–139, 141, 148, 152, 153].
- [49] James L. Lee. “Reduced-order physics-based model of lithium-ion batteries”. PhD thesis. University of Colorado Colorado Springs, 2012, p. 150. URL: <http://hdl.handle.net/10976/250> [cited on pages 55, 56, 62, 137].
- [50] James L. Lee, Lukas L. Aldrich, Kirk D. Stetzel and Gregory L. Plett. “Extended operating range for reduced-order model of lithium-ion cells”. *Journal of Power Sources* 255 (June 2014), pp. 85–100. ISSN: 03787753. DOI: [10.1016/j.jpowsour.2013.12.134](https://doi.org/10.1016/j.jpowsour.2013.12.134) [cited on pages 56, 57].
- [51] Albert Rodríguez, Gregory L. Plett and M. Scott Trimboli. “Fast computation of the electrolyte-concentration transfer function of a lithium-ion cell model”. *Journal of Power Sources* 360 (Aug. 2017), pp. 642–645. ISSN: 0378-7753. DOI: [10.1016/J.JPOWSOUR.2017.06.025](https://doi.org/10.1016/J.JPOWSOUR.2017.06.025) [cited on pages 57, 66].
- [52] Meng Guo, Xinfang Jin and Ralph E. White. “Nonlinear State-Variable Method for Solving Physics-Based Li-Ion Cell Model with High-Frequency Inputs”. *Journal of The Electrochemical Society* 164.11 (2017), E3001–E3015. ISSN: 0013-4651. DOI: [10.1149/2.0021711jes](https://doi.org/10.1149/2.0021711jes) [cited on pages 58, 66].
- [53] Githin K. Prasad and Christopher D. Rahn. “Development of a First Principles Equivalent Circuit Model for a Lithium Ion Battery”. *Volume 2: Legged Locomotion; Mechatronic Systems; Mechatronics; Mechatronics for Aquatic Environments; MEMS Control; Model Predictive Control; Modeling and Model-Based Control of Advanced IC Engines*; ASME, Oct. 2012, p. 369. ISBN: 978-0-7918-4530-1. DOI: [10.1115/DSCC2012-MOVIC2012-8607](https://doi.org/10.1115/DSCC2012-MOVIC2012-8607) [cited on page 58].
- [54] Githin K. Prasad and Christopher D. Rahn. “Reduced Order Impedance Models of Lithium Ion Batteries”. *Journal of Dynamic Systems, Measurement, and Control* 136.4 (Apr. 2014), p. 041012. ISSN: 0022-0434. DOI: [10.1115/1.4026652](https://doi.org/10.1115/1.4026652) [cited on pages 58, 66].
- [55] Xi Zhang, Jinling Lu, Shifei Yuan, Jun Yang and Xuan Zhou. “A novel method for identification of lithium-ion battery equivalent circuit model parameters considering electrochemical properties”. *Journal of Power Sources* 345 (Mar. 2017), pp. 21–29. ISSN: 0378-7753. DOI: [10.1016/J.JPOWSOUR.2017.01.126](https://doi.org/10.1016/J.JPOWSOUR.2017.01.126) [cited on pages 58, 59, 66].
- [56] Si Cheng, Yong Zhang, Xu-Feng Cheng and Xi Zhang. “State estimation using physics-based equivalent circuit models of a Li-ion cell and Kalman filter”. *IECON 2017 - 43rd Annual Conference of the IEEE Industrial Electronics Society*. IEEE, Oct. 2017, pp. 5280–5286. ISBN: 978-1-5386-1127-2. DOI: [10.1109/IECON.2017.8216914](https://doi.org/10.1109/IECON.2017.8216914) [cited on page 58].

- [57] Yu Merla, Billy Wu, Vladimir Yufit, Ricardo F. Martinez-Botas and Gregory J. Offer. “An easy-to-parameterise physics-informed battery model and its application towards lithium-ion battery cell design, diagnosis, and degradation”. *Journal of Power Sources* 384 (Apr. 2018), pp. 66–79. ISSN: 0378-7753. DOI: [10.1016/J.JPOWSOUR.2018.02.065](https://doi.org/10.1016/J.JPOWSOUR.2018.02.065) [cited on pages 58, 59, 66].
- [58] J. E. B. Randles. “Kinetics of rapid electrode reactions”. *Discussions of the Faraday Society* 1 (Jan. 1947), p. 11. ISSN: 0366-9033. DOI: [10.1039/df9470100011](https://doi.org/10.1039/df9470100011) [cited on page 58].
- [59] Xiaoyu Li, Guodong Fan, Giorgio Rizzoni, Marcello Canova, Chunbo Zhu and Guo Wei. “A simplified multi-particle model for lithium ion batteries via a predictor-corrector strategy and quasi-linearization”. *Energy* 116 (Dec. 2016), pp. 154–169. ISSN: 0360-5442. DOI: [10.1016/J.ENERGY.2016.09.099](https://doi.org/10.1016/J.ENERGY.2016.09.099) [cited on page 60].
- [60] Xing Xu, Wei Wang and Long Chen. “Order Reduction of Lithium-Ion Battery Model Based on Solid State Diffusion Dynamics via Large Scale Systems Theory”. *Journal of The Electrochemical Society* 163.7 (May 2016), A1429–A1441. ISSN: 0013-4651. DOI: [10.1149/2.1251607jes](https://doi.org/10.1149/2.1251607jes) [cited on page 60].
- [61] Matteo Corno, Nimitt Bhatt, Sergio M. Savaresi and Michel Verhaegen. “Electrochemical model-based state of charge estimation for li-ion cells”. *IEEE Transactions on Control Systems Technology* 23.1 (2015), pp. 117–127. ISSN: 10636536. DOI: [10.1109/TCST.2014.2314333](https://doi.org/10.1109/TCST.2014.2314333) [cited on page 60].
- [62] Jocelyn Sabatier, Mathieu Merveillaut, Junior M. Francisco, Franck Guillemard and Denis Porcelatto. “Lithium-ion batteries modeling involving fractional differentiation”. *Journal of Power Sources* 262 (Sept. 2014), pp. 36–43. ISSN: 0378-7753. DOI: [10.1016/J.JPOWSOUR.2014.02.071](https://doi.org/10.1016/J.JPOWSOUR.2014.02.071) [cited on page 60].
- [63] Jocelyn Sabatier, Junior M. Francisco, Franck Guillemard, Loic Lavigne, Mathieu Moze and Mathieu Merveillaut. “Lithium-ion batteries modeling: A simple fractional differentiation based model and its associated parameters estimation method”. *Signal Processing* 107 (Feb. 2015), pp. 290–301. ISSN: 0165-1684. DOI: [10.1016/J.SIGPRO.2014.06.008](https://doi.org/10.1016/J.SIGPRO.2014.06.008) [cited on page 60].
- [64] Xiaoyu Li, Guodong Fan, Ke Pan, Guo Wei, Chunbo Zhu, Giorgio Rizzoni and Marcello Canova. “A physics-based fractional order model and state of energy estimation for lithium ion batteries. Part I: Model development and observability analysis”. *Journal of Power Sources* 367 (Nov. 2017), pp. 187–201. ISSN: 0378-7753. DOI: [10.1016/J.JPOWSOUR.2017.09.049](https://doi.org/10.1016/J.JPOWSOUR.2017.09.049) [cited on page 60].
- [65] Hao Mu, Rui Xiong, Hongfei Zheng, Yuhua Chang and Zeyu Chen. “A novel fractional order model based state-of-charge estimation method for lithium-ion battery”. *Applied Energy* 207 (Dec. 2017), pp. 384–393. ISSN: 0306-2619. DOI: [10.1016/J.APENERGY.2017.07.003](https://doi.org/10.1016/J.APENERGY.2017.07.003) [cited on page 60].
- [66] Baojin Wang, Zhiyuan Liu, Shengbo E. Li, Scott J. Moura and Huei Peng. “State-of-Charge Estimation for Lithium-Ion Batteries Based on a Nonlinear Fractional Model”. *IEEE Transactions on Control Systems Technology* 25.1 (2017), pp. 3–11. ISSN: 10636536. DOI: [10.1109/TCST.2016.2557221](https://doi.org/10.1109/TCST.2016.2557221) [cited on page 60].
- [67] Chris Manzie, Changfu Zou and Dragan Nesic. “Simplification techniques for PDE-based Li-Ion battery models”. *2015 54th IEEE Conference on Decision and Control (CDC)*. IEEE, Dec. 2015, pp. 3913–3921. ISBN: 978-1-4799-7886-1. DOI: [10.1109/CDC.2015.7402828](https://doi.org/10.1109/CDC.2015.7402828) [cited on pages 60, 67].

- [68] Adolph Fick. "On liquid diffusion". *Journal of Membrane Science* 100.1 (Mar. 1995), pp. 33–38. ISSN: 0376-7388. DOI: [10.1016/0376-7388\(94\)00230-V](https://doi.org/10.1016/0376-7388(94)00230-V) [cited on pages 61, 158, 161].
- [69] Noble B. Ferguson. "Orthogonal collocation as a method of analysis in chemical reaction engineering". Dissertation. University of Washington, 1971, p. 201. URL: <https://digital.lib.washington.edu/researchworks/bitstream/handle/1773/9876/7207350.pdf?sequence=1> [cited on page 61].
- [70] Lloyd N. Trefethen. *Spectral methods in MATLAB*. Society for Industrial and Applied Mathematics (SIAM, 3600 Market Street, Floor 6, Philadelphia, PA 19104), 2000, p. 165. ISBN: 0898719593 [cited on pages 61, 108–110].
- [71] John P. Boyd. *Chebyshev and Fourier spectral methods*. Dover Publications, 2001, p. 668. ISBN: 0486411834 [cited on page 61].
- [72] Bernie D. Shizgal. *Spectral methods in chemistry and physics : applications to kinetic theory and quantum mechanics*. 2015, p. 415. ISBN: 9789401794541 [cited on page 61].
- [73] Denys Dutykh. "A brief introduction to pseudo-spectral methods: application to diffusion problems". June 2016. URL: <http://arxiv.org/abs/1606.05432> [cited on page 61].
- [74] Paul W. Northrop, Venkatasailanathan Ramadesigan, Sumitava De and Venkat R. Subramanian. "Coordinate Transformation, Orthogonal Collocation, Model Reformulation and Simulation of Electrochemical-Thermal Behavior of Lithium-Ion Battery Stacks". *Journal of The Electrochemical Society* 158.12 (Jan. 2011), A1461–A1477. ISSN: 00134651. DOI: [10.1149/2.058112jes](https://doi.org/10.1149/2.058112jes) [cited on pages 61, 67, 100, 121, 122, 126, 181, 186, 308].
- [75] Bharatkumar Suthar, Paul W. Northrop, Richard D. Braatz and Venkat R. Subramanian. "Optimal Charging Profiles with Minimal Intercalation-Induced Stresses for Lithium-Ion Batteries Using Reformulated Pseudo 2-Dimensional Models". *Journal of the Electrochemical Society* 161.11 (Oct. 2014), F3144–F3155. ISSN: 0013-4651. DOI: [10.1149/2.0211411jes](https://doi.org/10.1149/2.0211411jes) [cited on pages 61, 67].
- [76] Adrien M. Bizeray, Shi Zhao, Stephen R. Duncan and David A. Howey. "Lithium-ion battery thermal-electrochemical model-based state estimation using orthogonal collocation and a modified extended Kalman filter". *Journal of Power Sources* 296 (Nov. 2015), pp. 400–412. ISSN: 0378-7753. DOI: [10.1016/J.JPOWSOUR.2015.07.019](https://doi.org/10.1016/J.JPOWSOUR.2015.07.019) [cited on pages 61, 67, 108].
- [77] Venkat R. Subramanian, Deepak Tapriyal and Ralph E. White. "A Boundary Condition for Porous Electrodes". *Electrochemical and Solid-State Letters* 7.9 (Sept. 2004), A259. ISSN: 10990062. DOI: [10.1149/1.1773751](https://doi.org/10.1149/1.1773751) [cited on page 62].
- [78] Venkat R. Subramanian, Vinten D. Diwakar and Deepak Tapriyal. "Efficient Macro-Micro Scale Coupled Modeling of Batteries". *Journal of The Electrochemical Society* 152.10 (Oct. 2005), A2002. ISSN: 00134651. DOI: [10.1149/1.2032427](https://doi.org/10.1149/1.2032427) [cited on pages 62, 161–163].
- [79] Venkat R. Subramanian, Vijayasekaran Boovaragavan and Vinten D. Diwakar. "Toward Real-Time Simulation of Physics Based Lithium-Ion Battery Models". *Electrochemical and Solid-State Letters* 10.11 (Nov. 2007), A255. ISSN: 10990062. DOI: [10.1149/1.2776128](https://doi.org/10.1149/1.2776128) [cited on pages 63, 67].
- [80] Horatio S. Carslaw and John C. Jaeger. *Conduction of heat in solids*. 1st ed. Oxford: Clarendon Press, 1947, p. 386 [cited on page 63].

- [81] Shengyi Liu. “An analytical solution to Li/Li⁺ insertion into a porous electrode”. *Solid State Ionics* 177.1-2 (Jan. 2006), pp. 53–58. ISSN: 0167-2738. DOI: [10.1016/J.SSI.2005.09.053](https://doi.org/10.1016/J.SSI.2005.09.053) [cited on pages 63, 161].
- [82] Meng Guo and Ralph E. White. “An approximate solution for solid-phase diffusion in a spherical particle in physics-based Li-ion cell models”. *Journal of Power Sources* 198 (Jan. 2012), pp. 322–328. ISSN: 0378-7753. DOI: [10.1016/J.JPOWSOUR.2011.08.096](https://doi.org/10.1016/J.JPOWSOUR.2011.08.096) [cited on page 63].
- [83] Zhongwei Deng, Lin Yang, Hao Deng, Yishan Cai and Dongdong Li. “Polynomial approximation pseudo-two-dimensional battery model for online application in embedded battery management system”. *Energy* 142 (Jan. 2018), pp. 838–850. ISSN: 0360-5442. DOI: [10.1016/J.ENERGY.2017.10.097](https://doi.org/10.1016/J.ENERGY.2017.10.097) [cited on pages 64, 67, 201, 202, 310].
- [84] Mohammed Farag, Matthias Fleckenstein and Saeid Habibi. “Continuous piecewise-linear, reduced-order electrochemical model for lithium-ion batteries in real-time applications”. *Journal of Power Sources* 342 (2017), pp. 351–362. ISSN: 03787753. DOI: [10.1016/j.jpowsour.2016.12.044](https://doi.org/10.1016/j.jpowsour.2016.12.044) [cited on page 64].
- [85] Bala S. Haran, Branko N. Popov and Ralph E. White. “Determination of the hydrogen diffusion coefficient in metal hydrides by impedance spectroscopy”. *Journal of Power Sources* 75.1 (Sept. 1998), pp. 56–63. ISSN: 0378-7753. DOI: [10.1016/S0378-7753\(98\)00092-5](https://doi.org/10.1016/S0378-7753(98)00092-5) [cited on page 68].
- [86] Gang Ning and Branko N. Popov. “Cycle Life Modeling of Lithium-Ion Batteries”. *Journal of The Electrochemical Society* 151.10 (Oct. 2004), A1584. ISSN: 00134651. DOI: [10.1149/1.1787631](https://doi.org/10.1149/1.1787631) [cited on page 68].
- [87] Shriram Santhanagopalan and Ralph E. White. “Online estimation of the state of charge of a lithium ion cell”. *Journal of Power Sources* 161.2 (Oct. 2006), pp. 1346–1355. ISSN: 03787753. DOI: [10.1016/j.jpowsour.2006.04.146](https://doi.org/10.1016/j.jpowsour.2006.04.146) [cited on pages 68, 155].
- [88] Shriram Santhanagopalan and Ralph E. White. “State of charge estimation for electrical vehicle batteries”. *2008 IEEE International Conference on Control Applications*. IEEE, 2008, pp. 690–695. ISBN: 978-1-4244-2222-7. DOI: [10.1109/CCA.2008.4629656](https://doi.org/10.1109/CCA.2008.4629656) [cited on page 68].
- [89] Shriram Santhanagopalan, Qingzhi Guo and Ralph E. White. “Parameter Estimation and Model Discrimination for a Lithium-Ion Cell”. *Journal of The Electrochemical Society* 154.3 (Mar. 2007), A198. ISSN: 00134651. DOI: [10.1149/1.2422896](https://doi.org/10.1149/1.2422896) [cited on page 68].
- [90] Shriram Santhanagopalan, Qi Zhang, Karthikeyan Kumaresan and Ralph E. White. “Parameter Estimation and Life Modeling of Lithium-Ion Cells”. *Journal of The Electrochemical Society* 155.4 (Apr. 2008), A345. ISSN: 00134651. DOI: [10.1149/1.2839630](https://doi.org/10.1149/1.2839630) [cited on page 68].
- [91] M. Safari, Mathieu Morcrette, A. Teysot and Charles Delacourt. “Multimodal Physics-Based Aging Model for Life Prediction of Li-Ion Batteries”. *Journal of The Electrochemical Society* 156.3 (Mar. 2009), A145. ISSN: 00134651. DOI: [10.1149/1.3043429](https://doi.org/10.1149/1.3043429) [cited on page 68].
- [92] Shriram Santhanagopalan, Qingzhi Guo, Premanand Ramadass and Ralph E. White. “Review of models for predicting the cycling performance of lithium ion batteries”. *Journal of Power Sources* 156.2 (2006), pp. 620–628. ISSN: 0378-7753. DOI: [DOI: 10.1016/j.jpowsour.2005.05.070](https://doi.org/10.1016/j.jpowsour.2005.05.070) [cited on pages 68, 107, 155].

- [93] Nalin A. Chaturvedi, Reinhardt Klein, Jake Christensen, Jasim Ahmed and Aleksandar Kojic. "Algorithms for Advanced Battery-Management Systems: Modeling, estimation, and control challenges for lithium-ion batteries". *IEEE Control Systems* 30.3 (2010), pp. 49–68. ISSN: 1066033X. DOI: [10.1109/MCS.2010.936293](https://doi.org/10.1109/MCS.2010.936293) [cited on page 68].
- [94] Alexander P. Schmidt, Matthias Bitzer, Árpád W. Imre and Lino Guzzella. "Experiment-driven electrochemical modeling and systematic parameterization for a lithium-ion battery cell". *Journal of Power Sources* 195.15 (2010), pp. 5071–5080. ISSN: 03787753. DOI: [10.1016/j.jpowsour.2010.02.029](https://doi.org/10.1016/j.jpowsour.2010.02.029) [cited on pages 69, 77].
- [95] Meng Guo, Godfrey Sikha and Ralph E. White. "Single-Particle Model for a Lithium-Ion Cell: Thermal Behavior". *Journal of The Electrochemical Society* 158.2 (Feb. 2011), A122. ISSN: 00134651. DOI: [10.1149/1.3521314](https://doi.org/10.1149/1.3521314) [cited on pages 69, 77].
- [96] Domenico Di Domenico, Anna Stefanopoulou and Giovanni Fiengo. "Lithium-Ion Battery State of Charge and Critical Surface Charge Estimation Using an Electrochemical Model-Based Extended Kalman Filter". *Journal of Dynamic Systems, Measurement, and Control* 132.6 (2010), p. 061302. ISSN: 00220434. DOI: [10.1115/1.4002475](https://doi.org/10.1115/1.4002475) [cited on pages 70, 78, 155, 160, 166, 167, 275].
- [97] Anupama Guduru, Paul W. Northrop, Shruti Jain, Andrew C. Crothers, T. R. Marchant and Venkat R. Subramanian. "Analytical solution for electrolyte concentration distribution in lithium-ion batteries". *Journal of Applied Electrochemistry* 42.4 (Apr. 2012), pp. 189–199. ISSN: 0021-891X. DOI: [10.1007/s10800-012-0394-4](https://doi.org/10.1007/s10800-012-0394-4) [cited on page 71].
- [98] Venkat R. Subramanian, James A. Ritter and Ralph E. White. "Approximate Solutions for Galvanostatic Discharge of Spherical Particles I. Constant Diffusion Coefficient". *Journal of The Electrochemical Society* 148.11 (Nov. 2001), E444. ISSN: 00134651. DOI: [10.1149/1.1409397](https://doi.org/10.1149/1.1409397) [cited on pages 71, 161].
- [99] Eric Prada, Domenico Di Domenico, Y. Creff, J. Bernard, V. Sauvant-Moynot and F. Huet. "Simplified Electrochemical and Thermal Model of LiFePO₄-Graphite Li-Ion Batteries for Fast Charge Applications". *Journal of the Electrochemical Society* 159.9 (Aug. 2012), A1508–A1519. ISSN: 0013-4651. DOI: [10.1149/2.064209jes](https://doi.org/10.1149/2.064209jes) [cited on pages 73, 78, 216, 255, 256].
- [100] Saeed K. Rahimian, Sean Rayman and Ralph E. White. "Extension of physics-based single particle model for higher charge–discharge rates". *Journal of Power Sources* 224 (Feb. 2013), pp. 180–194. ISSN: 0378-7753. DOI: [10.1016/J.JPOWSOUR.2012.09.084](https://doi.org/10.1016/J.JPOWSOUR.2012.09.084) [cited on pages 73, 75, 78].
- [101] Paulo Kemper and Dongsuk Kum. "Extended Single Particle Model of Li-Ion Batteries Towards High Current Applications". *2013 IEEE Vehicle Power and Propulsion Conference (VPPC)* (2013), pp. 1–6. DOI: [10.1109/VPPC.2013.6671682](https://doi.org/10.1109/VPPC.2013.6671682) [cited on page 74].
- [102] Weilin Luo, Chao Lyu, Lixin Wang and Liqiang Zhang. "An approximate solution for electrolyte concentration distribution in physics-based lithium-ion cell models". *Microelectronics Reliability* 53.6 (2013), pp. 797–804. ISSN: 00262714. DOI: [10.1016/j.microrel.2012.11.002](https://doi.org/10.1016/j.microrel.2012.11.002) [cited on pages 74, 75, 78].
- [103] Weilin Luo, Chao Lyu, Lixin Wang and Liqiang Zhang. "A new extension of physics-based single particle model for higher charge–discharge rates". *Journal of Power Sources* 241 (Nov. 2013), pp. 295–310. ISSN: 0378-7753. DOI: [10.1016/J.JPOWSOUR.2013.04.129](https://doi.org/10.1016/J.JPOWSOUR.2013.04.129) [cited on pages 74, 78].

- [104] Changfu Zou, Chris Manzie, Dragan Nešić and Abhijit G. Kallapur. “Multi-time-scale observer design for state-of-charge and state-of-health of a lithium-ion battery”. *Journal of Power Sources* 335.October 2016 (Dec. 2016), pp. 121–130. ISSN: 03787753. DOI: [10.1016/j.jpowsour.2016.10.040](https://doi.org/10.1016/j.jpowsour.2016.10.040) [cited on pages 75, 79].
- [105] Xuebing Han, Minggao Ouyang, Languang Lu and Jianqiu Li. “Simplification of physics-based electrochemical model for lithium ion battery on electric vehicle. Part II: Pseudo-two-dimensional model simplification and state of charge estimation”. *Journal of Power Sources* 278 (Mar. 2015), pp. 814–825. ISSN: 0378-7753. DOI: [10.1016/J.JPOWSOUR.2014.08.089](https://doi.org/10.1016/J.JPOWSOUR.2014.08.089) [cited on page 75].
- [106] Tanvir R. Tanim, Christopher D. Rahn and Chao-Yang Wang. “A Temperature Dependent, Single Particle, Lithium Ion Cell Model Including Electrolyte Diffusion”. *Journal of Dynamic Systems, Measurement, and Control* 137.1 (2014), p. 011005. ISSN: 0022-0434. DOI: [10.1115/1.4028154](https://doi.org/10.1115/1.4028154) [cited on pages 75, 78].
- [107] Robert D. Middlebrook. “Low-entropy expressions: the key to design-oriented analysis”. *Proceedings Frontiers in Education Twenty-First Annual Conference. Engineering Education in a New World Order*. West Lafayette: IEEE, 1991, pp. 399–403. ISBN: 0-7803-0222-2. DOI: [10.1109/FIE.1991.187513](https://doi.org/10.1109/FIE.1991.187513) [cited on page 76].
- [108] Robert D. Middlebrook, Vatche Vorperian and John Lindal. “The N Extra Element Theorem”. *IEEE Transactions on Circuits and Systems I: Fundamental Theory and Applications* 45.9 (1998), pp. 919–935. ISSN: 10577122. DOI: [10.1109/81.721258](https://doi.org/10.1109/81.721258) [cited on page 76].
- [109] Vatché Vorpérian. *Fast analytical techniques for electrical and electronic circuits*. Cambridge University Press, 2002, p. 476. ISBN: 0521624428 [cited on page 76].
- [110] Tanvir R. Tanim, Christopher D. Rahn and Chao-Yang Wang. “A reduced order electrolyte enhanced single particle lithium ion cell model for hybrid vehicle applications”. *Proceedings of the American Control Conference*. 2. 2014, pp. 141–146. DOI: [10.1109/ACC.2014.6858617](https://doi.org/10.1109/ACC.2014.6858617) [cited on page 76].
- [111] Scott J. Moura, Federico B. Argomedeo, Reinhardt Klein, Anahita Mirtabatabaei and Miroslav Krstic. “Battery State Estimation for a Single Particle Model with Electrolyte Dynamics”. *IEEE Transactions on Control Systems Technology* 25.2 (Mar. 2017), pp. 453–468. ISSN: 10636536. DOI: [10.1109/TCST.2016.2571663](https://doi.org/10.1109/TCST.2016.2571663) [cited on pages 77, 79].
- [112] Nima Lotfi, J. Li, Robert G. Landers and Jonghyun Park. “Li-ion Battery State of Health Estimation based on an improved Single Particle model”. *2017 American Control Conference (ACC)*. IEEE, May 2017, pp. 86–91. ISBN: 978-1-5090-5992-8. DOI: [10.23919/ACC.2017.7962935](https://doi.org/10.23919/ACC.2017.7962935) [cited on page 77].
- [113] J. Li, Nima Lotfi, Robert G. Landers and Jonghyun Park. “A Single Particle Model for Lithium-Ion Batteries with Electrolyte and Stress-Enhanced Diffusion Physics”. *Journal of The Electrochemical Society* 164.4 (2017), A874–A883. ISSN: 0013-4651. DOI: [10.1149/2.1541704jes](https://doi.org/10.1149/2.1541704jes) [cited on page 79].
- [114] J. Li, K. Adewuyi, Nima Lotfi, Robert G. Landers and Jonghyun Park. “A single particle model with chemical/mechanical degradation physics for lithium ion battery State of Health (SOH) estimation”. *Applied Energy* 212 (Feb. 2018), pp. 1178–1190. ISSN: 0306-2619. DOI: [10.1016/J.APENERGY.2018.01.011](https://doi.org/10.1016/J.APENERGY.2018.01.011) [cited on page 79].

- [115] Yuan Chaochun, Bingjian. Wang, Zhang Houzhong, Chen. Long and Li Huanhuan. “State-of-Charge Estimation of Lithium-ion Battery Based on a Novel Reduced Order Electrochemical Model”. *International Journal of Electrochemical Science* (Jan. 2018), pp. 1131–1146. ISSN: 14523981. DOI: [10.20964/2018.01.133](https://doi.org/10.20964/2018.01.133) [cited on page 79].
- [116] Cheng Lin, Jilei Xing and Aihua Tang. “Lithium-ion Battery State of Charge/State of Health Estimation Using SMO for EVs”. *Energy Procedia* 105 (May 2017), pp. 4383–4388. ISSN: 1876-6102. DOI: [10.1016/J.EGYPRO.2017.03.931](https://doi.org/10.1016/J.EGYPRO.2017.03.931) [cited on page 79].
- [117] Ngoc T. Tran, Mahinda Vilathgamuwa, Yang Li, Troy Farrell, San S. Choi and Joseph Teague. “State of charge estimation of lithium ion batteries using an extended single particle model and sigma-point Kalman filter”. *2017 IEEE Southern Power Electronics Conference (SPEC)*. IEEE, Dec. 2017, pp. 1–6. ISBN: 978-1-5090-6425-0. DOI: [10.1109/SPEC.2017.8333564](https://doi.org/10.1109/SPEC.2017.8333564) [cited on page 79].
- [118] H. E. Perez, S. Dey, X. Hu and S. J. Moura. “Optimal Charging of Li-Ion Batteries via a Single Particle Model with Electrolyte and Thermal Dynamics”. *Journal of The Electrochemical Society* 164.7 (June 2017), A1679–A1687. ISSN: 0013-4651. DOI: [10.1149/2.1301707jes](https://doi.org/10.1149/2.1301707jes) [cited on page 79].
- [119] H. E. Perez, X. Hu and S. J. Moura. “Optimal charging of batteries via a single particle model with electrolyte and thermal dynamics”. *Proceedings of the American Control Conference*. Vol. 2016-July. 7. 2016, pp. 4000–4005. ISBN: 9781467386821. DOI: [10.1109/ACC.2016.7525538](https://doi.org/10.1109/ACC.2016.7525538) [cited on page 79].
- [120] Leonardo K. Maia, Zeynep Güven, Fabio La Mantia and Edwin Zondervan. “Model-based Optimization of Battery Energy Storage Systems”. *Computer Aided Chemical Engineering* 40 (Jan. 2017), pp. 2563–2568. ISSN: 1570-7946. DOI: [10.1016/B978-0-444-63965-3.50429-3](https://doi.org/10.1016/B978-0-444-63965-3.50429-3) [cited on page 79].
- [121] Yang Li, D. Mahinda Vilathgamuwa, Troy W. Farrell, San Shing Choi and Ngoc T. Tran. “An equivalent circuit model of li-ion battery based on electrochemical principles used in grid-connected energy storage applications”. *2017 IEEE 3rd International Future Energy Electronics Conference and ECCE Asia (IFEEC 2017 - ECCE Asia)*. IEEE, June 2017, pp. 959–964. ISBN: 978-1-5090-5157-1. DOI: [10.1109/IFEEC.2017.7992170](https://doi.org/10.1109/IFEEC.2017.7992170) [cited on page 79].
- [122] Junfu Li, Lixin Wang, Chao Lyu, Enhui Liu, Yinjiao Xing and Michael Pecht. “A parameter estimation method for a simplified electrochemical model for Li-ion batteries”. *Electrochimica Acta* (Apr. 2018). ISSN: 00134686. DOI: [10.1016/j.electacta.2018.04.098](https://doi.org/10.1016/j.electacta.2018.04.098) [cited on page 79].
- [123] Barzin Rajabloo, Ali Jokar, Martin Désilets and Marcel Lacroix. “An Inverse Method for Estimating the Electrochemical Parameters of Lithium-Ion Batteries”. *Journal of The Electrochemical Society* 164.2 (Dec. 2017), A99–A105. ISSN: 0013-4651. DOI: [10.1149/2.0221702jes](https://doi.org/10.1149/2.0221702jes) [cited on page 79].
- [124] Adrien M. Bizeray, Jin-Ho Kim, Stephen R. Duncan and David A. Howey. “Identifiability and parameter estimation of the single particle lithium-ion battery model”. *IEEE Transactions on Control Systems Technology* PP (Feb. 2017), pp. 1–16. DOI: [10.1109/TCST.2018.2838097](https://doi.org/10.1109/TCST.2018.2838097) [cited on page 79].
- [125] Emil Namor, Dimitri Torregrossa, Rachid Cherkaoui and Mario Paolone. “Parameter identification of a lithium-ion cell single-particle model through non-invasive testing”. *Journal of Energy Storage* 12 (Aug. 2017), pp. 138–148. ISSN: 2352-152X. DOI: [10.1016/J.EST.2017.04.008](https://doi.org/10.1016/J.EST.2017.04.008) [cited on page 79].

- [126] Donald J. Docimo and Hosam K. Fathy. “Analysis and Control of Charge and Temperature Imbalance Within a Lithium-Ion Battery Pack”. *IEEE Transactions on Control Systems Technology* (2018), pp. 1–14 [cited on page 79].
- [127] Pedro Ascencio, Alessandro Astolfi and Thomas Parisini. “Backstepping PDE-based adaptive observer for a Single Particle Model of Lithium-Ion Batteries”. *55th Conference on Decision and Control Cdc* (2016), pp. 5623–5628. doi: [10.1109/CDC.2016.7799133](https://doi.org/10.1109/CDC.2016.7799133) [cited on page 79].
- [128] Alexander P. Bartlett. *Electrochemical Model-Based State of Charge and State of Health Estimation of Lithium-Ion Batteries*. 2015. URL: http://rave.ohiolink.edu/etdc/view?acc%7B%5C_%7Dnum=osu1432640190 [cited on page 79].
- [129] Carolyn R. Pals and John S. Newman. “Thermal Modeling of the Lithium/Polymer Battery”. *Journal of The Electrochemical Society* 142.10 (1995), p. 3282. ISSN: 00134651. DOI: [10.1149/1.2049975](https://doi.org/10.1149/1.2049975) [cited on pages 87, 96].
- [130] Marie-Therese von Srbik. “Advanced Lithium-Ion Battery Modelling for Automotive Applications”. PhD thesis. Imperial College London, 2015, p. 162. URL: <https://spiral.imperial.ac.uk/handle/10044/1/51498> [cited on pages 87, 307].
- [131] Jinming Liu, Mohammad Anwar, Peter Chiang, Shawn Hawkins, Youngsoo Jeong, Faizul Momen, Stephen Poulos and Seunghan Song. “Design of the Chevrolet Bolt EV Propulsion System”. *SAE International Journal of Alternative Powertrains* 5.1 (2016), pp. 1153–2016. ISSN: 2167-4205. DOI: [10.4271/2016-01-1153](https://doi.org/10.4271/2016-01-1153) [cited on pages 93, 99, 127].
- [132] C. Veth, D. Dragicevic and C. Merten. “Thermal characterizations of a large-format lithium ion cell focused on high current discharges”. *Journal of Power Sources* 267 (2014), pp. 760–769. ISSN: 03787753. DOI: [10.1016/j.jpowsour.2014.05.139](https://doi.org/10.1016/j.jpowsour.2014.05.139) [cited on page 95].
- [133] Stephen J. Bazinski and Xia Wang. “Thermal Effect of Cooling the Cathode Grid Tabs of a Lithium-Ion Pouch Cell”. *Journal of The Electrochemical Society* 161.14 (2014), A2168–A2174. DOI: [10.1149/2.0731414jes](https://doi.org/10.1149/2.0731414jes) [cited on page 95].
- [134] Yan Zhao, Yatish Patel, Teng Zhang and Gregory J. Offer. “Modeling the Effects of Thermal Gradients Induced by Tab and Surface Cooling on Lithium Ion Cell Performance”. *Journal of The Electrochemical Society* 165.13 (2018), A3169–A3178. DOI: [10.1149/2.0901813jes](https://doi.org/10.1149/2.0901813jes) [cited on page 95].
- [135] Ian A. Hunt, Yan Zhao, Yatish Patel and J Offer. “Surface Cooling Causes Accelerated Degradation Compared to Tab Cooling for Lithium-Ion Pouch Cells”. *Journal of The Electrochemical Society* 163.9 (2016), A1846–A1852. ISSN: 0013-4651. DOI: [10.1149/2.0361609jes](https://doi.org/10.1149/2.0361609jes) [cited on pages 95, 96].
- [136] Gregory L. Plett. *Lecture Notes 07: ECE5710 - Modeling, Simulation, and Identification of Battery Dynamics*. Colorado Springs, 2018. URL: <http://mocha-java.uccs.edu/ECE5710/ECE5710-Notes07.pdf> [cited on page 96].
- [137] Venkat R. Subramanian, Vijayasekaran Boovaragavan, Venkatasailanathan Ramadesigan and Mounika Arabandi. “Mathematical Model Reformulation for Lithium-Ion Battery Simulations : Galvanostatic Boundary Conditions”. *Journal of the Electrochemical Society* 156.4 (2009), A260–A271. DOI: [10.1149/1.3065083](https://doi.org/10.1149/1.3065083) [cited on pages 100, 126, 180, 181, 184, 185].

- [138] General Motors. *Drive Unit and Battery at the Heart of Chevrolet Bolt EV*. 2016. URL: <https://media.chevrolet.com/media/us/en/chevrolet/home.detail.html/content/Pages/news/us/en/2016/Jan/naias/chevy/0111-bolt-du.html> (visited on 18/07/2017) [cited on pages 100, 126].
- [139] Oliver Gröger, Hubert a. Gasteiger and Jens-Peter Suchsland. “Review—Electromobility: Batteries or Fuel Cells?” *Journal of The Electrochemical Society* 162.14 (2015), A2605–A2622. ISSN: 0013-4651. DOI: [10.1149/2.0211514jes](https://doi.org/10.1149/2.0211514jes) [cited on pages 101, 126].
- [140] Automotive E. S. Corporation. *Cell, Module and Packs for EV Applications: High energy cell*. 2018. URL: http://www.eco-aesc-lb.com/en/product/liion_ev/ (visited on 10/12/2018) [cited on page 101].
- [141] Kokam Inc. *Datasheet of large format cells*. 2018. URL: <http://kokam.com/cell/> (visited on 10/12/2018) [cited on page 101].
- [142] Dennis W. Dees, Vincent S. Battaglia and Andre Belanger. “Electrochemical modeling of lithium polymer batteries”. *Journal of Power Sources* 110.2 (2002), pp. 310–320. ISSN: 0378-7753. DOI: [10.1016/S0378-7753\(02\)00193-3](https://doi.org/10.1016/S0378-7753(02)00193-3) [cited on page 104].
- [143] Alan C. Hindmarsh, Peter N. Brown, Keith E. Grant, Steven L. Lee, Radu Serban, Dan E. Shumaker and Carol S. Woodward. “SUNDIALS: Suite of nonlinear and differential/algebraic equation solvers”. *ACM Transactions on Mathematical Software (TOMS)* 31.3 (2005), pp. 363–396 [cited on page 107].
- [144] Joel Andersson. “Faculty of Engineering Science A General-Purpose Software Framework for Dynamic Optimization”. PhD thesis. Katholieke Univeriteit Leuven, 2013. ISBN: 9789460187506 [cited on page 108].
- [145] Steven G. Johnson. *Chebyshev Nodes by Projection*. 2018. URL: <https://commons.wikimedia.org/wiki/File:Chebyshev-nodes-by-projection.svg> (visited on 03/12/2018) [cited on pages 109, 307].
- [146] Society of Automotive Engineers. “Surface vehicle recommended practice : SAE electric vehicle and plug in hybrid electric vehicle conductive charge coupler” (2010), p. 116. URL: https://saemobilus.sae.org/content/j1772%7B%5C_%7D201710 [cited on pages 111, 126, 128].
- [147] Song Y. Choe, Xueyan Li and Meng Xiao. “Fast charging method based on estimation of ion concentrations using a reduced order of electrochemical thermal model for lithium ion polymer battery”. *World Electric Vehicle Journal* 6.3 (2013), pp. 782–792. ISSN: 20326653. DOI: [10.1109/EVS.2013.6914966](https://doi.org/10.1109/EVS.2013.6914966) [cited on page 115].
- [148] Thomas H. Cormen. *Introduction to algorithms*. 3rd ed. Cambridge Mass.: MIT Press, 2009, p. 1292. ISBN: 9780262270830 [cited on page 117].
- [149] Toby Bond, Jigang Zhou and Jeffrey Cutler. “Electrode Stack Geometry Changes during Gas Evolution in Pouch-Cell-Type Lithium Ion Batteries”. *Journal of The Electrochemical Society* 164.1 (Nov. 2017), A6158–A6162. ISSN: 0013-4651. DOI: [10.1149/2.0241701jes](https://doi.org/10.1149/2.0241701jes) [cited on pages 120, 184, 307].
- [150] Riza Kizilel, Rami Sabbah, J R. Selman and Said Al-Hallaj. “An alternative cooling system to enhance the safety of Li-ion battery packs”. *Journal of Power Sources* 194.2 (Dec. 2009), pp. 1105–1112. ISSN: 03787753. DOI: [10.1016/j.jpowsour.2009.06.074](https://doi.org/10.1016/j.jpowsour.2009.06.074) [cited on page 126].

- [151] Pontus Svens, Maria H. Kjell, Carl Tengstedt, Göran Flodberg and Göran Lindbergh. “Li-ion pouch cells for vehicle applications-studies of water transmission and packing materials”. *Energies* 6 (2013), pp. 400–410. ISSN: 19961073. DOI: [10.3390/en6010400](https://doi.org/10.3390/en6010400) [cited on page 126].
- [152] S C. Chen, C C. Wan and Y Y. Wang. “Thermal analysis of lithium-ion batteries”. *Journal of Power Sources* 140.1 (2005), pp. 111–124. ISSN: 0378-7753. DOI: [10.1016/j.jpowsour.2004.05.064](https://doi.org/10.1016/j.jpowsour.2004.05.064) [cited on page 126].
- [153] W Martienssen and Hans Warlimont. *Springer Handbook of Condensed Matter and Materials Data*. Berlin: Springer Berlin Heidelberg, 2005, p. 1119. ISBN: 978-3-540-44376-6. DOI: [10.1007/3-540-30437-1](https://doi.org/10.1007/3-540-30437-1) [cited on page 126].
- [154] Guifang Guo, Bo Long, Bo Cheng, Shiqiong Zhou, Peng Xu and Binggang Cao. “Three-dimensional thermal finite element modeling of lithium-ion battery in thermal abuse application”. *Journal of Power Sources* 195.8 (2010), pp. 2393–2398. ISSN: 0378-7753. DOI: [10.1016/j.jpowsour.2009.10.090](https://doi.org/10.1016/j.jpowsour.2009.10.090) [cited on page 126].
- [155] Dong H. Jeon and Seung M. Baek. “Thermal modeling of cylindrical lithium ion battery during discharge cycle”. *Energy Conversion and Management* 52.8-9 (2011), pp. 2973–2981. ISSN: 0196-8904. DOI: [10.1016/j.enconman.2011.04.013](https://doi.org/10.1016/j.enconman.2011.04.013) [cited on page 126].
- [156] Daniel Worwood, Quirin Kellner, Elham Hosseinzadeh, David Mullen, David Greenwood, James Marco, Ryan McGlen and Kevin Lynn. “Thermal Analysis of Fin Cooling Large Format Automotive Lithium-Ion Pouch Cells”. *2017 IEEE Vehicle Power and Propulsion Conference (VPPC)*. IEEE, Dec. 2017, pp. 1–6. ISBN: 978-1-5386-1317-7. DOI: [10.1109/VPPC.2017.8330874](https://doi.org/10.1109/VPPC.2017.8330874) [cited on page 126].
- [157] Li Song and James W. Evans. “Electrochemical-Thermal Model of Lithium Polymer Batteries”. *Journal of The Electrochemical Society* 147.6 (June 2000), p. 2086. ISSN: 00134651. DOI: [10.1149/1.1393490](https://doi.org/10.1149/1.1393490) [cited on page 126].
- [158] Ui S. Kim, Chee B. Shin and Chi S. Kim. “Modeling for the scale-up of a lithium-ion polymer battery”. *Journal of Power Sources* 189.1 (2009), pp. 841–846. ISSN: 03787753. DOI: [10.1016/j.jpowsour.2008.10.019](https://doi.org/10.1016/j.jpowsour.2008.10.019) [cited on page 126].
- [159] The Mathworks Inc. *MATLAB*. Natick, 2017. URL: <https://www.mathworks.com/products/matlab.html> [cited on page 125].
- [160] Paul Albertus and John S. Newman. *FORTTRAN Programs for the Simulation of Electrochemical Systems*. 2007. URL: <http://www.cchem.berkeley.edu/jsngrp/fortran.html> [cited on page 125].
- [161] Nisewanger; Jeff. *2017 Chevy Bolt EV Is Less of a Drag Than Originally Believed*. 2017. URL: <http://www.hybridcars.com/2017-chevy-bolt-ev-is-less-of-a-drag-than-originally-believed/> [cited on page 127].
- [162] *Chevrolet Bolt Features - Dimensions*. URL: <http://www.chevrolet.com/byo-vc/client/en/US/chevrolet/bolt-ev/2017/bolt-ev/features/trims/?section=Highlights%7B%5C%7Dsection=Exterior%7B%5C%7Dsection=Dimensions%7B%5C%7DstyleOne=388584> [cited on page 127].
- [163] Society of Automotive Engineers. *SAE Standard J1666 ”Hybrid Electric Vehicle Acceleration, Gradeability, and Deceleration Test Procedure”*. Tech. rep. Society of Automotive Engineers, 2004, p. 25 [cited on page 127].

- [164] *Chevrolet Bolt - Overview*. URL: <http://www.chevrolet.com/bolt-ev-electric-vehicle-2> [cited on page 127].
- [165] Mehrdad Ehsani, Yimin Gao and Ali Emadi. *Modern Electric, Hybrid Electric, and Fuel Cell Vehicles. Fundamentals, Theory and Design*. Second. Boca Raton: CRC Press. Taylor & Francis Group, 2010. ISBN: 9781420053982 [cited on pages 127, 128].
- [166] Murat Yilmaz and Philip T. Krein. "Review of charging power levels and infrastructure for plug-in electric and hybrid vehicles". *2012 IEEE International Electric Vehicle Conference, IEVC 2012* 28.5 (2012), pp. 2151–2169. ISSN: 08858993. DOI: [10.1109/IEVC.2012.6183208](https://doi.org/10.1109/IEVC.2012.6183208) [cited on page 128].
- [167] Ratil H. Ashique, Zainal Salam, Mohd J. Bin Abdul Aziz and Abdul R. Bhatti. "Integrated photovoltaic-grid dc fast charging system for electric vehicle: A review of the architecture and control". *Renewable and Sustainable Energy Reviews* 69.May 2016 (2017), pp. 1243–1257. ISSN: 18790690. DOI: [10.1016/j.rser.2016.11.245](https://doi.org/10.1016/j.rser.2016.11.245) [cited on page 128].
- [168] Srdjan Srdic, Chi Zhang, Xinyu Liang, Wensong Yu and Srdjan Lukic. "A SiC-based Power Converter Module for Medium- Voltage Fast Charger for Plug-in Electric Vehicles". *Proceedings of the 2016 IEEE Applied Power Electronics Conference and Exposition (APEC)*. Long Beach, CA, IEEE, 2016, pp. 2714–2719. ISBN: 9781467395502. DOI: [10.1109/APEC.2016.7468247](https://doi.org/10.1109/APEC.2016.7468247) [cited on page 128].
- [169] *Chevrolet Bolt EV Specifications*. URL: <http://media.chevrolet.com/media/us/en/chevrolet/vehicles/bolt-ev/2017.tab1.html> [cited on page 128].
- [170] Frank Markus. *General Motors Details New Modular I-3, I-4 Engines*. 2014. URL: <http://www.motortrend.com/news/gm-introduces-extra-small-block-ecotec-engine-family/> [cited on page 128].
- [171] SAE Hybrid Committee. *SAE Charging Configurations and Ratings Terminology*. 2011. URL: <http://www.sae.org/smartgrid/chargingspeeds.pdf> [cited on page 129].
- [172] Gregory L. Plett. *Lecture Notes 03: ECE5710 - Modeling, Simulation, and Identification of Battery Dynamics*. Colorado Springs, 2018. URL: <http://mocha-java.uccs.edu/ECE5710/ECE5710-Notes03.pdf> [cited on page 132].
- [173] Krishnakumar Gopalakrishnan, Teng Zhang and Gregory J. Offer. "A Fast, Memory-Efficient Discrete-Time Realization Algorithm for Reduced-Order Li-Ion Battery Models". *Journal of Electrochemical Energy Conversion and Storage* 14.1 (Feb. 2017), p. 011001. ISSN: 2381-6872. DOI: [10.1115/1.4035526](https://doi.org/10.1115/1.4035526) [cited on pages 136, 309].
- [174] John D. Pryce. *Numerical solution of Sturm-Liouville problems*. Oxford: Clarendon Press, 1993, p. 322. ISBN: 9780198534150 [cited on page 137].
- [175] James L. Lee, Andrew Chemistruck and Gregory L. Plett. "Discrete-time realization of transcendental impedance models, with application to modeling spherical solid diffusion". *Journal of Power Sources* 206 (May 2012), pp. 367–377. ISSN: 0378-7753. DOI: [10.1016/J.JPOWSOUR.2012.01.134](https://doi.org/10.1016/J.JPOWSOUR.2012.01.134) [cited on page 138].
- [176] B. L. Ho and Rudolph E. Kalman. "Effective construction of linear state-variable models from input/output functions". *Automatisierungstechnik* 14.1-12 (Jan. 1966), pp. 545–548. ISSN: 2196-677X. DOI: [10.1524/auto.1966.14.112.545](https://doi.org/10.1524/auto.1966.14.112.545) [cited on page 138].
- [177] Lennart Ljung. "System Identification". Ed. by Alex Procházka, Jan Uhlíř, P.W.J. Rayner and N.G. Kingsbury. Birkhäuser, Boston, MA, 1998. Chap. Signal Ide, pp. 163–173. ISBN: 978-1-4612-1768-8. DOI: [10.1007/978-1-4612-1768-8_11](https://doi.org/10.1007/978-1-4612-1768-8_11) [cited on page 139].

- [178] G. H. Golub. *Matrix computations*. Fourth edi. Baltimore: Johns Hopkins University Press, 2013, p. 756. ISBN: 9781421407944. URL: <http://imperialcollegelondon.worldcat.org/title/matrix-computations/oclc/824733531?referer=br%7B%5C%7Dht=edition> [cited on pages 142, 145].
- [179] E. Anderson, Z. Bai, C. Bischof, S Blackford, J. Demmel, J. Dongarra, J. Du Croz, A. Greenbaum, S. Hammarling, A. McKenney, D. Sorensen, L. S. Blackford, J. Demmel, J. Dongarra, J. Du Croz, A. Greenbaum, S. Hammarling, A. McKenney and D. Sorensen. *{LAPACK} Users' Guide*. 3rd editio. Philadelphia: Society for Industrial and Applied Mathematics, Jan. 1999, p. 407. ISBN: 0-89871-447-8 (paperback). DOI: [10.1137/1.9780898719604](https://doi.org/10.1137/1.9780898719604) [cited on pages 142, 145].
- [180] Ichitaro Yamazaki, Kesheng Wu and Horst Simon. *nu-TRLan User Guide Version 1.0: A High-Performance Software Package for Large-Scale Harmitian Eigenvalue Problems*. Tech. rep. Berkeley, CA: Lawrence Berkeley National Laboratory (LBNL), Oct. 2008. DOI: [10.2172/944532](https://doi.org/10.2172/944532) [cited on page 145].
- [181] R. B. (Richard B. Lehoucq, D. C. (Danny C. Sorensen, C. (Chao) Yang and Society for Industrial and Applied Mathematics. *ARPACK users' guide : solution of large-scale eigenvalue problems with implicitly restarted Arnoldi methods*. Philadelphia: Society for Industrial and Applied Mathematics (SIAM, 3600 Market Street, Floor 6, Philadelphia, PA 19104), 1998, p. 142. ISBN: 9780898719628. DOI: [10.1137/1.9780898719628](https://doi.org/10.1137/1.9780898719628) [cited on page 145].
- [182] Rasmus M. Larsen. *PROPACK-software for large and sparse SVD calculations*. 2004. URL: <http://sun.stanford.edu/%7B~%7Drmunk/PROPACK/> [cited on page 145].
- [183] Rasmus M. Larsen. “*Lanczos Bidiagonalization With Partial Reorthogonalization*”. *DAIMI Report Series 27.537* (Dec. 1998), p. 101. ISSN: 2245-9316. DOI: [10.7146/dpb.v27i537.7070](https://doi.org/10.7146/dpb.v27i537.7070) [cited on page 145].
- [184] Å. Björck. “*Numerics of Gram-Schmidt orthogonalization*”. *Linear Algebra and its Applications* 197-198 (Jan. 1994), pp. 297–316. ISSN: 0024-3795. DOI: [10.1016/0024-3795\(94\)90493-6](https://doi.org/10.1016/0024-3795(94)90493-6) [cited on page 145].
- [185] James B. Elsner and Anastasios A. Tsonis. *Singular Spectrum Analysis: A New Tool in Time Series Analysis*. Boston, MA: Springer US, 1996, p. 164. ISBN: 0306454726. DOI: [10.1007/978-1-4757-2514-8](https://doi.org/10.1007/978-1-4757-2514-8) [cited on page 146].
- [186] Anton Korobeynikov. “*Computation- and space-efficient implementation of SSA*”. *Statistics and Its Interface* 3.3 (2010), pp. 357–368. ISSN: 19387989. DOI: [10.4310/SII.2010.v3.n3.a9](https://doi.org/10.4310/SII.2010.v3.n3.a9) [cited on page 146].
- [187] Nina E. Golyandina and Konstantin D. Usevitch. “*2D-Extension of Singular Spectrum Analysis : Algorithm and elements of theory*”. *Matrix Methods: Theory, Algorithms and Applications*. Ed. by Vadim Olshevsky and Eugene Tyrtyshnikov. WORLD SCIENTIFIC, Apr. 2014, pp. 449–473. ISBN: 978-981-4469-55-5. DOI: [10.1142/9789812836021_0029](https://doi.org/10.1142/9789812836021_0029) [cited on page 146].
- [188] Nina E. Golyandina, Anton Korobeynikov, Alex Shlemov and Konstantin D. Usevich. “*Multivariate and 2D Extensions of Singular Spectrum Analysis with the Rssa Package*”. *Journal of Statistical Software* 67.2 (Oct. 2015), pp. 1–78. ISSN: 1548-7660. DOI: [10.18637/jss.v067.i02](https://doi.org/10.18637/jss.v067.i02) [cited on pages 146, 147].
- [189] COMSOL Inc. *COMSOL Multiphysics*. Burlington, MA, 2012. URL: <https://www.comsol.com/> [cited on page 152].

- [190] John S. Newman and Charles W. Tobias. “Theoretical Analysis of Current Distribution in Porous Electrodes”. *Journal of The Electrochemical Society* 109.12 (Dec. 1962), p. 1183. ISSN: 00134651. DOI: [10.1149/1.2425269](https://doi.org/10.1149/1.2425269) [cited on page 157].
- [191] Qi Zhang and Ralph E. White. “Comparison of approximate solution methods for the solid phase diffusion equation in a porous electrode model”. *Journal of Power Sources* 165.2 (Mar. 2007), pp. 880–886. ISSN: 0378-7753. DOI: [10.1016/J.JPOWSOUR.2006.12.056](https://doi.org/10.1016/J.JPOWSOUR.2006.12.056) [cited on page 161].
- [192] Chao-Yang Wang, W. B. Gu and B. Y. Liaw. “Micro-Macroscopic Coupled Modeling of Batteries and Fuel Cells”. *Journal of The Electrochemical Society* 145.10 (Oct. 1998), p. 3407. ISSN: 00134651. DOI: [10.1149/1.1838820](https://doi.org/10.1149/1.1838820) [cited on page 161].
- [193] Chao-Yang Wang and Venkat Srinivasan. “Computational battery dynamics (CBD)—electrochemical/thermal coupled modeling and multi-scale modeling”. *Journal of Power Sources* 110.2 (Aug. 2002), pp. 364–376. ISSN: 0378-7753. DOI: [10.1016/S0378-7753\(02\)00199-4](https://doi.org/10.1016/S0378-7753(02)00199-4) [cited on page 161].
- [194] Christophe R. Birkl, E. McTurk, M. R. Roberts, Peter G. Bruce and David A. Howey. “A Parametric Open Circuit Voltage Model for Lithium Ion Batteries”. *Journal of The Electrochemical Society* 162.12 (Sept. 2015), A2271–A2280. ISSN: 0013-4651. DOI: [10.1149/2.0331512jes](https://doi.org/10.1149/2.0331512jes) [cited on page 164].
- [195] Gregory L. Plett. “High-Performance Battery-Pack Power Estimation Using a Dynamic Cell Model”. *IEEE Transactions on Vehicular Technology* 53.5 (Sept. 2004), pp. 1586–1593. ISSN: 0018-9545. DOI: [10.1109/TVT.2004.832408](https://doi.org/10.1109/TVT.2004.832408) [cited on page 169].
- [196] Gregory L. Plett. “Extended Kalman filtering for battery management systems of LiPB-based HEV battery packs: Part 1. Background”. *Journal of Power Sources* 134.2 (Aug. 2004), pp. 262–276. ISSN: 0378-7753. DOI: [10.1016/j.jpowsour.2004.02.032](https://doi.org/10.1016/j.jpowsour.2004.02.032) [cited on page 169].
- [197] Gregory L. Plett. “Extended Kalman filtering for battery management systems of LiPB-based HEV battery packs: Part 2. Modeling and identification”. *Journal of Power Sources* 134.2 (Aug. 2004), pp. 262–276. ISSN: 0378-7753. DOI: [10.1016/J.JPOWSOUR.2004.02.032](https://doi.org/10.1016/J.JPOWSOUR.2004.02.032) [cited on page 169].
- [198] Cleve Moler and Charles Van Loan. “Nineteen Dubious Ways to Compute the Exponential of a Matrix, Twenty-Five Years Later”. *SIAM Review* 45.1 (Jan. 2003), pp. 3–49. ISSN: 0036-1445. DOI: [10.1137/S00361445024180](https://doi.org/10.1137/S00361445024180) [cited on page 170].
- [199] Steve C. Southward. *ME5506 Advanced Control Engineering: Lecture Notes 03, Spring 2011*. Blacksburg, VA [cited on pages 174, 309].
- [200] Gregory L. Plett. *Lecture Notes 02: ECE 4540/5540- Digital Control Systems*. Colorado Springs, 2017. URL: <http://mocha-java.uccs.edu/ECE5540/ECE5540-CH02.pdf> [cited on pages 175, 310].
- [201] Uri M. Ascher and Linda R. Petzold. *Computer Methods for Ordinary Differential Equations and Differential-Algebraic Equations*. Philadelphia: Society for Industrial and Applied Mathematics, 1997, p. 332. ISBN: 0898714125 [cited on page 177].
- [202] Lars O. Valøen and Jan N. Reimers. “Transport Properties of LiPF₆-Based Li-Ion Battery Electrolytes”. *Journal of The Electrochemical Society* 152.5 (May 2005), A882. ISSN: 00134651. DOI: [10.1149/1.1872737](https://doi.org/10.1149/1.1872737) [cited on pages 181, 182, 187].
- [203] Linda R. Petzold. *DASSL code*. Livermore, CA, 1989 [cited on page 206].

- [204] P. E. Van Keken, D. A. Yuen and L. R. Petzold. “DASPK: A new high order and adaptive time-integration technique with applications to mantle convection with strongly temperature-and pressure-dependent rheology”. *Geophysical & Astrophysical Fluid Dynamics* 80.1-2 (Sept. 1995), pp. 57–74. ISSN: 0309-1929. DOI: [10.1080/03091929508229763](https://doi.org/10.1080/03091929508229763) [cited on page 206].
- [205] Dominic P. Searson. “GPTIPS 2: An Open-Source Software Platform for Symbolic Data Mining”. *Handbook of Genetic Programming Applications*. Cham: Springer International Publishing, 2015, pp. 551–573. DOI: [10.1007/978-3-319-20883-1_22](https://doi.org/10.1007/978-3-319-20883-1_22) [cited on page 213].
- [206] Max Neumann-Coto and Macarena C. R. Arenas. “Measuring complexity of curves on surfaces” (Dec. 2017). URL: <http://arxiv.org/abs/1712.06671> [cited on page 213].
- [207] Lennart. Ljung. *System identification : theory for the user*. 2nd ed. Upper Saddle River N.J. ;London: Prentice Hall PTR, 1999, p. 609. ISBN: 9780136566953 [cited on pages 219, 223, 240].
- [208] Kumpati S. Narendra and Anuradha M. Annaswamy. “Persistent Excitation in Dynamical Systems”. *1984 American Control Conference*. IEEE, July 1984, pp. 336–338. DOI: [10.23919/ACC.1984.4788399](https://doi.org/10.23919/ACC.1984.4788399) [cited on page 223].
- [209] Kumpati S. Narendra and Anuradha M. Annaswamy. “Persistent excitation in adaptive systems”. *International Journal of Control* 45.1 (Jan. 1987), pp. 127–160. ISSN: 0020-7179. DOI: [10.1080/00207178708933715](https://doi.org/10.1080/00207178708933715) [cited on page 223].
- [210] The Mathworks Inc. *System Identification Overview - MATLAB & Simulink - MathWorks United Kingdom*. URL: <https://uk.mathworks.com/help/ident/gs/about-system-identification.html%7B%5C%23%7Dbsguh6g-1> (visited on 13/07/2018) [cited on page 223].
- [211] Gregory L. Plett. *Lecture Notes 02: ECE5560-System Identification*. Colorado Springs, 2015. URL: <http://mocha-java.uccs.edu/ECE5560/ECE5560-Notes02.pdf> [cited on pages 228, 231, 234].
- [212] Gregory L. Plett. *Lecture Notes 03: ECE5560 - System Identification*. Colorado Springs, 2015. URL: <http://mocha-java.uccs.edu/ECE5560/ECE5560-Notes03.pdf> [cited on page 234].
- [213] Gregory L. Plett. *Lecture Notes 04: ECE5560 - System Identification*. Colorado Springs, 2015. URL: <http://mocha-java.uccs.edu/ECE5560/ECE5560-Notes04.pdf> [cited on page 234].
- [214] L. E. Scales. *Introduction to non-linear optimization*. Springer-Verlag, 1985, p. 243. ISBN: 0387912525. URL: <https://dl.acm.org/citation.cfm?id=2973> [cited on page 241].
- [215] The Mathworks Inc. *System Identification Toolbox*. Natick, 2017 [cited on page 242].
- [216] John Christensen, Venkat Srinivasan and John Newman. “Optimization of Lithium Titanate Electrodes for High-Power Cells”. *Journal of The Electrochemical Society* 153.3 (Mar. 2006), A560. ISSN: 00134651. DOI: [10.1149/1.2172535](https://doi.org/10.1149/1.2172535) [cited on page 271].
- [217] Andrea Pozzi, Gabriele Ciaramella, Krishnakumar Gopalakrishnan, Stefan Volkwein and Davide M. Raimondo. “Optimal Design of Experiment for Parameter Estimation of a Single Particle Model for Lithiumion Batteries”. *2018 IEEE Conference on Decision and Control (CDC)*. Dec. 2018, pp. 6482–6487. DOI: [10.1109/CDC.2018.8619340](https://doi.org/10.1109/CDC.2018.8619340) [cited on page 278].

A

Full Listing of Program Codes

A.1	MATLAB codes for continuous-time SPM	298
A.2	MATLAB codes for discrete-time SPM	301

Listing A.1 MATLAB code for simulation of continuous time SPM

```

1  % Copyright (c) 2018 Gopalakrishnan, Krishnakumar <krishnak@vt.edu>
2  % Author: Gopalakrishnan, Krishnakumar <krishnak@vt.edu>
3
4  clear;clc; format short g; format compact; close all;
5
6  %% User-entered data
7  % case-sensitive string descriptive of cell to be simulated.
8  cellIdentifier = 'Northrop';
9
10 % string describing starting soc% and csv filename of load profile (time vs current through
    ↳ external circuit)
11 load_profile_name = 'cnst_dischg'; % a) 'cnst_dischg' b) 'cnst_chg' c) 'udds' etc
12
13 % Input CSV-profile setup. Note: Offsets use a 0-base numbering system
14 soc_col = 1; % The starting SOC is in this column of top row
15 profile_row_offset = 2; % Load profile input data begins only from this row
16
17 Ts = 0.5; % sec (how often are results needed?)
18 tf_user = 1.5; % sec (user-entered desired simulation end-time)
19 % Simulation might prematurely end if voltage/soc cutoffs are hit
20
21 termination_choice = 'max'; % valid choices are 'max' and 'min'
22 % The 'min' choice is helpful for trials. Whilst retaining the characteristics
23 % of the load profile, the user may do a short time trial simulation.
24
25 %% Pre-Process user data
26 profile_filename = [load_profile_name, '.csv'];
27
28 % Note: a positive C-rate implies discharge and vice-versa for charge
29 try
30     C_rate_profile = csvread(profile_filename,profile_row_offset,0);
31 catch
32     error('Invalid load profile specified. Quitting simulation ...');
33 end
34
35 % Compute expected end-time for allocation of storage & maximum loop indices
36 if strcmp(termination_choice,'max')
37     t_finish = max(tf_user,C_rate_profile(end,1)); % longer of the two prevails
38     % If the last time-entry in the input csv file is shorter than user-entered
39     % value, then the last C-rate from the csv file is held for rest of the
40     % simulation.
41 elseif strcmp(termination_choice,'min')
42     t_finish = min(tf_user,C_rate_profile(end,1)); % longer of the two prevails
43 else
44     error("Invalid termination choice. Valid strings are: 'max' or 'min'.");
45 end
46
47 % Starting SoC percentage
48 soc_init_pct = csvread(profile_filename,0,soc_col,[0 soc_col 0 soc_col]);
49
50 % struct of cell parameters
51 spm_params = parameters_spm_basic(soc_init_pct,cellIdentifier);
52
53 I_1C = spm_params.I_1C;
54 clear tf_user profile_row_offset soc_col profile_filename termination_choice;
55
56 %% Define the State-eqn and Output equation for simulation
57 stateEqn = @spm_cts_stateEqn_three_states;
58 outputEqn = @spm_three_states_battery_voltage;
59
60 %% Allocate storage for simulated quantities
61 num_iterations = ceil(t_finish/Ts) + 1; % max no. of steps (assuming no cutoff)

```

A.1 MATLAB codes for continuous-time SPM

```

62
63 spm_sim_time_vector      = nan(num_iterations,1);
64 load_current_vector      = nan(num_iterations,1);
65 v_cell_sim_results_spm   = nan(num_iterations,1);
66 soc_pct_results_spm     = nan(num_iterations,1);
67 cs_avg_neg_sim_results_spm = nan(num_iterations,1);
68 q_pos_sim_results_spm    = nan(num_iterations,1);
69 q_neg_sim_results_spm    = nan(num_iterations,1);
70
71 %% Initialise SPM state vector and all other simulated quantities
72 spm_sim_time_vector(1)   = 0;
73 soc_pct_results_spm(1)   = soc_init_pct;
74 cs_avg_neg_sim_results_spm(1) = spm_params.cs_n_init;
75 q_pos_sim_results_spm(1) = 0;
76 q_neg_sim_results_spm(1) = 0;
77
78 % load current applied at t = t0
79 load_current_vector(1) = I_1C*interp1(C_rate_profile(:,1),C_rate_profile(:,2),spm_sim_time_vecto
   ↪ r(1), 'previous', 'extrap');
80
81 x_spm_init = [q_pos_sim_results_spm(1); ...
82              q_neg_sim_results_spm(1); ...
83              cs_avg_neg_sim_results_spm(1)];
84
85 v_cell_sim_results_spm(1) = outputEqn(x_spm_init,load_current_vector(1),spm_params);
86
87 t_local_start      = 0;
88 t_local_finish     = Ts;
89 x_spm_local_finish = x_spm_init;
90
91 clear x_init t_finish q_pos_init q_neg_init;
92
93 %% Simulate the SPM
94 progressBarText(0);
95
96 for k = 2:num_iterations % Need solution at k-th time-step
97     load_current_vector(k) = I_1C*interp1(C_rate_profile(:,1),C_rate_profile(:,2),spm_sim|
   ↪ _time_vector(1), 'previous', 'extrap'); % load current that was held constant from (k-1)
   ↪ to (k)
98     t_span = [t_local_start t_local_finish];
99     [~,x_spm_local_finish_matrix] = ode45(@(t,x)stateEqn(x_spm_local_finish,load_current_vector(k),spm_params), t_span,
   ↪ x_spm_local_finish);
100    x_spm_local_finish = x_spm_local_finish_matrix(end,:);
101
102    q_pos_sim_results_spm(k) = x_spm_local_finish(1);
103    q_neg_sim_results_spm(k) = x_spm_local_finish(2);
104    cs_avg_neg_sim_results_spm(k) = x_spm_local_finish(3);
105
106    soc_pct_results_spm(k) = 100*((cs_avg_neg_sim_results_spm(k)/spm_params.cs_max_n) -
   ↪ spm_params.theta_min_neg)/(spm_params.theta_max_neg - spm_params.theta_min_neg);
107    v_cell_sim_results_spm(k) =
   ↪ outputEqn(x_spm_local_finish,load_current_vector(k),spm_params);
108
109    overall_exit_status =
   ↪ check_termination(soc_pct_results_spm(k),v_cell_sim_results_spm(k),spm_params);
110    if overall_exit_status ~= 0 % check for violation of cut-off conditions
111        k = k - 1; % Values in the last simulated index are incorrect.
112        fprintf('Exiting simulation ... \n');
113        break;
114    end
115
116    spm_sim_time_vector(k) = t_local_finish;
117    t_local_start = t_local_finish;

```

A.1 MATLAB codes for continuous-time SPM

```

118     t_local_finish          = t_local_start + Ts;
119     progressBarText((k-1)/num_iterations);
120 end
121 fprintf('\n');
122
123 spm_sim_time_vector        = spm_sim_time_vector(1:k);
124 load_current_vector        = load_current_vector(1:k);
125 q_pos_sim_results_spm     = q_pos_sim_results_spm(1:k);
126 q_neg_sim_results_spm     = q_neg_sim_results_spm(1:k);
127 cs_avg_neg_sim_results_spm = cs_avg_neg_sim_results_spm(1:k);
128 soc_pct_results_spm       = soc_pct_results_spm(1:k);
129 v_cell_sim_results_spm    = v_cell_sim_results_spm(1:k);
130
131 %% Save results to disk
132 if exist('spm_results','dir')==0
133     mkdir('spm_results');
134 end
135
136 % Replace decimal point chars in soc% string with 'p' (stands for point)
137 soc_init_pct_savestr = strrep(num2str(soc_init_pct), '.', 'p');
138
139 % clear A_disc B_disc; % potentially useful variables. comment out for debugging
140 clear soc_init_pct C_rate_profile I_1C k num_iterations; % redundant info
141 clear x_spm_init x_spm_local_finish t_local_finish t_local_start;
142 save(['spm_results/cts_sim_', cellIdentifier, '_', load_profile_name, ...
143     '_initial_soc_', soc_init_pct_savestr, 'pct', ...
144     datestr(now, '_mmm_dd_yyyy_HH_MM_SS')]); % save workspace to file
145
146 %% Plot results
147 close all;
148 figure(1);
149 h1 = subplot(211);
150 plot(spm_sim_time_vector, load_current_vector, '-');
151 ylabel('Current');
152 ylim([min(load_current_vector)-5 max(load_current_vector)+5]);
153
154 h2 = subplot(212);
155 plot(spm_sim_time_vector, v_cell_sim_results_spm, 'm');
156 ylim([spm_params.CutoffVoltage spm_params.CutoverVoltage]);
157 ylabel('Cell Voltage [V]');
158
159 linkaxes([h1 h2], 'x');
160 xlim([spm_sim_time_vector(1) spm_sim_time_vector(end)]);
161 xlabel('Time [sec]');
162
163
164 figure(2);
165 h1 = subplot(211);
166 plot(spm_sim_time_vector, load_current_vector, '-');
167 ylabel('Current');
168 ylim([min(load_current_vector)-5 max(load_current_vector)+5]);
169
170 h2 = subplot(212);
171 plot(spm_sim_time_vector, soc_pct_results_spm, 'r');
172 ylabel('SOC [%]');
173
174 linkaxes([h1 h2], 'x');
175 xlim([spm_sim_time_vector(1) spm_sim_time_vector(end)]);
176 xlabel('Time [sec]');
177
178 clear h1 h2;
179 figure(1);
180 shg;

```

Listing A.2 MATLAB code for simulation of discrete time SPM

```

1  % Copyright (c) 2018 Gopalakrishnan, Krishnakumar <krishnak@vt.edu>
2  % Author: Gopalakrishnan, Krishnakumar <krishnak@vt.edu>
3
4  clear;clc; format short g; format compact; close all;
5
6  %% User-entered data
7  % case-sensitive string descriptive of cell to be simulated.
8  cellIdentifier = 'Northrop';
9
10 % string describing starting soc% and csv filename of load profile
11 % (time vs current through external circuit)
12 % a) 'cnst_dischg_soc_100_1C' b) 'cnst_chg_soc_100_1C' c) 'udds_soc_50' etc.
13 load_profile_name = 'cnst_dischg_soc_100_2C';
14
15 % Input CSV-profile setup. Note: Offsets use a 0-base numbering system
16 soc_col          = 1; % The starting SOC is in this column of top row
17 profile_row_offset = 2; % Load profile input data begins only from this row
18
19 Ts              = 1; % sec (how often are results needed?)
20 tf_user        = 100; % sec (user-entered desired simulation end-time)
21 % Simulation might prematurely end if voltage/soc cutoffs are hit
22
23 termination_choice = 'max'; % valid choices are 'max' and 'min'
24 % The 'min' choice is helpful for trials. Whilst retaining the characteristics
25 % of the load profile, the user may do a short time trial simulation.
26
27 %% Pre-Process user data
28 profile_filename = [load_profile_name, '.csv'];
29
30 % Note: a positive C-rate implies discharge and vice-versa for charge
31 try
32     C_rate_profile = csvread(profile_filename,profile_row_offset,0);
33 catch
34     error('a) Error in specified file, OR b)the load profile is not in PATH. Quitting
35     ↪ simulation ...');
36 end
37
38 % Compute expected end-time for allocation of storage & maximum loop indices
39 if strcmp(termination_choice,'max')
40     t_finish = max(tf_user,C_rate_profile(end,1)); % longer of the two prevails
41     % If the last time-entry in the input csv file is shorter than user-entered
42     % value, then the last C-rate from the csv file is held for rest of the
43     % simulation.
44 elseif strcmp(termination_choice,'min')
45     t_finish = min(tf_user,C_rate_profile(end,1)); % longer of the two prevails
46 else
47     error("Invalid termination choice. Valid strings are: 'max' or 'min'.");
48 end
49
50 % Starting SoC percentage
51 soc_init_pct = csvread(profile_filename,0,soc_col,[0 soc_col 0 soc_col]);
52
53 % struct of cell parameters
54 spm_params = parameters_spm_basic(soc_init_pct,cellIdentifier);
55
56 I_1C = spm_params.I_1C;
57 clear tf_user profile_row_offset soc_col profile_filename termination_choice;
58
59 %% Pre-Compute the System and Input Matrices
60 clc;
61 F = param.F;

```

```

62 A = param.A;
63
64 R_pos = param.R_p;
65 R_neg = param.R_n;
66
67 Ds_pos = param.D_p;
68 Ds_neg = param.D_n;
69
70 a_pos = param.a_p;
71 a_neg = param.a_n;
72
73 L_pos = param.len_p;
74 L_neg = param.len_n;
75
76 %% System & Input matrices for continuous and discrete-time implementations
77
78 A_cts = [-30*D_s_pos/(R_pos^2),          0, 0; ...
79         0, -30*D_s_neg/(R_neg^2), 0; ...
80         0,          0, 0];
81
82 A_disc = expm(A_cts*Ts);
83
84 B_cts = [ (45/2)/(R_pos^2*a_pos*L_pos*F*A); ...
85         (-45/2)/(R_neg^2*a_neg*L_neg*F*A); ...
86         (-3/(R_neg*a_neg*L_neg*F*A))];
87
88 B_disc = nan(size(B_cts));
89 B_disc(1) = B_cts(1)*(exp(A_cts(1,1)*Ts)-1)/A_cts(1,1);
90 B_disc(2) = B_cts(2)*(exp(A_cts(2,2)*Ts)-1)/A_cts(2,2);
91 B_disc(3) = B_cts(3)*Ts;
92
93 % Through built-in 'c2d' command by the dummy system-method (tricking MATLAB
94 % to believe we have an LTI system). The output matrix, C is chosen so that the
95 % states-themselves are the outputs with no feed-through term involved.
96
97 C_dummy = [1, 1, 1]; D_dummy = 0;
98 sys_cts = ss(A_cts,B_cts,C_dummy,D_dummy);
99 sys_disc = c2d(sys_cts,Ts);
100
101 outputEqn = @spm_three_states_battery_voltage;
102
103 %% Allocate storage for simulated quantities
104 num_iterations = ceil(t_finish/Ts) + 1; % max no. of steps (assuming no cutoff)
105
106 spm_sim_time_vector      = nan(num_iterations,1);
107 load_current_vector      = nan(num_iterations,1);
108 v_cell_sim_results_spm  = nan(num_iterations,1);
109 soc_pct_results_spm     = nan(num_iterations,1);
110 cs_avg_neg_sim_results_spm = nan(num_iterations,1);
111 q_pos_sim_results_spm   = nan(num_iterations,1);
112 q_neg_sim_results_spm   = nan(num_iterations,1);
113
114 %% Initialise SPM state vector and all other simulated quantities
115 spm_sim_time_vector(1)   = 0;
116 soc_pct_results_spm(1)  = soc_init_pct;
117 cs_avg_neg_sim_results_spm(1) = spm_params.cs_n_init;
118 q_pos_sim_results_spm(1) = 0;
119 q_neg_sim_results_spm(1) = 0;
120
121 % load current applied at t = t0
122 load_current_vector(1) = I_1C*interp1(C_rate_profile(:,1),C_rate_profile(:,2),spm_sim_time_vecto
123 ↪ r(1),'previous','extrap');
124
125 x_spm_init = [q_pos_sim_results_spm(1); ...

```

A.2 MATLAB codes for discrete-time SPM

```

125     q_neg_sim_results_spm(1); ...
126     cs_avg_neg_sim_results_spm(1)];
127
128     v_cell_sim_results_spm(1) = outputEqn(x_spm_init,load_current_vector(1),spm_params);
129
130     t_local_finish      = Ts;
131     x_spm_local_finish = x_spm_init;
132
133     clear x_init q_pos_init q_neg_init;
134
135     %% Simulate the SPM
136     progressBarText(0);
137
138     for k = 2:num_iterations % Need solution at k-th time-step
139         load_current_vector(k) = I_1C*interp1(C_rate_profile(:,1),C_rate_profile(:,2),spm_sim|
140         ↪ _time_vector(k-1),'previous','extrap'); % load current that was held constant from (k-1)
141         ↪ to (k)
142         x_spm_local_finish      = A_disc*x_spm_local_finish + B_disc*load_current_vector(k);
143
144         q_pos_sim_results_spm(k) = x_spm_local_finish(1);
145         q_neg_sim_results_spm(k) = x_spm_local_finish(2);
146         cs_avg_neg_sim_results_spm(k) = x_spm_local_finish(3);
147
148         soc_pct_results_spm(k) = 100*((cs_avg_neg_sim_results_spm(k)/spm_params.cs_max_n) -
149         ↪ spm_params.theta_min_neg)/(spm_params.theta_max_neg - spm_params.theta_min_neg);
150         v_cell_sim_results_spm(k) =
151         ↪ outputEqn(x_spm_local_finish,load_current_vector(k),spm_params);
152
153         overall_exit_status =
154         ↪ check_termination(soc_pct_results_spm(k),v_cell_sim_results_spm(k),spm_params);
155         if overall_exit_status ~= 0 % check for violation of cut-off conditions
156             k = k - 1; % Values in the last simulated index are incorrect.
157             fprintf('Exiting simulation ... \n');
158             break;
159         end
160
161         spm_sim_time_vector(k) = t_local_finish;
162         t_local_start          = t_local_finish;
163         t_local_finish         = t_local_start + Ts;
164         progressBarText((k-1)/num_iterations);
165     end
166     fprintf('\n');
167
168     spm_sim_time_vector      = spm_sim_time_vector(1:k);
169     load_current_vector      = load_current_vector(1:k);
170     q_pos_sim_results_spm    = q_pos_sim_results_spm(1:k);
171     q_neg_sim_results_spm    = q_neg_sim_results_spm(1:k);
172     cs_avg_neg_sim_results_spm = cs_avg_neg_sim_results_spm(1:k);
173     soc_pct_results_spm      = soc_pct_results_spm(1:k);
174     v_cell_sim_results_spm   = v_cell_sim_results_spm(1:k);
175
176     %% Save results to disk
177     save_foldername = ['spm_results/', cellIdentifier, '/', load_profile_name];
178     if exist(save_foldername,'dir')==0
179         mkdir(save_foldername);
180     end
181
182     % Replace decimal point chars in soc% string with 'p' (stands for point)
183     soc_init_pct_savestr = strrep(num2str(soc_init_pct),'.','p');
184
185     clear soc_init_pct C_rate_profile I_1C k num_iterations; % redundant info
186     clear x_spm_init x_spm_local_finish t_local_finish t_local_start;
187     save([save_foldername, '/disc_sim_', ...
188         datestr(now, 'mmm_dd_yyyy_HH_MM_SS')]); % save workspace to file

```

```

184
185 function v_cell = spm_three_states_battery_voltage(x,u,param)
186     % returns v_cell given the vector x and input u at any given time-step
187     % x(1) = q_pos, x(2) = q_neg, x(3) = cs_avg_neg
188     % u = load current (A). Positive implies discharge.
189
190     % Copyright (c) 2018 Gopalakrishnan, Krishnakumar <krishnak@vt.edu>
191     % Author: Gopalakrishnan, Krishnakumar <krishnak@vt.edu>
192
193     R      = param.R;
194     T      = param.Tref;
195     F      = param.F;
196
197     R_pos  = param.R_p;
198     R_neg  = param.R_n;
199
200     Ds_pos = param.D_p;
201     Ds_neg = param.D_n;
202
203     a_pos  = param.a_p;
204     a_neg  = param.a_n;
205
206     L_pos  = param.len_p;
207     L_neg  = param.len_n;
208
209     k_p    = param.k_p;
210     k_n    = param.k_n;
211
212     ce     = param.ce_init;
213     A      = param.A;
214
215     cs_max_n = param.cs_max_n;
216     cs_max_p = param.cs_max_p;
217
218     theta_min_neg = param.theta_min_neg;
219     theta_min_pos = param.theta_min_pos;
220     theta_max_neg = param.theta_max_neg;
221     theta_max_pos = param.theta_max_pos;
222
223     % Extract permissible bounds for solid concentrations
224     cs_surf_pos_lb = param.theta_max_pos*param.cs_max_p;
225     cs_surf_pos_ub = param.theta_min_pos*param.cs_max_p;
226     cs_surf_neg_lb = param.theta_min_neg*param.cs_max_n;
227     cs_surf_neg_ub = param.theta_max_neg*param.cs_max_n;
228
229     % Extract the function handles for Uocp_pos and Uocp_neg
230     compute_Uocp_pos = param.compute_Uocp_pos;
231     compute_Uocp_neg = param.compute_Uocp_neg;
232
233     %% Compute surface concentrations
234     cs_surf_neg = x(3) + (8*R_neg/35)*x(2) - (R_neg/(35*D_s_neg*a_neg*L_neg*F*A))*u;
235     cs_surf_neg = min(cs_surf_neg_ub, max(cs_surf_neg_lb, cs_surf_neg)); % saturation
236
237     cs_avg_pos = cs_max_p*(theta_min_pos + ((x(3) - theta_min_neg*cs_max_n)./(theta_max_neg -
     ↪ theta_min_neg)*cs_max_n))*(theta_max_pos - theta_min_pos)); % average concentration in
     ↪ pos electrode (analytical expn using conservation of Li)
238     cs_surf_pos = cs_avg_pos + (8*R_pos/35)*x(1) + (R_pos/(35*D_s_pos*a_pos*L_pos*F*A))*u; %
     ↪ surface concentration of pos electrode
239     cs_surf_pos = min(cs_surf_pos_ub, max(cs_surf_pos_lb, cs_surf_pos)); % saturation
240
241     % Compute overpotentials
242     eta_p = (2*R*T/F)*asinh(-u/(2*A*F*a_pos*L_pos*k_p*sqrt(ce*cs_surf_pos*(cs_max_p -
     ↪ cs_surf_pos))));

```


A.2 MATLAB codes for discrete-time SPM

```
243     eta_n = (2*R*T/F)*asinh(u/(2*A*F*a_neg*L_neg*k_n*sqrt(ce*cs_surf_neg*(cs_max_n -
    ↪ cs_surf_neg))));
244
245     %% Compute OCPs
246     surf_theta_p = cs_surf_pos/param.cs_max_p;
247     surf_theta_n = cs_surf_neg/param.cs_max_n;
248
249     U_p = compute_Uocp_pos(surf_theta_p);
250     U_n = compute_Uocp_neg(surf_theta_n);
251
252     phi_pos = eta_p + U_p;
253     phi_neg = eta_n + U_n;
254
255     v_cell = phi_pos - phi_neg;
256
257 end
258
259 function U_p = compute_Uocp_pos(theta_p)
260
261     U_p = (-4.656+88.669*theta_p.^2 - 401.119*theta_p.^4 + 342.909*theta_p.^6 -
    ↪ 462.471*theta_p.^8 + 433.434*theta_p.^10);
262     U_p = U_p./(-1+18.933*theta_p.^2-79.532*theta_p.^4+37.311*theta_p.^6-73.083*theta_p.^8+95.96
    ↪ *theta_p.^10);
263
264 end
265
266 function U_n = compute_Uocp_neg(theta_n)
267
268     U_n = 0.7222 + 0.1387*theta_n + 0.029*theta_n.^0.5 - 0.0172./theta_n +
    ↪ 0.0019./theta_n.^1.5 + 0.2808*exp(0.9-15*theta_n)-0.7984*exp(0.4465*theta_n - 0.4108);
269
270 end
```

B

Permissions Summary

B.1	Summary of Copyright Permissions	307
B.2	Copyright Permissions for reuse of Figure 3.4	311
B.3	Copyright Permissions for reuse of Figure 3.8	313
B.4	Copyright Permissions for reuse of text, figures and tables of Chapter 4	315
B.5	Copyright Permissions for reuse of Figure 5.1	318
B.6	Copyright Permissions for reuse of Figure 5.3	322
B.7	Copyright Permissions for reuse of Figure 5.4	323
B.8	Copyright Permissions for reuse of Figure 5.13	324

Table B.1 Summary of permissions for reuse of third-party copyrighted material

Page no.	Usage in thesis	Source	Copyright holder & contact (organisations only)	Date of last correspondence	Have permission?	Permission remarks
Page 87	Figure 3.1	Marie-Therese von Srbik. "Advanced Lithium-Ion Battery Modelling for Automotive Applications". PhD thesis. Imperial College London, 2015, p. 162	Marie-Therese von Srbik	N/A	Yes	CC-BY-NC-ND
Page 89	Figure 3.2	Ian D. Campbell, Krishnakumar Gopalakrishnan, Monica Marinescu, Marcello Torchio, Gregory J. Offer and Davide M. Raimondo. "Optimising lithium-ion cell design for plug-in hybrid and battery electric vehicles". <i>Journal of Energy Storage</i> 22 (Apr. 2019), pp. 228–238. ISSN: 2352-152X. <i>The highlighted authors are official joint first authors with equal contributions.</i>	Pending transfer to Elsevier by Ian D. Campbell permissions@elsevier.com	05/01/2019 (manuscript accepted)	No	Pending publication
Page 105	Figure 3.4	Marcello Torchio, Lalo Magni, R. B. Gopaluni, Richard D. Braatz and Davide M. Raimondo. "LIONSIMBA: A Matlab Framework Based on a Finite Volume Model Suitable for Li-Ion Battery Design, Simulation, and Control". <i>Journal of The Electrochemical Society</i> 163.7 (2016), A1192–A1205. ISSN: 0013-4651	The Electrochemical Society copyright@electrochem.org	27/09/2018	Yes	'Rightslink' agreement attached (see B.2)
Page 109	Figure 3.5	Steven G. Johnson. <i>Chebyshev Nodes by Projection</i> . 2018	Steven G. Johnson	N/A	Yes	CC-BY-SA
Page 120	Figure 3.7	Toby Bond, Jigang Zhou and Jeffrey Cutler. "Electrode Stack Geometry Changes during Gas Evolution in Pouch-Cell-Type Lithium Ion Batteries". <i>Journal of The Electrochemical Society</i> 164.1 (Nov. 2017), A6158–A6162. ISSN: 0013-4651	Bond, Zhou and Cutler	N/A	Yes	CC-BY

Continued on next page

Table B.1 — continued from previous page

Page no.	Usage in thesis	Source	Copyright holder & contact (organisations only)	Date of last correspondence	Have permission?	Permission remarks
Page 122	Figure 3.8	Paul W. Northrop, Venkatasailanathan Ramadesigan, Sumitava De and Venkat R. Subramanian. “Coordinate Transformation, Orthogonal Collocation, Model Reformulation and Simulation of Electrochemical-Thermal Behavior of Lithium-ion Battery Stacks”. <i>Journal of The Electrochemical Society</i> 158.12 (Jan. 2011), A1461–A1477. ISSN: 00134651	The Electrochemical Society copyright@electrochem.org	27/09/2018	Yes	‘Rightslink’ agreement attached (see B.3)
Page 131	Figure 3.9	Ian D. Campbell , Krishnakumar Gopalakrishnan , Monica Marinescu, Marcello Torchio, Gregory J. Offer and Davide M. Raimondo. “Optimising lithium-ion cell design for plug-in hybrid and battery electric vehicles”. <i>Journal of Energy Storage</i> 22 (Apr. 2019), pp. 228–238. ISSN: 2352-152X. <i>The highlighted authors are official joint first authors with equal contributions.</i>	Pending transfer to Elsevier by Ian D. Campbell permissions@elsevier.com	05/01/2019 (manuscript accepted)	No	Pending publication
Page 131	Figure 3.10	Ian D. Campbell , Krishnakumar Gopalakrishnan , Monica Marinescu, Marcello Torchio, Gregory J. Offer and Davide M. Raimondo. “Optimising lithium-ion cell design for plug-in hybrid and battery electric vehicles”. <i>Journal of Energy Storage</i> 22 (Apr. 2019), pp. 228–238. ISSN: 2352-152X. <i>The highlighted authors are official joint first authors with equal contributions.</i>	Pending transfer to Elsevier by Ian D. Campbell permissions@elsevier.com	05/01/2019 (manuscript accepted)	No	Pending publication

Continued on next page

Table B.1 — continued from previous page


Page no.	Usage in thesis	Source	Copyright holder & contact (organisations only)	Date of last correspondence	Have permission?	Permission remarks
Page 133	Figure 3.11	Ian D. Campbell , Krishnakumar Gopalakrishnan , Monica Marinescu, Marcello Torchio, Gregory J. Offer and Davide M. Raimondo. “Optimising lithium-ion cell design for plug-in hybrid and battery electric vehicles”. <i>Journal of Energy Storage</i> 22 (Apr. 2019), pp. 228–238. ISSN: 2352-152X. <i>The highlighted authors are official joint first authors with equal contributions.</i>	Pending transfer to Elsevier by Ian D. Campbell permissions@elsevier.com	05/01/2019 (manuscript accepted)	No	Pending publication
Page 136	All figures, tables and captions of chapter 4	Krishnakumar Gopalakrishnan, Teng Zhang and Gregory J. Offer. “A Fast, Memory-Efficient Discrete-Time Realization Algorithm for Reduced-Order Li-Ion Battery Models”. <i>Journal of Electrochemical Energy Conversion and Storage</i> 14.1 (Feb. 2017), p. 011001. ISSN: 2381-6872	The American Society of Mechanical Engineers (ASME) journalcopyright@asme.org	18/04/2016	Yes	Copyright agreement attached (see B.4)
Page 156	Figure 5.1	Scott J. Moura, Miroslav Krstic and Nalin A. Chaturvedi. “Adaptive PDE Observer for Battery SOC/SOH Estimation”. <i>Volume 1: Adaptive Control; Advanced Vehicle Propulsion Systems; Aerospace Systems; Autonomous Systems; Battery Modeling; Biochemical Systems; Control Over Networks; Control Systems Design; Cooperativ. ASME</i> , Oct. 2012, pp. 101–110. ISBN: 978-0-7918-4529-5	The American Society of Mechanical Engineers journalcopyright@asme.org	02/10/2018	Yes	‘Rightslink’ agreement attached (see B.5)
Page 174	Figure 5.3	Steve C. Southward. <i>ME5506 Advanced Control Engineering: Lecture Notes 03, Spring 2011</i> . Blacksburg, VA	Steve C. Southward	09/10/2018	Yes	Granted via email (see B.6)

Continued on next page

Table B.1 — continued from previous page

Page no.	Usage in thesis	Source	Copyright holder & contact (organisations only)	Date of last correspondence	Have permission?	Permission remarks
Page 175	Figure 5.4	Gregory L. Plett. <i>Lecture Notes 02: ECE 4540/5540- Digital Control Systems</i> . Colorado Springs, 2017	Gregory L. Plett	28/09/2018	Yes	Granted via email (see B.7)
Page 202	Figure 5.13	Zhongwei Deng, Lin Yang, Hao Deng, Yishan Cai and Dongdong Li. “Polynomial approximation pseudo-two-dimensional battery model for online application in embedded battery management system”. <i>Energy</i> 142 (Jan. 2018), pp. 838–850. ISSN: 0360-5442	Elsevier permissions@elsevier.com	27/09/2018	Yes	Elsevier license attached (see B.8)

B.2 Copyright Permissions for reuse of Figure 3.4

	
Confirmation Number: 11751937 Order Date: 09/27/2018	
Customer Information	
Customer: Krishnakumar Gopalakrishnan Account Number: 3001303559 Organization: Krishnakumar Gopalakrishnan Email: [REDACTED] Phone: [REDACTED] Payment Method: Invoice	
<p>This is not an invoice</p>	
Order Details	
Journal of the Electrochemical Society	
Billing Status: N/A	
Order detail ID: 71574235 ISSN: 1945-7111 Publication Type: e-Journal Volume: Issue: Start page: Publisher: Electrochemical Society Author/Editor: Electrochemical Society	Permission Status: ✔ Granted Permission type: Republish or display content Type of use: Republish in a thesis/dissertation Order License Id: 4437101409759 Requestor type: Academic institution Format: Electronic Portion: chart/graph/table/figure Number of charts/graphs/tables/figures: 1 The requesting person/organization: Krishnakumar Gopalakrishnan Title or numeric reference of the portion (s): Figure 2 Title of the article or chapter the portion is from: LIONSIMBA: A Matlab Framework Based on a Finite Volume Model Suitable for Li-Ion Battery Design, Simulation, and Control Editor of portion(s): Robert Savinell Marcello Torchio, Lalo Magni, R Bhushan Gopaluni, Richard D Braatzand, Davide M Raimondo Author of portion(s): Volume of serial or monograph: 163 Issue, if republishing an article from a serial: 7 Page range of portion: A1192-A1205 Publication date of portion: April 12, 2016 Rights for: Main product Duration of use: Life of current edition Creation of copies for the disabled: no With minor editing privileges: yes For distribution to: Worldwide In the following language(s): Original language of publication With incidental promotional use: no Lifetime unit quantity of new product: Up to 499


B.2 Copyright Permissions for reuse of Figure 3.4

Title	Computational modelling of lithium ion batteries for electric vehicle applications: analysis, design and implementation	
Instructor name	Dr Gregory J Offer	
Institution name	Imperial College London	
Expected presentation date	Oct 2018	
Note: This item was invoiced separately through our RightsLink service . More info		\$ 0.00
Total order items: 1		Order Total: \$0.00

[About Us](#) | [Privacy Policy](#) | [Terms & Conditions](#) | [Pay an Invoice](#)

Copyright 2018 Copyright Clearance Center

B.3 Copyright Permissions for reuse of Figure 3.8

	
Confirmation Number: 11751910 Order Date: 09/27/2018	
Customer Information	
Customer: Krishnakumar Gopalakrishnan Account Number: 3001303559 Organization: Krishnakumar Gopalakrishnan Email: [REDACTED] Phone: [REDACTED] Payment Method: Invoice	
This is not an invoice	
Order Details	
Journal of the Electrochemical Society	
Billing Status: N/A	
Order detail ID: 71574169 ISSN: 1945-7111 Publication Type: e-Journal Volume: Issue: Start page: Publisher: Electrochemical Society Author/Editor: Electrochemical Society	Permission Status: ✔ Granted Permission type: Republish or display content Type of use: Republish in a thesis/dissertation Order License Id: 4437051316162 Requestor type: Academic Institution Format: Electronic Portion: chart/graph/table/figure Number of charts/graphs/tables/figures: 1 The requesting person/organization: Krishnakumar Gopalakrishnan Title or numeric reference of the portion(s): Figure 2 Title of the article or chapter the portion is from: Coordinate Transformation, Orthogonal Collocation, Model Reformulation and Simulation of Electrochemical-Thermal Behavior of Lithium-Ion Battery Stacks Editor of portion(s): Robert Savinell Author of portion(s): Paul W. C. Northrop, Venkatasailanathan Ramadesigan, Sumitava De and Venkat R. Subramanian Volume of serial or monograph: 158 Issue, if republishing an article from a serial: 12 Page range of portion: A1461-A1477 Publication date of portion: November 30, 2011 Rights for: Main product Duration of use: Life of current edition Creation of copies for the disabled: no With minor editing privileges: yes For distribution to: Worldwide In the following language(s): Original language of publication With incidental promotional use: no

B.3 Copyright Permissions for reuse of Figure 3.8

Lifetime unit quantity of new product	Up to 499
Title	Computational modeling of lithium ion batteries for electric vehicle applications: analysis, design and implementation
Instructor name	Dr Gregory J Offer
Institution name	Imperial College London
Expected presentation date	Oct 2018
Note: This item was invoiced separately through our RightsLink service . More info	
\$ 0.00	
<hr/>	
Total order items: 1	Order Total: \$0.00

[About Us](#) | [Privacy Policy](#) | [Terms & Conditions](#) | [Pay an Invoice](#)

Copyright 2018 Copyright Clearance Center

B.4 Copyright Permissions for reuse of text, figures and tables of Chapter 4

COPYRIGHT AGREEMENT (as of February 2010)

ASME Publishing • Two Park Avenue • New York, NY 10016

For questions about Conference paper copyright, please e-mail copyright@asme.org

For questions about Journal paper copyright, please email journalcopyright@asme.org

Before publication of your paper in a conference proceedings or journal, ASME must receive a signed Copyright Agreement. For conference papers, this form should be received by the deadline indicated by the Conference. Other forms may NOT be substituted for this form, nor may any wording on the form be changed.

PAPER NUMBER (for conference/journal papers): JEECS-16-1050

TITLE: A Fast, Memory-Efficient Discrete-Time Realization Algorithm for Reduced-Order Li-ion Battery Models

AUTHOR(s): Krishnakumar Gopalakrishnan

CONFERENCE NAME: _____

JOURNAL NAME: Journal of Electrochemical Energy Conversion and Storage

ASME requests that authors/copyright owners assign copyright to ASME in order for a conference or journal paper to be published by ASME. Authors exempt from this request are direct employees of the U.S. Government, whereby papers are not subject to copyright protection in the U.S., or non-U.S. government employees, whose governments hold the copyright to the paper. Otherwise, the author/copyright owner(s) of the Paper should sign this form as instructed below. Please refer to the section below "Who Should Sign" and also to ASME's [FAQ page](#) for more information regarding copyright ownership and the copyright process.

WHO SHOULD SIGN

Only the copyright owner(s) of the Paper, or an authorized representative, can sign this form. If one of the following applies, you may not own the copyright to the paper, or you may not be authorized to sign this agreement, and you may need to have the appropriate copyright owner(s) or organization representative sign this Agreement:

- (1) You created the Paper within the scope of your employment, and your employer is the copyright owner
- (2) You created the Paper under an independent contractor agreement**
- (3) You received a grant that funded your Paper.

Please review your company policies regarding copyright, and if you are not authorized to sign this agreement, please forward to the appropriate organization representative. Please review applicable company, institutional, and grant policies and your employment/independent contractor agreement to determine who holds the rights to your Paper. For more information, please refer to the [FAQs](#).

****Note to U.S. Government Contractors:** If you created the Paper under contract with the U.S. Government, e.g., U.S. Government labs, the paper may be subject to copyright, and you or your employer may own the copyright. Please review your company/institutional policies and your contractor agreement. Your Paper may also require a footer acknowledging contract information and also the following statement:

"The United States Government retains, and by accepting the article for publication, the publisher acknowledges that the United States Government retains, a non-exclusive, paid-up, irrevocable, worldwide license to publish or reproduce the published form of this work, or allow others to do so, for United States Government purposes."

It is your responsibility to ensure that the final PDF version of the Paper you submit includes all necessary footers and statements required under your contract.

COPYRIGHT ASSIGNMENT

The following terms of copyright assignment refer to Sections 1, 2, and 3. Sections 4 and 5 may not be subject to copyright.

The undersigned hereby assigns irrevocably to ASME all worldwide rights under copyright in the Paper.

Authors retain all proprietary rights in any idea, process, procedure, or articles of manufacture described in the Paper, including the right to seek patent protection for them. Authors may perform, lecture, teach, conduct related research, display all

B.4 Copyright Permissions for reuse of text, figures and tables of Chapter 4

or part of the Paper, and create derivative works in print or electronic format. Authors may reproduce and distribute the Paper for non-commercial purposes only. Non-commercial applies only to the sale of the paper per se. For all copies of the Paper made by Authors, Authors must acknowledge ASME as original publisher and include the names of all author(s), the publication title, and an appropriate copyright notice that identifies ASME as the copyright holder.

PLEASE READ THE TERMS AND CONDITIONS WHICH ARE FULLY INCORPORATED IN THIS AGREEMENT.

PAPERS OWNED BY ONE AUTHOR OR JOINT AUTHORS; DESIGNATED AUTHORS (For jointly authored works, all authors should submit a signed Agreement, or one Designated Author may sign on behalf of the other authors, but ONLY IF the designated author has secured written authorization to do so from all other authors. The designated author must be able to produce such written authorization if requested.)

Author, Co-Author, or Designated Author

Name: Krishnakumar Gopalakrishnan Signature: Krishnakumar Gopalakrishnan 18 Apr 2016

Affiliation: Imperial College London Title: Ph.D. Student
(Company or Institution)

Street Address: [REDACTED]

London [REDACTED] United Kingdom
(City) (State) (Zip Code) (Country)

Phone: [REDACTED] Fax: [REDACTED] Email: [REDACTED]

Author: (Applied only if you are signing for other)

Name: _____ Signature: _____ Date: _____

Affiliation: _____ Title: _____
(Company or Institution)

Street Address: _____

(City) (State) (Zip Code) (Country)

Phone: _____ Fax: _____ Email: _____

B.4 Copyright Permissions for reuse of text, figures and tables of Chapter 4

ASME COPYRIGHT FORM TERMS AND CONDITIONS

The following terms and conditions are fully incorporated into the Copyright Form. Please read them carefully.

REPRESENTATIONS, OBLIGATIONS, ACKNOWLEDGEMENTS, AND INDEMNIFICATION

You represent and acknowledge that:

(A) This Paper represents: either the first publication of material or the first publication of an original compilation of information from a number of sources as specifically noted by footnotes and/or bibliography.

(B) You have the right to enter into this Copyright Form and to make the assignment of rights to ASME. If the Paper contains excerpts from other copyrighted material (including without limitation any diagrams, photographs, figures or text), you have acquired in writing all necessary rights from third parties to include those materials in the Paper, and have provided appropriate credit for that third-party material in footnotes or in a bibliography.

(C) If you are signing this Form on behalf of any co-authors or other copyright holders, you have obtained express authorizations from all those authors and/or copyright holders to make this assignment of rights to ASME.

(D) To the best of the author's knowledge, all statements contained in the Paper purporting to be facts are true or supported by reasonable scientific research, the Paper does not contain any defamatory or libelous material and does not infringe any third party's copyright, patent, trade secret, or other proprietary rights and does not violate the right of privacy or publicity of any third party or otherwise violate any other applicable law; furthermore that to the best of your ability, you are responsible for ensuring the accuracy of your research and the Paper's content.

(E) If the Paper was produced in the course of an author's employment by, or contractual relationship with, the U.S. Federal or State Government and/or contains classified material, it has been appropriately cleared for public release and such is indicated in the paper.

(F) The Paper is not subject to any prior claim, encumbrance or form and is not under consideration for publication elsewhere.

(G) You have appropriately cited and acknowledged all third parties who have contributed significantly in the Paper's technical aspects.

(H) ASME is not responsible for any misrepresentation, errors or omissions by those signing this copyright form.

(I) All print and electronic copies of the Paper submitted to ASME become ASME's physical property regardless of whether or not ASME publishes the Paper, and that ASME is not obligated to publish your paper (see the Termination Section below if your paper is not published).

(J) ASME is not responsible for any of your expenses incurred in connection with preparing the Paper or attending meetings to present it, nor will ASME pay you any financial compensation if it publishes your Paper.

(K) Subject to and to the maximum extent permitted by law, you agree to indemnify and hold harmless ASME from any damage or expense related to a breach of any of the representations and warranties above.

TERMINATION

If ASME decides not to publish your Paper, this Form, including all of ASME's rights in your Paper, terminates and you are thereafter free to offer the Paper for publication elsewhere.

GENERAL PROVISIONS

This Copyright Form, the Terms & Conditions, and [ASME Copyright Guidelines](#), constitutes the entire agreement between you and ASME, and supersedes all prior or current negotiations, understandings and representations, whether oral or written, between you and ASME concerning the Paper.

This Agreement is governed by, and should be construed in accordance with, the laws of the State of New York, United States of America, applicable to agreements made and performed there, except to the extent that your institution is prohibited by law from entering contracts governed by New York law, in which limited case this Agreement is governed by, and should be construed in accordance with, the laws of the jurisdiction in which your institution is located. Any claim, dispute, action or proceeding relating to this Agreement may be brought only in the applicable state and federal courts in the State and County of New York, and you expressly consent to personal jurisdiction and venue in any of those courts.

B.5 Copyright Permissions for reuse of Figure 5.1

American Society of Mechanical Engineers ASME LICENSE TERMS AND CONDITIONS


Oct 02, 2018

This is a License Agreement between Krishnakumar Gopalakrishnan ("You") and American Society of Mechanical Engineers ASME ("American Society of Mechanical Engineers ASME") provided by Copyright Clearance Center ("CCC"). The license consists of your order details, the terms and conditions provided by American Society of Mechanical Engineers ASME, and the payment terms and conditions.

All payments must be made in full to CCC. For payment instructions, please see information listed at the bottom of this form.

License Number	4440801185924
License date	Sep 25, 2018
Licensed content publisher	American Society of Mechanical Engineers ASME
Licensed content title	Journal of dynamic systems, measurement, and control
Licensed content date	Jan 1, 1959
Type of Use	Thesis/Dissertation
Requestor type	Academic institution
Format	Electronic
Portion	chart/graph/table/figure
Number of charts/graphs/tables/figures	1
The requesting person/organization is:	Krishnakumar Gopalakrishnan
Title or numeric reference of the portion(s)	Fig. 1
Title of the article or chapter the portion is from	Adaptive Partial Differential Equation Observer for Battery State-of-Charge/State-of-Health Estimation Via an Electrochemical Model
Editor of portion(s)	Joseph Beaman
Author of portion(s)	Scott J. Moura, Nalin A. Chaturvedi, Miroslav Krstic
Volume of serial or monograph.	136
Issue, if republishing an article from a serial	1
Page range of the portion	2
Publication date of portion	Oct 15, 2013
Rights for	Main product
Duration of use	Life of current edition
Creation of copies for the disabled	no
With minor editing privileges	yes
For distribution to	Worldwide
In the following language(s)	Original language of publication
With incidental promotional use	no
The lifetime unit quantity of new product	Up to 499
Title	Computational modelling of lithium ion batteries for electric vehicle applications: analysis, design and implementation

B.5 Copyright Permissions for reuse of Figure 5.1

Instructor name Dr Gregory J Offer
Institution name Imperial College London
Expected presentation date Oct 2018
Billing Type Invoice
Billing Address Krishnakumar.Gopalakrishnan

Attn: Krishnakumar Gopalakrishnan

Total (may include CCC user fee) 0.00 USD

Terms and Conditions

TERMS AND CONDITIONS

The following terms are individual to this publisher:

None

Other Terms and Conditions:

STANDARD TERMS AND CONDITIONS

1. Description of Service; Defined Terms. This Republication License enables the User to obtain licenses for republication of one or more copyrighted works as described in detail on the relevant Order Confirmation (the "Work(s)"). Copyright Clearance Center, Inc. ("CCC") grants licenses through the Service on behalf of the rightsholder identified on the Order Confirmation (the "Rightsholder"). "Republication", as used herein, generally means the inclusion of a Work, in whole or in part, in a new work or works, also as described on the Order Confirmation. "User", as used herein, means the person or entity making such republication.

2. The terms set forth in the relevant Order Confirmation, and any terms set by the Rightsholder with respect to a particular Work, govern the terms of use of Works in connection with the Service. By using the Service, the person transacting for a republication license on behalf of the User represents and warrants that he/she/it (a) has been duly authorized by the User to accept, and hereby does accept, all such terms and conditions on behalf of User, and (b) shall inform User of all such terms and conditions. In the event such person is a "freelancer" or other third party independent of User and CCC, such party shall be deemed jointly a "User" for purposes of these terms and conditions. In any event, User shall be deemed to have accepted and agreed to all such terms and conditions if User republishes the Work in any fashion.

3. Scope of License; Limitations and Obligations.

3.1 All Works and all rights therein, including copyright rights, remain the sole and exclusive property of the Rightsholder. The license created by the exchange of an Order Confirmation (and/or any invoice) and payment by User of the full amount set forth on that document includes only those rights expressly set forth in the Order Confirmation and in these terms and conditions, and conveys no other rights in the Work(s) to User. All rights not expressly granted are hereby reserved.

3.2 General Payment Terms: You may pay by credit card or through an account with us payable at the end of the month. If you and we agree that you may establish a standing account with CCC, then the following terms apply: Remit Payment to: Copyright Clearance Center, 29118 Network Place, Chicago, IL 60673-1291. Payments Due: Invoices are payable upon their delivery to you (or upon our notice to you that they are available to you for downloading). After 30 days, outstanding amounts will be subject to a service charge of 1-1/2% per month or, if less, the maximum rate allowed by applicable law. Unless otherwise specifically set forth in the Order Confirmation or in a separate written agreement signed by CCC, invoices are due and payable on "net 30" terms. While User may exercise the rights licensed immediately upon issuance of the Order Confirmation, the license is automatically revoked and is null and void, as if it had never been issued, if complete payment for the license is not received on a timely basis either from User directly or through a payment agent, such as a credit card company.

3.3 Unless otherwise provided in the Order Confirmation, any grant of rights to User (i) is "one-time" (including the editions and product family specified in the license), (ii) is non-

B.5 Copyright Permissions for reuse of Figure 5.1

exclusive and non-transferable and (iii) is subject to any and all limitations and restrictions (such as, but not limited to, limitations on duration of use or circulation) included in the Order Confirmation or invoice and/or in these terms and conditions. Upon completion of the licensed use, User shall either secure a new permission for further use of the Work(s) or immediately cease any new use of the Work(s) and shall render inaccessible (such as by deleting or by removing or severing links or other locators) any further copies of the Work (except for copies printed on paper in accordance with this license and still in User's stock at the end of such period).

3.4 In the event that the material for which a republication license is sought includes third party materials (such as photographs, illustrations, graphs, inserts and similar materials) which are identified in such material as having been used by permission, User is responsible for identifying, and seeking separate licenses (under this Service or otherwise) for, any of such third party materials; without a separate license, such third party materials may not be used.

3.5 Use of proper copyright notice for a Work is required as a condition of any license granted under the Service. Unless otherwise provided in the Order Confirmation, a proper copyright notice will read substantially as follows: "Republished with permission of [Rightsholder's name], from [Work's title, author, volume, edition number and year of copyright]; permission conveyed through Copyright Clearance Center, Inc." Such notice must be provided in a reasonably legible font size and must be placed either immediately adjacent to the Work as used (for example, as part of a by-line or footnote but not as a separate electronic link) or in the place where substantially all other credits or notices for the new work containing the republished Work are located. Failure to include the required notice results in loss to the Rightsholder and CCC, and the User shall be liable to pay liquidated damages for each such failure equal to twice the use fee specified in the Order Confirmation, in addition to the use fee itself and any other fees and charges specified.

3.6 User may only make alterations to the Work if and as expressly set forth in the Order Confirmation. No Work may be used in any way that is defamatory, violates the rights of third parties (including such third parties' rights of copyright, privacy, publicity, or other tangible or intangible property), or is otherwise illegal, sexually explicit or obscene. In addition, User may not conjoin a Work with any other material that may result in damage to the reputation of the Rightsholder. User agrees to inform CCC if it becomes aware of any infringement of any rights in a Work and to cooperate with any reasonable request of CCC or the Rightsholder in connection therewith.

4. Indemnity. User hereby indemnifies and agrees to defend the Rightsholder and CCC, and their respective employees and directors, against all claims, liability, damages, costs and expenses, including legal fees and expenses, arising out of any use of a Work beyond the scope of the rights granted herein, or any use of a Work which has been altered in any unauthorized way by User, including claims of defamation or infringement of rights of copyright, publicity, privacy or other tangible or intangible property.

5. Limitation of Liability. UNDER NO CIRCUMSTANCES WILL CCC OR THE RIGHTSHOLDER BE LIABLE FOR ANY DIRECT, INDIRECT, CONSEQUENTIAL OR INCIDENTAL DAMAGES (INCLUDING WITHOUT LIMITATION DAMAGES FOR LOSS OF BUSINESS PROFITS OR INFORMATION, OR FOR BUSINESS INTERRUPTION) ARISING OUT OF THE USE OR INABILITY TO USE A WORK, EVEN IF ONE OF THEM HAS BEEN ADVISED OF THE POSSIBILITY OF SUCH DAMAGES. In any event, the total liability of the Rightsholder and CCC (including their respective employees and directors) shall not exceed the total amount actually paid by User for this license. User assumes full liability for the actions and omissions of its principals, employees, agents, affiliates, successors and assigns.

6. Limited Warranties. THE WORK(S) AND RIGHT(S) ARE PROVIDED "AS IS". CCC HAS THE RIGHT TO GRANT TO USER THE RIGHTS GRANTED IN THE ORDER CONFIRMATION DOCUMENT. CCC AND THE RIGHTSHOLDER DISCLAIM ALL OTHER WARRANTIES RELATING TO THE WORK(S) AND RIGHT(S), EITHER EXPRESS OR IMPLIED, INCLUDING WITHOUT LIMITATION IMPLIED WARRANTIES OF MERCHANTABILITY OR FITNESS FOR A PARTICULAR PURPOSE. ADDITIONAL RIGHTS MAY BE REQUIRED TO USE ILLUSTRATIONS, GRAPHS, PHOTOGRAPHS, ABSTRACTS, INSERTS OR OTHER PORTIONS OF THE WORK (AS OPPOSED TO THE ENTIRE WORK) IN A MANNER CONTEMPLATED

B.5 Copyright Permissions for reuse of Figure 5.1

BY USER; USER UNDERSTANDS AND AGREES THAT NEITHER CCC NOR THE RIGHTSHOLDER MAY HAVE SUCH ADDITIONAL RIGHTS TO GRANT.

7. Effect of Breach. Any failure by User to pay any amount when due, or any use by User of a Work beyond the scope of the license set forth in the Order Confirmation and/or these terms and conditions, shall be a material breach of the license created by the Order Confirmation and these terms and conditions. Any breach not cured within 30 days of written notice thereof shall result in immediate termination of such license without further notice. Any unauthorized (but licensable) use of a Work that is terminated immediately upon notice thereof may be liquidated by payment of the Rightsholder's ordinary license price therefor; any unauthorized (and unlicensable) use that is not terminated immediately for any reason (including, for example, because materials containing the Work cannot reasonably be recalled) will be subject to all remedies available at law or in equity, but in no event to a payment of less than three times the Rightsholder's ordinary license price for the most closely analogous licensable use plus Rightsholder's and/or CCC's costs and expenses incurred in collecting such payment.

8. Miscellaneous.

8.1 User acknowledges that CCC may, from time to time, make changes or additions to the Service or to these terms and conditions, and CCC reserves the right to send notice to the User by electronic mail or otherwise for the purposes of notifying User of such changes or additions; provided that any such changes or additions shall not apply to permissions already secured and paid for.

8.2 Use of User-related information collected through the Service is governed by CCC's privacy policy, available online here:

<http://www.copyright.com/content/cc3/en/tools/footer/privacypolicy.html>.

8.3 The licensing transaction described in the Order Confirmation is personal to User. Therefore, User may not assign or transfer to any other person (whether a natural person or an organization of any kind) the license created by the Order Confirmation and these terms and conditions or any rights granted hereunder; provided, however, that User may assign such license in its entirety on written notice to CCC in the event of a transfer of all or substantially all of User's rights in the new material which includes the Work(s) licensed under this Service.

8.4 No amendment or waiver of any terms is binding unless set forth in writing and signed by the parties. The Rightsholder and CCC hereby object to any terms contained in any writing prepared by the User or its principals, employees, agents or affiliates and purporting to govern or otherwise relate to the licensing transaction described in the Order Confirmation, which terms are in any way inconsistent with any terms set forth in the Order Confirmation and/or in these terms and conditions or CCC's standard operating procedures, whether such writing is prepared prior to, simultaneously with or subsequent to the Order Confirmation, and whether such writing appears on a copy of the Order Confirmation or in a separate instrument.

8.5 The licensing transaction described in the Order Confirmation document shall be governed by and construed under the law of the State of New York, USA, without regard to the principles thereof of conflicts of law. Any case, controversy, suit, action, or proceeding arising out of, in connection with, or related to such licensing transaction shall be brought, at CCC's sole discretion, in any federal or state court located in the County of New York, State of New York, USA, or in any federal or state court whose geographical jurisdiction covers the location of the Rightsholder set forth in the Order Confirmation. The parties expressly submit to the personal jurisdiction and venue of each such federal or state court. If you have any comments or questions about the Service or Copyright Clearance Center, please contact us at 978-750-8400 or send an e-mail to info@copyright.com.

v 1.1

Questions? customercare@copyright.com or +1-855-239-3415 (toll free in the US) or +1-978-646-2777.

B.6 Copyright Permissions for reuse of Figure 5.3

Gopalakrishnan, Krishnakumar

From: Southward, Steve <[REDACTED]@exchange.vt.edu>
Sent: 09 October 2018 17:41
To: Gopalakrishnan, Krishnakumar
Subject: Re: Request for permission to adapt a schematic from your lecture notes for thesis reuse

Hi Krishna,

Sorry for the delay in responding. You are welcome to use my slide with citation as you have done. Good luck!

Dr. Southward

On Sep 26, 2018, at 2:55 PM, Gopalakrishnan, Krishnakumar <[REDACTED]@imperial.ac.uk> wrote:

Dear Prof Southward,

Greetings!

Hope you remember me from our previous interactions. I am Krishnakumar Gopalakrishnan (Krishna), who was registered at Virginia Tech from Fall 2009 through Fall 2011 as an M.Eng student in the Electrical and Computer Engineering (ECE) department. In Spring 2011, I had registered for and completed the credit-bearing course 'ME5506 – Advanced Control Engineering', taught by you. I am therefore in possession of the electronic PDFs of the lecture notes among other associated material for this course.

For use in my PhD thesis (non-profit CC-BY-NC-ND use), I'd like to adapt a schematic from L03 of your course notes that presents the timing diagram of a real-time control/software loop. I shall of course cite the source of the original schematic in the figure caption.

I have attached my adapted version herewith for your perusal. I hope you can accord me with your permissions for thesis reuse.

Best Regards,
Krishna

<timing_diagram_large.png>

B.7 Copyright Permissions for reuse of Figure 5.4

Gopalakrishnan, Krishnakumar

From: Gregory Plett <[REDACTED]>
Sent: 28 September 2018 20:28
To: Gopalakrishnan, Krishnakumar
Subject: Re: Request for permission to reuse a schematic from your lecture notes in my PhD thesis

Yes, you are welcome to use/adapt the figure. I'm sure I stole it from somewhere myself.

Congratulations for reaching this point!

Dr. Gregory L. Plett
Professor, Department of Electrical and Computer Engineering
Director, GATE Center of Excellence in Innovative Drivetrains in Electric Automotive Technology Education
University of Colorado Colorado Springs
1420 Austin Bluffs Parkway, Colorado Springs, CO 80918
p: [REDACTED]; email: [REDACTED]

On Sep 28, 2018, at 10:13 AM, Gopalakrishnan, Krishnakumar <[REDACTED]@imperial.ac.uk> wrote:

Dear Prof Plett,

Greetings! How are you doing? I am about to submit the thesis of my thesis (hopefully early next week).

For use in my PhD thesis (non-profit, non-commercial CC-BY-NC-ND use), I'd like to adapt a schematic from Lecture 2 of ECE5540 notes that depicts a cartoon representation of the timing diagram of a real-time control/software loop. I shall of course cite the source of the original schematic in the caption.

I have attached the relevant schematic herewith for your perusal. I hope you can accord me with your permissions for thesis reuse.

Best Regards,
Krishna


<timing_diagram_simplified.PNG>

B.8 Copyright Permissions for reuse of Figure 5.13

ELSEVIER LICENSE TERMS AND CONDITIONS

Sep 27, 2018

This Agreement between Krishnakumar Gopalakrishnan ("You") and Elsevier ("Elsevier") consists of your license details and the terms and conditions provided by Elsevier and Copyright Clearance Center.

License Number	4436780559225
License date	Sep 26, 2018
Licensed Content Publisher	Elsevier
Licensed Content Publication	Energy
Licensed Content Title	Polynomial approximation pseudo-two-dimensional battery model for online application in embedded battery management system
Licensed Content Author	Zhongwei Deng,Lin Yang,Hao Deng,Yishan Cai,Dongdong Li
Licensed Content Date	Jan 1, 2018
Licensed Content Volume	142
Licensed Content Issue	n/a
Licensed Content Pages	13
Start Page	838
End Page	850
Type of Use	reuse in a thesis/dissertation
Portion	figures/tables/illustrations
Number of figures/tables/illustrations	1
Format	electronic
Are you the author of this Elsevier article?	No
Will you be translating?	No
Original figure numbers	Figure 1
Title of your thesis/dissertation	Computational modelling of lithium ion batteries for electric vehicle applications: analysis, design and implementation
Publisher of new work	Imperial College London
Author of new work	Dr Gregory J Offer
Expected completion date	Oct 2018
Estimated size (number of pages)	1
Requestor Location	Krishnakumar Gopalakrishnan  London, other W12 0UE United Kingdom Attn:
Publisher Tax ID	GB 494 6272 12
Total	0.00 GBP
Terms and Conditions	

INTRODUCTION

B.8 Copyright Permissions for reuse of Figure 5.13

1. The publisher for this copyrighted material is Elsevier. By clicking "accept" in connection with completing this licensing transaction, you agree that the following terms and conditions apply to this transaction (along with the Billing and Payment terms and conditions established by Copyright Clearance Center, Inc. ("CCC"), at the time that you opened your Rightslink account and that are available at any time at <http://myaccount.copyright.com>).

GENERAL TERMS

2. Elsevier hereby grants you permission to reproduce the aforementioned material subject to the terms and conditions indicated.

3. Acknowledgement: If any part of the material to be used (for example, figures) has appeared in our publication with credit or acknowledgement to another source, permission must also be sought from that source. If such permission is not obtained then that material may not be included in your publication/copies. Suitable acknowledgement to the source must be made, either as a footnote or in a reference list at the end of your publication, as follows:

"Reprinted from Publication title, Vol /edition number, Author(s), Title of article / title of chapter, Pages No., Copyright (Year), with permission from Elsevier [OR APPLICABLE SOCIETY COPYRIGHT OWNER]." Also Lancet special credit - "Reprinted from The Lancet, Vol. number, Author(s), Title of article, Pages No., Copyright (Year), with permission from Elsevier."

4. Reproduction of this material is confined to the purpose and/or media for which permission is hereby given.

5. Altering/Modifying Material: Not Permitted. However figures and illustrations may be altered/adapted minimally to serve your work. Any other abbreviations, additions, deletions and/or any other alterations shall be made only with prior written authorization of Elsevier Ltd. (Please contact Elsevier at permissions@elsevier.com). No modifications can be made to any Lancet figures/tables and they must be reproduced in full.

6. If the permission fee for the requested use of our material is waived in this instance, please be advised that your future requests for Elsevier materials may attract a fee.

7. Reservation of Rights: Publisher reserves all rights not specifically granted in the combination of (i) the license details provided by you and accepted in the course of this licensing transaction, (ii) these terms and conditions and (iii) CCC's Billing and Payment terms and conditions.

8. License Contingent Upon Payment: While you may exercise the rights licensed immediately upon issuance of the license at the end of the licensing process for the transaction, provided that you have disclosed complete and accurate details of your proposed use, no license is finally effective unless and until full payment is received from you (either by publisher or by CCC) as provided in CCC's Billing and Payment terms and conditions. If full payment is not received on a timely basis, then any license preliminarily granted shall be deemed automatically revoked and shall be void as if never granted. Further, in the event that you breach any of these terms and conditions or any of CCC's Billing and Payment terms and conditions, the license is automatically revoked and shall be void as if never granted. Use of materials as described in a revoked license, as well as any use of the materials beyond the scope of an unrevoked license, may constitute copyright infringement and publisher reserves the right to take any and all action to protect its copyright in the materials.

9. Warranties: Publisher makes no representations or warranties with respect to the licensed material.

10. Indemnity: You hereby indemnify and agree to hold harmless publisher and CCC, and their respective officers, directors, employees and agents, from and against any and all claims arising out of your use of the licensed material other than as specifically authorized pursuant to this license.

11. No Transfer of License: This license is personal to you and may not be sublicensed, assigned, or transferred by you to any other person without publisher's written permission.

12. No Amendment Except in Writing: This license may not be amended except in a writing signed by both parties (or, in the case of publisher, by CCC on publisher's behalf).

13. Objection to Contrary Terms: Publisher hereby objects to any terms contained in any purchase order, acknowledgment, check endorsement or other writing prepared by you, which terms are inconsistent with these terms and conditions or CCC's Billing and Payment

terms and conditions. These terms and conditions, together with CCC's Billing and Payment terms and conditions (which are incorporated herein), comprise the entire agreement between you and publisher (and CCC) concerning this licensing transaction. In the event of any conflict between your obligations established by these terms and conditions and those established by CCC's Billing and Payment terms and conditions, these terms and conditions shall control.

14. **Revocation:** Elsevier or Copyright Clearance Center may deny the permissions described in this License at their sole discretion, for any reason or no reason, with a full refund payable to you. Notice of such denial will be made using the contact information provided by you. Failure to receive such notice will not alter or invalidate the denial. In no event will Elsevier or Copyright Clearance Center be responsible or liable for any costs, expenses or damage incurred by you as a result of a denial of your permission request, other than a refund of the amount(s) paid by you to Elsevier and/or Copyright Clearance Center for denied permissions.

LIMITED LICENSE

The following terms and conditions apply only to specific license types:

15. **Translation:** This permission is granted for non-exclusive world **English** rights only unless your license was granted for translation rights. If you licensed translation rights you may only translate this content into the languages you requested. A professional translator must perform all translations and reproduce the content word for word preserving the integrity of the article.

16. **Posting licensed content on any Website:** The following terms and conditions apply as follows: Licensing material from an Elsevier journal: All content posted to the web site must maintain the copyright information line on the bottom of each image; A hyper-text must be included to the Homepage of the journal from which you are licensing at

<http://www.sciencedirect.com/science/journal/xxxxx> or the Elsevier homepage for books at <http://www.elsevier.com>; Central Storage: This license does not include permission for a scanned version of the material to be stored in a central repository such as that provided by Heron/XanEdu.

Licensing material from an Elsevier book: A hyper-text link must be included to the Elsevier homepage at <http://www.elsevier.com>. All content posted to the web site must maintain the copyright information line on the bottom of each image.

Posting licensed content on Electronic reserve: In addition to the above the following clauses are applicable: The web site must be password-protected and made available only to bona fide students registered on a relevant course. This permission is granted for 1 year only. You may obtain a new license for future website posting.

17. **For journal authors:** the following clauses are applicable in addition to the above:

Preprints:

A preprint is an author's own write-up of research results and analysis, it has not been peer-reviewed, nor has it had any other value added to it by a publisher (such as formatting, copyright, technical enhancement etc.).

Authors can share their preprints anywhere at any time. Preprints should not be added to or enhanced in any way in order to appear more like, or to substitute for, the final versions of articles however authors can update their preprints on arXiv or RePEc with their Accepted Author Manuscript (see below).

If accepted for publication, we encourage authors to link from the preprint to their formal publication via its DOI. Millions of researchers have access to the formal publications on ScienceDirect, and so links will help users to find, access, cite and use the best available version. Please note that Cell Press, The Lancet and some society-owned have different preprint policies. Information on these policies is available on the journal homepage.

Accepted Author Manuscripts: An accepted author manuscript is the manuscript of an article that has been accepted for publication and which typically includes author-incorporated changes suggested during submission, peer review and editor-author communications.

Authors can share their accepted author manuscript:

- immediately

B.8 Copyright Permissions for reuse of Figure 5.13

- via their non-commercial person homepage or blog
- by updating a preprint in arXiv or RePEc with the accepted manuscript
- via their research institute or institutional repository for internal institutional uses or as part of an invitation-only research collaboration work-group
- directly by providing copies to their students or to research collaborators for their personal use
- for private scholarly sharing as part of an invitation-only work group on commercial sites with which Elsevier has an agreement
- After the embargo period
 - via non-commercial hosting platforms such as their institutional repository
 - via commercial sites with which Elsevier has an agreement

In all cases accepted manuscripts should:

- link to the formal publication via its DOI
- bear a CC-BY-NC-ND license - this is easy to do
- if aggregated with other manuscripts, for example in a repository or other site, be shared in alignment with our hosting policy not be added to or enhanced in any way to appear more like, or to substitute for, the published journal article.

Published journal article (JPA): A published journal article (PJA) is the definitive final record of published research that appears or will appear in the journal and embodies all value-adding publishing activities including peer review co-ordination, copy-editing, formatting, (if relevant) pagination and online enrichment.

Policies for sharing publishing journal articles differ for subscription and gold open access articles:

Subscription Articles: If you are an author, please share a link to your article rather than the full-text. Millions of researchers have access to the formal publications on ScienceDirect, and so links will help your users to find, access, cite, and use the best available version.

Theses and dissertations which contain embedded PJAs as part of the formal submission can be posted publicly by the awarding institution with DOI links back to the formal publications on ScienceDirect.

If you are affiliated with a library that subscribes to ScienceDirect you have additional private sharing rights for others' research accessed under that agreement. This includes use for classroom teaching and internal training at the institution (including use in course packs and courseware programs), and inclusion of the article for grant funding purposes.

Gold Open Access Articles: May be shared according to the author-selected end-user license and should contain a [CrossMark logo](#), the end user license, and a DOI link to the formal publication on ScienceDirect.

Please refer to Elsevier's [posting policy](#) for further information.

18. **For book authors** the following clauses are applicable in addition to the above:

Authors are permitted to place a brief summary of their work online only. You are not allowed to download and post the published electronic version of your chapter, nor may you scan the printed edition to create an electronic version. **Posting to a repository:** Authors are permitted to post a summary of their chapter only in their institution's repository.

19. **Thesis/Dissertation:** If your license is for use in a thesis/dissertation your thesis may be submitted to your institution in either print or electronic form. Should your thesis be published commercially, please reapply for permission. These requirements include permission for the Library and Archives of Canada to supply single copies, on demand, of the complete thesis and include permission for Proquest/UMI to supply single copies, on demand, of the complete thesis. Should your thesis be published commercially, please reapply for permission. Theses and dissertations which contain embedded PJAs as part of the formal submission can be posted publicly by the awarding institution with DOI links back to the formal publications on ScienceDirect.

Elsevier Open Access Terms and Conditions

You can publish open access with Elsevier in hundreds of open access journals or in nearly 2000 established subscription journals that support open access publishing. Permitted third

B.8 Copyright Permissions for reuse of Figure 5.13

party re-use of these open access articles is defined by the author's choice of Creative Commons user license. See our [open access license policy](#) for more information.

Terms & Conditions applicable to all Open Access articles published with Elsevier:

Any reuse of the article must not represent the author as endorsing the adaptation of the article nor should the article be modified in such a way as to damage the author's honour or reputation. If any changes have been made, such changes must be clearly indicated.

The author(s) must be appropriately credited and we ask that you include the end user license and a DOI link to the formal publication on ScienceDirect.

If any part of the material to be used (for example, figures) has appeared in our publication with credit or acknowledgement to another source it is the responsibility of the user to ensure their reuse complies with the terms and conditions determined by the rights holder.

Additional Terms & Conditions applicable to each Creative Commons user license:

CC BY: The CC-BY license allows users to copy, to create extracts, abstracts and new works from the Article, to alter and revise the Article and to make commercial use of the Article (including reuse and/or resale of the Article by commercial entities), provided the user gives appropriate credit (with a link to the formal publication through the relevant DOI), provides a link to the license, indicates if changes were made and the licensor is not represented as endorsing the use made of the work. The full details of the license are available at <http://creativecommons.org/licenses/by/4.0>.

CC BY NC SA: The CC BY-NC-SA license allows users to copy, to create extracts, abstracts and new works from the Article, to alter and revise the Article, provided this is not done for commercial purposes, and that the user gives appropriate credit (with a link to the formal publication through the relevant DOI), provides a link to the license, indicates if changes were made and the licensor is not represented as endorsing the use made of the work. Further, any new works must be made available on the same conditions. The full details of the license are available at <http://creativecommons.org/licenses/by-nc-sa/4.0>.

CC BY NC ND: The CC BY-NC-ND license allows users to copy and distribute the Article, provided this is not done for commercial purposes and further does not permit distribution of the Article if it is changed or edited in any way, and provided the user gives appropriate credit (with a link to the formal publication through the relevant DOI), provides a link to the license, and that the licensor is not represented as endorsing the use made of the work. The full details of the license are available at <http://creativecommons.org/licenses/by-nc-nd/4.0>.

Any commercial reuse of Open Access articles published with a CC BY NC SA or CC BY NC ND license requires permission from Elsevier and will be subject to a fee.

Commercial reuse includes:

- Associating advertising with the full text of the Article
- Charging fees for document delivery or access
- Article aggregation
- Systematic distribution via e-mail lists or share buttons

Posting or linking by commercial companies for use by customers of those companies.

20. Other Conditions:

v1.9

Questions? customercare@copyright.com or +1-855-239-3415 (toll free in the US) or +1-978-646-2777.



Colophon

This thesis was created using $\text{\LaTeX} 2_{\epsilon}$ and Bib \LaTeX /Biber wherein the source code was edited in neovim using the vimtex plugin. The typesetting engine is Lua \TeX , Version 1.10.0 (TeX Live 2019). The body copy is set in a 12pt Libertinus Serif text with the section headers set in Libertinus Sans. A value of 1.618 (golden ratio) is used as the spacing factor between baselines in the body copy. Source code listings are set in 9pt Latin Modern Mono.